A Numerical Model of Glaciohydraulic Supercooling

Thermodynamics and Sediment Entrainment

by

Timothy Thomas Creyts

B.Sc. (Honours), The Pennsylvania State University, 1998

A THESIS SUBMITTED IN PARTIAL FULFILMENT OF
THE REQUIREMENTS FOR THE DEGREE OF

Doctor of Philosophy

in

The Faculty of Graduate Studies

(Geophysics)

The University Of British Columbia

July 26, 2007

Abstract

Beneath many glaciers and ice sheets, hydrology influences or controls a variety of basal processes. Glaciohydraulic supercooling is a process whereby water freezes englacially or subglacially because its internal temperature is below the bulk freezing temperature. Water supercools when it is at its freezing point and flows from an area of higher pressure (lower ambient temperature) to an area of lower pressure (higher ambient temperature) without equilibrating its internal energy. The process is dependent on the configuration of the water flow path relative to the pressure gradient driving flow.

I formulate the governing equations of mass, linear momentum, and internal energy for time-dependent clear water flow based on previous work (Clarke, 2003; Spring & Hutter, 1981, 1982). Because field evidence and steady-state theory point to water distributing laterally across the bed, I modify this theory to account for an aperture that is much wider than deep, which I refer to as a sheet. Ice accretion terms are formulated with porosity because accreting ice has residual porosity. Ice intrusion into such a water sheet is not described in the literature, and I formulate intrusion based on previous work as well as ideas gained from subglacial cavity formation. In addition, I modify the clear water equations to include erosion and deposition of sediment along the glacier bed and incorporation of sediment into the accreted ice. Furthermore, water may leave the ice–bed interface and flow through the glacier pore space because subglacial water pressure is relatively high when supercooling occurs. To this end, I develop an englacial water-flow model that incorporates changes in ice porosity based on creep closure and ice melt or accretion.

Simulations reveal behavior that cannot be inferred from simplified models. For example, while total ice accretion is comparable to field estimates, locations of simulated ice accretion along the ice–bed interface conflict with steady state models, which tend to overpredict accretion amounts. Simulations also indicate that much sediment deposition occurs prior to water being supercooled. Sediment deposition tends to smooth subglacial topography rather than enhance it. Additional results and implications of numerical simulations are discussed.

Table of Contents

List of Tables

List of Figures

List of Symbols

Notation

Superscripts are both geometrical and phasic. The geometrical superscripts $^{\mathrm{b}}$, $^{\mathrm{e}}$, and $^{\mathrm{r}}$ are used for variables in the subglacial, englacial, and supraglacial water systems, respectively. In addition, an upstream crevasse is denoted by $^{\mathrm{c}}$. Phasic quantities, such as mass densities, will be referred to with the superscripts $^{\mathrm{w}}$, $^{\mathrm{i}}$, and $^{\mathrm{s}}$, for water, ice or glacier, and sediment, respectively. Throughout the thesis, if any term with a superscript is raised to a power, then the term is enclosed in parentheses before the index is placed on the term.

Subscripts are less systematic and will be defined for quantities as they appear. Common subscripts include but are not limited to $_i$ and $_j$ as indices, $_a$ for areal, $_e$ for effective or equilibrium, $_T$ for thermal, $_H$ for hydraulic, and $_v$ for volumetric. Where closure of the ice into the subglacial water sheet is discussed, $_r$ indicates the process of regelation, and $_c$ indicates viscous creep of ice. Where sediments are discussed, the subscripts $_b$ and $_s$ indicate bedload and suspended load, respectively; and $_{cr}$ indicates a critical parameter relating to the threshold of sediment motion.

Latin Letters

$\mathcal{A}$	Flow law coefficient (compare with $\mathcal{B}$ below)	$\mathrm{s}^{-1}\ \mathrm{Pa}^{-n}$	eq. (3.7), p. 37,
A^{c}	Cross-sectional area of a crevasse	m^2	eq. (F.10), p. 195,
A^{i}	Area of ice exposed to subglacial water and sediment	m^2	eq. (3.10), p. 38,
A_i^{s}	Total area of ith grain size opposing ice intrusion	m^2	eq. (3.11), p. 39,
A^{s}	Area of sediment touching the glacier base	m^2	eq. (3.10), p. 38,
A^{w}	Area of water touching the glacier base	m^2	eq. (3.10), p. 38,
A_e	Effective area	m^2	eq. (3.3), p. 35,
A_{ij}	Area of the ijth grid cell	m^2	eq. (G.2), p. 211,
$\mathcal{B}$	Flow law coefficient ($= \mathcal{A}^{-1/n}$)	$\mathrm{Pa}\ \mathrm{s}^{1/n}$	eq. (2.17), p. 23,
C'	Grain Chézy coefficient	$\mathrm{m}^{1/2}\ \mathrm{s}^{-1}$	eq. (E.3), p. 185,
C_1	Nondimensional coefficient	[unitless]	eq. (2.34), p. 28,
C_2	Nondimensional coefficient, $(1 - \beta c_p^{\mathrm{w}} \rho^{\mathrm{w}})$	[unitless]	eq. (2.41), p. 31,
C_3	Sediment entrainment coefficient for basal ice	[unitless]	eq. (4.34), p. 69,
C_x	Arbitrary geometrical constant for a synthetic overdeepening	$\mathrm{m}^{1/2o_x}$	eq. (A.2), p. 169,
D	Grain size diameter	m	eq. (4.18), p. 61,
D_*	Nondimensional particle parameter	[unitless]	eq. (4.21), p. 65,
D_0	Reference grain size diameter	m	eq. (4.18), p. 61,
D_s	Characteristic grain diameter for suspended sediment	m	eq. (E.19), p. 189,
D_X	Representative grain diameter of the Xth percentile of the grain size distribution	m	eq. (4.20), p. 65,

E	Enthalpy	J	eq. (2.6), p. 18,
E^{w}	Internal energy of water	J	eq. (5.16), p. 76,
$\mathcal{F}_s$	Suspended load distribution correction parameter	[unitless]	eq. (4.28), p. 66,
F	Force on an obstacle	N	eq. (3.2), p. 35,
F^{i}	Force of overlying ice	N	eq. (3.11), p. 39,
F^{s}	Force of sediment against ice	N	eq. (3.11), p. 39,
F^{w}	Force of water against ice	N	eq. (3.11), p. 39,
F_ℓ^{w}	Fracture density per unit length	m^{-1}	eq. (5.19), p. 77,
G	Error function for the ice intrusion solution	*varies*	eq. (C.1), p. 174,
H^{b}	Subglacial water sheet thickness	m	eq. (2.2), p. 17,
$H^{\mathrm{b}}_{\mathrm{max}}$	Maximum value of H^{b}	m	eq. (F.45), p. 208,
H^{r}	Supraglacial water depth	m	eq. (5.29), p. 81,
$\mathbf{K}^{\mathrm{r}}_{\mathbf{H}}$	Supraglacial hydraulic conductivity tensor	$\mathrm{m\ s}^{-1}$	eq. (5.30), p. 82,
K^{w}_H	Hydraulic conductivity	$\mathrm{m\ s}^{-1}$	eq. (5.1), p. 73,
K^{w}_T	Thermal conductivity of water	$\mathrm{W\ m}^{-1}\ \mathrm{K}^{-1}$	eq. (2.33), p. 28,
$K_{e:T}$	Effective thermal conductivity	$\mathrm{W\ m}^{-1}\ \mathrm{K}^{-1}$	eq. (3.2), p. 35,
L	Latent heat of water	$\mathrm{J\ kg}^{-1}$	eq. (2.29), p. 27,
L^{s}_e	Adaptation length for sediment motion	m	eq. (4.4), p. 56,
$M^{\mathrm{b:e}}$	Mass of accreted ice	kg	eq. (D.15), p. 181,
M^{f}	Fluid mixture mass of water and sediment	kg	eq. (D.1), p. 177,
M^{s}	Mass of sediment	kg	eq. (4.1), p. 55,
M^{w}	Mass of water	kg	eq. (2.10), p. 21,
M_0	Mass of the bed below z^{s}	kg	eq. (4.5), p. 57,
Nu	Nusselt number	[unitless]	eq. (2.34), p. 28,
N	Number	[unitless]	eq. (3.11), p. 39,
N^{s}	Number of grains	[unitless]	eq. (4.18), p. 61,
N^{s}_0	Reference number of grains of radius r_0	[unitless]	eq. (3.23), p. 43,
$N^{\mathrm{s}}_{a:i}$	Number of sediments of the i grain size	[unitless]	eq. (3.21), p. 42,
Pr	Prandtl number	[unitless]	eq. (2.34), p. 28,
P^{i}	Melting perimeter	m	eq. (2.5), p. 18,
P^{w}	Hydraulic perimeter	m	eq. (2.2), p. 17,
Q^{b}	Subglacial water discharge	$\mathrm{m}^3\ \mathrm{s}^{-1}$	eq. (2.41), p. 31,
Q_{melt}	Flux of meltwater into a crevasse	$\mathrm{m}^3\ \mathrm{s}^{-1}$	eq. (F.10), p. 195,
$\mathcal{R}$	Bed to surface slope ratio	[unitless]	eq. (2.44), p. 31,
Re	Reynolds number	[unitless]	eq. (2.34), p. 28,
R	Radius	m	eq. (5.24), p. 79,
R^{b}	Channel radius	m	eq. (2.2), p. 17,
R_h	Hydraulic mean radius	m	eq. (2.3), p. 17,
$\widehat{S}$	Instantaneous ice cross-sectional area, $S^{\mathrm{i}} - S^{\mathrm{w}}$	m^2	eq. (2.11), p. 21,
S	Englacial water cross section	m^2	eq. (5.2), p. 73,
S^{b}	Subglacial channel cross section	m^2	eq. (2.15), p. 22,
S^{i}	Channel cross-sectional area of ice	m^2	eq. (2.11), p. 21,
S^{w}	Hydraulic cross section	m^2	eq. (2.2), p. 17,
$\mathcal{T}$	Transport stage parameter	[unitless]	eq. (4.20), p. 65,
T	Temperature	K or °C	eq. (2.6), p. 18,
T^{b}	Water temperature in the subglacial system	T	eq. (2.9), p. 20,

T^{c}	Crevasse water temperature	°C	eq. (F.12), p. 195,
T_{mp}	Temperature of the melting point	K or °C	eq. (2.8), p. 19,
T^{w}	Temperature of water	K	eq. (5.17), p. 77,
T_0	Reference temperature	K	eq. (2.6), p. 18,
V	Volume	m^3	eq. (2.6), p. 18,
V_e	Effective volume	m^3	eq. (3.2), p. 35,
W	Hydraulic/glacier unit width	m	eq. (2.2), p. 17,
X	General independent coordinate for the vertical coordinate transformation	m or s	eq. (F.27), p. 201,
$\mathcal{Z}$	Suspension parameter	[unitless]	eq. (E.12), p. 188,
$\mathcal{Z}'$	Suspension parameter for sediment	[unitless]	eq. (4.29), p. 66,
$Z^{\mathrm{b:e}}$	Accreted ice thickness	m	eq. (2.19), p. 23,
$Z_0^{\mathrm{b:e}}$	Threshold accreted ice thickness	m	eq. (D.17), p. 181,
Z^{c}	Water depth in an upstream crevasse	m	eq. (F.10), p. 195,
Z^{i}	Glacier thickness	m	eq. (2.18), p. 23,
a^{s}	Individual grain area	m^2	eq. (3.11), p. 38,
b	Fracture width	m	eq. (5.19), p. 77,
c_p^{w}	Specific heat of water	$\mathrm{J\ kg^{-1}\ K^{-1}}$	eq. (2.29), p. 27,
d^{b}	Representative water depth for suspended sediment load	m	eq. (4.26), p. 66,
d_v	Englacial pore closure rate	$\mathrm{kg\ m^{-3}\ s^{-1}}$	eq. (5.2), p. 73,
f_d^{i}	Darcy-Weisbach friction coefficient for ice	[unitless]	eq. (2.25), p. 25,
f_d^{i}	Darcy-Weisbach friction coefficient for sediment	[unitless]	eq. (2.25), p. 25,
f_a^{s}	Number of grains per unit size of a given texture per unit area of the bed	m^{-4}	eq. (3.11), p. 38,
f_d	Darcy-Weisbach friction coefficient	[unitless]	eq. (2.24), p. 25,
f_d'	Grain Darcy-Weisbach friction coefficient	[unitless]	eq. (4.31), p. 67,
f_d''	Form Darcy-Weisbach friction coefficient	[unitless]	eq. (4.31), p. 67,
f_f	Fanning friction coefficient ($f_d/4$))	[unitless]	eq. (2.24), p. 25,
g	Gravitational acceleration	$\mathrm{m\ s^{-2}}$	eq. (2.21), p. 24,
h	Heat transfer coefficient	$\mathrm{W\ m^{-2}\ K^{-1}}$	eq. (2.33), p. 28,
i	Subscript for ith grain size	[unitless]	eq. (3.11), p. 39,
i	Subscript for ith horizontal grid location	[unitless]	eq. (F.1), p. 190,
j	Subscript for jth vertical grid location	[unitless]	eq. (F.31), p. 202,
k	Permeability	m^2	eq. (5.1), p. 73,
k^{s}	Nikuradse sand bed roughness	m	eq. (E.17), p. 188,
ℓ_1	Length scale	m	eq. (2.33), p. 28,
l_e	Effective length scale	m	eq. (3.8), p. 37,
$\tilde{m}$	Melt rate per unit width	$\mathrm{kg\ m^{-2}\ s^{-1}}$	eq. (2.16), p. 22,
m	Fractal index (as an exponent)	[unitless]	eq. (3.23), p. 43,
m	Melt rate	$\mathrm{kg\ m^{-1}\ s^{-1}}$	eq. (2.13), p. 21,
m_v	Volumetric melt rate	$\mathrm{kg\ m^{-3}\ s^{-1}}$	eq. (5.2), p. 73,
n	Flow law index (as an exponent)	[unitless]	eq. (2.17), p. 23,
n_p^{i}	Porosity of ice	[unitless]	eq. (2.12), p. 21,

n_a^{s}	Mobile fraction of the bed	[unitless]	eq. (4.23), p. 65,
n_p^{s}	Porosity of the unlithified bed	[unitless]	eq. (4.5), p. 57,
n_a^{w}	Fractional area of the bed not covered by sediment	[unitless]	eq. (F.45), p. 208,
o_x	Index for a synthetic overdeepening	[unitless]	eq. (A.2), p. 169,
p	Pressure	Pa	eq. (2.6), p. 18,
p^{b}	Subglacial water pressure	Pa	eq. (2.15), p. 22,
p^{c}	Pressure in the upstream crevasse	Pa	eq. (F.12), p. 195,
p^{i}	Ice overburden pressure	Pa	eq. (2.17), p. 23,
p^{w}	Water pressure	Pa	eq. (2.8), p. 19,
$\mathbf{q}^{\mathrm{w}}$	Volumetric water flow rate per unit surface area	m s^{-1}	eq. (5.1), p. 73,
$\mathbf{q_T}$	Heat flux vector	W m^{-2}	eq. (2.33), p. 28,
$\tilde{q}^{\mathrm{s}}$	Volumetric sediment flux per unit water width	m^2 s^{-1}	eq. (4.3), p. 56,
$\tilde{q}_e^{\mathrm{s}}$	Equilibrium sediment flux per unit water width	m^2 s^{-1}	eq. (4.4), p. 56,
$\tilde{q}_{e:b}$	Equilibrium bed load flux per unit width	m^2 s^{-1}	eq. (4.19), p. 65,
$\tilde{q}_{e:s}$	Equilibrium suspended load flux per unit width	m^2 s^{-1}	eq. (4.26), p. 66,
q_z^{b}	Specific water flux between the englacial and subglacial water systems	m s^{-1}	eq. (5.31), p. 82,
q^{s}	Volumetric sediment flux	m^3 s^{-1}	eq. (4.9), p. 57,
q_z^{r}	Water flux from a perched supraglacial aquifer	m s^{-1}	eq. (5.29), p. 81,
q^{w}	Magnitude of $\mathbf{q}^{\mathrm{w}}$	m s^{-1}	eq. (5.24), p. 79,
q_T	Magnitude of $\mathbf{q_T}$	W m^{-2}	eq. (2.33), p. 28,
r_0	Reference grain radius	m	eq. (3.23), p. 43,
r_i	Grain radius the i grain size	m	eq. (3.18), p. 42,
s	Along-path coordinate	m	eq. (2.1), p. 15,
t	Time	s	eq. (2.9), p. 20,
$\mathbf{u}^{\mathrm{r}}$	Supraglacial water velocity vector	m s^{-1}	eq. (5.30), p. 82,
$\mathbf{u}^{\mathrm{w}}$	Water velocity vector	m s^{-1}	eq. (5.2), p. 73,
u^{b}	Along-path subglacial water velocity	m s^{-1}	eq. (2.9), p. 20,
u_s^{s}	Sediment velocity along s	m s^{-1}	eq. (D.6), p. 178,
u^{w}	Magnitude of $\mathbf{u}^{\mathrm{w}}$	m s^{-1}	eq. (5.24), p. 79,
u_s^{w}	Water velocity along s	m s^{-1}	eq. (2.13), p. 21,
$u_{*,cr}$	Critical bed shear velocity	m s^{-1}	eq. (E.2), p. 185,
u_*	Bed shear velocity	m s^{-1}	eq. (E.4), p. 185,
u_*'	Bed shear velocity related to grains	m s^{-1}	eq. (E.2), p. 185,
u_b	Bed load velocity	m s^{-1}	eq. (4.19), p. 65,
v	Total ice velocity past an obstacle	m s^{-1}	eq. (3.1), p. 34,
v_c	Creep velocity past an obstacle	m s^{-1}	eq. (3.1), p. 34,
v_i	Intrusion velocity for the i grain size	m s^{-1}	eq. (3.16), p. 40,
v_r	Regelation velocity past an obstacle	m s^{-1}	eq. (3.1), p. 34,
w^{s}	Grain fall velocity	m s^{-1}	eq. (E.10), p. 187,
x	Horizontal coordinate longitudinal to water flow	m	eq. (2.1), p. 15,
x_0	Terminal horizontal location of the overdeepening	m	eq. (A.2), p. 169,
x_l	Maximum length of a synthetic overdeepening	m	eq. (A.2), p. 169,
x_u	Horizontal location of the start of a synthetic adverse slope	m	eq. (A.2), p. 169,

x_w	Horizontal location of the onset of a constant synthetic adverse slope (wedge-shape)	m	eq. (A.2), p. 169,
y	Horizontal coordinate transverse to water flow	m	eq. (2.1), p. 15,
z	Vertical coordinate	m	eq. (2.1), p. 15,
z^{b}	Elevation of the subglacial water–ice interface	m	eq. (2.21), p. 24,
z_0^{b}	Water exit elevation from a synthetic overdeepening	m	eq. (A.2), p. 169,
z_l^{b}	Water entrance elevation in a synthetic overdeepening	m	eq. (A.2), p. 169,
z^{c}	Elevation of water in an upstream crevasse	m	eq. (F.10), p. 195,
z^{s}	Elevation of the subglacial sediment horizon at the base of the water system	m	eq. (4.1), p. 55,
z_0	Elevation of an arbitrary datum below z^{s}	m	eq. (4.5), p. 57,

Greek Letters

α^{b}	Angle of the glacier base	rad	eq. (2.41), p. 31,
α^{r}	Angle of the glacier surface	rad	eq. (2.41), p. 31,
β	Pressure melting coefficient, $\partial T/\partial p$	K Pa^{-1}	eq. (2.8), p. 19,
β^{s}	Turbulent eddy parameter	[unitless]	eq. (E.12), p. 188,
γ^{b}	Subglacial water compressibility	Pa^{-1}	eq. (2.15), p. 22,
γ^{i}	Compressibility of ice	Pa^{-1}	eq. (5.12), p. 75,
γ_e^{i}	Effective compressibility of an ice matrix	Pa^{-1}	eq. (5.13), p. 75,
γ^{w}	Compressibility of water	Pa^{-1}	eq. (5.10), p. 75,
δ_T	Thermal boundary layer thickness	m	eq. (2.39), p. 30,
Δ^{s}	Bedform height	m	eq. (E.17), p. 188,
δ_b	Bed load layer thickness	m	eq. (4.19), p. 65,
δ_{ij}	Kronecker delta	[unitless]	eq. (C.1), p. 174,
δ_s	Suspended load reference height	m	eq. (4.29), p. 66,
$\dot{\epsilon}_z$	Vertical strain rate	s^{-1}	eq. (3.7), p. 37,
ε^{w}	Internal energy density of water	J kg^{-1}	eq. (5.16), p. 76,
θ	Azimuthal angle of a spherical sediment grain	rad	eq. (B.1), p. 172,
θ_{cr}	Critical mobility parameter	[unitless]	eq. (E.5), p. 185,
κ_T^{w}	Thermal diffusivity of water	$\mathrm{m}^2\ \mathrm{s}^{-1}$	eq. (2.35), p. 29,
κ^{s}	von Karman's constant	[unitless]	eq. (E.12), p. 188,
λ^{b}	Volumetric concentration of sediment in subglacial water	[unitless]	eq. (4.1), p. 55,
$\lambda_{e:b}^{\mathrm{b}}$	Equilibrium bed load concentration	[unitless]	eq. (4.19), p. 65,
λ^{i}	Volumetric sediment concentration in the ice	[unitless]	eq. (4.11), p. 58,
$\lambda_{e:s}$	Equilibrium suspended load concentration	[unitless]	eq. (4.26), p. 66,
$\lambda_{s:0}$	Reference suspended load concentration	[unitless]	eq. (4.28), p. 66,
μ	Dynamic viscosity of water	$\mathrm{kg}\ \mathrm{m}^{-1}\ \mathrm{s}^{-1}$	eq. (2.35), p. 29,
ν	Kinematic viscosity of water	$\mathrm{m}^2\ \mathrm{s}^{-1}$	eq. (2.35), p. 29,
ξ^{w}	Transformed vertical coordinate for englacial water	[unitless]	eq. (F.25), p. 200,
ϖ	Reynolds number exponent	[unitless]	eq. (2.34), p. 28,
ρ^{i}	Mass density of ice	$\mathrm{kg}\ \mathrm{m}^{-3}$	eq. (2.7), p. 18,

ρ^{w}	Mass density of water	kg m^{-3}	eq. (2.7), p. 18,
ρ^{f}	Fluid density of sediment–water mixture	kg m^{-3}	eq. (4.13), p. 59,
ρ_0^{i}	Density of ice at reference conditions	kg m^{-3}	eq. (5.12), p. 75,
ρ^{s}	Sediment mass density	kg m^{-3}	eq. (4.1), p. 55,
ρ_0^{w}	Density of water at reference conditions	kg m^{-3}	eq. (5.10), p. 75,
σ^{i}	Ice overburden stress	Pa	eq. (3.11), p. 39,
σ_i^{s}	Stress on the ith grain size	Pa	eq. (3.11), p. 39,
σ_c	Deviatoric stress available for creep in the vertical direction	Pa	eq. (3.4), p. 36,
σ_e	Total effective stress	Pa	eq. (3.14), p. 39,
σ_r	Normal stress available for regelation	Pa	eq. (3.3), p. 35,
$\sigma_{e:i}$	Effective stress on the i grain size	Pa	eq. (3.14), p. 39,
σ_i	Intermediate stress	Pa	eq. (3.13), p. 39,
σ_s	Geometric standard deviation of the sediment distribution	[unitless]	eq. (E.19), p. 189,
ς	Prandtl number exponent	[unitless]	eq. (2.34), p. 28,
τ	Equivalent shear stress	Pa	eq. (3.4), p. 36,
τ_0	Shear along the hydraulic perimeter	Pa	eq. (2.21), p. 24,
τ_0'	Grain shear along the bed	Pa	eq. (4.32), p. 67,
τ_0''	Form shear along the bed	Pa	eq. (4.32), p. 67,
τ_{xz}	Basal shear stress	Pa	eq. (3.4), p. 36,
$\tau^{\mathrm{b:e}}$	Time constant for accreted ice	s	eq. (D.17), p. 181,
τ^{c}	Time constant for a crevasse	s	eq. (F.11), p. 195,
τ^{r}	Supraglacial water infiltration time constant	s	eq. (5.27), p. 80,
τ_{cr}	Critical shear stress necessary for grain motion	Pa	eq. (E.6), p. 185,
ϕ^{b}	Subglacial hydraulic potential	Pa	eq. (2.22), p. 24,
Φ	Φ scale for grain size classification	$\log_2$(mm)	eq. (F.44), p. 206,
ϕ^{r}	Hydraulic potential of the glacier surface hydrology	Pa	eq. (5.28), p. 81,
ϕ^{w}	Hydraulic potential	Pa	eq. (5.1), p. 73,
φ	Suspension parameter correction	[unitless]	eq. (E.14), p. 188,
ψ	Polar angle of a spherical sediment grain	rad	eq. (B.1), p. 172,
Ψ^{i}	Sediment supply from the ice	kg m^{-1} s^{-1}	eq. (4.9), p. 57,
$\tilde{\Psi}^{\mathrm{i}}$	Sediment supply from the ice per unit width	kg m^{-2} s^{-1}	eq. (4.3), p. 56,
$\tilde{\Psi}^{\mathrm{s}}$	Sediment supply from the bed per unit width	kg m^{-2} s^{-1}	eq. (4.3), p. 56,
Ω	General variable on the centered grid	*varies*	eq. (F.1), p. 190,
ω	General variable on the staggered grid	*varies*	eq. (F.2), p. 190,

Acknowledgements

In many ways, this dissertation has been an extended effort in exploring phenomena that are captivating and complex. Over the course of my time in Vancouver, I have many people to thank for their kind criticisms, useful suggestions, editorial reviews, and other helpful actions that have contributed to this dissertation. There are many people who have helped, and I regret that their names have been unintentionally omitted from these acknowledgements.

The glaciology group has expanded and contracted throughout my time at UBC. Interactions with Paul Barclay, Etienne Berthier, Helgi Björnsson, Eric Degiuli, Rob Eso, Sean Fleming, Gwenn Flowers, Tom-Pierre Frappe-Seneclauze, Neil Hall, Mike Hambrey, Dave Hildes, Jeff Kavanaugh, Gaute Lappegard, Nicolas Lhomme, Shawn Marshall, Andrew Schaeffer, Christian Schoof, Tanya Stickford, Fern Webb, and Frank Wilschut made working in glaciology not only stimulating but also fun. Of these, Gwenn Flowers needs to be singled out for discussions of englacial and subglacial hydrology. Tom-Pierre Frappe-Seneclauze gave me elegant solutions to Matlab conundrums. Christian Schoof generously presented me with ideas from his work on cavities that appear in Chapter 3. Christian was also gracious enough to discuss, selflessly and often at length, boundary conditions, englacial thermodynamics, penalty functions, and other concepts that appear in this thesis.

Within the glaciology community at large, several people have provided ideas or other help through discussions or email. Foremost among these scientists is Richard Alley. Richard fleshed out the theory behind glaciohydraulic supercooling in a few short papers that contain a wealth of information. Richard and I sent pages of email back and forth. His speed at writing is unique in that for every five minutes he spent at the keyboard, I'm sure that I spent 2 hours in defense, rebuttal, or explanation. I should note, too, Dan Lawson's help at describing processes. Dan remains a clearinghouse for unpublished glaciohydraulic supercooling observations—some of which have only made sense when we compared notes at meetings. Dan continues to be helpful in putting me on a correct path regarding the observations. Joe Walder provided a steady source of constructive criticism, and he pushed me to add components to the model that would otherwise have been left out. Helgi Björnsson, Jon Denner, Finnur Palsson, Peter Jansson, Todd Johnston, and Justin Pearce provided both published and unpublished data. While only a portion of this data appears in this dissertation, I am grateful to each of them. Kurt Cuffey, Andrew Fountain, Andrew Fowler, Richard Hindmarsh, Roger Hooke, Kolumban Hutter, Neal Iverson, Tony Payne, Charlie Raymond, Hung-Tao Shen, Slawek Tulaczyk, and John Wettlaufer all provided stimulating discussions on this research, relevant references, or both. I also wish to thank Michael Manga for discussions on writing and helping me focus my ideas to make them concise and pertinent.

At the University of British Columbia, the faculty and staff have been extremely helpful. John Amor, Sukhi Hundal, David Jones, and Cornel Pop provided help with my computer requests. Alex Allen is a graduate secretary extraordinaire. For her help, I am extremely grateful. Michael Bostock and Liz Hearn helped me focus several external applications to present my work in a manner other earth scientists could understand. Neil Balmforth's group

meetings provided opportunities to examine other problems in fluids research. Bruce Buffett showed me how to construct and deconstruct equations to understand fundamental processes. Mike Church graciously endured what I thought were simple questions on sediment transport. His answers revealed that I was never asking a simple question. Both Mike Church and Phil Austin deserve praise for reading this dissertation at length and providing me with relevant editorial and scientific suggestions. Thank you, Phil and Mike. This work would not be possible without the enduring support of Garry Clarke. His patience with my slow progress is kindly acknowledged. I have learned, and will continue to learn many things from Garry, from writing techniques to local and global forms of the balance laws. He has single-handedly turned the tiller on this thesis to avoid the rocky coastline of the ordinary. I am very grateful to have worked with him.

I would like to thank my family. My siblings Maria, Don, Chris, Jon, Katie, Kiara, and Pat have broken up my days with phone calls, emails, and events. I am very happy to be a member of such a supportive group. When I started this dissertation, there was not a younger generation. Since 1999, five children were born: my nieces Savannah, Eve, Kalea, and Abigail, and my nephew Benjamin. Finally, my parents Don and Mary Lou continue to help me, and I am grateful for all the support they have given me. As I write this, my mother is battling cancer. Given that British Columbia is far from Pennsylvania, travels home have been too few. I look forward to visiting home and seeing Mom healthy again.

This work is both an endeavor of hard work and intrigue. As a research community, we do not understand glacier hydrology sufficiently to use theory as a predictive tool. This thesis attempts to use theory as a diagnostic tool. When new tools are developed, they are prone to errors. Any errors, where apparent, are my responsibility. I have tried to find and eliminate all of them.

I hope the reader finds this thesis useful.

Dedication

To Thomas Robert Brucker (Uncle Tom or UT), 9 February, 1933–30 August, 2002:
Uncle, friend, and roommate.

I have a goldfish in a bowl:
A lonely little fellow,
with nothing in the world to do,
but sit there and be yellow.

Chapter 1

Introduction

Water flow and ice–water interactions in glaciers provide a complex and captivating area of research. One phenomenon associated with en- and subglacial water flow is glaciohydraulic supercooling: under the proper conditions, water flowing through a glacier's hydrologic system will freeze. Supercooling implies that the water temperature is below its equilibrium freezing temperature. Glaciohydraulic supercooling depends on the configuration of the hydrologic system as well as the change in the freezing point of water. Because glaciohydraulic supercooling is an unusual process whereby the hydraulic pathways operate in concert with the phase change of water, an understanding of the both glacier hydrology and supercooling are necessary.

This thesis focuses on glaciohydraulic supercooling. The goal of the present work is to investigate supercooling in the subglacial environment from a theoretical and computational perspective. Water flow englacially and, in particular, subglacially will be of principal importance throughout this thesis.

1.1 Glacier hydrology

During summer months, meltwater generated at a glacier surface flows to the margin along pathways that may be supraglacial, englacial, or subglacial. Surface waters may channelize as they flow across the top of the glacier and flow down moulins or crevasses. Once water drains from the surface, its flow path may not be straightforward. Water may continue englacially; or alternatively, water can proceed to the ice–bed interface. Path selection is dictated by potential gradients. Provided that water is flowing down gradient, it is not restricted to flowing downhill.

Water that flows englacially may use any passageway available. Passageways can be conduits (*e.g.,* Shreve, 1972), englacial fractures (*e.g.,* Fountain *et al.*, 2005a), or a network of small veins at the boundaries of ice crystals (*e.g.,* Nye, 1976). An englacial conduit network would be a series of connected tubes. A fracture network would likely be a series of intersecting crevasses that have not refrozen sufficiently to block water flow. Veins exist at ice grain-boundary junctions. Because of their small size, veins are only weakly hydraulically conductive but may be the only mode of water transport in glaciers that lack englacial fractures or conduits. Other types of englacial passageways are clearly possible, but would likely be variants of the aforementioned types.

After entering the englacial plumbing system, water can continue to the ice–bed interface to enter subglacial passageways that have a substrate floor and an ice ceiling. A substrate floor can be either rock, sediment, or some combination of the two depending on what is available below the glacier. Any passageway can be subglacial, or basal, if it meets the criterion that it has an ice roof and a substrate floor. These subglacial passageways have received copious attention in the literature (for recent reviews, see Clarke, 2005; Fountain & Walder, 1998; Hubbard & Nienow, 1997).

Subglacial passages fall into broad categories based on the drainage network morphology, cross section, and the water flow velocity. Hubbard & Nienow (1997) reviewed the predomi-

nant types of passageways and grouped them according to water velocity. Their premise was that passageways that conduct fast-flowing water would form an arborescent drainage network. The remaining passageways would form a distributed network. They distinguished seven major types of cross-sections: Röthlisberger- or R-channels, Nye- or N-channels, broad-and-flat channels, films, linked cavities, porous media, and canals (Fig. 1.1). Generally, high-conducting passageways (R-, N-, and broad-and-flat channels) have higher ratios of cross-sectional area to wetted perimeter. As a result, water is able to flow faster and loses more momentum to friction along the wetted perimeter that enables melting of the surrounding ice (Röthlisberger, 1972). This melting allows the pressure gradient driving flow to increase. In contrast, low-conducting passageways (films, linked cavities, porous media, and canals) have lower ratios of cross-sectional area to wetted perimeter. In consequence, these passageways operate at pressures at or near the ice overburden pressure and have extremely low pressure gradients driving flow. Water flowing through these passageways loses less momentum to the perimeter of flow. Because flow is slow, there is little melt induced by friction at the hydraulic perimeter (Walder, 1986).

Hubbard & Nienow's (1997) review concludes by noting that the understanding of temporal and spatial changes in morphology is incomplete. The transformation of one cross-section and its corresponding network morphology to a different cross-section and morphology is unclear. Morphological switching would occur, for example, if a film terminated at an R-channel (Fig. 1.1 a,d; Weertman & Birchfield, 1983). Passageways may switch temporally from one flow regime to another depending on the supply of water (*e.g.,* Kamb, 1987). A water supply difference from upstream to downstream could also cause a switch in morphology. For example, an overabundance of water moving downstream may cause a film to be downstream of the conduit, as in the case of the 1998 outburst flood (jökulhlaup) moving down Skeiðararjökull, Iceland (Björnsson, 2002). Similarly, during the spring thaw when glacier hydrology awakens from its winter hibernation, the subglacial hydraulic system may evolve from one type of morphology to another (*e.g.,* Iken & Bindschadler, 1986). In sum, water is capable of utilizing any morphology or cross section depending on the water flow conditions at the ice–bed interface. Different types of passageways may be spatially contiguous, and there is a rich continuum of network morphologies and cross sections.

Access to the basal plumbing system is limited by the overlying glacier. As a result, little is known about subglacial network morphologies, cross-sections, and water velocities relative to subaerial fluvial systems. Interpretations of the hydraulic system are therefore limited to observing properties of input and output water (*e.g.,* Kohler, 1995; Lawson *et al.*, 1998; Seaberg *et al.*, 1988), drilling through the glacier to install instruments (*e.g.,* Flowers & Clarke, 2002b; Harper *et al.*, 2002), or altering the flow regime via slug or other tests that introduce a pressure transient into the subglacial system (*e.g.,* Kulessa *et al.*, 2005; Stone & Clarke, 1993). One result of this limitation is that testable physical and numerical models become crucial to understanding spatial and temporal changes in subglacial hydraulic characteristics.

Supercooling

Any liquid that is at a temperature below its bulk freezing temperature is said to be supercooled. The term "supercooling" is slightly misleading because as liquid water freezes its temperature must be at least a small amount below the freezing point. The sensible heat associated with the supercooling is then converted to latent heat as the water freezes. This conversion drives the temperature of the liquid back toward the bulk freezing temperature. Normally, explicit use of

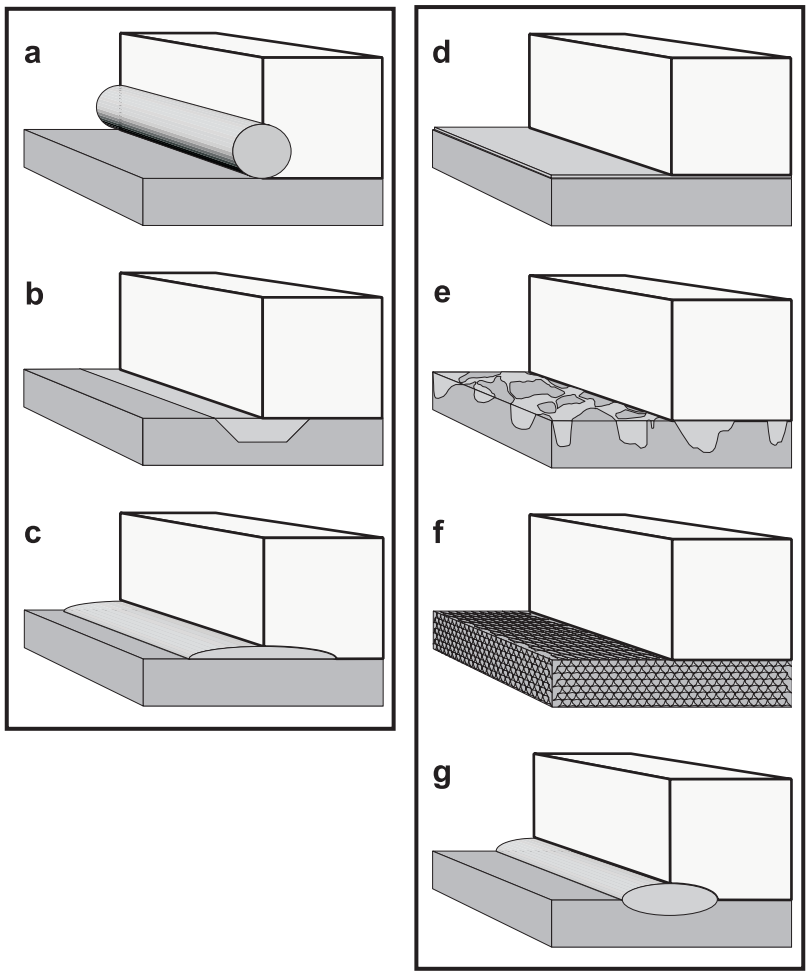

Figure 1.1: Illustration of simple subglacial hydraulic systems. Not to scale. White ice overlies a light gray water system and a dark gray substrate. Figures a, b, and c are the high-conducting water systems. Figures d, e, f, and g are the low-flow water systems. (a) R-channel typified as an ice-walled tube (Röthlisberger, 1972) overlying sediment or bedrock. (b) N-channel cut into bedrock (Nye, 1973b). (c) Broad-and-flat channel (Hooke *et al.*, 1990) over sediment or bedrock. (d) Thin water film (*e.g.,* Weertman, 1972) overlying either sediment or bedrock. Films are typically microns thick and overlie microtopography on the bed. (e) Linked cavity system (Kamb, 1987; Walder, 1986) overlying bedrock. Flow through linked cavities is governed by the small orifices connecting the cavities. (f) Porous medium through sediment or bedrock. (g) Subglacial canal (Walder & Fowler, 1994) partially cut into sediment. Canals can occur only where a glacier overlies sediment.

the word supercooling implies that the freezing process is not at equilibrium. Undercooling and supercooling are interchangeable terms with both found in the literature.

Water can supercool to different levels depending on when ice crystallization occurs. Lack of sites for crystallization typically enhances the level of supercooling. For example, at atmospheric pressure, pure water without condensation nuclei from any source will freeze at a temperature of about $-40\ ^{o}$C, well below its bulk freezing temperature (Hobbs, 1974, p. 468). In this case, water

nucleates on itself, termed homogeneous nucleation[1]. Heterogeneous nucleation, however, occurs when water freezes to non-ice particles within the liquid. Depending on the composition of the particles, the freezing point can be anywhere between −40 °C and 0 °C at atmospheric pressure (Hobbs, 1974, p. 502–504). For natural streams, Osterkamp & Gilfillian (1975) found that heterogeneous nucleation occurs between about −4.9 and −13.9 °C. When the seed particles are ice crystals, this is termed secondary nucleation. The temperature depression can be a fraction of a degree for this type of freezing. Martin (1981) reviewed the observational basis of secondary nucleation and found that ice can begin to crystallize at about −0.05 °C in natural streams, and possibly at higher temperatures.

Glaciohydraulic supercooling is a special case of supercooling where the flow of water either sub- or englacially causes the water to be below its freezing point. This natural phenomenon arises from water's freezing point being linearly dependent on pressure. When water at the freezing point moves rapidly from one area of the glaciohydraulic system to another where the ambient pressure is lower, and if the internal energy of the water does not adjust to the ambient pressure, then the water supercools. Glaciohydraulic supercooling is a process that is dependent on water velocity. The water needs to flow faster than it can equilibrate its internal energy. As a result of this velocity dependence, glaciohydraulic supercooling favors network morphologies and hydraulic cross sections that are most conducive to fast water flow.

Water can change its freezing point by moving vertically through a glacier's hydraulic system. A decrease in the amount of ice above the water decreases the water pressure, and results in an increase in the freezing point. The amount of the increase in freezing point is governed by the linearized Clausius-Clapeyron relationship. Thus, water that moves rapidly upwards in the glacier from an area with a lower freezing point than the ambient freezing point will supercool. Upward flow of water is the most obvious way of changing the freezing point, commonly called the pressure melting point. Because englacial pathways are ice-bound and subglacial pathways are ice-roofed, secondary nucleation at relatively low levels of supercooling is possible. Figure (1.2) shows a downward view of a moulin where overpressured water spouted out of the glacier. Because of supercooling, ice accreted along the perimeter of the moulin.

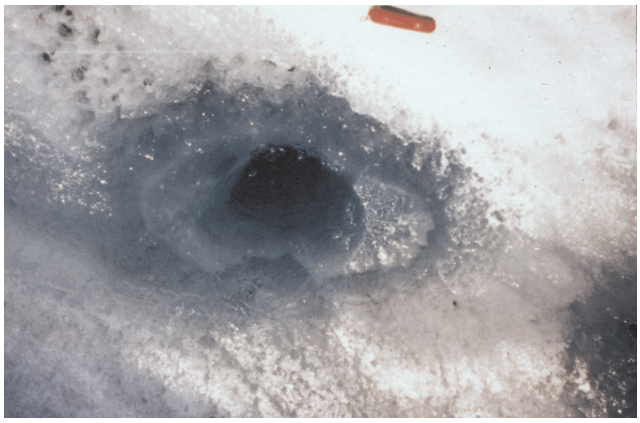

Figure 1.2: A downward view of a moulin with accreted ice from Llewellyn Glacier, B.C. Water spouted several meters above the glacier surface from this moulin immediately before this photograph was taken. The accreted ice surrounds the black moulin. Pocket knife for scale.

[1]A detailed discussion of homogeneous nucleation can be found in Chapter 7 of Pruppacher & Klett (1997)

Subglacial passageways tend to be horizontal or sub-horizontal over scales of meters. For glaciohydraulic supercooling to occur, these passageways must be inclined such that upward motion occurs and the pressure melting point rises faster than the water warms. The simplest way of meeting these criteria is illustrated in Figure 1.3. In this case, water flows in subglacial passageways along the ice–bed interface up a slope adverse to flow. As water ascends an adverse slope beneath a glacier, it progresses from a region of higher pressure to a region of lower pressure (Alley *et al.*, 1998; Röthlisberger & Lang, 1987). Because the freezing point of water is pressure dependent, if the water moves rapidly from high pressure to low pressure without warming sufficiently, the water will supercool. If water flow is slow, the internal energy of the water may equilibrate and prevent supercooling. The same arguments hold for water that flows vertically rather than subhorizontally. Presentation of the detailed physics of flow and supercooling will appear in subsequent chapters of this thesis.

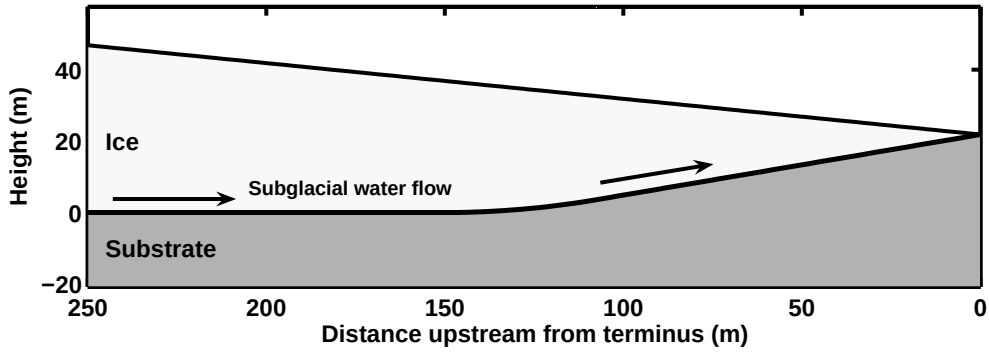

Figure 1.3: A synthetic geometry. Water flows along the ice–substrate boundary and ascends the adverse slope from 150-0 meters from the terminus.

Figure 1.3 displays a synthetic example of a longitudinal glacier section[2] for which the surface and bed arrangement may yield supercooling. Water may flow through a subglacial passageway from left to right at the ice–substrate interface. The glacier surface height decreases monotonically, suggesting that the freezing point increases because of the decrease in pressure. From 150–0 meters upstream from the terminus, water would travel up a slope adverse to flow. If supercooling were to occur, it would occur as water flows out of this overdeepening. The term overdeepening indicates a large closed depression beneath a glacier. Water is not able to flow out of the overdeepening without a boost from the ice overburden pressure.

1.2 Previous work

Röthlisberger (1968) was the first to recognize the possibility of supercooling water in the subglacial system. His thoughts are supplementary to the main body of the paper but capture the essence of subglacial supercooling:

[2]In this case, a longitudinal section indicates that ice flow is parallel or nearly parallel to the section. A cross section would indicate flow normal to the plane of the page. The formulation for the synthetic section of a glacier can be found in Appendix A. All longitudinal sections will be shown such that water flow would be from page left to page right.

> When the water moves to a higher pressure in a basin the equilibrium temperature decreases. The water has to be cooled, and the heat sink is provided by ice which melts. Ascending water has to become warmer again: ice forms, or heat comes from other sources which would otherwise be available for melting. ...
>
> We see that ice may form on the upper side of a riegel [a transverse bedrock bump] if water ascends steeply. Under these conditions, where the water channels cannot be kept open by continuous melting, the flow will presumably occur in a sheet or a system of flat cavities rather than in a channel or tunnel.

Röthlisberger envisioned water flowing up a riegel out of a rock overdeepening.

Subsequently, Röthlisberger & Lang (1987) described the effect of water flow out of overdeepenings when they discussed enlargement of conduits via melting at the hydraulic perimeter. They assumed that water flow was in steady state and derived relationships for water flow through circular conduits, but then found that water approaches the ice overburden pressure when it ascends the adverse slope. As a result of this elevated water pressure, they reasoned that any of the plausible hydraulic cross-sections, notably conduits or sheets, are possible when water flows up adverse slopes. Where a bed slope exceeds the surface slope by a factor of -2.02 for pure water and -1.30 for air-saturated water, Röthlisberger & Lang determined that supercooling would occur. They also suggested that the conduits may freeze shut in overdeepenings depending on the flow conditions.

Röthlisberger & Lang worked primarily from a theoretical perspective, whereas most investigations of glacier hydrology concentrate on specific field sites. Studies of glaciohydraulic supercooling follow this trend. In particular, many relevant observations come from two glaciers: Storglaciären, Sweden and Matanuska Glacier, Alaska, USA. Work conducted at Storglaciären has focused primarily on the englacial hydrology of the system (*e.g.,* Fountain *et al.*, 2005a; Hooke, 1991; Hooke & Pohjola, 1994; Hooke *et al.*, 1988; Seaberg *et al.*, 1988). Observations at Matanuska Glacier have focused on subglacial hydrology and its relationship to subglacial and basal sediments (*e.g.,* Evenson *et al.*, 1999; Lawson, 1979; Lawson *et al.*, 1998; Pearce *et al.*, 2003). Work at both of these glaciers is ongoing. Less extensive observations have been made at other glaciers.

1.2.1 Storglaciären

Storglaciären, Sweden, possesses an active hydrology and, in part, lies in an overdeepening (Figs. 1.4 and 1.5). The main overdeepening is bounded on its downglacier side by a bedrock riegel (R in Fig. 1.5). This riegel–overdeepening configuration corresponds to the description of Röthlisberger (see above). Below this riegel, there is another overdeepening called the terminal overdeepening (OD in Fig. 1.5). Seaberg *et al.* (1988) poured dye into moulins draining to the subglacial water system. From these studies, Seaberg *et al.* concluded that the subglacial hydraulic system below the riegel and through the terminal overdeepening was either an arborescent network of linked cavities or was a braided, tortuous system of conduits. In a companion paper, Hooke *et al.* (1988) discussed the hydrology above the riegel and determined that the hydraulic pathways are both englacial and subglacial. The englacial and subglacial water flow velocities above the riegel are slow relative to the water velocities below the riegel. Hooke & Pohjola (1994) attributed the difference in hydrology to supercooled water freezing and constricting the subglacial passages. As a result of this constriction, the water is diverted and forced to flow through a low-conductivity englacial system. Hooke & Pohjola also observed frazil ice, a strong indicator of supercooled water, discharging from several of the boreholes they

had drilled.

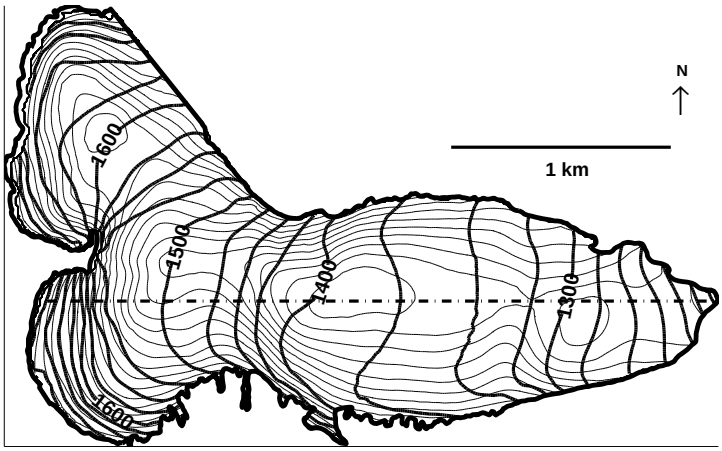

Figure 1.4: Map view of Storglaciären, Sweden. Thin black lines are the bed elevations. Thick, labeled contours are the surface elevations. Contour intervals for both the surface and bed are 25 meters. Ice flows from west to east. The horizontal dashed line is the section for Figure 1.5. Figure after Aschwanden & Blatter (2005). Data courtesy of P. Jansson.

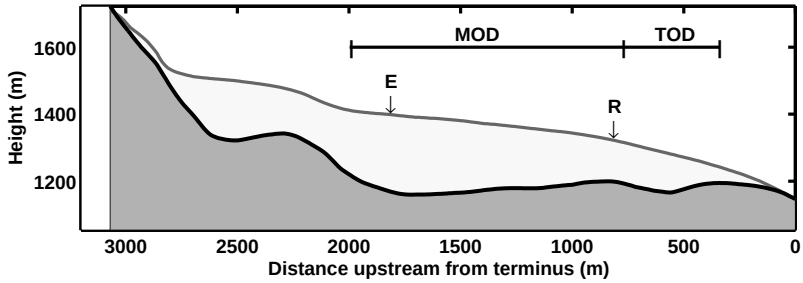

Figure 1.5: Storglaciären, Sweden, longitudinal section. **E** denotes the approximate equilibrium line location. **R** denotes the location of a riegel underlying the glacier. **MOD** and **TOD** denote the horizontal limits of the main and terminal overdeepenings, respectively. Vertical exaggeration is 1.5. Length is the same as the dashed horizontal line in Figure 1.4.

Hydraulic studies at Storglaciären led Hooke (1991) to suggest that overdeepenings play a substantial role in bedrock erosion. Part of his argument is that as water flows up the adverse slope, the discharge diminishes and sediment is deposited. The discharge lessens because higher water pressures force water to flow englacially. Sediment deposited when water leaves the subglacial pathways mantles the bedrock and prevents further erosion. For a sufficiently steep overdeepening, the water will move out of conduits and into a thin film along the ice–bed interface. Hooke envisioned the thin film as being mildly hydraulically conductive. He asserted that most of the drainage in the overdeepening must be englacial. Using additional borehole data, Fountain *et al.* (2005a) extended Hooke's (1991) idea and concluded that fractures may be the main hydraulic pathway through glaciers and, specifically, Storglaciären. However, when Fountain *et al.* drilled boreholes and observed a hydraulic connection, they stopped drilling. As a result, it is difficult to ascertain what percentage, if any, of the hydraulic discharge occurs at the ice–bed interface. Fountain *et al.* did not provide estimates of discharge through the fracture system but proposed that the flow was significant.

1.2.2 Matanuska Glacier

In a pair of papers assessing Matanuska Glacier, Alaska, a team spearheaded by Lawson and Alley described data related to subglacial supercooling (Lawson *et al.*, 1998) and presented the basic mathematical formulation (Alley *et al.*, 1998). At the base of Matanuska Glacier, a debris-rich package of basal ice is overlain by cleaner glacier ice (Fig. 1.6). The debris-laden ice exhibits a higher tritium content than the overlying englacial ice, which is tritium-poor (Lawson *et al.*, 1998). The difference in tritium concentration signifies that the basal ice accreted after the early 1950s when large-scale production of tritium via free air nuclear weapons testing commenced. The tritium-poor englacial ice is older. Co-isotopic analyses of water and ice revealed that the accreted ice is isotopically lighter than the englacial ice and subglacial water discharge (Lawson *et al.*, 1998). Isotopic analyses of frazil and anchor ice present in water issuing from the subglacial passageways have values equivalent to the accreted ice layers. The formation of the debris-rich basal layer directly from supercooled water is consistent with these data (Lawson *et al.*, 1998). As a result, there is little doubt that the subglacial package of accreted ice and sediment is formed from actively supercooling water.

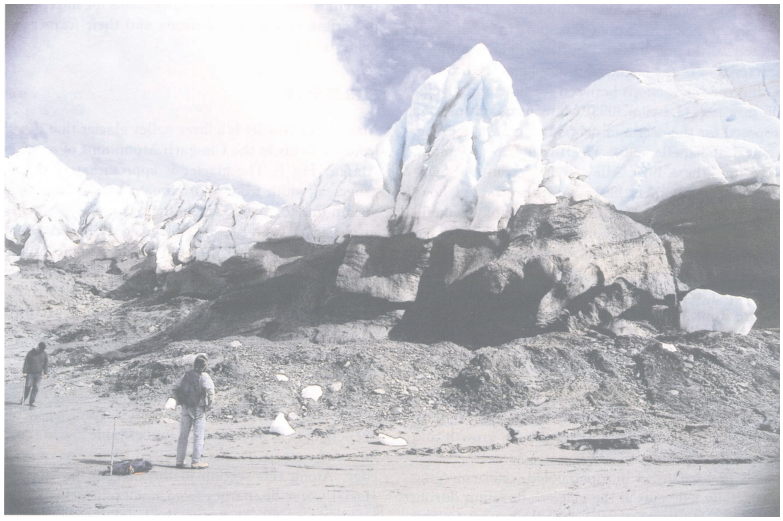

Figure 1.6: Terminus of Matanuska Glacier. White to grey meteoric ice overlies dark-grey to black, sediment-rich basal ice that formed from glaciohydraulic supercooling subsequent to the most recent surface testing of nuclear weapons. Illumination is from the upper right. From Lawson *et al.* (1998).

Water flows through the overdeepening in conduits or a distributed drainage system. Near the terminus, water emerges at several localized vents. Radar profiles taken near these vents reveal what appear to be channels extending back toward the subglacial system (Arcone *et al.*, 1995; Lawson *et al.*, 1998). Debris layers in the basal ice are laterally continuous, suggesting accretion via a distributed system (Lawson *et al.*, 1998). Frozen features resembling cross-sections of ice-choked subglacial conduits exist in the accreted ice but are rare. In addition, analyses of dye-tracing studies suggest that water distributes laterally beneath Matanuska Glacier (Lawson *et al.*, 1998).

Generally, the debris content ranges from 15–60% by volume but can range from practically none to entirely sediment (Lawson *et al.*, 1998). Large clasts, such as pebbles and cobbles,

found in the accreted ice are rounded and suggest a glaciofluvial origin, provided that those sediments have not been reworked by other subglacial processes. Fine sediment dominates the debris layers with fewer coarse-grained layers. The coarse layers can be clast-supported or ice-supported. Clast-supported layers may indicate regelation entrainment (*e.g.,* Iverson & Semmens, 1995), but ice-supported layers form as water supercools and freezes (Lawson *et al.*, 1998). Overall, material that is entrained via regelation accounts for a small percentage of the material in the basal layers. In addition, Lawson *et al.* discussed the similarity of parts of the basal ice facies dominated by silt. These layers resemble features that have formed as frazil ice flocs entrain sediment. The presence of frazil ice is indicative of turbulent water flow (*e.g.,* Daly, 1984) as is the presence of high concentrations of sediment in the flowing water.

1.2.3 Other glaciers

Supercooled water and ice accretion are observed at other glaciers. Roberts *et al.* (2002) gave an overview of supercooling in Iceland. They separated the subglacial supercooling into two broad categories: supercooling under ablation conditions and supercooling under jökulhlaup conditions. Roberts *et al.* used ablation conditions to describe supercooling that occurs on a daily basis at Skaftafellsjökull under normal melt conditions. Data acquired at Skaftafellsjökull includes evidence of active frazil and anchor ice accretion. Here, the sediment-rich basal ice is several meters thick. In addition, water that flows up crevasses near the terminus supercools and accretes sediment. These conditions would be analogous to daily summertime conditions at Matanuska Glacier.

Jökulhlaup conditions are strikingly different. Water under high pressure fractured the surface near the terminus of Skeiðarárjökull during the 1996 jökulhlaup (Roberts *et al.*, 2002). These high angle shear fractures acted as an overdeepened slope that Roberts *et al.* estimated was a factor of -44.5 times the surface slope, well beyond Röthlisberger & Lang's (1987) supercooling criterion. Within the fractures, Roberts *et al.* identified intercalated platelets of ice and lozenge shaped ice crystals up to 40 mm in diameter that resembled deposits at Matanuska Glacier (Evenson *et al.*, 1999).

Recent observations at Taku Glacier, Alaska, included artesian water flowing from the terminus and freezing (M. Truffer, personal communication, 2003). There is also some accreted basal ice; however, detailed descriptions are not available. Observations are in concert with Taku Glacier's recent down valley advance and modification of its bed (Motyka & Echelmeyer, 2003; Nolan *et al.*, 1995). Radar data point to the lower 1500 meters of the glacier lying in a sediment-floored overdeepening (Nolan *et al.*, 1995). This area of the glacier is well below the equilibrium line, and the bed most likely receives abundant meltwater.

Few data exist at other glaciers. Radar echo soundings of Muir Glacier, Alaska, reveal an overdeepening as well as accreted debris-rich basal ice (Alley *et al.*, 2003a). However, there are no direct observations from the terminus. Observations from the terminus of Kvíárjökull, Iceland indicate that subglacial supercooling is occurring and accreting debris (Spedding & Evans, 2002), but direct observations of supercooled water were not made. In addition, Spedding & Evans suspected that their observations were uncertain because co-isotopic studies of the accreted ice had not been completed at the time of publication.

1.3 Importance and scope

1.3.1 Importance

Recently, Alley *et al.* (2003b) highlighted glaciohydraulic supercooling as being an important process through which glaciers modulate subglacial sediment erosion and deposition. Alley *et al.* argued that glaciers that rapidly erode and transport sediment will tend to develop an adverse slope because these glaciers cannot evacuate sediment as rapidly as they accumulate it. As a result, the bed steepens to its supercooling threshold which prevents the glacier from eroding its bed further. Hence, glaciohydraulic supercooling stabilizes the subglacial sediment erosion and deposition processes by preventing additional erosion. These arguments recapitulate and extend Hooke's (1991) ideas on the subject.

However, if glaciohydraulic supercooling is a stabilizing feedback, why is it not more commonly observed at glaciers with sedimentary bases? Questions such as this illustrate the lack of knowledge surrounding the phenomenon. Foremost, glaciohydraulic supercooling needs to be placed in the context of the larger subglacial and englacial hydrology. A general understanding of exchanges between different hydraulic network morphologies and how these influence erosion of the bed would be useful. In addition, Hooke *et al.*'s (1988) contention that englacial pathways matter to the subglacial system appears to be corroborated by Fountain *et al.*'s (2005a) work. Understanding why or how water leaves the subglacial system would aid in determining when supercooling is important to the subglacial hydrology.

Fountain *et al.* made their observations upglacier from an adverse slope. If englacial water transport is fundamental to water flow through an overdeepening, then the water may not have the opportunity to be in contact with the bed. Obviously if water does not access the bed, then sediment at the ice–bed interface will not be mobilized. If this is the case, then the Alley *et al.* (2003b) hypothesis may need to be modified. Furthermore, it may be possible that the Fountain *et al.* (2005a) observations are enhanced by the presence of an overdeepening. Water may not be permitted to drain subglacially because the riegel acts as a dam. Water would then flow englacially.

Ideally, issues such as these need to be resolved so that interpretations of glaciohydraulic supercooling can be applied to modern or past glaciers and ice sheets. In particular, the southern lobes of the Laurentide Ice Sheet occupied overdeepenings. For instance, the Lake Michigan Lobe may have had glaciohydraulic supercooling affecting the sediment budget, and the nearby Saginaw Lobe had active sediment transport in what appear to be, locally, subglacial sheets (Fisher *et al.*, 2005) that could have been flowing up adverse slopes.

A better understanding of glaciohydraulic supercooling may aid paleoclimatic and dynamic interpretations of ice sheets. For example large iceberg discharges, termed Heinrich Events, occurred quasi-periodically throughout the Pleistocene when northern outlets of the Laurentide Ice Sheet discharged icebergs to the North Atlantic (for a recent review, see Hemming, 2004). These icebergs had sediment-rich basal layers and rafted debris over much of the North Atlantic (Dowdeswell *et al.*, 1995). Sediment package thickness decreases away from Hudson Strait, but lithologies point to an origin from regions that were ice-covered. The exact mechanisms of subglacial erosion and subsequent entrainment are not well understood. However, glaciohydraulic supercooling may be the phenomenon responsible for accreting sediment to the base of the ice sheet (Hemming, 2004; Hulbe *et al.*, 2004). Water could have flowed up the sill of Hudson Strait, supercooled, and accreted water and sediment to the base of the ice sheet. The sill would act as the adverse slope necessary for glaciohydraulic supercooling. Similar situations may have occurred for other Pleistocene and contemporary ice sheets.

1.3.2 Scope

Three areas of interest center on glaciohydraulic supercooling and overdeepenings: the shape of the hydraulic cross-section, exchanges between the englacial and subglacial system, and sediment transport within the overdeepenings. For the most part, information on these individual areas can be inferred from hydraulic, geomorphic, and geologic data. However, the rates, locations, and other analytic information throughout overdeepenings are difficult to quantify either from downhole englacial or near-terminus proglacial studies.

The first area of interest is the cross-section that is favored by the hydraulic system. Data appear to indicate that a fast-flowing distributed sheet is preferred. The large body of theory on R-channels makes them, in a way, the default model of subglacial flow. Röthlisberger & Lang (1987) made no allowance for the absence of a conduit, while Hooke & Pohjola (1994) and Alley *et al.* (1998) favor distributed subglacial water systems. Furthermore, stratigraphic observations at the front of Matanuska Glacier seem to indicate that a distributed system, possibly a water sheet, is prevalent.

There is also an informal "clogged artery" hypothesis. Because R-channels can act as hydraulic arteries, the freezing point of the water may be well below that of the ambient ice. Freezing of the water then occurs rapidly, and the artery clogs itself and cannot reform faster than the water distributes into a sheet. Knowing the conditions for which the cross section is a conduit or a sheet would be useful, especially because both appear to be supported by different parts of the stratigraphic data (Lawson *et al.*, 1998).

The second area of interest is sediment transport. Both Hooke and Alley *et al.* (2003b) supposed that deposition occurs on the adverse slope. If this is true, the slope may change, possibly obtaining some kind of critical value; or the ice–bed profile may change, possibly assuming some kind of characteristic shape. Alternatively, there may be no feedback loop. While their arguments are persuasive, Alley *et al.* reason through how the system operates without presenting new field data or numerical results. I attempt to evaluate their proposed feedbacks associated with sediment transport at the bed.

Glaciohydraulic supercooling can be an important component of subglacial sediment transfer. With its high rates of sediment accretion and glaciofluvial transport, Matanuska Glacier illustrates this significance; but questions still surround the process. For example, why is the process so well developed there relative to other locales? An understanding of the factors controlling subglacial sediment motion is incomplete. Clearly, surface and bed slopes are crucial (Röthlisberger & Lang, 1987), but how these interact with other hydraulic conditions to mobilize and accrete sediment is not clear.

The third area of interest is the movement of water between the englacial system and the subglacial one. Principally, why does water leave a subglacial pathway to travel through an englacial one? Alternatively, the water might never enter a subglacial system, instead remaining englacial. Meltwater at Storglaciären appears to favor englacial flow while meltwater at Matanuska Glacier appears to prefer to flow subglacially, but both locales show signs of glaciohydraulic supercooling. The difference in the location of flow, englacial versus subglacial, must result from a physical mechanism that is active in one situation but not the other. Finding a pertinent trade-off would be extremely useful, especially if discernible characteristics could be qualified for different types of glaciers.

My approach is to develop and use a numerical model of en- and subglacial water flow. Much of the theory for the model is extracted from other glaciological studies or from other areas of the earth sciences. The notable exception is the closure of the sheet cross-section, which is entirely

new. Attempts to link this same material either have not been tried or not been published. For example, the results from the simultaneous reconstructions of both englacial and subglacial water temperature from a hydrologic model are the first of their kind.

On one hand, the numerical model and the physical model on which it is based are necessarily subject to assumptions to make the problem tractable. The diversity of material presented here rules against an exhaustive search of parameter space. I have attempted to minimize these effects or quantify them. On the other hand, the numerical model allows solutions over contiguous space and time that field measurements may not capture. The model allows detailed comparisons and contrasts of different variables and parameters both in space and time. In sum, there are notable deficiencies to numerical modeling, but there are also conspicuous advantages that I exploit.

1.4 Structure of the thesis

This thesis is structured around the major components of the modeling effort. The aim is to elucidate factors controlling glaciohydraulic supercooling and to provide direction for future process-based studies. In general, shorter, simpler chapters are favored over longer, more elaborate ones.

- Chapter 1, the present chapter, focuses on introducing glacier hydrology and how glaciohydraulic supercooling fits into this larger picture. The process is identified and the scope of the work is established.

- Chapter 2 introduces the fluid flow physics and the strategy for examining the subglacial hydrology. This physical model is modified from Clarke's (2003) effort. Reasonable approximations are used to determine pertinent length and time scales for glaciohydraulic supercooling.

- Chapter 3 acquaints the reader with the way in which hydraulic sheets close and open in a vertical sense. These arguments provide a fresh look at regelation and creep closure from the work of Nye (1967) and Weertman (1972). In addition, the strong arguments put forth by Walder (1982) for the instability of sheets allow an easy access point for reassessing the stability of locally distributed sheets along the adverse slope.

- The sediment transport relations are advanced in Chapter 4. Semiempirical sediment transport relations culled from the fluvial literature are recapitulated, modified, if necessary, and applied to the subglacial environment.

- Chapter 5 captures the flow physics and their necessary approximations for englacial fluid flow in a Darcian model. This model describes the evolution of the pore space in the ice through melting or freezing along the perimeter of the pores. Formulation of the englacial model is included to provide a thorough elucidation of the water sources and sinks that may influence flow under and through overdeepenings.

- Chapter 6 discusses the simulations and the implications of these simulations. I construct synthetic longitudinal sections that have characteristics of both Matanuska Glacier and Storglaciären to simplify numerical results. Each simulation type provides insight into the governing processes. Furthermore, different components of the previous chapters are turned on or off to produce stark contrasts and allow comparison. Simulations focus on flow at the ice–bed interface. Englacial aquifer simulations are omitted for brevity and simplicity.

- The conclusions to this thesis are found in Chapter 7. The summary of the major results can also be found here along with the important additions and modifications of our present understanding of glaciohydraulic supercooling. These are placed in the context of the larger body of glacier hydrology. Finally, ideas for future work and a synopsis of unfinished details are presented.

Some of these chapters rely on useful auxiliary relations. These auxiliary relations appear in appendices at the end of the thesis. The appendices are presented in the order in which they are referenced in the chapters.

Chapter 2

Subglacial flow equations

Physical models have been used as both diagnostic and prognostic tools in glacier hydrology. These models tend to be process-specific. Extensive examples of these types of models can be found in jökuhlhaup studies (*e.g.,* Clarke, 2003, 1986; Fowler, 1999; Ng & Björnsson, 2003; Nye, 1976). Fewer examples can be found in studies of cavities (*e.g.,* Walder, 1986) or descriptions of morphological switching during surging (*e.g.,* Kamb, 1987). A class of broader comprehensive numerical models is difficult to construct because of the feedbacks among ice dynamics, water flow, and basal conditions. In particular, capturing the essential physics of some processes, morphological switching (*e.g.,* Kamb, 1987), for example, in numerical models is challenging and requires creative parameterizations (*e.g.,* Flowers *et al.*, 2004). Presently, the use of comprehensive glaciohydrological models is limited to feedbacks between ice dynamics and subglacial hydrology (Arnold & Sharp, 2002; Johnson & Fastook, 2002) and feedbacks among different units of glacier hydrology (Flowers & Clarke, 2002a). The model I present here is not necessarily process specific, as it could easily be modified for other sub- and englacial uses, but I choose to present it with the specific intention of explaining glaciohydraulic supercooling. This model is not coupled to a model of ice flow and, therefore, attempts to capture feedbacks only within the glaciohydrologic system.

Röthlisberger & Lang (1987) and Alley *et al.* (1998) described the physics of supercooling subglacial water. Aside from the hydraulic cross-section, both papers treated water flow similarly inasmuch as they make use of the same assumptions. For example, they both assumed that the water is always at the freezing point along the flow path. In addition, they assumed steady and uniform flow. Indeed, Alley *et al.* followed much of Röthlisberger & Lang's representation but added parameter analyses specific to glaciohydraulic supercooling.

Any model of subglacial water flow that treats the thermodynamics appropriately can be used to simulate subglacial supercooling. Clarke (2003) provided one of these models. Clarke's work is based on the work of Spring & Hutter (1981, 1982) for flow through ice-walled conduits. This model formulates the physics in terms of the continuum balance laws. Clarke modified the original theory by utilizing a common compressibility assumption to solve the two simultaneous mass balance equations. In addition, he modified the conduit geometry, adding a simple sediment-floored conduit.

Following Clarke's (2003) modification of the hydraulic cross-section, I introduce a distributed water sheet as an appropriate hydraulic cross-section for water-flow through an overdeepening. There are several reasons for the introduction of this cross-section. Most importantly, accreted basal layers at Matanuska Glacier are broader than they are high (Lawson *et al.*, 1998). Additionally, results from dye-tracing studies suggest that water distributes laterally at the ice-bed interface (Lawson *et al.*, 1998). There is also evidence that water pressure is above flotation in parts of overdeepenings. Hooke (1991) suggested that water distributes laterally across the bed when overpressures occur. Furthermore, a turbulent sheet parallels the concept of broad-and-flat channels that were originally developed for water flow through overdeepenings (Hooke *et al.*, 1990); however, in the case of sheets, it is not necessary to calculate the lateral extent

of the channel. Alley *et al.* (1998) also envisioned a laterally distributed system but selected slower types of cross-sections (Fig. 1.1). I adopt a type of cross section that is consistent with turbulent conditions indicated by the presence of frazil ice and a considerable sediment load at the front of Matanuska Glacier (Lawson *et al.*, 1998). Both fast and slow types of hydrology are not exclusive of one another as there is most likely longitudinal and lateral variation within the hydraulic system (*e.g.,* Lappegard *et al.*, 2006). Furthermore, water discharged through sheets as envisioned here can move fast or slow.

Within this chapter, I review the formulation of the basic governing equations for the case of steady flows, which Röthlisberger & Lang (1987) and Alley *et al.* (1998) used in their analyses, and time dependent flows, which Clarke (2003) used. Equations from the Spring-Hutter formulation can be reduced to the steady-state representation, and this feature will be exploited in this chapter. In addition, I revisit the necessary fundamentals for simulation of water flow and glaciohydraulic supercooling. The Clausius-Clapeyron equation will be used throughout the thesis and requires illumination. The hydraulic geometry also requires parameterization, but these assumptions appear to be supported by observations reasonably well, suggesting that model results are pertinent to conditions in the subglacial system.

2.1 Conceptual model

Water flows along the ice–bed interface (Fig. 1.3), in either a channel or sheet (Fig. 1.1). Flow in both R-channels and sheets can be formulated as a one-dimensional process using an along-path coordinate, s. The location of the water pathway is defined in x and z, the horizontal and vertical coordinate, respectively. The third coordinate, y, perpendicular to flow, is not simulated, and any variation in the flow path is assumed to be only in the x and z coordinates. The along-path coordinate is a line integral along the ice–bed interface in x and z. The change in any increment of the flow path is given by

$$\Delta s = \sqrt{\Delta x^2 + \Delta z^2}. \tag{2.1}$$

The glacier overlies this water system, sealing it. The water layer has a substrate floor, which can be either rock or sediment. Data at both Matanuska Glacier (Lawson, 1979) and Storglaciären (Hooke *et al.*, 1997) suggest that much sediment exists at the base of these glaciers, such that I refer to the floor as being sediment. For the purposes of this study, the main difference between a rock and sediment floor is that a sediment bed may be mobile, whereas a rock bed would be static. I anticipate that both rock and sediment floors may be found under different areas of overdeepenings within the same glacier, but do not anticipate simulating this transition directly. The dynamical behavior of the water system and its interaction with the overlying ice and underlying sediment is described as each of the individual balance laws is introduced subsequently in this chapter.

2.1.1 Hydraulic geometry

Generally, I consider geometries with cross sections that are circular, or Röthlisberger (R-) channels (Röthlisberger, 1972), the semicircular R-channels envisioned by Clarke (2003), and water flow in sheets. Both R-channels and sheets can conduct water at a relatively high velocity. Other types of cross-sections have been described (*e.g.,* Ng, 1998), but these representations are mathematically bold, and would require diligent modification of the Spring-Hutter formulation. Because circular channels have a well-described theory in the literature (*e.g.,* Clarke,

2003; Fowler, 1999; Röthlisberger, 1972; Shoemaker, 1987; Shreve, 1972; Spring & Hutter, 1982; Weertman & Birchfield, 1983), these will not be discussed in as much detail as the subglacial sheets. Sheets are not nearly as well described in the literature (Walder, 1982; Weertman, 1972). These sheets are a layer of water having a mean thickness and a width that is much greater than that thickness. Furthermore, a water sheet compatible with the work of Alley *et al.* (1998) or Hooke (1991) is not adequately characterized in relation to high velocity water flows. I resist the flow velocity characterizations of Hubbard & Nienow (1997) and envision sheets as being akin to broad-and-flat channels in flow characteristics (Fig. 1.1c) but more like films in cross section (Fig. 1.1d). Within the glaciological community, the terms sheet and film are commonly applied for thin subglacial water layers. However, I draw the distinction that sheets are capable of conducting water rapidly. The term film will assume its conventional use to describe melt associated with regelation (*e.g.,* Lliboutry, 1993; Nye, 1973a; Weertman, 1964).

Röthlisberger & Lang (1987) performed their analysis for water flowing in conduits but acknowledged that any hydraulic cross section is possible. Alley *et al.* (1998) suggested a distributed water system, and as a geometrical simplification, performed analyses for a one-dimensional water layer. Alley *et al.* cited evidence from Matanuska Glacier that shows that the bulk of accreted ice is from water flow that is laterally distributed over the base (Lawson, 1979; Lawson *et al.*, 1998). Because I am investigating channel and sheet cross-sections, both must be perpetuated throughout the theory.

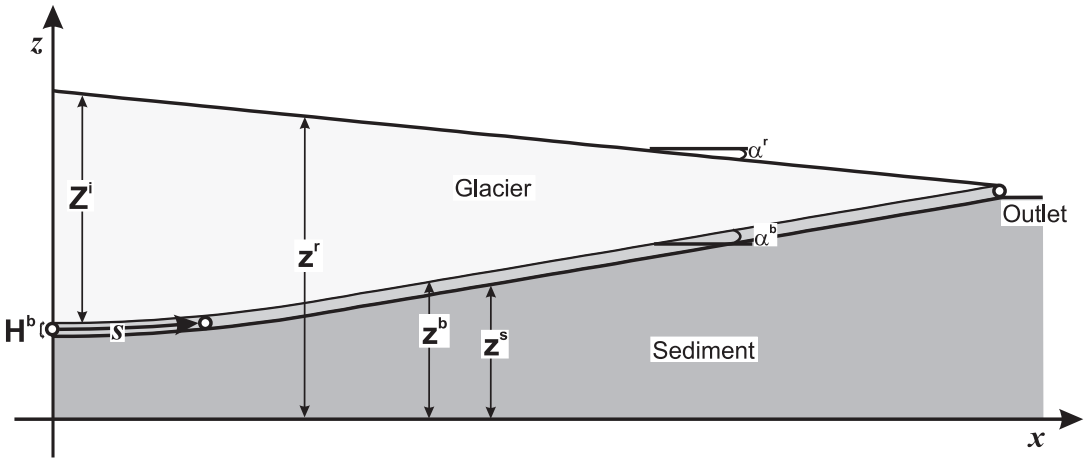

Figure 2.1: Subglacial flow path. Not to scale. Front of the section presented in Figure 1.3. Water flows up the ice–sediment interface along path coordinate s. From left to right: H^{b} is the water layer height, which is equivalent to $2R^{\mathrm{b}}$. Z^{i} is the ice thickness. The along path coordinate s follows the water layer. The surface elevation is z^{r}. The elevation of the glacier base is z^{b}. The elevation of the base of the water layer is z^{s}. The angle of the surface and the bed are α^{r} and α^{b}, respectively.

Water flows along the ice–sediment interface until exiting the glacier section downstream of an overdeepening. From input to output, an element of water is described in terms of the 1-D coordinate (Fig. 2.1). The base of the water lies at an elevation z^{s}. The roof of the water is at an elevation z^{b}. A glacier of thickness Z^{i} overlies the water layer. Both R-channels and sheets

can be defined in terms of their hydraulic perimeter P^{w}, and cross-sectional area S^{w},

$$P^{\mathrm{w}} = \begin{cases} 2\pi R^{\mathrm{b}} & \text{circular channel,} \\ (\pi + 2)\, R^{\mathrm{b}} & \text{semicircular channel,} \\ 2H^{\mathrm{b}} + 2W & \text{sheet,} \end{cases} \tag{2.2a}$$

$$S^{\mathrm{w}} = \begin{cases} \pi (R^{\mathrm{b}})^2 & \text{circular channel,} \\ \frac{\pi}{2} (R^{\mathrm{b}})^2 & \text{semicircular channel,} \\ H^{\mathrm{b}} W & \text{sheet,} \end{cases} \tag{2.2b}$$

where R^{b} is the channel radius, H^{b} is the sheet thickness, and W is the sheet width. These cross-sectional geometries are summarized in Figure 2.2. In the along-path coordinate, these cross-sections vary smoothly, growing larger or smaller depending on flow conditions (Nye, 1976; Spring & Hutter, 1982). In loose terms, the channels behave as tubes, while the sheets behave as ducts. Sheets have a cross sectional area; but for a sheet continuous in y, its thickness H^{b} determines the behavior of the cross-section. Equations governing flow become width-averaged quantities. This sheet thickness spans the average elevation of the subglacial sediments z^{s} to the average elevation of the base of the glacier z^{b}. These two horizons are locally parallel.

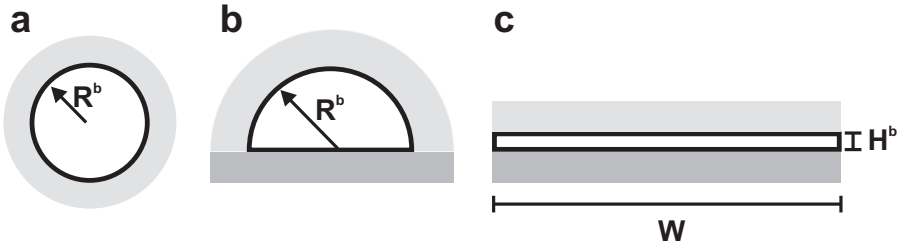

Figure 2.2: Subglacial water cross sections. White represents water flow area, light grey areas represent ice, and dark grey areas represent subglacial material. (a) R-channel surrounded by ice. (b) Semicircular R-channel. (c) Water sheet. Cross-sectional areas for both channels are equal. The cross-sectional area of the sheet is approximately half of the other two. Water flow is perpendicular to the plane of the page.

The hydraulic radius, which is the ratio of the cross-sectional area to the wetted perimeter, $R_h = S^{\mathrm{w}}/P^{\mathrm{w}}$, is commonly used in fluid flow engineering applications,

$$R_h = \begin{cases} \dfrac{R^{\mathrm{b}}}{2} & \text{circular channel,} \\ \dfrac{\pi R^{\mathrm{b}}}{2(\pi + 2)} & \text{semicircular channel.} \end{cases} \tag{2.3}$$

For tubes with circular cross sections, the hydraulic radius is simply half the radius. For a semicircular conduit bounded on its base by sediment, the hydraulic radius is given as one quarter of the radius. Water sheets are relatively shallow. The width of the flow is then much greater than its height ($W \gg H^{\mathrm{b}}$), and the hydraulic radius for sheets can be approximated by

$$R_h = \frac{H^{\mathrm{b}}}{2}. \tag{2.4}$$

For the semicircular case, if the roughness of the bed is significantly less than the radius of the channel, then equation (2.3) is sufficient. For subglacial sheets, this approximation depends on how the water floods the roughness elements. For lack of a better parameterization, this hydraulic radius (eq. 2.4) will be used.

The melting perimeter P^{i}, will be different for each of the geometries,

$$P^{\mathrm{i}} = \begin{cases} 2\pi R^{\mathrm{b}} & \text{circular channel,} \\ \pi R^{\mathrm{b}} & \text{semicircular channel,} \\ 2H^{\mathrm{b}} + W & \text{sheet.} \end{cases} \tag{2.5}$$

Only for the circular case will the melting perimeter be exactly the wetted perimeter. For the both the semicircular cross-section and the sheet, only the ceiling will melt. The bed is excluded from any melt relation. Clarke (2003) noted that the melt rate depends on the melting perimeter along the flow rather than simply the hydraulic perimeter. Assuming that the water layer is ice-roofed, the melting perimeter is the width of the layer. If the water layer is bound on either side by ice, then the small height approximation can be applied: melt on vertical ice walls can be ignored. However, if the sheet has sediment walls, then the melting perimeter is exactly the roof width. Either way, melt from the wall of the sheet is not immediately important.

Supercooled water need not form ice on the underside of the glacier. Examples from fluvial studies (*e.g.,* Osterkamp & Gosink, 1983; Kerr *et al.*, 2002) illustrate that much ice can form on rocks at the base of rivers. This fluvial process may be paralleled subglacially such that ice forms on the sediment below the water. Ice could encase some of the sediments, and then mobilize the sediments into the flow or float them to the ice–water interface where they freeze to the underside of the glacier. This idea merits attention but is not of primary importance. For simplicity, crystallization of ice can be assumed to occur along the melting perimeter. The melting and freezing perimeter are exactly the same for the remainder of this study but need not be.

2.1.2 Clausius-Clapeyron equation

Figure 2.3 illustrates the phase diagram of water. Lines of coexistence separate water vapor, liquid water, and water ice. The unique feature of these lines is that the change in Gibbs free energy required to cross from one phase to another is zero along them. By setting the change in Gibbs free energy to zero, the Clausius-Clapeyron equation can be derived for the change of phase (*e.g.,* Krauskopf & Bird, 1995, p. 420),

$$\frac{\partial p}{\partial T} = \frac{\Delta E}{T_0 \Delta V}, \tag{2.6}$$

where the slope of the line $\partial p/\partial T$, is defined by the change in enthalpy ΔE, a change in volume ΔV, and a reference temperature for the phase change T_0.

The inverse slope, $\partial T/\partial p$, is the quantity of interest. This slope is obtained by inverting equation (2.6) to obtain

$$\frac{\partial T}{\partial p} = \left(\frac{1}{\rho^{\mathrm{w}}} - \frac{1}{\rho^{\mathrm{i}}} \right) \frac{T_0}{L}. \tag{2.7}$$

In moving from (2.6) to (2.7), the latent heat of fusion per unit mass L is substituted for the enthalpy; and the change in volume is replaced with the change in mass densities. The

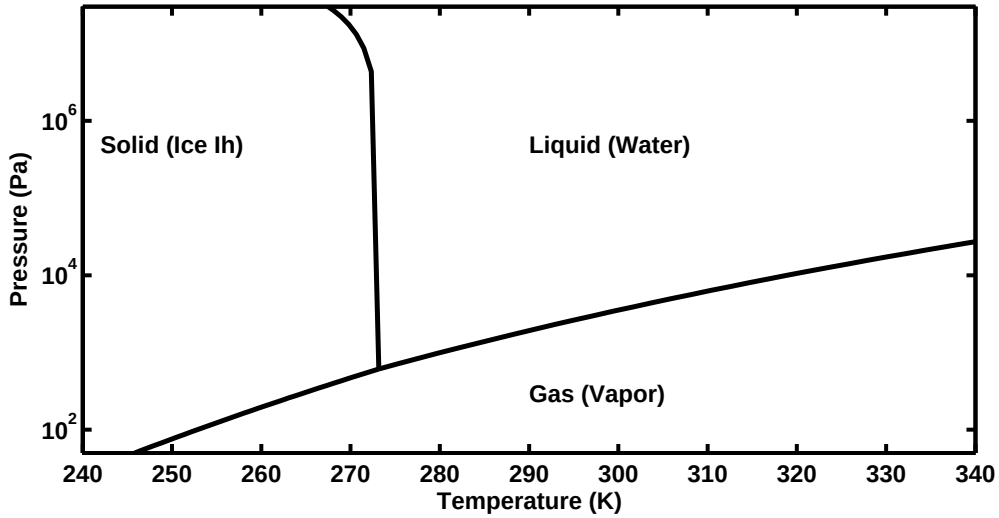

Figure 2.3: Phase diagram of water. Lines indicate where both phases are stable. All three phases are stable at the triple point ($\sim$ 612 Pa, 273.16 K). The maximum pressure on this diagram (3.0×10^7 Pa) is equivalent to an ice thickness of 3300 m. Adapted from Wagner & Pruss (1993) and Wagner *et al.* (1994).

quantities ρ^{i} and ρ^{w} are the usual mass densities of ice and water. Because the slope of the line of coexistence between water and ice is relatively smooth, the change in $\partial T/\partial p$ can be held constant for values near T_0. The change in the zero point from the reference value T_0 when the interfacial pressure p^{w}, changes is given by

$$T_{\mathrm{mp}} = T_0 + \beta p^{\mathrm{w}}, \tag{2.8}$$

where the coefficient β is equal to the inverse Clausius-Clapeyron slope $\partial T/\partial p$. The reference freezing point is 273.15 K in equation (2.7), but could also be 0 °C in (2.8) because this equation denotes only a relative change. From equation (2.7) the parameter β will be negative because ice is less dense than water at the freezing point. However, when these equations are applied to the subglacial environment, the density of water must include air within the water. The effect of air on the water density was noted by both Röthlisberger & Lang (1987) and Alley *et al.* (1998).

The interfacial pressure was discussed by Spring & Hutter (1982). The two obvious choices are the overburden stress from the ice or the water pressure at the ice–water contact. Spring & Hutter used the water pressure, which makes sense given that the ice overburden may not govern the local variations in stress at the ice–water contact. I apply this interfacial pressure parameterization to equation (2.8) throughout the thesis.

The Clausius-Clapeyron equation determines how the change in water pressure can modulate the melting point. Generally, β takes a value from -7.4×10^{-8} to -9.8×10^{-8} K Pa^{-1} depending on whether the water is pure or air-saturated, respectively. From the synthetic glacier section in Figure 1.3 with maximum ice thickness of about 47 m, assuming that the water pressure varies directly with ice overburden thickness, the maximum change of the melting point would be -0.03 or -0.04 °C for pure or air-saturated water, respectively. These example temperature depressions scale linearly with ice thickness, but water pressure at the base may deviate significantly from ice overburden.

One aspect of equation (2.7) that I have not discussed is the role of salts or other impurities. Salts typically depress the freezing point further. Equation (2.6) sets the change in Gibbs free energy to zero, making the change in entropy equal to the change in enthalpy divided by the reaction temperature. If salts are included, an additional term draws from the entropy term. Lawson (pers. comm., 2005) stated that all water quality measurements at Matanuska Glacier have pointed to the water being fresh. However, Björnsson (2002) noted that a sulphurous odor preceded jökulhlaups at Skeiðarárjökull. The presence of chemical components suggests that supercooling under jökulhlaup conditions would necessitate the additional temperature depression terms in the Clausius-Clapeyron equation. The effect of salts on the freezing temperature has been studied (*e.g.,* Chen & Millero, 1977, 1986) but is not included because water quality data at most field sites are not readily available.

2.2 Balance laws

The continuum balance laws provide the foundation for the model (Spring & Hutter, 1981, 1982). In total, there are four time-dependent equations: two mass balance equations, one momentum balance equation, and one energy balance equation. The four dependent variables are hydraulic cross-section, water pressure, water velocity, and water temperature. Each of these variables represents a local average in space and time. The balance equations are equivalent to the St. Venant equations that are commonly used in fluvial engineering. The main differences between the St. Venant equations and the Spring-Hutter formulation are that water flow is sealed and, to a degree, pressurized by an overlying glacier and that a phase change from water to ice is permissible (Spring & Hutter, 1981, 1982). Because the phase change is temperature dependent, an energy equation governing the temperature evolution appears that would not necessarily be present in the St. Venant equations.

Furthermore, these equations have an accessible relationship to the previously published material of Röthlisberger & Lang (1987) and Alley *et al.* (1998). Röthlisberger & Lang provided the basic relationship for melting or freezing of flowing water because of a change in the temperature-dependent melting point. In addition to assuming that the flow is steady and uniform, they assumed that the water is always at the pressure melting point. These assumptions in a mathematical sense, using the linear subglacial water velocity u^{b} in the s direction and the temperature of the subglacial water T^{b} are

$$\frac{du^{\mathrm{b}}}{dt} = 0, \tag{2.9a}$$

$$\frac{\partial T^{\mathrm{b}}}{\partial t} = 0, \tag{2.9b}$$

where equation (2.9a) denotes steady, uniform flow. This equation is somewhat misleading because it states that the source terms are equal to zero as well, which is the desired relationship. Equation (2.9b) indicates that the water is at the pressure melting point regardless of its location. The Spring-Hutter formulation has a reduced form that corresponds to equations (2.9a) and (2.9b). The relationship between both sets of equations will be presented in detail in subsequent parts of this chapter.

Higher-order models of subglacial water flow have been proposed. For example, Bates *et al.* (2003) formulated flow based on the Reynolds averaged Navier–Stokes (RANS) equations. The main difference between a RANS representation and the Spring-Hutter formulation is that the dissipation terms from viscous stresses are parameterized as a shear stress along the hydraulic

perimeter in the Spring-Hutter formulation. In general, the dissipation along the hydraulic perimeter is several orders of magnitude larger than the dissipation within the flow (Hinze, 1975). A RANS representation is also more complex in the case of subglacial flow because the exact hydraulic geometry is not known but would be required. Solution of a RANS representation is also computationally intensive. As a result, simulation of water flow via a RANS or other higher-order model representation is beyond the scope of the present work.

2.2.1 Mass balance

Spring & Hutter derived the mass balance specifically for curvilinear tubes using the transport theorem. They assumed that the tube could vary in s. Spring & Hutter were chiefly interested in jökuhlhaups, and as a result, thought of the channel simply as melting open rather than freezing closed. For the phenomena described here, a negative melt rate is equivalent to an ice accretion rate. Because there are two phases, water and ice, there must also be two mass balance equations that include the processes of creep and melt closure to describe how cross-section changes through time (Spring & Hutter, 1981, 1982).

In a one dimensional system, the second dimension is approximated by having the cross section evolve. In the case of R-channels, the cross-sectional area evolves directly, while the other pertinent parameters can be calculated from that area. For example, hydraulic radius can be calculated from the area and the assumed cross-section. For the sheet, the second dimension is not critical; and as a result, it is not modeled. The mass balance relations then reduce to cross-sectional evolution and height evolution equations for their respective cross-sectional geometries.

Equation (2.10) shows the general form for the mass of water in the hydraulic cross section,

$$M^{\mathrm{w}} = \int_s \int_{S^{\mathrm{w}}} \rho^{\mathrm{w}} \, dS \, ds. \tag{2.10}$$

Following Spring & Hutter (1982), I define a difference in cross section,

$$\widehat{S} = S^{\mathrm{i}} - S^{\mathrm{w}}, \tag{2.11}$$

that represents the instantaneous misfit resulting from ice melted away per unit time. The mass of this misfit cross-section is

$$\widehat{M} = \int_s \int_{\widehat{S}} \left\{ \left(1 - n_p^{\mathrm{i}}\right) \rho^{\mathrm{i}} + n_p^{\mathrm{i}} \rho^{\mathrm{w}} \right\} dS \, ds, \tag{2.12}$$

where n_p^{i} is the porosity of the ice. Equation (2.12) assumes that the surrounding ice is porous and that the mass is a mixture of water and ice. Moving equations (2.10) and (2.12) to a local balance per unit channel length along s via the material derivative yields

$$\rho^{\mathrm{w}} \frac{\partial S^{\mathrm{w}}}{\partial t} + \rho^{\mathrm{w}} \frac{\partial}{\partial s} \left(u_s^{\mathrm{w}} S^{\mathrm{w}}\right) = m + \frac{n_p^{\mathrm{i}} \rho^{\mathrm{w}}}{\left(1 - n_p^{\mathrm{i}}\right) \rho^{\mathrm{i}}} m, \tag{2.13a}$$

$$\left\{ \left(1 - n_p^{\mathrm{i}}\right) \rho^{\mathrm{i}} + n_p^{\mathrm{i}} \rho^{\mathrm{w}} \right\} \left\{ \frac{\partial \widehat{S}}{\partial t} + \frac{\partial}{\partial s} \left(u_s^{\mathrm{i}} \widehat{S} \right) \right\} = - m - \frac{n_p^{\mathrm{i}} \rho^{\mathrm{w}}}{\left(1 - n_p^{\mathrm{i}}\right) \rho^{\mathrm{i}}} m. \tag{2.13b}$$

where m is the mass of melt per unit time per unit channel length, u_s^{w} is the water velocity along s, and u_s^{i} is the ice velocity along s. In these equations, the density of water and ice are

assumed to be constant. Equations (2.13) show that the rate of change of mass in either cross section is equal to the amount of water produced from melting or freezing. Rewriting both of these equations for $\partial S^{\mathrm{w}}/\partial t$ yields

$$\frac{\partial S^{\mathrm{w}}}{\partial t} = \frac{\left(1-n_p^{\mathrm{i}}\right)\rho^{\mathrm{i}} + n_p^{\mathrm{i}}\rho^{\mathrm{w}}}{\left(1-n_p^{\mathrm{i}}\right)\rho^{\mathrm{i}}\rho^{\mathrm{w}}} m - \frac{\partial}{\partial s}\left(u_s^{\mathrm{w}} S^{\mathrm{w}}\right), \tag{2.14a}$$

$$\frac{\partial S^{\mathrm{w}}}{\partial t} = \frac{m}{\left(1-n_p^{\mathrm{i}}\right)\rho^{\mathrm{i}}} + \left(\frac{\partial S^{\mathrm{i}}}{\partial t}\right)_{\mathrm{close}}, \tag{2.14b}$$

where equation (2.14a) is the mass balance for the water and equation (2.14b) is the mass balance for the ice. In moving from equation (2.13b) to (2.14b), the time derivative of the right hand side of equation (2.11) is used to substitute for the time rate of change of the area melted, $\partial\widehat{S}/\partial t = \partial S^{\mathrm{i}}/\partial t - \partial S^{\mathrm{w}}/\partial t$. Furthermore, the velocity of the ice along s is neglected. In consequence, $\left(\partial S^{\mathrm{i}}/\partial t\right)_{\mathrm{close}}$ is the velocity of ice normal to water flow and represents ice closure. The form of the closure velocity $\left(\partial S^{\mathrm{i}}/\partial t\right)_{\mathrm{close}}$ will depend on whether the cross-section is a sheet or a channel.

Solving these two equations for the hydraulic cross-section requires that a numerical solver set both results equal to the same value. This forced equality makes the problem numerically stiff. If instead, an approximation to one of the equations is made, then the equality can be relaxed. Clarke (2003, appendix A) detailed this relaxation. The salient feature of the relaxation is that the water is assumed to be compressible. One can then use the equation of state for water to substitute for the time rate of change of the water density. The net result is that the mass balance equation for water becomes an equation for the pressure of water p^{b},

$$\frac{\partial p^{\mathrm{b}}}{\partial t} = -\frac{1}{\gamma^{\mathrm{b}} S^{\mathrm{b}}}\left\{\frac{\partial S^{\mathrm{b}}}{\partial t} + \frac{\partial (S^{\mathrm{b}} u^{\mathrm{b}})}{\partial s} - \frac{\left(1-n_p^{\mathrm{i}}\right)\rho^{\mathrm{i}} + n_p^{\mathrm{i}}\rho^{\mathrm{w}}}{\left(1-n_p^{\mathrm{i}}\right)\rho^{\mathrm{i}}\rho^{\mathrm{w}}} m\right\}, \tag{2.15}$$

where u^{b} replaces u_s^{w}, and S^{b} replaces S^{w}. The notation S^{b} has sole reference to subglacial channels, and S^{w} will refer to the general forms of the cross section presented in equation (2.2b). Use of both S^{b} and u^{b} makes notation simpler throughout the remainder of the thesis. Solving this equation in conjunction with (2.14b) and γ^{b} set as the compressibility of the water yields the exact solution produced by solving both equations (2.14a) and (2.14b). Relaxing γ^{b} physically approximates water being more compressible but enhances the convergence of the numerical solution. This relaxation has no noticeable effect on the overall mass balance. Clarke also noted that the mass balance of the ice could be used instead of the water balance. This approximation is equivalent to making the channel walls distensible, or stretchable. Compressibility assumptions such as these are common in the fluid dynamics literature, and the compressibility has been used in hydrogeology to represent compressible aquifers (*e.g.,* Bear, 1988, p. 204).[3]

For the subglacial sheet, the final equations are given by,

$$\frac{\partial H^{\mathrm{b}}}{\partial t} = \frac{\tilde{m}}{\left(1-n_p^{\mathrm{i}}\right)\rho^{\mathrm{i}}} + \left(\frac{\partial H^{\mathrm{b}}}{\partial t}\right)_{\mathrm{close}}, \tag{2.16a}$$

$$\frac{\partial p^{\mathrm{b}}}{\partial t} = -\frac{1}{\gamma^{\mathrm{b}} H^{\mathrm{b}}}\left\{\frac{\partial H^{\mathrm{b}}}{\partial t} + \frac{\partial (H^{\mathrm{b}} u^{\mathrm{b}})}{\partial s} - \frac{\left(1-n_p^{\mathrm{i}}\right)\rho^{\mathrm{i}} + n_p^{\mathrm{i}}\rho^{\mathrm{w}}}{\left(1-n_p^{\mathrm{i}}\right)\rho^{\mathrm{i}}\rho^{\mathrm{w}}}\tilde{m}\right\}. \tag{2.16b}$$

[3]In Chapter 5, I show the details of the compressibility assumption in deriving the pressure evolution in the englacial water system.

In these equations, $\tilde{m}$ is the mass of melt per second per square meter or m per unit width. The sheet closure velocity $(\partial H/\partial t)_{\text{close}}$ is the subject of Chapter 3 and will not be given additional attention here.

Expanding equation (2.14b) using the closure relationship yields the evolution of the cross section for the R-channels,

$$\frac{\partial S^{\text{b}}}{\partial t} = \frac{m}{\rho^{\text{i}}\left(1-n_p^{\text{i}}\right)} - 2S^{\text{b}}\,\text{sgn}(p^{\text{i}}-p^{\text{b}})\left(\frac{|p^{\text{i}}-p^{\text{b}}|}{n\mathcal{B}}\right)^n, \tag{2.17}$$

where p^{i} the is ice overburden pressure, n is the flow law exponent, and $\mathcal{B}$ is the flow law coefficient, or fluidity of ice. The term on the extreme right of (2.17) is the Glen's law formulation of creep closure that Spring & Hutter (1981) used for conduits. The mass balance system for the channels is given by equations (2.15) and (2.17). These equations can be contrasted with those for the sheet in equation set (2.16). I will present the momentum and energy equations twice also: once for the channels and once for the sheets.

Because these equations have a melt rate term, they affect the overlying ice by melting or freezing along the melt perimeter. The thickness of the ice changes as ice is accreted or melted from the base. For the sheet, a simple mass balance term for overlying ice is given by

$$\frac{\partial Z^{\text{i}}}{\partial t} = -\frac{\tilde{m}}{\left(1-n_p^{\text{i}}\right)\rho^{\text{i}}}. \tag{2.18}$$

In this equation, the total derivative is equal to the negative melt rate term. Because I neglect ice flow, there is no convective velocity. While glaciers are rarely static, adding a convective term and the corresponding strain terms for the ice is beyond the scope of the present work. In addition, I use the notation Z^{i} for the thickness of the glacier itself (Fig. 2.1). When the porosity is reduced to zero, equation (2.18) reduces to a solid accretion rate.

An alternative to equation (2.18) is to define an accreted ice thickness $Z^{\text{b:e}}$. The evolution of the accreted ice thickness is simply

$$\frac{\partial Z^{\text{b:e}}}{\partial t} = -\frac{\tilde{m}}{\left(1-n_p^{\text{i}}\right)\rho^{\text{i}}} \quad \text{sheet.} \tag{2.19}$$

Furthermore, the thickness of accreted ice for the channels is

$$\frac{\partial Z^{\text{b:e}}}{\partial t} = \begin{cases} -\dfrac{1}{R^{\text{b}}+Z^{\text{b:e}}}\left[\dfrac{m}{2\pi(1-n_p^{\text{i}})\rho^{\text{i}}} + \dfrac{Z^{\text{b:e}}}{2\pi R^{\text{b}}}\left(\dfrac{\partial S^{\text{b}}}{\partial t}\right)_{\text{close}}\right] & \text{circular channel,} \\ -\dfrac{1}{R^{\text{b}}+Z^{\text{b:e}}}\left[\dfrac{m}{\pi(1-n_p^{\text{i}})\rho^{\text{i}}} + \dfrac{Z^{\text{b:e}}}{\pi R^{\text{b}}}\left(\dfrac{\partial S^{\text{b}}}{\partial t}\right)_{\text{close}}\right] & \text{semicircular channel,} \end{cases} \tag{2.20}$$

where the closure term on the right hand side accounts for the contraction of the accreted ice layer. Equation (2.19) does not account for this contraction because ice moves vertically into and out of the sheet without the radial divergence present in the case of channels.

Porosity of the accreted ice

Ice that accretes may be discontinuous and preserve a residual porosity. Direct observations of ice actively accreting subglacially are nonexistent. Instead, observations made at glacier termini

are commonly used as proxies for the subglacial environment. Frazil ice near the terminus of Matanuska Glacier forms in water that ascends vents local to the terminus (Lawson *et al.*, 1998). When water ascended a shear fracture extending from the bed to the surface of Skeiðarárjökull frazil ice formed (Roberts *et al.*, 2002). It is not immediately clear that water that ascends steep local features is representative of the subglacial environment. However, the formation of frazil is certainly a viable method of accreting ice and appears to be dominant in subglacial environments. Another method of accreting ice would be the formation of a mushy layer (*e.g.,* Worster, 1997). Mushy layers typically form in low-velocity flows with the prominent analog being sea ice growing downward at the sea surface (*e.g.,* Wettlaufer, 2001). Depending on conditions, the porosity in mushy layers can be high. In contrast, Gilpin's (1981) experiments of flow through closed conduits showed that accreting ice is not very porous. However, these experiments were run with high pressure gradients and high velocities. With a wide range of porosity to choose from depending on the choice of analog for the subglacial environment, it stands to reason that the accreting ice will be somewhat porous. Moreover, porosity of an accreted layer will be a function of flow conditions.

In the absence of an exact relationship for the evolution of the ice porosity, n_p^{i} becomes an adjustable parameter that affects the cross-section evolution, water pressure, and, for the sheet, ice thickness. The rate of change of the hydraulic cross-section is governed not only by melt but by the addition of water that is in the pore space. The rate of water addition from the pore space is the final term on the right hand side of equations (2.13). The rate of change of the thickness of the water sheet resulting from melting or freezing is $\tilde{m}/\left[(1-n_p^{\mathrm{i}})\rho^{\mathrm{i}}\right]$. This relationship appears in equations (2.16a), and (2.18).

2.2.2 Momentum balance

Steady flow

While flow may be steady and uniform, the supply and flux of momentum are governed by the geometry of the ice–bed interface and the overlying ice. As is typical of steady conditions, momentum supply from gravitational head loss and a change in pressure gradient is balanced by shear along the perimeter (*e.g.,* Bird *et al.*, 1960, p. 182),

$$-\left(\Delta p^{\mathrm{b}} + \rho^{\mathrm{w}} g \Delta z^{\mathrm{b}}\right) S^{\mathrm{w}} = P^{\mathrm{w}} \Delta s \; \tau_0, \tag{2.21}$$

where Δp^{b} is a change in water pressure, g is the gravitational acceleration, Δz^{b} is the elevation change of the ice–water interface, and τ_0 is the shear along the hydraulic perimeter. Moving this macroscopic balance to a differential balance is straightforward,

$$\tau_0 = -\frac{S^{\mathrm{w}}}{P^{\mathrm{w}}}\left(\frac{\partial p^{\mathrm{b}}}{\partial s} + \rho^{\mathrm{w}} g \frac{\partial z^{\mathrm{b}}}{\partial s}\right), \tag{2.22a}$$

$$= -\frac{S^{\mathrm{w}}}{P^{\mathrm{w}}}\frac{\partial \phi^{\mathrm{b}}}{\partial s}. \tag{2.22b}$$

The left hand side of equation (2.22a) is identifiable as the scaled negative gradient of the hydraulic potential,

$$\phi^{\mathrm{b}} = p^{\mathrm{b}} + \rho^{\mathrm{w}} g z^{\mathrm{b}}. \tag{2.23}$$

The Darcy-Weisbach formulation is an empirical relation for the shear stress along the hydraulic perimeter,[4]

$$\tau_0 = \frac{1}{8}\rho^{\mathrm{w}} f_d (u^{\mathrm{b}})^2, \tag{2.24}$$

where f_d is a friction coefficient. Clarke (2003) suggested that the friction coefficient was a combination of the ice and bed friction coefficients,

$$f_d = \begin{cases} f_d^{\mathrm{i}} & \text{circular conduit} \\ \dfrac{P^{\mathrm{i}} f_d^{\mathrm{i}} + \left(P^{\mathrm{w}} - P^{\mathrm{i}}\right) f_d^{\mathrm{s}}}{P^{\mathrm{w}}} & \text{semicircular conduit} \\ \frac{1}{2}\left(f_d^{\mathrm{i}} + f_d^{\mathrm{s}}\right) & \text{sheet} \end{cases} \tag{2.25}$$

where f_d^{i} and f_d^{s} are the friction coefficients for the ice and bed, respectively. In equation (2.25), I make the simple assumption that the roof and floor of the sheet account for an equal portion of the shear stress; but they need not be equal depending on roughness features of the ice or characteristics of the bed. For turbulent water flow, f_d must be assigned as parameter. Values for f_d for relatively smooth open channel flow range from 0.0012 to 0.06 (Schlichting, 1979, p. 617, Fig. 20.18). Clarke (2003) used hydraulic roughness parameters equivalent those for rough streams to simulate outburst floods. For laminar water flow, the friction factor is usually based on the Reynolds number. Because these relationships are based on data for smooth-walled conduits and have low accuracy (Bird *et al.*, 1960, p. 187), the laminar relationships are not of interest here.

A relationship for the velocity follows from equations (2.22b) and (2.24),

$$u^{\mathrm{b}} = -\left(\frac{8}{\rho^{\mathrm{w}} f_d}\frac{S^{\mathrm{b}}}{P^{\mathrm{w}}}\right)^{\frac{1}{2}} \operatorname{sgn}\!\left(\frac{\partial \phi^{\mathrm{b}}}{\partial s}\right)\left|\frac{\partial \phi^{\mathrm{b}}}{\partial s}\right|^{\frac{1}{2}} \qquad \text{channel,} \tag{2.26a}$$

$$u^{\mathrm{b}} = -\left(\frac{8}{\rho^{\mathrm{w}} f_d}\frac{H^{\mathrm{b}}}{2}\right)^{\frac{1}{2}} \operatorname{sgn}\!\left(\frac{\partial \phi^{\mathrm{b}}}{\partial s}\right)\left|\frac{\partial \phi^{\mathrm{b}}}{\partial s}\right|^{\frac{1}{2}} \qquad \text{sheet.} \tag{2.26b}$$

Stone & Clarke (1993) used a similar relationship for turbulent flow in a horizontal water layer beneath a glacier. Other shear stress parameterizations could be used to create equations (2.26). For example, the Manning-Strickler formula could be used in the place of the Darcy-Weisbach formula. Clarke (2003) used both but reasoned that the Manning-Strickler formula is more realistic for floods.

[4]Bird *et al.* (1960) gave their derivation in terms of the Fanning friction coefficient f_f. However, Schlichting (1979, p. 597) gave a similar derivation using the Darcy-Weisbach friction coefficient f_d. These two coefficients are related via $f_f = f_d/4$. The difference of 1/4 results from a discrepancy in transferring the coefficient from Hagen-Poiseuille flow to turbulent pipe flow. The Schlichting form is more common in the fluvial geomorphology literature; yet both are used and often carelessly given the notation f without proper identification. I thus adopt f_d as the more common Darcy-Weisbach coefficient in place of the Fanning coefficient f_f.

Time dependent flow

Modification of the velocity evolution of Spring & Hutter (1981) to include the porosity of the ice gives,

$$\frac{\partial u^{\mathrm{b}}}{\partial t} = - u^{\mathrm{b}} \frac{\partial u^{\mathrm{b}}}{\partial s} - \frac{\left(1 - n_p^{\mathrm{i}}\right) \rho^{\mathrm{i}} + n_p^{\mathrm{i}} \rho^{\mathrm{w}}}{\left(1 - n_p^{\mathrm{i}}\right) \rho^{\mathrm{i}}} \frac{m u^{\mathrm{b}}}{\rho^{\mathrm{w}} S^{\mathrm{b}}} - \frac{1}{\rho^{\mathrm{w}}} \frac{\partial p^{\mathrm{b}}}{\partial s} - g \frac{\partial z^{\mathrm{b}}}{\partial s} - \frac{P^{\mathrm{w}} \tau_0}{S^{\mathrm{b}} \rho^{\mathrm{w}}} \quad \text{channel,} \tag{2.27a}$$

$$\frac{\partial u^{\mathrm{b}}}{\partial t} = - u^{\mathrm{b}} \frac{\partial u^{\mathrm{b}}}{\partial s} - \frac{\left(1 - n_p^{\mathrm{i}}\right) \rho^{\mathrm{i}} + n_p^{\mathrm{i}} \rho^{\mathrm{w}}}{\left(1 - n_p^{\mathrm{i}}\right) \rho^{\mathrm{i}}} \frac{\tilde{m} u^{\mathrm{b}}}{\rho^{\mathrm{w}} H^{\mathrm{b}}} - \frac{1}{\rho^{\mathrm{w}}} \frac{\partial p^{\mathrm{b}}}{\partial s} - g \frac{\partial z^{\mathrm{b}}}{\partial s} - \frac{2 \tau_0}{H^{\mathrm{b}} \rho^{\mathrm{w}}} \quad \text{sheet,} \tag{2.27b}$$

where both equations include the porosity change discussed previously. These equations are derived from the material balance of the local momentum. Multiplying these equations by the water density and cross sectional area would yield the momentum balance in its original one-dimensional form. Beginning with the left hand side, the first two terms are the material derivative of the velocity. The next term, with m or $\tilde{m}$, is the impulse lost (or gained) from melt (or accretion) along the hydraulic perimeter. The next two terms result from the change in the hydraulic potential along flow. The final term on the right is shear along the hydraulic perimeter. These equations are subject to the supplementary relations in equations (2.24) and (2.38b).

Equivalent discharge

The amount of meltwater that reaches the ice–bed interface will be independent of whether the water runs through sheets or conduits. Water discharge must then be equivalent for either a sheet or a channel. Exact equivalence of discharge might never occur subglacially. For example, in examining Figures 2.1 and 2.2, there are several competing features among the cross sections. In particular the momentum expended on shear along the hydraulic perimeter will be much greater for the sheet than for the conduits despite the expectation that hydraulic potential will be the same for all the cross-sections. For the steady case, the discharge $Q^{\mathrm{b}} = S^{\mathrm{b}} u^{\mathrm{b}}$ can be set equal using equations (2.26). The radii of the channels can then be found in terms of the geometry of the sheet,

$$R^{\mathrm{b}} = \left(H^{\mathrm{b}}\right)^{\frac{3}{5}} \left(\frac{W}{\pi}\right)^{\frac{2}{5}} \qquad \text{circular channel,} \tag{2.28a}$$

$$R^{\mathrm{b}} = (4\pi + 8)^{\frac{1}{5}} \left(\frac{H^{\mathrm{b}}}{\pi}\right)^{\frac{3}{5}} W^{\frac{2}{5}} \qquad \text{semicircular channel.} \tag{2.28b}$$

Time dependent flow is not necessarily subject to these relationships because the flow will adjust according to the upstream boundary conditions.

2.2.3 Energy balance

Time dependent flow

Spring & Hutter (1981, 1982) derived the energy balance equation for one-dimensional pipe flow incorporating the ice–water phase change. Expanding the material derivative and rearranging

the heat balance yields a partial differential equation for temperature,

$$\frac{\partial T^{\mathrm{b}}}{\partial t} = - u^{\mathrm{b}} \frac{\partial T^{\mathrm{b}}}{\partial s} - \frac{m}{\rho^{\mathrm{w}} c_p^{\mathrm{w}} S^{\mathrm{b}}} \left\{ L + c_p^{\mathrm{w}} \Delta T_{\mathrm{mp}} - \frac{\left(1 - n_p^{\mathrm{i}}\right) \rho^{\mathrm{i}} + n_p^{\mathrm{i}} \rho^{\mathrm{w}}}{\left(1 - n_p^{\mathrm{i}}\right) \rho^{\mathrm{i}}} \frac{(u^{\mathrm{b}})^2}{2} \right\} + \frac{P^{\mathrm{w}}}{S^{\mathrm{b}}} \frac{\tau_0 u^{\mathrm{b}}}{\rho^{\mathrm{w}} c_p^{\mathrm{w}}}, \tag{2.29a}$$

$$\frac{\partial T^{\mathrm{b}}}{\partial t} = - u^{\mathrm{b}} \frac{\partial T^{\mathrm{b}}}{\partial s} - \frac{\tilde{m}}{\rho^{\mathrm{w}} c_p^{\mathrm{w}} H^{\mathrm{b}}} \left\{ L + c_p^{\mathrm{w}} \Delta T_{\mathrm{mp}} - \frac{\left(1 - n_p^{\mathrm{i}}\right) \rho^{\mathrm{i}} + n_p^{\mathrm{i}} \rho^{\mathrm{w}}}{\left(1 - n_p^{\mathrm{i}}\right) \rho^{\mathrm{i}}} \frac{(u^{\mathrm{b}})^2}{2} \right\} + \frac{2}{H^{\mathrm{b}}} \frac{\tau_0 u^{\mathrm{b}}}{\rho^{\mathrm{w}} c_p^{\mathrm{w}}}, \tag{2.29b}$$

where the specific heat of water is c_p^{w}, and equations (2.29a) and (2.29b) are for the channel and sheet, respectively. In these equations, the time derivative of the change in energy per unit volume is equal to the changes in latent heat L, sensible heat $c_p^{\mathrm{w}} \Delta T_{\mathrm{mp}}$, and specific kinetic energy $(u^{\mathrm{b}})^2/2$ released through melting, m or $\tilde{m}$, plus the shear heating along the hydraulic perimeter $P^{\mathrm{w}} \tau_0 u^{\mathrm{b}}$. The specific kinetic energy term results from the impulse term from equation (2.27) being dotted by the velocity to make an energy term. The primary difference between the energy equation for conduit flow and a distributed macroporous sheet is the hydraulic perimeter and cross-section of flow. Again, equations (2.3) provide supplementary relationships for one of the hydraulic cross sections.

Steady flow: Röthlisberger heat transfer

Because the water is always in contact with ice along its flow path, the only reasonable interpretation of the assumption in equation (2.9b) is that the temperature of the water must be equal to that of the overlying ice. Additionally, the overlying ice and underlying bed must be at the local melting point. As a result, the subglacial temperature must remain at the steady value of the pressure melting point. The assumption of the time rate of change being zero fixes the melt rate, and the energy balance becomes a statement of the melt rate.

Because the water is at the melting point, the sensible heat term is unimportant in isolating the melt rate from (2.29). I also discard the energy imparted from the impulse term because it is approximately five orders of magnitude smaller than the latent heat term. Rewriting equation set (2.29) for the melt rate gives the equations,

$$m = - \frac{S^{\mathrm{b}} u^{\mathrm{b}}}{L} \left(\rho^{\mathrm{w}} c_p^{\mathrm{w}} \frac{\partial T^{\mathrm{b}}}{\partial s} + \frac{P^{\mathrm{w}} \tau_0 u^{\mathrm{b}}}{S^{\mathrm{b}}} \right) \qquad \text{channel,} \tag{2.30a}$$

$$\tilde{m} = - \frac{H^{\mathrm{b}} u^{\mathrm{b}}}{L} \left(\rho^{\mathrm{w}} c_p^{\mathrm{w}} \frac{\partial T^{\mathrm{b}}}{\partial s} + \frac{2 \tau_0 u^{\mathrm{b}}}{H^{\mathrm{b}}} \right) \qquad \text{sheet.} \tag{2.30b}$$

Another modification to the melt rate is to use the chain rule in conjunction with the inverse Clausius-Clapeyron slope (eq. 2.8) for the change in temperature with pressure,

$$\frac{\partial T}{\partial s} = \beta \frac{\partial p}{\partial s}. \tag{2.31}$$

By substituting equation (2.31) into equation (2.30) and parameterizing the shear stress by equation (2.22b) in equation (2.30), I obtain a melt rate that is dependent on the discharge

through the water horizon, the water pressure, and the hydraulic gradient,

$$m = -\frac{S^{\mathrm{b}} u^{\mathrm{b}}}{L}\left(\rho^{\mathrm{w}} c_p^{\mathrm{w}} \beta \frac{\partial p^{\mathrm{b}}}{\partial s} + \frac{\partial \phi^{\mathrm{b}}}{\partial s}\right) \qquad \text{channel,} \tag{2.32a}$$

$$\tilde{m} = -\frac{H^{\mathrm{b}} u^{\mathrm{b}}}{L}\left(\rho^{\mathrm{w}} c_p^{\mathrm{w}} \beta \frac{\partial p^{\mathrm{b}}}{\partial s} + \frac{\partial \phi^{\mathrm{b}}}{\partial s}\right) \qquad \text{sheet.} \tag{2.32b}$$

This melt rate falls directly out of the assumptions proposed by Röthlisberger & Lang (1987). As a result, I refer to this steady state melt rate as "Röthlisberger heat transfer" in a similar spirit to Clarke's (2003) reference to Nye's (1976) heat transfer assumption.[5]

2.3 The melt rate

A heat flux formulated from Newton's law of cooling (*e.g.,* Bird *et al.*, 1960, p. 267) gives an estimate for the heat that can be conducted over a given length scale, which relates directly to the melt rate,

$$q_T = h\Delta T, \tag{2.33a}$$

$$h = -\frac{K_T^{\mathrm{w}}}{\ell_1},$$

$$m = \frac{q_T}{L}. \tag{2.33b}$$

Here, h is the heat transfer coefficient, ℓ_1 is a length scale, ΔT is the temperature change across that length scale, and K_T^{w} is the thermal conductivity of water. The heat flux q_T is the magnitude of the heat flux vector $\mathbf{q_T}$ normal to the phase change boundary, which is the melting perimeter in this case. The heat flux is in W m^{-2}. For water flowing in either of the cross sections, there is an inner region of the flow where the temperature is relatively homogenous because the water is well-mixed. Near the boundary, heat is conducted across a boundary layer. The length scale ℓ_1 is the height of the conductive boundary layer δ_H, between the well-mixed inner region and the ice wall.

The Nusselt number is the ratio of the total heat transfer to the conductive heat transfer. A Nusselt number greater than unity indicates that there is convective heat transfer. Multiplying the conductive heat flux in equation (2.33a) by the Nusselt number gives a heat flux that includes convection. After this multiplication, the length scale ℓ_1 ceases to be the conductive boundary layer and becomes the entire thermal boundary layer.

2.3.1 Semiempirical correlations

There are numerous empirical relationships for the heat transfer coefficient from the engineering literature. In general, these fall into a broad class of correlations for the Nusselt Number,

$$\mathsf{Nu} = C_1 \, \mathsf{Re}^{\varpi} \mathsf{Pr}^{\varsigma}, \tag{2.34}$$

where C_1 is a nondimensional constant, and ϖ and ς are indices (*e.g.,* Hutter, 1982; Schlichting, 1979). In this equation, the Reynolds number (Re) and Prandtl number (Pr) are given by the

[5] Nye's heat transfer assumption is that $dT^{\mathrm{b}}/dt = 0$ whereas Röthlisberger's is $\partial T^{\mathrm{b}}/\partial t = 0$ (eq. 2.9b).

usual definitions,

$$\mathsf{Re} = \begin{cases} \dfrac{4R_h|u^{\mathrm{b}}|\rho^{\mathrm{w}}}{\mu} & \text{channel,} \\ \dfrac{H^{\mathrm{b}}|u^{\mathrm{b}}|\rho^{\mathrm{w}}}{\mu} & \text{sheet,} \end{cases} \tag{2.35a}$$

$$\mathsf{Pr} = \frac{\nu}{\kappa_T^{\mathrm{w}}} = \frac{\mu c_p^{\mathrm{w}}}{K_T^{\mathrm{w}}}, \tag{2.35b}$$

where μ is the viscosity of water, ν is the dynamic viscosity of water, and κ_T^{w} is the thermal diffusivity of water. The Reynolds number is the ratio of the inertial forces to the viscous forces. The distinction between the thermal boundary layer and the inertial boundary layer is given by the Prandtl number. For water at the freezing point, the Prandtl number is approximately 13; or the thermal boundary layer is 13 times the inertial boundary layer.

McAdams (1954) presented several formulae for flow in ducts, pipes, and sheets. From these relationships, the Dittus-Boelter heat transfer relationship for flow in turbulent pipes stands out because of its use in outburst flood studies (Mathews, 1973; Nye, 1976; Spring & Hutter, 1981, 1982). The Nusselt number becomes (McAdams, 1954, p. 219),

$$\mathsf{Nu} = 0.023\,\mathsf{Re}^{4/5}\mathsf{Pr}^{2/5}. \tag{2.36}$$

Alternative formulations exist for the Nusselt number, but these are less popular. For example, Isenko *et al.* (2005)[6] used the relationship,

$$\mathsf{Nu} = 0.003\,\mathsf{Re}\,\mathsf{Pr}^{2/5}, \tag{2.37}$$

to interpret experimental work. For the remainder of this analysis, I employ the more popular Dittus-Boelter relationship (eq. 2.36). However, any relationship in the form of (2.34) could be suitable.

Because the height of the boundary layer is not obvious from the momentum equations (eq. 2.27), the Dittus-Boelter relationship substitutes the characteristic hydraulic cross-section length scale for the boundary layer thickness. For conduits, the characteristic length is $4R_h$, which is the diameter of the circular channel or the radius of the semicircular channel. The same heat transfer in a macroporous sheet depends on the thickness of the water layer instead of the diameter.

The mass melt rate per unit channel length can be formulated with appropriate substitutions of equations. The melt rate per unit area $\tilde{m}$ is simply the equivalent melt rate for the channel (eq. 2.38a) divided by the melting perimeter,

$$m = \frac{0.023\,\mathsf{Re}^{4/5}\mathsf{Pr}^{2/5}K_T^{\mathrm{w}}\Delta T_{\mathrm{mp}}P^{\mathrm{i}}}{4R_hL} \qquad \text{channel,} \tag{2.38a}$$

$$\tilde{m} = \frac{0.023\,\mathsf{Re}^{4/5}\mathsf{Pr}^{2/5}K_T^{\mathrm{w}}\Delta T_{\mathrm{mp}}}{H^{\mathrm{b}}L} \qquad \text{sheet.} \tag{2.38b}$$

[6]Isenko *et al.* (2005) gave their relationship in terms of a volumetric energy density per degree multiplied by the along path velocity. The Nusselt number presented here is equivalent to their formulation.

Ultimately, the Dittus-Boelter relationship approximates heat transfer across the turbulent boundary layer. This relationship is found via equations (2.33a) and (2.36),

$$\delta_T = \begin{cases} \dfrac{4R_h}{0.023\,\mathsf{Re}^{4/5}\mathsf{Pr}^{2/5}} & \text{channel,} \\ \dfrac{H^{\mathrm{b}}}{0.023\,\mathsf{Re}^{4/5}\mathsf{Pr}^{2/5}} & \text{sheet.} \end{cases} \tag{2.39}$$

A rough estimate of the thermal boundary layer for water flowing in sheets is 3×10^{-4} m—assuming $\mathsf{Re} = 2100$, the transition from laminar to turbulent flows in plane-parallel apertures, $\mathsf{Pr} = 13$, and $H^{\mathrm{b}} = 0.01$ m.[7] For a circular channel a radius equivalent to a sheet with unit width (2.28), the thermal boundary layer is approximately 1×10^{-3} m.[8] While there is no guarantee that these examples are compatible with the balance equations presented thus far, this value does suggest limitations on the height and radius of the subglacial cross sections.

Much of the heat transfer literature rests on a few correlations, one of these being the Dittus-Boelter relation. The Dittus-Boelter heat transfer relationship was originally designed for heat transfer within smooth-walled pipes. While the ice ceiling above the flow and the bed below are most likely not smooth, there are few published engineering Nusselt number correlations for rough boundaries. Other correlations exist for flat plates, concentric tubes, and tube bundles, but it is not clear that additional insight or accuracy can be gained by using these for rough-walled boundaries.

Bird *et al.* (1960, p. 401) pointed out that these correlations can be applied but are less reliable in the transition region, defined approximately as $\mathsf{Re} = 2100$–$10\,000$. Despite this limited range, the relationship proposed in equation (2.38b) appears to be the most relevant above the laminar flow regime. Within the laminar flow regime, Bird *et al.* (1960, p. 399) suggested

$$\mathsf{Nu} = 1.86 \left(\frac{\mathsf{Re}\,\mathsf{Pr}\,4R_h}{\Delta s} \right)^{\frac{1}{3}} \qquad \text{channel,} \tag{2.40a}$$

$$\mathsf{Nu} = 1.86 \left(\frac{\mathsf{Re}\,\mathsf{Pr} H^{\mathrm{b}}}{\Delta s} \right)^{\frac{1}{3}} \qquad \text{sheet,} \tag{2.40b}$$

where an equivalent scaling to equation (2.39), assuming $H^{\mathrm{b}}/\Delta s$ as 0.01, gives the Nusselt number as approximately 6 for the laminar case and 27 using equation (2.36). In general, water flowing in subglacial sheets is not expected to be flowing below a Reynolds number of about 2100 for the model proposed here; however, I leave this option available should the flow ever drop below this value.

[7] The corresponding velocity from equation 2.35a is approximately 0.4 m s^{-1}.
[8] The corresponding velocity from equation 2.35a is approximately 0.1 m s^{-1}.

2.4 Steady state accretion rate

Alley *et al.* (1998) arrived at an accretion rate via a heat balance,

$$-\frac{m}{\rho^{\mathrm{i}}} = \frac{Q^{\mathrm{b}} g \cos\alpha^{\mathrm{b}}}{\rho^{\mathrm{i}} L}\left\{\rho^{\mathrm{i}} C_2 \alpha^{\mathrm{r}} + \left(\rho^{\mathrm{w}} - \rho^{\mathrm{i}} C_2\right)\alpha^{\mathrm{b}}\right\}, \tag{2.41a}$$

$$C_2 \equiv 1 - \beta c_p^{\mathrm{w}} \rho^{\mathrm{w}}, \tag{2.41b}$$

where $\tan\alpha^{\mathrm{r}}$ is the glacier surface slope, and $\tan\alpha^{\mathrm{b}}$ is the energy slope of the water layer (Fig. 2.1).[9] Furthermore, Alley *et al.* made small angle approximations such that $\alpha^{\mathrm{r}} \sim \tan\alpha^{\mathrm{r}}$ and $\alpha^{\mathrm{b}} \sim \tan\alpha^{\mathrm{b}}$. The discharge Q^{b} in (2.41a) is constant such that both H^{b} and u^{b} are both held constant. The bed slope and surface slope of the glacier are also held constant along the flow path, similar to Figure 2.1. The final $\cos\alpha^{\mathrm{b}}$ term is a result of the flow path's inclination relative to the horizontal.

Equation (2.32b) is essentially the relationship that Alley *et al.* (1998) outlined previously (eq. 2.41) without some of their additional assumptions. They reasoned that the water pressure gradient, $\partial p^{\mathrm{w}}/\partial s$ is adequately approximated by the ice overburden pressure gradient $\partial p^{\mathrm{i}}/\partial s$. Furthermore, Alley *et al.* (1998) assumed a wedge-shaped ice configuration such as the area near the outlet in Figure 2.1. These assumptions lead to

$$\tilde{m} = -\frac{H^{\mathrm{b}} u^{\mathrm{b}}}{L}\left(\frac{\partial p^{\mathrm{b}}}{\partial s}\left(\rho^{\mathrm{w}} c_p^{\mathrm{w}} \beta + 1\right) + \rho^{\mathrm{w}} g \frac{\partial z^{\mathrm{b}}}{\partial s}\right), \tag{2.42a}$$

$$\frac{m}{W} = -\frac{g H^{\mathrm{b}} u^{\mathrm{b}}}{L}\left(\rho^{\mathrm{i}}\left(\sin\alpha^{\mathrm{r}} - \sin\alpha^{\mathrm{b}}\right)\left(\rho^{\mathrm{w}} c_p^{\mathrm{w}} \beta + 1\right) + \rho^{\mathrm{w}} \sin\alpha^{\mathrm{b}}\right). \tag{2.42b}$$

After grouping the terms like Alley *et al.*, an equation that parallels their work is quickly realized,

$$-\frac{m}{\rho^{\mathrm{i}}} = -\frac{g H^{\mathrm{b}} W u^{\mathrm{b}} \cos\alpha^{\mathrm{b}}}{\rho^{\mathrm{i}} L}\left(\tan\alpha^{\mathrm{b}}(\rho^{\mathrm{w}} - C_2\rho^{\mathrm{i}}) + C_2\rho^{\mathrm{i}}(-\tan\alpha^{\mathrm{r}})\right). \tag{2.43}$$

The assumption inherent in equation (2.43) is that $\cos\alpha^{\mathrm{b}} \sim \cos\alpha^{\mathrm{r}} \sim 1$. This assumption may not be valid depending on the slopes of the surface and bed but may be for relatively flat glaciers. Equations (2.41) and (2.43) illustrate that the Spring-Hutter formulation of the water flow equations can be reduced to a steady state representation.

By setting equation (2.43) equal to zero, the crossing from melting to freezing can be found in terms of the surface and bed slopes,

$$\mathcal{R} = -\frac{\sin\alpha^{\mathrm{b}}}{\sin\alpha^{\mathrm{r}}} = -\frac{\left(1 + \beta c_p^{\mathrm{w}} \rho^{\mathrm{w}}\right)\rho^{\mathrm{i}}}{\rho^{\mathrm{w}} - \left(1 + \beta c_p^{\mathrm{w}} \rho^{\mathrm{w}}\right)\rho^{\mathrm{i}}} \sim -\frac{\tan\alpha^{\mathrm{b}}}{\tan\alpha^{\mathrm{r}}}. \tag{2.44}$$

Röthlisberger & Lang (1987) gave this ratio as -2.02 for pure water and -1.30 for air-saturated water. Alley *et al.* (1998) gave the ratio as -1.7 for pure water and -1.2 for air-saturated water. Hooke (1991) also computed the ratio and found it to be -2.0 and -1.5 for pure and air saturated water, respectively. The large variability in these numbers results from small changes in the constants in equations (2.44) and (2.7). While the assumption that surface and bed topography are constant must be false, a simple ratio to predict glaciohydraulic supercooling from topography is extremely helpful.

[9] I have modified Alley *et al.*'s (1998) notation to match the present formulation. In addition, the surface and energy slopes are taken to be positive numbers.

2.5 Summary

Throughout this chapter, I have focused on glaciohydraulic supercooling in a subglacial water system. Glaciohydraulic supercooling occurs because water flows upwards in a hydraulic system without warming sufficiently to maintain water. The change of phase is governed by the Clausius-Clapeyron relation (eq. 2.8).

Three balance laws—mass (eqs. 2.15, 2.16, and 2.17), momentum (eqs. 2.26 and 2.27), and energy (eq. 2.29)—provide a mathematical representation through which water cross-section area or height, water pressure, water velocity, and water temperature can be simulated. Each of these equations has steady-state and time-dependent formulations. These formulations are subject to phenomenological conditions for heat transfer between the ice and water (eq. 2.32). In addition, the equations are subject to geometrical conditions on cross section (eqs. 2.2, 2.3, 2.4) and flow path (Fig. 2.1). For steady-state conditions there is a condition on the surface and base angles of the glacier, indicating the propensity towards supercooling (2.44).

Chapter 3

Sheet closure mechanisms

The aim of this chapter is to provide a concise relationship for ice intruding into a water sheet via the processes of regelation and viscous creep. A water passageway can close or open depending on the difference between the water pressure and the stress in the ice acting toward the water. For example, if the water pressure is below that of the ice overburden, ice will intrude into the cross-section, contracting it. If the water pressure is greater than the ice overburden pressure, it may be possible for the water to push the ice, dilating the cross-section.

For a conduit idealized as a tubular volume with a circular cross section, the relationship for closure is power-law creep (eq. 2.17). Creep closure of conduits in ice was observed and quantified by Glen (1952, 1954). To explain these observations, Nye (1953) constructed an extensive theory. Creep closure for conduits has proven effective in various forms and simulations (*e.g.,* Nye, 1976; Spring & Hutter, 1981). In these situations, the difference between the ice overburden stress and the water pressure determines whether the cross-section is shrinking or growing. Typically, ice overburden squeezes the conduit shut. However, if water is being forced through at a pressure higher than the ice overburden pressure, then the ice walls may be pushed outward, opening the conduit. Examples of water dilating the cross-section occur during jökulhlaups when a large supply of meltwater may force its way along the ice–bed interface (*e.g.,* Björnsson, 2002).

For sheets, the intrusion relationship is not well-defined. This ambiguity may be, in part, a result of sheets not appearing conspicuously at the front or surface of glaciers. As a water system nears the terminus of a glacier, water depressurizes in response to atmospheric pressure. Channelization is then favored at the ice–bed interface (*e.g.,* Fowler, 1987; Walder, 1982). Depressurization may explain the lack of observations of sheets emerging at the front of glaciers. Because observations of sheets are scarce, physical models help explain their development. Walder (1982) analyzed the dilation and contraction of water sheets and appraised their stability with respect to channelization. His exposition has not been extended but merits further attention because he was interested only in flat glacier beds.

Walder (1982) investigated the stability of a laterally continuous sheet of water at the glacier bed. He examined the two-dimensional, steady-state Navier-Stokes equations coupled to a simple diffusive thermodynamic model. In his model, ice sags into the water sheet, closing it. Walder approximated the rheology of ice by a linear viscosity rather than a nonlinear, power-law viscosity. He used linear perturbation analyses to determine what thickness of water would yield stable sheets under different conditions. Walder concluded that water sheets with flat beds were almost always unstable and would decay to channelized cross-sections. Sheets with rougher beds were stable to a thickness of about 4 mm. Unstable sheets would be discontinuous and give way to an arborescent drainage system.

3.1 Formulation

Glacier sliding and ice intruding into a sheet are analogous processes whereby ice moves past obstacles at the ice–bed interface. The difference between sliding and intrusion is the direction

of ice movement: horizontal for sliding, vertical for intrusion. This physical similarity opens the body of literature on sliding to closure of a water sheet. Glacier sliding is the result of two processes: viscous creep and regelation (*e.g.,* Weertman, 1964). Physically, creep is the movement of lattice dislocations in ice crystals in response to applied stresses. Regelation is the movement of ice past an obstacle by melting on a high pressure side and then refreezing on a low pressure side. Water flows in a thin film from the high pressure side of an obstacle to the low pressure side.

Weertman (1964) superposed the regelation velocity v_r and the creep velocity v_c to give the total ice velocity v, past an obstacle,

$$v = v_r + v_c. \tag{3.1}$$

Equation (3.1) is the statement for glacier sliding speed, and this equation also represents the closure speed of ice into the sheet $v = \partial H^{\mathrm{b}}/\partial t$ (see equation (2.16a)). Equation (3.1) holds for any individual obstacle that the ice is moving past. For ice at the melting point, regelation acts as a slip condition on the surface of the sediment. Creep acts on distances approximately the size of the obstacle that ice is moving past.

Both regelation and creep act jointly over different length scales to move the ice along the bed. Weertman (1964) observed that, for very large obstacles, creep will be the dominant mechanism. For very small obstacles, Weertman reasoned that the regelation velocity will be large. Near where the regelation velocity equals the creep velocity, both will be small. These obstacles will then control the speed at which the roof collapses. Nye (1969, 1970) suggested that a controlling obstacle size lies between 2 and 50 cm. In addition, Kamb (1970) concluded that a transition obstacle wavelength exists near 50 cm (Paterson, 1994, p. 142). A similar trade-off should occur for ice intrusion.

3.1.1 Regelation closure

Regelation is a thermodynamic process where ice in contact with another material melts because of the local change in the pressure melting point. Closure of the water system via regelation is not understood nearly as well as the effect of creep closure. For a cross section idealized as a sheet less than the transitional obstacle size, regelation should be the sole mechanism acting to close a water layer.

Nunn & Rowell (1967) performed laboratory experiments that have become classic examples of regelation. In these experiments a wire is loaded such that the pressure of the leading edge exceeds the local melting temperature of the ice (via eq. 2.8). Water produced flows in a thin film around the wire to the low pressure side, where it refreezes. Latent heat released from refreezing is conducted back through the wire, enhancing melt. Townsend & Vickery (1967) performed similar experiments and obtained similar results by pulling a metal ball though a block of ice. Weertman (1972) and Nye & Frank (1973) gained insight from these simple experiments to explain a glacier sliding past obstacles at the ice–bed interface and, subsequently, to determine sliding speed over a rock bed.

Nye (1967) constructed the theory for these experiments. He considered ice that is clean and separated from obstacles by a thin film of water and then solves for the force required for a steady regelation velocity. Nye noted if ice is below the melting point, regelation ceases unless there is an additional heat source. In this case, heat returning to the area of melting must first raise the temperature of the ice to the melting point before melting the ice. Because of this feature, I consider cases where the sensible heat is negligible. Other assumptions are inherent

in regelation: ice is clean, there is a thin film of water separating the ice from the sediment grains, and transient effects are negligible. Also, the mechanical properties of ice, such as fabric orientation, should not change when ice melts and then reforms.

Ice flow past bedrock obstacles implies that ice flow is roughly parallel to the bed for sliding. For the closure of the ice–bed interface in the presence of a water sheet, the direction of ice motion must be into the sheet, or nearly vertical. Figure 3.1 depicts ice resting on a sediment grain at the ice–bed interface. On the leading edge of the grains, ice melts. The water generated then flows around the sediment grain toward the water sheet. "Regelation" in this sense is somewhat of a misnomer because water is not necessarily refreezing on the low pressure side. However, the theoretical basis for regelation is applicable provided that heat is conducted through the sediment grain to melt the overlying ice.

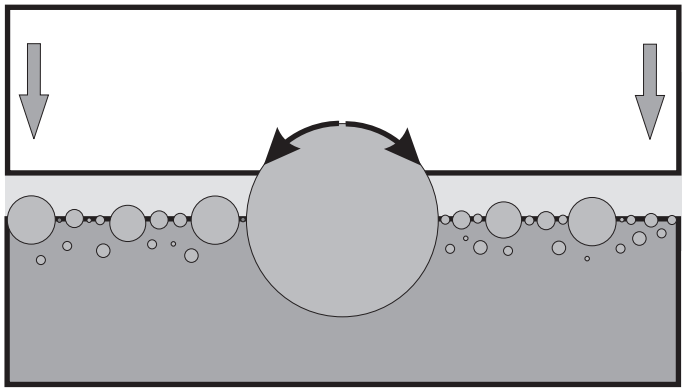

Figure 3.1: A simple picture of regelation closure. The water layer is the lightest gray. As the ice descends onto the grains, stress from the overlying ice is concentrated, and the ice melts. Grey arrows show the sense of ice motion. Black arrows indicate motion of water generated from ice melt.

Nye (1967) gave the formulation for regelation in terms of a single cylinder and altered the shape factor to account for spheres. He then gave an approximate formulation for any shape,

$$F = \frac{V_e \rho^{\mathrm{i}} L v_r}{\beta K_{e:T}}, \tag{3.2}$$

where V_e is the effective volume of the shape, $K_{e:T}$ is an effective thermal conductivity, v_r is the speed at which the ice is regelating past the object, and β is the linearized pressure-melting coefficient (eq. 2.8). Rewriting (3.2) in terms of the normal stress available for regelation gives

$$\sigma_r = -\frac{\rho^{\mathrm{i}} L}{\beta K_{e:T}} \frac{V_e}{A_e} v_r, \tag{3.3}$$

where A_e is an effective area. The effective area is an area of ice–object contact. The negative sign in equation (3.3) indicates that the direction of closure is opposite to the positive z-direction, or downwards, when the ice overburden stress is greater than the water pressure.

The definition of the effective area A_e in equation (3.3) involves both a sediment grain and an applied stress. Philip (1980) noted that the stress is the mean normal stress, and he defined the force as acting along the direction of ice flow. However, this is at odds with Nye (1967) who used

the stress normal to the surface of the obstacle. In this case, Nye's formulation is preferable. A_e is then the surface area opposing the motion of the ice. If there is a known relationship between the surface and cross-sectional areas of sediments, then the cross-sectional area could be substituted. The effective area is not the area of all grains on the bed, but the effective cross sectional area of those sediment grains emerged into the ice and partially submerged in the water. Obstacles that are completely submerged by water do not have an effect. Similarly, V_e is the volume of an obstacle encased in ice at the ice–bed interface that the ice is regelating past.

Philip (1980) investigated the effective thermal conductivity. He constructed an analytic model of ice regelating past arrays of equally spaced obstacles, cylinders or spheres, having an adjustable thermal conductivity. Philip solved for the effective thermal conductivity based on a given array geometry and an obstacle shape. If the thermal conductivity of an array is the same as that of ice, the effective thermal conductivity reverts to that of ice. As a result, obstacle spacing is irrelevant without varying the conductivities. For obstacles with thermal conductivities greater than that of ice, heat is preferentially moved through the cylinders. Conversely, if the thermal conductivity of a cylinder is less than that of ice, a greater relative heat flux occurs through the ice. It is not clear that Philip's (1980) method of applying different conductivities provides adequate compatibility because sediment grains at the ice–bed interface are usually irregularly spaced. However, his study does give an impression of what may happen when the thermal conductivity is varied. In addition, Rempel *et al.* (2004) noted that varying the conductivity of the grains makes the problem unnecessarily difficult. Iverson & Semmens (1995) avoided the issue completely in their experimental study by setting the conductivities of ice and sediment equal. Because the thermal conductivity appears to have a small impact on the problem, I set the thermal conductivity equal to that of ice as has been done by Iverson & Semmens (1995).

3.1.2 Creep closure

Creep is the process whereby ice deforms under an applied stress. For sediment grains with mean dimension larger than the transitional obstacle size, the primary mechanism of ice intrusion into the macroporous water layer will be power-law creep. The most common form of the flow law for ice was given by Glen (1954) where a strain rate is proportional to a stress raised to a power. If ice rests on grains that concentrate stress then ice will preferentially creep around these grains. Figure 3.2 shows the conceptual framework for creep closure of a sheet with ice sagging between two large sediment grains. If the ice were lower in the figure, overburden stress would be dissipated because the ice would rest on more grains. This dissipation may reduce the rate of creep closure.

Creep is driven by the stress deviator at the ice–bed interface. Equivalent shear τ can be written in terms of the stress deviation from a hydrostatic state,

$$2\tau^2 = \sigma_c^2 + 2\tau_{xz}^2, \tag{3.4}$$

where σ_c denotes a deviatoric stress available for creep. Weertman (1964) noted that there are two deviators. One deviator results from the compression on the obstacle. The other is a tension from the ice that passes the obstacle. This is clearly seen as (3.5) retains a 1/2. In addition,

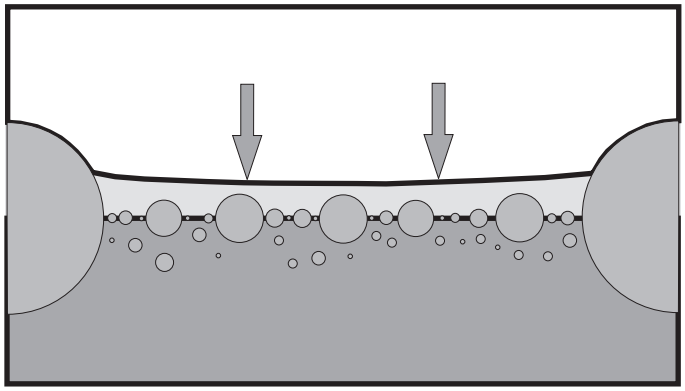

Figure 3.2: A simple picture of regelation closure. Ice preferentially sags into the water layer with a larger spacing between particles. Same color scheme as Figure 3.1

because shear from down glacier ice movement is neglected, τ_{xz} in (3.4) can be neglected[10],

$$\begin{aligned} 2\tau^2 &= (\sigma_c)^2 , \\ \tau &= \sqrt{\frac{1}{2}(\sigma_c)^2}. \end{aligned} \tag{3.5}$$

Because the water sheet experiences only vertical motion, the bed must be in compression or tension. As a result, the 1/2 in (3.5) is not critical. Weertman (1964) also argued that the 1/2 is not important for glacier sliding where obstacles at the ice–bed interface are in both tension and compression simultaneously, and

$$\tau = \sigma_c. \tag{3.6}$$

The strain rate in the ice can be approximated by the flow law (*e.g.,* Paterson, 1994). Substituting the creep closure stress directly into the flow law yields the strain rate in terms of the creep closure stress,

$$\dot{\epsilon}_z = \mathcal{A} \operatorname{sgn}(\sigma_c) |\sigma_c|^n, \tag{3.7}$$

where ϵ_z is the vertical strain into the sheet and $\mathcal{A}$ is a flow law coefficient. Multiplying (3.7) by a length scale produces a velocity,

$$v_c = \mathcal{A} \operatorname{sgn}(-\sigma_c) |\sigma_c|^n l_e, \tag{3.8}$$

where l_e is the creep length scale. The effective length scale provides an approximation to the spatial integral of the strain rate without solving the integral directly. Solving the integral directly would necessitate solving for the stress distribution in the ice. An attempt to integrate the stress would not necessarily give a better approximation because an integration would be dependent on the boundary conditions, which are not straightforward for a bed of irregularly shaped objects of variable horizontal spacing. By using a simple length scale, equation (3.8)

[10]By neglecting shear, I preclude the circumstances that would allow a sedimentary bed to develop cavities. These cavities might take an elongate form (*e.g.,* Weertman, 1986) that could then coalesce into laterally continuous cavities (*e.g.,* Kamb, 1987; Walder, 1986). This coalescence would lead to configurations similar to those discussed by Alley *et al.* (1998).

yields a tractable approximation of creep closure. The creep closure stress can be found by rearranging equation (3.8)

$$\sigma_c = -\operatorname{sgn}(v_c)\left(\frac{|v_c|}{\mathcal{A}l_e}\right)^{1/n}. \tag{3.9}$$

The natural scale for the effective length in equation (3.8) is the distance between the sediments at the bed because an ice roof will preferentially sag between supporting grains. Creep around the individual grains would be secondary to the sagging. This length scale will vary depending on the thickness of the water sheet.

3.2 Bed partitioning

The overlying ice rests on an unlithified sedimentary bed and water sheet. Within this water sheet, many smaller sediment grains are wholly submerged. Larger grains may penetrate the water to partially support the ice and stabilize the water layer. A combination of water pressure and sediment stresses jointly support the weight of the overlying ice. As a result, the total cross-sectional areas of water A^{w} and sediment A^{s} sum to the total area of the ice,

$$A^{\mathrm{i}} = A^{\mathrm{w}} + A^{\mathrm{s}}. \tag{3.10}$$

In this case, A^{i} is a cross-sectional area of ice normal to the direction of closure. The ice seals the water sheet and partially rests on sediment grains. This equation is consistent with the ice–water configuration of a sheet from Chapter 2.

Many different grain sizes may be present on the bed. Some grain sizes will be fully submerged in water and not touch the ice ceiling. The remaining grain sizes will support some of the weight of the glacier. The total contact area of sediments touching the ice A^{s} is equal to the integral

$$A^{\mathrm{s}} = \int_{A^{\mathrm{i}}}\int_{a^{\mathrm{s}}} f_a^{\mathrm{s}} a^{\mathrm{s}}\, da^{\mathrm{s}}\, dA^{\mathrm{i}} \tag{3.11}$$

where f_a^{s} is the number of grains per unit size (in area) of a given texture per unit area of the bed. The quantity f_a^{s} is a number density. Each of a variety of grain textures has an individual fractional area a^{s}. One of the geometric necessities of equation (3.11) is that A^{s} is defined at the average elevation of A^{i}, which is z^{b}. The cross-sectional area normal to intrusion for one grain size is then dependent on the mean size of the grains, the level of submergence, and the number of that grain size on the bed. Implicit assumptions include the sediment grains being exposed to the same level and having a cross-sectional area and volume that can be approximated by a known function of the mean grain size.

3.2.1 Stress partitioning

If the ice is resting on more than one grain size across the water horizon then the ice overburden stress can be partitioned among the different grain sizes and the water pressure. A reasonable analog for stress partitioning emerges from work on sliding and cavitation at the ice–bed interface (*e.g.,* Fowler, 1987; Lliboutry, 1979; Schoof, 2005). Fowler (1987) approximated a series of bumps at a glacier bed as a Fourier series. In his formulation, the largest wavelength bumps have the largest amplitude, and smaller wavelength bumps are superimposed on the larger bumps. When the glacier's sliding speed reaches a threshold, water cavities develop behind the smallest bumps. As the sliding speed of the glacier increases, larger cavities form behind the larger bumps. These

larger cavities drown a fraction of the smaller bumps and cavities. In order to cope with the areal changes in normal stress and water pressure at the bed, Fowler used a stress renormalization technique introduced by Lliboutry (1979).

A similar formulation can be used for ice intruding into a sheet of water. The downward force of the overlying ice F^{i} is partitioned among all grain sizes available at the bed and the water sheet,

$$\begin{aligned} F^{\mathrm{i}} =& F^{\mathrm{w}} + F^{\mathrm{s}}, \\ A^{\mathrm{i}}\sigma^{\mathrm{i}} =& A^{\mathrm{w}}p^{\mathrm{w}} + A^{\mathrm{s}}_1\sigma^{\mathrm{s}}_1 + \ldots + A^{\mathrm{s}}_N\sigma^{\mathrm{s}}_N, \\ =& A^{\mathrm{w}}p^{\mathrm{w}} + \sum_{i=1}^{N} A^{\mathrm{s}}_i\sigma^{\mathrm{s}}_i, \end{aligned} \tag{3.12}$$

where F^{s} and F^{w} are normal forces on the sediment and water, $\sigma^{\mathrm{i}} = \rho^{\mathrm{i}}gZ^{\mathrm{i}}$ is the ice overburden stress, A^{s}_i is the total area opposing flow for the ith grain size, and σ^{s}_i is the stress on the ith grain size. Shear from ice movement is ignored as are any other stresses.

Partitioning equation (3.12) into intermediate stresses σ_i yields a renormalization,

$$A^{\mathrm{i}}\sigma^{\mathrm{i}} = A^{\mathrm{s}}_1\sigma^{\mathrm{s}}_1 + \left(A^{\mathrm{i}} - A^{\mathrm{s}}_1\right)\sigma_1 \tag{3.13a}$$

$$\left(A^{\mathrm{i}} - A^{\mathrm{s}}_1\right)\sigma_1 = A^{\mathrm{s}}_2\sigma^{\mathrm{s}}_2 + \left(A^{\mathrm{i}} - A^{\mathrm{s}}_1 - A^{\mathrm{s}}_2\right)\sigma_2 \tag{3.13b}$$

$$\ldots$$

$$\left(A^{\mathrm{i}} - \ldots - A^{\mathrm{s}}_{N-1}\right)\sigma_{N-1} = A^{\mathrm{s}}_N\sigma^{\mathrm{s}}_N + A^{\mathrm{w}}p^{\mathrm{w}}. \tag{3.13c}$$

In these equations, larger i values indicate smaller grain sizes. Equations (3.13) are predicated on the largest grain sizes supporting a significant portion of the ice overburden stress. The remaining stress is distributed among the smaller grains. The summation of the N equations (3.13) yields equation (3.12). Renormalization of the stresses is the crucial step that differentiates this work from that of previous workers who were interested in both regelation and creep (*e.g.,* Weertman, 1964).

Solving (3.13) for σ^{s}_i yields a series of equations with a subtle relationship,

$$\sigma^{\mathrm{s}}_i = \frac{A_{i-1}}{A^{\mathrm{s}}_i}\left(\sigma_{i-1} - \sigma_i\right) + \frac{A^{\mathrm{s}}_i}{A^{\mathrm{s}}_i}\sigma_i, \tag{3.14a}$$

$$= \frac{A_{i-1}}{A^{\mathrm{s}}_i}\sigma_{e:i} + \sigma_i, \tag{3.14b}$$

where $\sigma_{e:i}$ is the relative effective stress for the ith grain size, and $i = 1 \ldots N$. The area A_0 is equal to A^{i} for the largest grain sizes, and σ_N is equal to p^{w} for the smallest grain sizes.

One grain size: a simple case

If there is only one grain size on the bed, then there is a simple stress division among the water and sediment. The stresses for regelation and creep are the deviatoric stress on the sediment grains and the effective stress, respectively. This stress must be obtained via a force balance on the bed, whereby the mass of the overlying ice must be supported by either the water or the grains at the base of the glacier:

$$\begin{aligned} \sigma^{\mathrm{i}}A^{\mathrm{i}} =& \sigma^{\mathrm{s}}A^{\mathrm{s}} + p^{\mathrm{w}}A^{\mathrm{w}}, \\ \sigma^{\mathrm{s}} =& \frac{A^{\mathrm{i}}}{A^{\mathrm{s}}}\sigma_e + p^{\mathrm{w}}\ . \end{aligned} \tag{3.15}$$

In this case, the three stress components available for ice closure are the vertical stress in the ice σ^{i}, the water pressure p^{w}, and the stress exerted by sediment grains on the ice σ^{s}.

3.3 Stress–velocity relation

There is one equation each for the total closure velocity (eq. 3.1), regelation (eq. 3.3), creep (eq. 3.9), and a constitutive relationship for stress at the bed (eq. 3.12). To solve these equations, three more relationships are necessary,

$$\sigma_{r:i} = \sigma_i^{\mathrm{s}} - \sigma_i = \frac{A_{i-1}}{A_i^{\mathrm{s}}}\sigma_{e:i}, \tag{3.16a}$$

$$\sigma_{c:i} = \sigma_{e:i}, \tag{3.16b}$$

$$v = v_1 = \ldots = v_N. \tag{3.16c}$$

Here, stress deviators driving regelation and creep closure are given by equations (3.16a) and (3.16b), respectively. These stresses, σ_r and σ_c, now have an unambiguous relationship to the stress renormalization. Equation (3.16a) states that stress driving regelation for a particular grain size is the stress on a grain less the intermediate stress. This stress difference is essentially the stress deviator of the renormalized system. Use of a stress on an individual size for regelation is equivalent to previous work (Nye, 1967; Weertman, 1964). Equation (3.16b) states that the total stress available for creep is simply the renormalized effective stress. The renormalized effective stress becomes the deviation from the local hydrostatic stress state away from the supporting grains.

Equation (3.16c) states that there is only one closure velocity and that the velocity around individual grains at the bed must be equal to each other. This final assumption is compatible with the theory of Weertman (1964) who assumed that the ice will flow past obstacles at only one sliding speed. One closure velocity for all individual grain sizes at the bed means not all stresses are equal on the sediment grains. The stress distribution in the ice reorganizes to allow only one closure velocity.

The total velocity is the addition of the creep closure velocity and the regelation closure velocity in the same vein as Weertman (1964) from equation (3.1). After substituting equations (3.3), (3.8), and (3.16), the total closure velocity becomes

$$v = -\frac{\beta K_{e:T}}{\rho^{\mathrm{i}} L}\left(\frac{A_e}{V_e}\right)_i \sigma_{r:i} + \mathcal{A} l_{e:i}\,\mathrm{sgn}\left(-\sigma_{c:i}\right)|\sigma_{c:i}|^n, \tag{3.17a}$$

$$= -\frac{\beta K_{e:T}}{\rho^{\mathrm{i}} L}\left(\frac{A_e}{V_e}\right)_i \left(\frac{A_{i-1}}{A_i^{\mathrm{s}}}\sigma_{e:i}\right) + \mathcal{A} l_{e:i}\,\mathrm{sgn}\left(-\sigma_{e:i}\right)|\sigma_{e:i}|^n. \tag{3.17b}$$

Because there are N grain sizes, there are N versions of equation (3.17b). Each of these versions is exactly equal to the same closure velocity as highlighted above. The sum of the stresses in equation (3.12) is the final condition necessary to solve for the $N+1$ equations. The intermediate stresses and grain stresses can be found from equations (3.14). Details of the solution of these equations using Newton's method can be found in Appendix C.

Negative effective stresses

Subglacial water pressures may exceed ice overburden stresses (*e.g.,* Murray & Clarke, 1995; Hooke & Pohjola, 1994) causing effective stresses to be negative. In particular, Hooke & Pohjola

noted that water pressure will be greater than ice overburden stress along an adverse slope. If water pressure is greater than ice overburden, then a subglacial water sheet will dilate. In this case, the stress partitioning is not valid, and the regelation terms in equations (3.17) do not play a role. Equations (3.17) then revert to a simple creep velocity governed by the smallest effective stress and effective creep scale (eq. 3.8).

This assessment of processes that occur when effective stresses are negative is necessarily simple. In nature, glacier ice may lift off the bed via a number of processes. For example, ice that has intruded around sediments may lift the sediments off the bed. Such mechanisms are not included here but can occur and merit further investigation.

3.4 Effective scales

Numerous sizes and shapes of sediment grains may lie on the bed. These grains may be buried to different depths and offer different sizes and shapes at different heights within the water layer for the ice to rest upon. Packing of a plane with particles can take many different patterns. For example, for one grain size, the closest and most common packing is hexagonal. Riverbeds do have structure in response to variations in shear stress; however, the exact order of grains at the bed is difficult to predict. Interactions of the water with the overlying ice and the underlying sediment will determine the effective scales (A_e, V_e, or l_e). The subglacial hydrology, in concert with the overlying glacier, impose structure on the subglacial bed; but it is difficult, if not impossible to observe this structure. As a result, an approximation to the variation of material at the bed is necessary, this includes the population of any individual grain size, N_i^{s}. This approximation allows a functional form for the effective length, volume, and area scales in equation (3.17).

The definition of these effective scales is somewhat delicate in that they may have a large effect on the closure of the bed. While the scale effects appear to be linear in v, they may produce nonlinear effects because of the grain distribution at the bed. In order to allay concerns regarding the effective scales, I first define the scales in terms of the grain distribution at the bed, and then provide examples illustrating how the effective scales may affect equation (3.17).

3.4.1 Regelation area and volume scales

The volume to area ratio in equation (3.17) for regelation closure is dependent on the individual grains lying on the bed. The exact relationship for either the effective volume to area ratio or the population can never be known exactly, but a reasonable approximation may be made for these parameters. As ice moves past sediment grains at the bed, the effective volume and area for each grain size change as H^{b} changes. In general, the population will not change; but the population exposed to the ice may change as H^{b} evolves. As ice descends, it will be in contact with more grain sizes depending on the sediment floor–ice ceiling distance. As ice rises off the bed, ice will make contact with fewer grains. Not only is it necessary to find a relationship that represents the material at the bed, but this representation must also be adjustable as H^{b} changes.

The simplest geometrical parameterization is to assume that each sediment grain is a sphere. Strictly speaking, sediment grains are rarely spherical, but the rates of closure should only differ by a shape factor. The effective volume is the spherical cap above H^{b}, and the effective area is the circular cross section at H^{b}. Where the base of the grain sits on the same datum as the water sheet z^{s}, the spherical cap and the cross-sectional disk have two values: (a) one when

$H^{\mathrm{b}} > r_i$ and (b) one when $H^{\mathrm{b}} < r_i$, where r_i is the individual grain radius. For the case of sediment grains lying on z^{s}, the effective volume is then given by

$$V_{e:i} = \frac{\pi}{3}\left\{2r_i - H^{\mathrm{b}}\right\}\left\{2r_i^2 + r_i H^{\mathrm{b}} - \left(H^{\mathrm{b}}\right)^2\right\}. \tag{3.18}$$

The effective cross section is the area of the disk,

$$A_{e:i} = \begin{cases} \pi\left\{2H^{\mathrm{b}} r_i - \left(H^{\mathrm{b}}\right)^2\right\} & \text{for} \quad H^{\mathrm{b}} > r_i \\ \pi r_i^2 & \text{for} \quad H^{\mathrm{b}} \leq r_i. \end{cases} \tag{3.19}$$

If all the grains are buried to their equator, then similar relationships exist for the effective volume and area. This case will be referred to as the half grain case. This case is illustrated in Figures 3.1 and 3.2. Equations similar to (3.18) and (3.19) are

$$V_{e:i} = \frac{\pi}{3}\left\{2r_i^3 - 3H^{\mathrm{b}} r_i^2 + \left(H^{\mathrm{b}}\right)^3\right\}, \tag{3.20a}$$

$$A_{e:i} = \pi\left\{r_i^2 - \left(H^{\mathrm{b}}\right)^2\right\}. \tag{3.20b}$$

Details of these derivations appear in Appendix B. As ice descends on the grain, the upper equation in the set of (3.19) describes the area as grain contact increases. Once the ice has passed the equator of the grain, the cross sectional area opposing ice flow does not lessen but remains the same.

From equation (3.19), the total area normal to ice motion for the ith grain size is accessible,

$$A_i^{\mathrm{s}} = N_{a:i}^{\mathrm{s}} A_{e:i}. \tag{3.21}$$

This equation simply states that A_i^{s} is the product of the population of sediment grains at the bed times their individual effective area.

3.4.2 Creep length scale

For an area at the bed, an effective length scale should capture an average spacing of the change in stress over that area. As shown in Figure 3.2, the length scale is the space over which an ice roof sags into a water sheet. Because the area of a water sheet varies with the height and number of sediments exposed at the bed, a creep length scale will be dependent on the spacing between the sediment grains. Naturally, this length scale is only an approximation to what the grain spacing is at the ice–bed interface. Furthermore, a parameterization that captures how the average length scale would vary at the ice–bed interface is given by

$$l_{e:i} = \left(\frac{A^{\mathrm{i}} - A_i^{\mathrm{s}}}{N_{a:i}^{\mathrm{s}}}\right)^{1/2}. \tag{3.22}$$

The length scale in equation (3.22) varies as water is exposed to the overlying ice. For a square with an area equivalent to that of water exposed to the ice, the length scale of interest would be the square root of the area of the water. The length scale should be inversely proportional to the number of grains touching the ice. If each of the grains is a point, and the points are equally spaced within the water, then each point can occupy a square. All squares would have an equal area. Alternatively, a circle with equivalent area could be used with a factor of 2π included, but it is not clear that the choice of geometry is fundamental. A different areal geometry will only change the length scale by a constant. A key assumption is that the grain spacing is regular at the bed. Most sedimentary beds are likely not regular.

3.4.3 Sediment grain size distribution

Sediment grain distributions on the bed have been discussed by numerous authors. The discussion about particular grain distributions is left to Chapter 4. One aspect that is important is that most subglacial sediments tend to be deformation tills. Hooke & Iverson (1995) found that deformation tills follow a fractal distribution in number,

$$N^{\mathrm{s}}_{a:i} = N^{\mathrm{s}}_0 \left(\frac{r_i}{r_0} \right)^{-m}, \tag{3.23}$$

where m is the fractal index, and the subscript 0 denotes a reference value. Moreover, Hooke & Iverson showed that the fractal index is approximately three, implying that each grain size occupies an equivalent amount of volume in the till. If there is a mixture of grain sizes in the till occupying a unit volume with a unit area on a face of that volume, then the face will have an equal distribution of those grain sizes in area (*e.g.,* Kellerhals & Bray, 1971). For the sediments exposed at a glacier bed, the fractal distribution would have an index of about 2. An equivalent relationship is presented in Chapter 4 (eq. 4.18) where m is approximately 3. The difference in the index value is a result of the use of an areal distribution ($m \simeq 2$) versus a volumetric distribution ($m \simeq 3$). This fractal distribution will be the baseline case for both the regelation and creep closure.

3.5 Example closure rates

In order to obtain a qualitative understanding of how these equations interact to produce closure, examples are necessary. There will be cases when either regelation or creep dominates closure of the water sheet, and as result, it is important to know where these lie and what effect they may have on a water layer below a glacier.

Rather than construct these examples around water layer thicknesses, I construct the examples based on possible grain size distributions at the ice-bed interface. This method of example construction provides insight into closure mechanisms at both the maximum possible sheet thickness and a minimum sheet thickness. However, I do not suggest that an extremely thick water layer is possible under a given set of hydraulic constraints. I assume that a thick water layer is permissible if the grain size distribution contains large clasts in order to explore process phenomena.

3.5.1 Closure rates for beds with uniform grain size

Large grains

The simplest illustrative cases have only one grain size. For very large clast sizes, the expectation is that creep dominates with regelation being of secondary importance. There should also be faster closure velocities for larger effective stresses because of the dependence of Glen's flow law on n (eq. 3.17). Finally, for large clasts, the closure rate should linearly increase for a linear increase in l_e.

Figures 3.3[11] and 3.4 show example closure velocities for the parameters in Table 3.1. These examples are consistent with boulders with a radius of 0.2 m. In this example, exactly half

[11] All figures that report closure velocities use positive values. These are absolute values of the closure velocities. All velocities are downward toward the bed. No closure velocities for negative effective pressures are plotted.

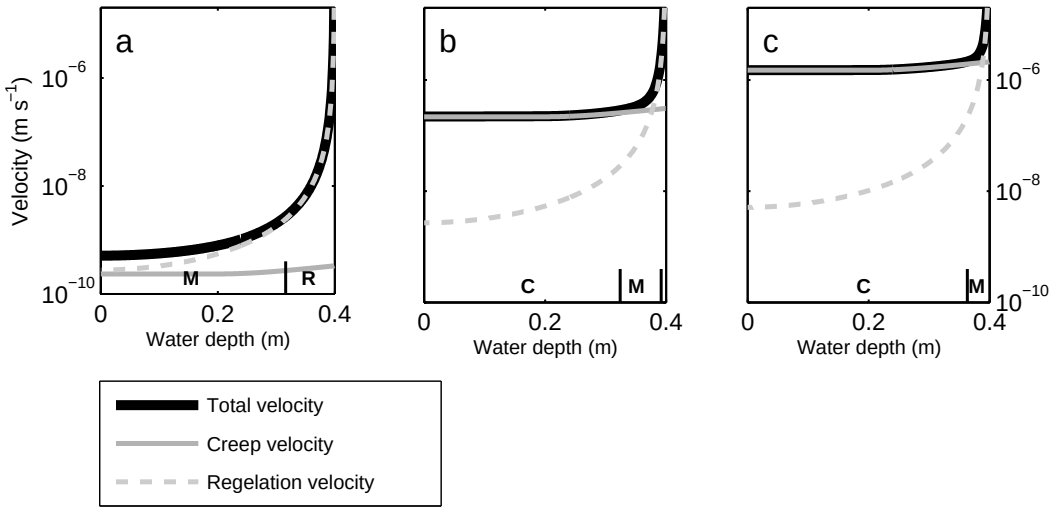

Figure 3.3: Example closure velocities for a grain size of $r_i = 0.2$ m. Parameters are given in Table 3.1. (a) $\sigma_e/p^{\mathrm{i}} = 0.05$ (b) $\sigma_e/p^{\mathrm{i}} = 0.5$ (c) $\sigma_e/p^{\mathrm{i}} = 0.95$. The letters (C, M, R) along the base of the plots correspond to the areas in Figure 3.4.

Table 3.1: Closure parameters.

Parameter	Value	Units	Notes
$\mathcal{A}$	6.8×10^{-24}	$\mathrm{s}^{-1}\ \mathrm{Pa}^{-n}$	(Paterson, 1994, p. 97)
c_p^{w}	4217.6	$\mathrm{J\ kg}^{-1}\ \mathrm{K}^{-1}$	
g	9.81	$\mathrm{m\ s}^{-2}$	
$K_{e:T}$	3.3	$\mathrm{W\ m}^{-1}\ \mathrm{K}^{-1}$	
L	3.336×10^5	$\mathrm{J\ kg}^{-1}$	
n	3.0		(Nye, 1953; Paterson, 1994)
p^{i}	8.99×10^5	Pa	Corresponds to 100 m of ice overburden
β	7.440×10^{-8}	$\mathrm{K\ Pa}^{-1}$	From equations (2.7) and (2.8)
ρ^{i}	916.7	$\mathrm{kg\ m}^{-3}$	
ρ^{w}	1000.0	$\mathrm{kg\ m}^{-3}$	

of the bed is covered by boulders. The boulders rest on a flat surface with the whole grain exposed according to equations (3.18) and (3.19). At the base of Figure 3.3 and in Figure 3.4, R (regelation regime) denotes that $v_r > 0.9v$, C (creep regime) denotes $v_c > 0.9v$, and M (mixed regime) denote that neither process is controlling. These and subsequent figures are constructed around the grain size(s) rather than realistic sheet water depths. Water depth of the sheet would not be as high as 0.4 meters but are probably less than one tenth that height (*e.g.,* Lawson *et al.*, 1998).

There are several striking features in Figures 3.3 and 3.4. The first feature is that regelation is an important process for several parameter choices. In the case of Figure 3.3a, the effective stress driving closure is relatively low. As a result, the creep velocity is quite small, and the regelation velocity is a greater part of the total closure velocity. However, throughout most of height of the water layer (as indicated by M), the creep velocity is greater than 10% of the total closure rate. In Figures 3.3b and 3.3c, the relative effective pressure is much higher. The result

is that creep is important for most of the grain height. Near 0.4 m for both Figures 3.3b and 3.3c, there is a sharp upturn in the total velocity. This upturn is a result of the ratio A_e/V_e being large as the ice initially settles on a grain.

Each creep velocity in Figure 3.3 curves slightly from 0.2 to 0.4 m. This curvature results from the cross-sectional area in equation (3.23) evolving until the equator is reached. Once ice intrudes below the grain equator of the grain, l_e is constant. As a result, from 0 to 0.2 m, the creep velocities are constant.

Figure 3.4 shows the overall pattern for the total closure velocity. In the region where creep dominates, the velocities rise to the left as a result of the rate dependence on n. The bend in the black contours at 0.2 m in the creep region is a result of the change in l_e, as indicated above. The transition to a mixed regime and a regelation regime near the top of the figure results from the combination of both the ratio A_e/V_e and the ratio A_i/A_i^{s} being large. From right to left, the transition from a creep regime to a mixed regime to a regelation regime results from a drop in the effective pressure that drives closure.

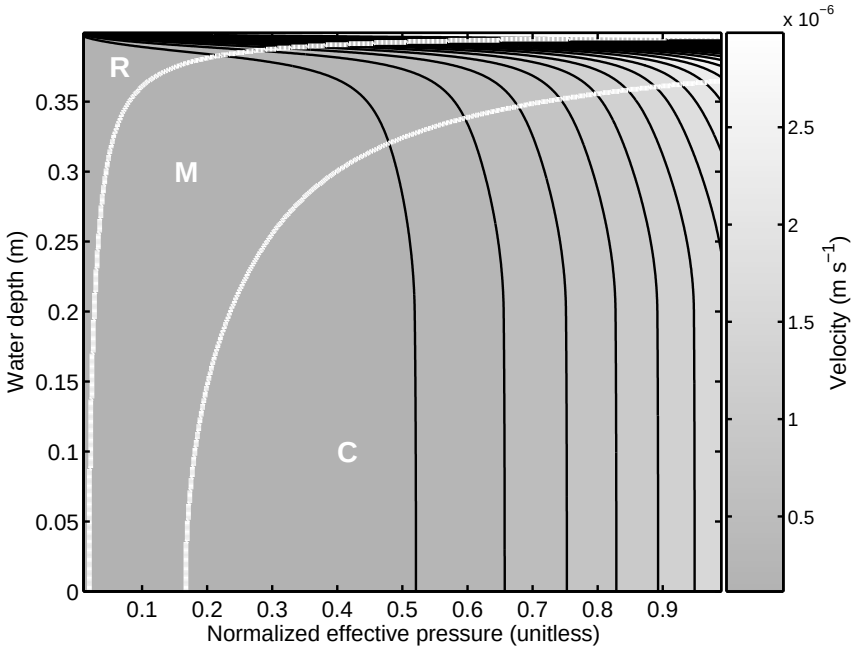

Figure 3.4: Total closure velocities for a grain size of $r_i = 0.2$ m with variable effective pressure. Parameters are given in Table 3.1. The fraction of the bed area covered with water is 0.5. These velocities are total closure velocities (eq. 3.1). Black contours are spaced at intervals of 0.25×10^{-6} m s^{-1}. Numbers and thick white lines denote different closure regimes. Area R indicates regelation dominated closure ($v_r > 0.9v$). Area C delimits creep dominated closure ($v_c > 0.9v$). In area M, both creep and regelation are important for closure.

Figure 3.5 shows the variability of the closure velocity for a change in the area of water. The practical course of creating a bed parameterization is to define the cross sectional area for a grain and then determine a number of grains based on a predetermined fractional area of water ($A^{\mathrm{w}}/A^{\mathrm{i}}$). The smallest fractional area of water is 0.09 because this is closest hexagonal packing for circles on a plane. A creep regime dominates most of this figure. The transition from a creep to a mixed to a regelation regime toward the top of the figure is a result of the change in the

ratio A_e/V_e. The gradual rise in the closure velocities toward the right hand side of the figure is the result of fewer grains and a larger grain spacing. The close contours in the upper right corner result from the product of A_e/V_e and A_i/A_i^{s} driving regelation. Figure 3.3b is a vertical slice of Figure 3.5 at a fractional area of 0.5.

Because l_e is dependent on the number of grains (eq. 3.22), the fractional area water is not a direct proxy for the creep length scale. However, l_e does increase as the fractional area water increases. Figure 3.6a shows the increase in closure rate as a function of l_e. This figure is a horizontal slice of Figure 3.5 at 0.15 m with the fractional area water converted to l_e. Figure 3.6a illustrates the creep velocity being linear in l_e despite the total closure velocity not being linear.

According to equations (3.17), the creep velocity should vary linearly with l_e and the regelation velocity should vary linearly with A_{i-1}/A_i^{s}. Figure 3.6a illustrates the linear dependence of the creep velocity on l_e. Figure 3.6b shows how that the regelation velocity is linear in A_{i-1}/A_i^{s}. In this case, $A_{i-1}/A_i^{\mathrm{s}} = A^{\mathrm{i}}/A^{\mathrm{s}}$. The water depths correspond to Figure 3.5 and were chosen to show the relative importance of the creep and regelation terms.

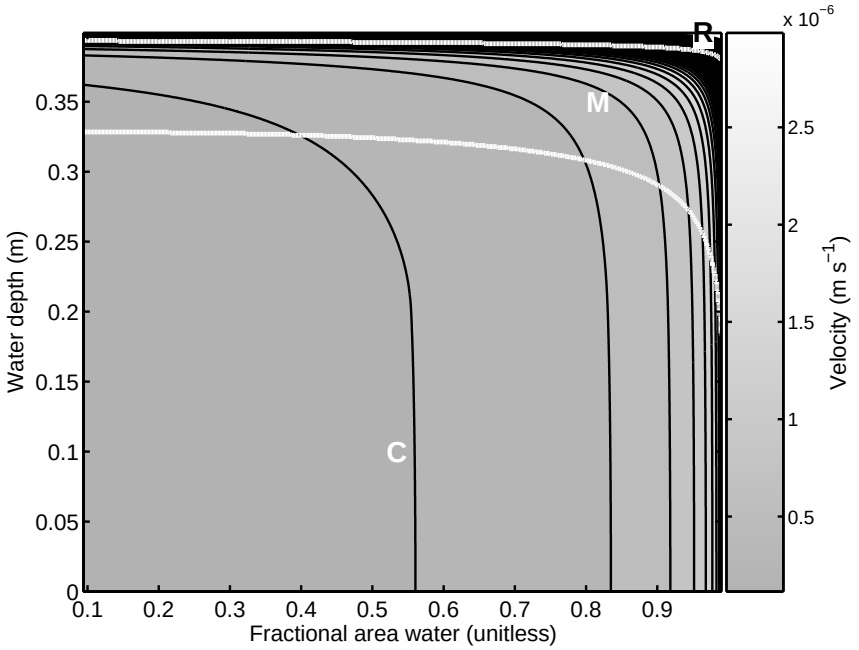

Figure 3.5: Total closure velocities for a grain size of $r_i = 0.2$ m with variable fractional area water. Parameters are given in Table 3.1. These velocities are total closure velocities (eq. 3.1). Black contours are spaced at intervals of 0.25×10^{-6} m s^{-1}. Letters and thick white lines denote different closure regimes. Area R indicates regelation dominated closure ($v_r > 0.9v$). Area C delimits creep dominated closure ($v_c > 0.9v$). In area M, both creep and regelation are important for closure. The regelation region saturates the colorbar and has a maximum value of 0.01 m s^{-1}.

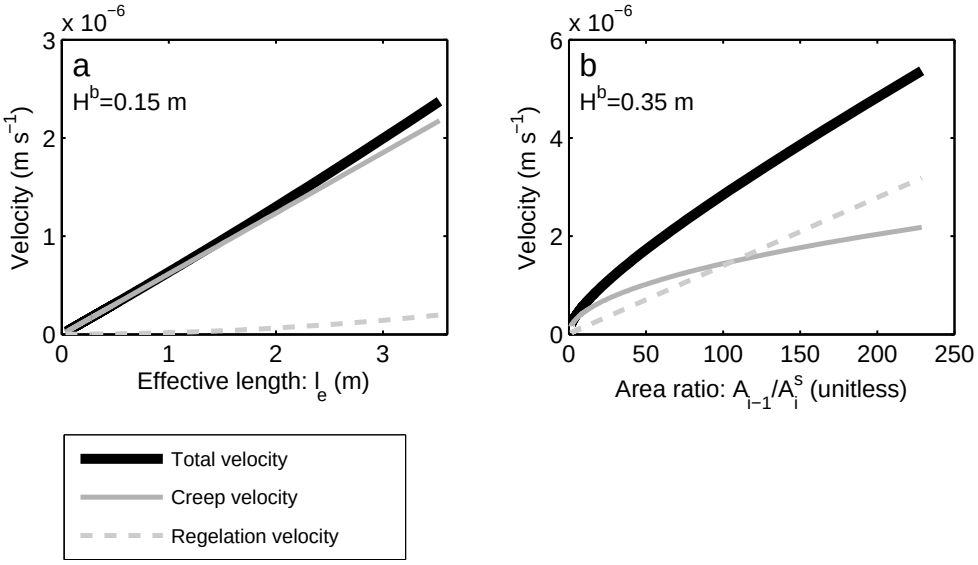

Figure 3.6: Example closure velocities for a grain size of $r_i = 0.2$ m. Parameters are given in Table 3.1. The normalized effective pressure is 0.5. Figures (a) and (b) are horizontal slices of Figure 3.5. (a) $H^{\mathrm{b}} = 0.15$, v_c varies linearly with l_e; (b) $\min(A^{\mathrm{w}}/A^{\mathrm{i}}) = 0.5$, $\min(l_e) = 0.35$ m.

Small grains

As Figure 3.7 illustrates, closure for small grain sizes is dominated by regelation. The ratio A_e/V_e is the controlling term in the regelation velocity with velocities increasing on the right side of the figure as a result of the velocity dependence on A_{i-1}/A_i^{s}. Figure 3.8 shows two cross sections through Figure 3.7, one horizontal and one vertical. The creep velocities throughout both figures are several orders of magnitude smaller than the regelation velocities. As effective stress increases, the creep velocity does increase but not to a magnitude where it becomes significant (Fig. 3.8b). The magnitude of closure velocities is approximately a factor of 100 greater for small grains than for large grains as noted in the colorbar (compare Fig. 3.4).

3.5.2 Multiple grain sizes

Sedimentary beds beneath glaciers will most likely not consist of only one grain size. Larger grains will be interspersed among smaller grains. As ice descends, different grain sizes will be submerged to different levels in the water with the ice resting on the remainder of those grains. Figure 3.9 illustrates several scenarios for 5, 10, 25, and 50 different grain sizes lying on the bed. The maximum grain size in each figure is 0.4 m, and the minimum grain size is 0.001 m. These figures are meant as illustrations of the processes. Grain size distributions for each of these figures are illustrated in Figure 3.10. The fractional areas for each grain size are the same within each distribution (eq. 3.23). Creep, mixed, and regelation regimes are determined by multiplying the individual creep and regelation velocities by the fraction of driving stress on each grain size (eq. 3.14b), summing the creep and regelation components for all grain sizes, and then comparing the magnitudes of those sums. As a result, the regimes indicated in Figure 3.9 are based on the relevant stress distributions.

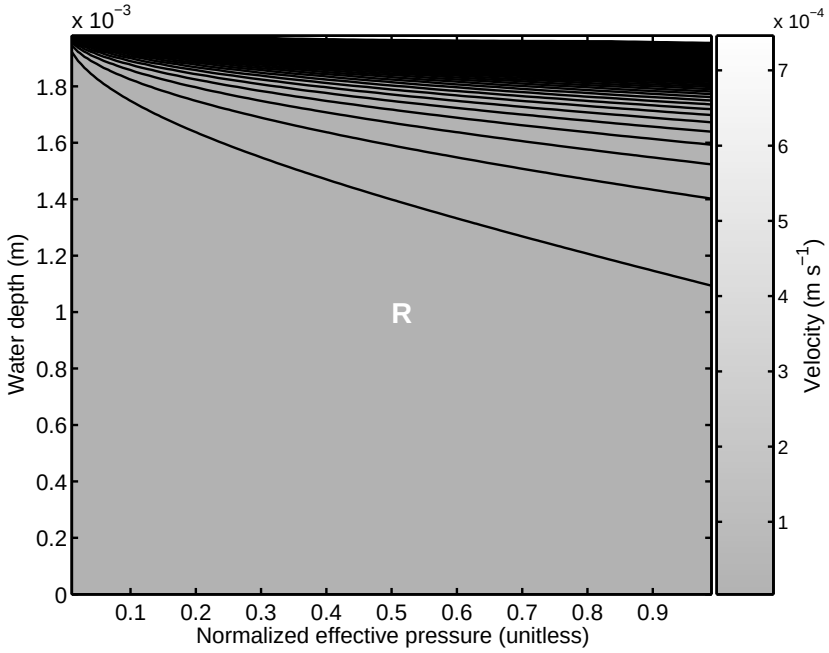

Figure 3.7: Total closure velocities for a grain size of $r_i = 0.001$ m with variable effective pressure. Parameters are given in Table 3.1. These velocities are total closure velocities (eq. 3.1). Black contours are spaced at intervals of 0.25×10^{-5} m s^{-1}. All closure velocities in this figure are dominated by regelation (R), ($v_r > 0.9v$).

The velocities in Figures 3.9a–d are extremely smooth given the amount of variability multiple grain sizes could introduce. In general, the closure velocities are less than 0.4×10^{-5} m s^{-1} for all distributions. Structure in the different closure regimes for 5 and 10 grain sizes (Figs. 3.9a,b) results from ice sequentially resting on smaller grain sizes. In Figures 3.9c and 3.9d, the creep regime is absent because each grain size has a relatively large value of A_e/V_e. The process of ice resting on the tops of grains is reasonably continuous for many grain sizes. For water depths of less than 0.1 m (*e.g.,* Lawson *et al.*, 1998; Seaberg *et al.*, 1988) either a regelation or mixed regime is favored to close the sheet. Creep closure is more important for larger water layer thicknesses (*e.g.,* Vogel *et al.*, 2005).

Figure 3.11 shows the fraction of stress available for each grain size for the case of ten grain sizes. These six figures represent the largest of those ten grain sizes. Between Figures 3.11a and 3.11b the introduction of the second grain size at 0.22 m divides the driving stress between the two grains. The fraction is not exactly half until the water depth is 0.18 m for high effective stresses. Similarly, introduction of the third grain size at 0.12 m water depth divides the the stresses among the first three grain sizes. Perhaps the most striking feature of these figures is that the stress used by each grain size is never equal across all grain sizes. Larger grains require larger stresses to achieve the same closure velocity associated with smaller grains.

Grain burial

Instead of using the whole grain parameterization for sediment shape on the bed, the half grain parameterization can be used (eqs. 3.20). This parameterization gives an estimate for grain

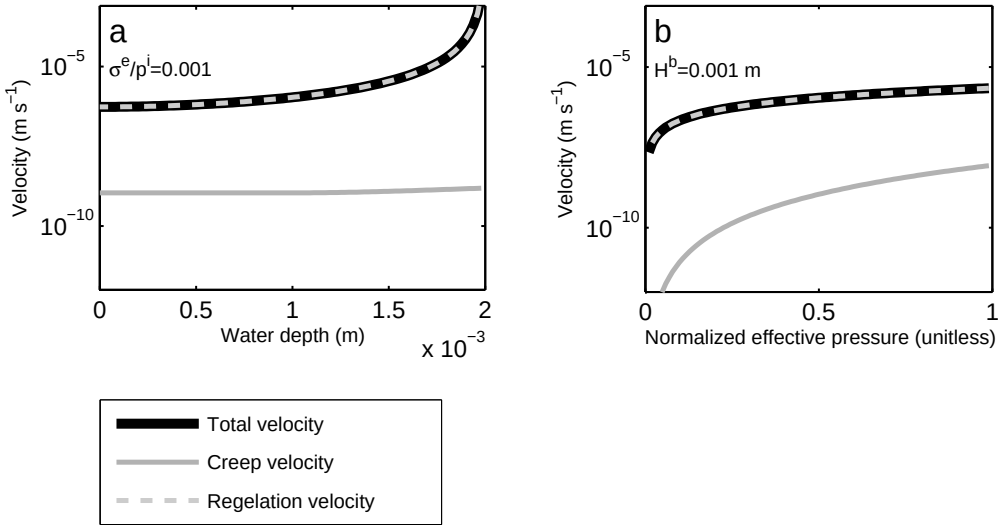

Figure 3.8: Total closure velocities for a grain size of $r_i = 0.001$ m with variable fractional area water. Parameters are given in Table 3.1. These velocities are total closure velocities (eq. 3.1). (a) A vertical slice of Fig. 3.7 where $\sigma_e/p^{\mathrm{i}} = 0.5$ (b) A horizontal slice of Fig. 3.7 where $H^{\mathrm{b}} = 0.01$ m

burial. Relief introduced by the sediments on the bed is reduced. Closure velocity trends and magnitudes are similar to Figure 3.9 and are not plotted. Figure 3.12 displays the stress partitioning for the largest six grain sizes. The noticeable difference is that stress levels are significantly reduced as ice descends onto smaller grain sizes. The smaller grain sizes play less of a role in this case.

Transitional obstacle size

Weertman (1964) noted that only one of the two terms in either of equations (3.17) would be significant. This appraisal is based on the regelation velocity being proportional to an inverse length scale while the creep closure velocity being proportional to a length scale. For a very small length scale, regelation would be the dominant mechanism of closure. For a large length scale, creep closure should dominate the system. Thus, intersection of two length scales would produce a limiting length scale. The actual effective area, volume, and length scale will depend on the distribution, arrangement, and shapes of grain sizes at the ice–bed interface.

The theory presented here does not strongly support or oppose Weertman's idea but offers an alternative view of the processes. When water depth is shallow and the effective stress is low, larger grains tend to support more of the available stress (Figs. 3.11 and 3.12). These grains lessen the available stress that the other grains could use to produce faster velocities. When water depth is shallow and effective stress is high, intermediate-sized grains carry nearly as much stress as larger grains. When the driving stress is low, perhaps one could say that the large grains sizes are the controlling obstacle size.

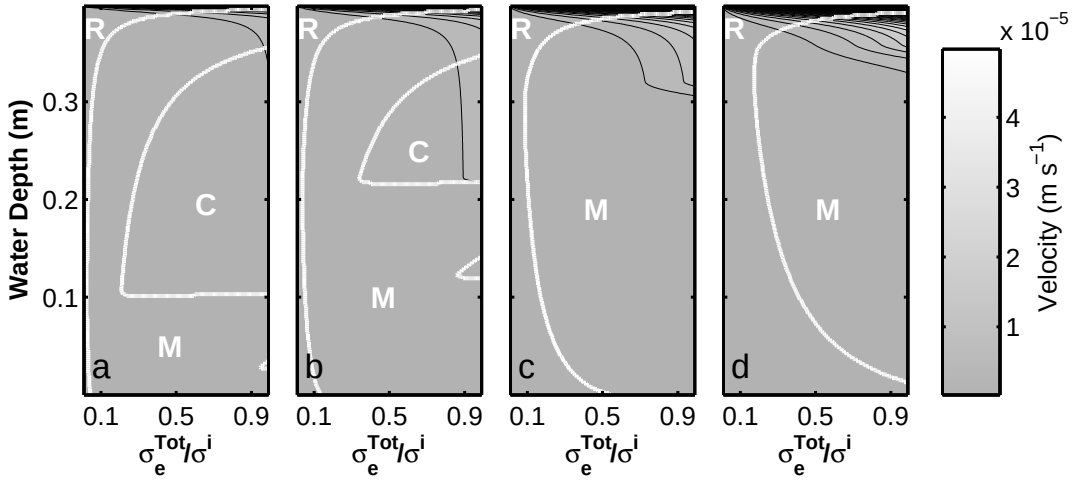

Figure 3.9: Closure velocities for multiple grain sizes. Figure labels are in the lower left corner. Parameters are given in Table 3.1. These velocities are total closure velocities (eq. 3.1). Black contours are spaced at intervals of 0.4×10^{-5} m s^{-1}. Letters and thick white lines denote different closure regimes. (a) Five different grain sizes. (b) Ten grain sizes. (c) 25 grain sizes. The closure velocity saturates the color scale in the upper right of the figure and has a maximum value of 9.9×10^{-4} m s^{-1}. (d) 50 grain sizes. The closure velocity saturates the color scale in the upper right of the figure and has a maximum value of 2.0×10^{-4} m s^{-1}.

3.6 Summary

In this chapter, a method of calculating the rate at which ice closes a subglacial sheet is introduced. The method is based upon steady-state formulations of two processes that occur subglacially: viscous creep and regelation. Creep is the deformation of ice from an applied stress, and regelation results from the change in the melting point from an applied stress. The rates of closure can be calculated numerically from equations (3.17) and (3.14). Parameterizations are necessary for appropriate length, area, and volume scales (eqs. 3.18, 3.19, 3.20, and 3.22) that are based on a distribution of idealized grain sizes lying on the bed. Simulations show that instantaneous closure velocities range from about 1×10^{-7} m s^{-1} to 1×10^{-4} m s^{-1} but can be as high as 1×10^{-2} m s^{-1}. These example velocities do not account for the lessening of the driving stress as ice pressurizes the subglacial sheet. Consequentially, they are not indicative of yearly closure rates. The formulation for these closure rates can be applied directly to equation (2.16a) to complete the balance equations of the subglacial sheet.

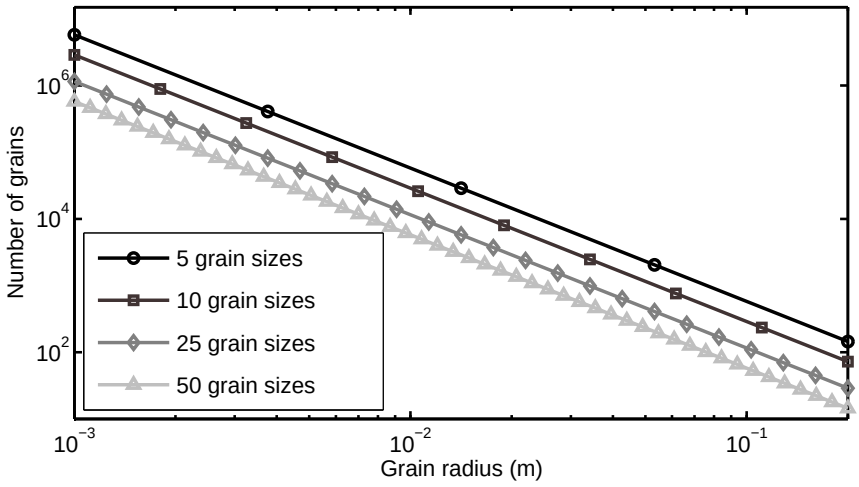

Figure 3.10: Logarithmic grain size distributions for the 5, 10, 25, and 50 grain size cases. The total area of the bed is 100 m^2 with 9% of the bed unoccupied by sediment.

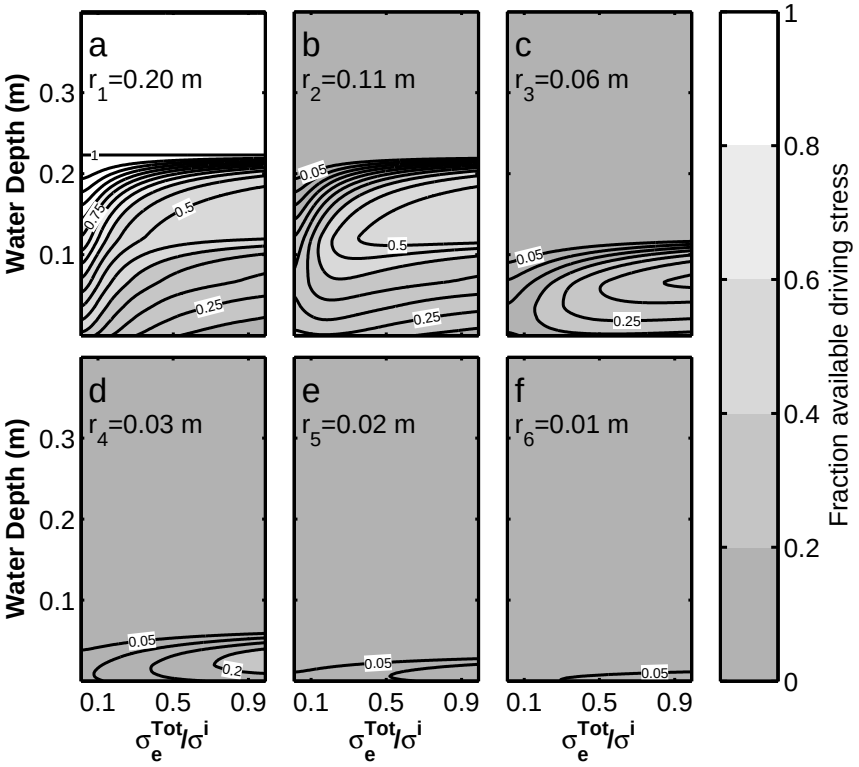

Figure 3.11: Stress partitioning for ten grain sizes. Fraction of stress available for closure that rests on each of the indicated grain sizes. These are the six largest grain sizes with velocities corresponding to Figure 3.9b. Stresses for $r_{7...10}$ plot below the threshold. Black contours are spaced at intervals of 0.05. (a) Fractional available stress for $r_1 = 0.2$ m. (b) Fractional available stress for $r_2 = 0.11$ m. (c) Fractional available stress for $r_3 = 0.06$ m. (d) Fractional available stress for $r_4 = 0.03$ m. (e) Fractional available stress for $r_5 = 0.02$ m. (f) Fractional available stress for $r_6 = 0.01$.

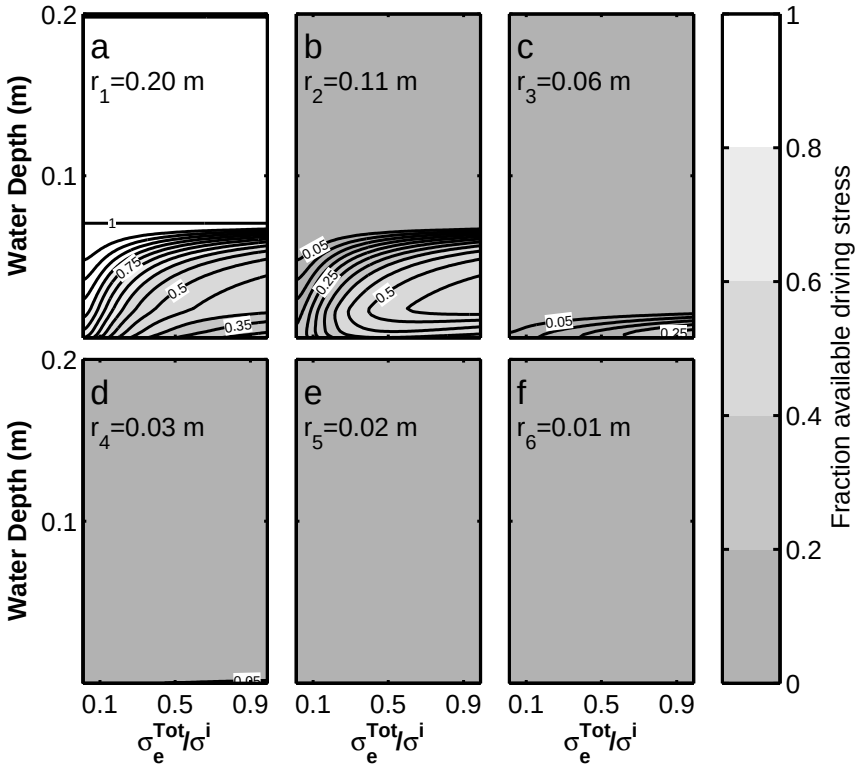

Figure 3.12: Stress partitioning for ten grain sizes exposed to their equator. Fraction of stress available for closure that rests on each of the indicated grain sizes. These are the six largest grain sizes. Stresses for $r_{7...10}$ plot below the threshold. Black contours are spaced at intervals of 0.05. (a) Fractional available stress for $r_1 = 0.2$ m. (b) Fractional available stress for $r_2 = 0.11$ m. (c) Fractional available stress for $r_3 = 0.06$ m. (d) Fractional available stress for $r_4 = 0.03$ m. (e) Fractional available stress for $r_5 = 0.02$ m. (f) Fractional available stress for $r_6 = 0.01$.

Chapter 4

Subglacial sediment transport

The efficacy of glaciers and ice sheets in modifying an unconsolidated bed is well-documented from both glaciological and glacial geologic perspectives (*e.g.,* Alley *et al.*, 1997; Benn & Evans, 1998; Clark & Walder, 1994; Prest *et al.*, 1968; Shreve, 1985). Numerical studies of subglacial sediment transfer usually do not focus on unconsolidated beds. For ice sheets, models of erosion and sediment transport have focused on quarrying, abrasion, and englacial entrainment (*e.g.,* Hildes *et al.*, 2004) or movement of deformable sediment via ice motion (*e.g.,* Bougamont & Tulaczyk, 2003). For alpine glaciers, models of sediment erosion and transportation have been based on abrasion (Braun *et al.*, 1999) or parameterizations relating erosion to sliding velocity (*e.g.,* Harbor, 1992; MacGregor *et al.*, 2000). In general, these studies are not motivated by hypotheses related to movement of sediment through the subglacial water system.

Other studies have included subglacial sediment transport. These studies are chiefly concerned with the occurrence and stability of subglacial canals (Ng, 2000; Walder & Fowler, 1994; Fig. 1.1g). Rather than being specifically interested in the geomorphological consequences of eroding and transporting sediment, these models focus on whether canals can occur subglacially. Subglacial canals undoubtedly have a geomorphological impact, but these effects have not been quantified using a numerical model.

Fluvial studies, however, have a rich history of numerical process-oriented models that focus on movement of unconsolidated sediment. These models range in scale from individual reaches and hillslopes to total valley systems. The models can be either one or two dimensions. Examples of the application of the models include valley genesis over geologic timescales, sorting of sediments, and river meandering.

The goal of this chapter is to explain the glaciofluvial modification of the bed with quantitative transport relations used in fluvial studies. Blending these two areas of research requires a formulation suited to the subglacial environment but retaining the essential attributes of the fluvial relation. Because the flow cross section is not necessarily conducive to some fluvial relationships, I have modified them. Furthermore, many of the same issues that are confronted in fluvial studies also apply to subglacial water flow. For example, the performance of sediment transport equations at making strong predictions is limited. The work of Gomez & Church (1989) and Garcia & Parker (1991) demonstrates that no individual sediment transport relation can cope with all natural conditions. The result is that a transport relation may not provide an accurate prediction but can provide a consistently scaled argument for or against the amount of sediment being transported.

In many ways, subglacial fluvial systems behave similarly to subaerial fluvial systems. Potential gradients driving subglacial water flow for many glaciers are commonly inferred to be proportional to the surface slope of the glacier. These gradients are within the range of gradients that drive subaerial water flow: the land surface slope. Surface slopes in glaciated areas fall within the approximate range 0.001–0.1 but can be locally higher or lower. Because these gradients driving flow are similar to river surface slopes, it is reasonable to assume that sediment concentrations in subglacial hydraulic systems should be similar to those of fluvial systems.

Lawson (1993) noted that typical subglacial sediment concentrations are approximately 5 g L^{-1} whereas proglacial rivers may have sediment concentrations as high as 3 g L^{-1} but more commonly have concentrations of 1.5 g L^{-1}. These observed sediment concentrations are well below the commonly accepted Newtonian/non-Newtonian threshold for water of nine percent solids. Above this threshold, flows are hyperconcentrated and do not behave as simple fluids. Subglacial water flow should rarely exceed this threshold, suggesting that fluvial relationships are adequate.

With a model of sediment transport it is possible to investigate sediment transport along the ice–bed interface. For example, part of the hypothesis proposed by Alley *et al.* (2003b) is that erosion occurs upstream of an adverse slope and sedimentation occurs along the adverse slope. Sediment erosion and deposition rates in the overdeepening can be simulated with a sediment transport model and an appropriate ice–bed configuration. The model presented here is not limited to testing this hypothesis. Erosion and sedimentation rates throughout any subglacial system can be simulated.

4.1 Balance laws for sediment transport

In the case of subglacial water flow in a sheet or channel, water flows over a floor of unconsolidated sediments and under a ceiling of ice. As the water flows, it may exceed a threshold and entrain sediment. When sediment is entrained, the sediment floor lowers and the fluid becomes a mixture of water and sediment. In addition, the ice ceiling can melt or water can freeze along that ceiling. If water freezes along the ceiling while transporting sediment, the accreted ice will contain sediment. If this ice is subsequently melted, then sediment is added to the flow based on the sediment concentration in the ice. The foregoing description is the basis of the model presented here. The balance laws for a continuum provide a reasonable entry to this description of subglacial sediment transport.

4.1.1 Sediment mass balances

Most models of sediment transport begin with the mass balance equation, often called the Exner equation (*e.g.,* Armanini & di Silvio, 1988; Bridge & Bennett, 1992; Correia *et al.*, 1992; Cui *et al.*, 1996; Hoey & Ferguson, 1994; Park & Jain, 1987; van Niekerk *et al.*, 1992; Wu *et al.*, 2004). The Exner equation has several forms (*e.g.,* Paola & Voller, 2005), the form presented here is specifically for subglacial water flow.

Sheet

The mass of sediment in the flowing water is

$$M^{\mathrm{s}} = \int_s \int_W \int_{z^{\mathrm{s}}}^{z^{\mathrm{b}}} \lambda^{\mathrm{b}}(s, y, z, t)\, \rho^{\mathrm{s}}\, dz\, dy\, ds, \tag{4.1}$$

where M^{s} is the mass of sediment, $\lambda^{\mathrm{b}}(s, y, z, t)$ is the local volume fraction of sediment in the water, and ρ^{s} is the mass density of sediment. Vertically and horizontally integrating this equation yields the mass per unit width of the flow $\tilde{M}^{\mathrm{s}}$,

$$\tilde{M}^{\mathrm{s}} = \int_s \lambda^{\mathrm{b}}(s, t)\, \rho^{\mathrm{s}} \left(z^{\mathrm{b}} - z^{\mathrm{s}} \right) ds. \tag{4.2}$$

Instead of using $\lambda^{\mathrm{b}}(s,t)$, I drop explicit dependence on s and t with the assumption that any further appearance of λ^{b} is $\lambda^{\mathrm{b}}(s,t)$. At this point, it is clear that $z^{\mathrm{b}} - z^{\mathrm{s}} = H^{\mathrm{b}}$ (Fig. 2.1). Using Reynolds transport theorem, the local rate of change of the sediment mass is

$$\rho^{\mathrm{s}} \frac{\partial}{\partial t}\left(\lambda^{\mathrm{b}} H^{\mathrm{b}}\right) + \rho^{\mathrm{s}} \frac{\partial}{\partial s}\left(u^{\mathrm{b}}_{s:b} \lambda^{\mathrm{b}} H^{\mathrm{b}}\right) = \rho^{\mathrm{s}} \frac{\partial}{\partial t}\left(\lambda^{\mathrm{b}} H^{\mathrm{b}}\right) + \rho^{\mathrm{s}} \frac{\partial \tilde{q}^{\mathrm{s}}}{\partial s}, \tag{4.3a}$$

$$= \tilde{\Psi}^{\mathrm{s}} + \tilde{\Psi}^{\mathrm{i}}, \tag{4.3b}$$

where $\tilde{q}^{\mathrm{s}} = u^{\mathrm{b}}_{s:b} \lambda^{\mathrm{b}} H^{\mathrm{b}}$ is the magnitude of the volumetric flux of sediment per unit flow width, $\tilde{\Psi}^{\mathrm{s}}$ is the mass supply per unit width from the bed, and $\tilde{\Psi}^{\mathrm{i}}$ is the mass supply of sediment per unit width from the ice. Typically, the sediment velocity is kept inside the derivative in equation (4.3a), making this the transport equation rather than the material derivative (*e.g.,* Paola & Voller, 2005). This flux term requires the transport velocity of the sediments $u^{\mathrm{b}}_{s:b}$. To solve for $u^{\mathrm{b}}_{s:b}$, ideally there would be a momentum equation for the sediment. Numerous attempts in the literature at deriving a momentum equation have been met with limited success. Most authors resort to a semiempirical relation for sediments moving in traction at the bed. These relations are typically a function of the fluid velocity and shear stress on the bed (*e.g.,* van Rijn, 1984a; Bagnold, 1973). For sediment that is fully suspended within the flow, the mean water velocity is usually applied (*e.g.,* Wu *et al.*, 2004; van Rijn, 1984b).

The mass supply of sediments at the sediment–water interface $\tilde{\Psi}^{\mathrm{s}}$ requires elaboration. For nonequilibrium conditions, the sediment load should be slightly out of equilibrium. However, the sediment load should be driven back to equilibrium such that

$$\tilde{\Psi}^{\mathrm{s}} = \frac{\rho^{\mathrm{s}}}{L^{\mathrm{s}}} \left(\tilde{q}^{\mathrm{s}}_{e} - \tilde{q}^{\mathrm{s}}\right) \tag{4.4}$$

is exactly zero when equilibrium conditions are met (Einstein, 1968). In this equation, $\tilde{q}^{\mathrm{s}}_{e}$ is the equilibrium sediment flux per unit width and L^{s} is an adaptation length. The equilibrium sediment flux can be determined from any of a number of semiempirical relations (see Garcia & Parker, 1991; Gomez & Church, 1989, for recent reviews). The surface production is the erosion or sedimentation rate depending on whether it is positive or negative, respectively.

The adaptation length is a spatial measure of how close the sediment load is to equilibrium. In loose terms, equation (4.4) states that $(\tilde{q}^{\mathrm{s}}_{e} - \tilde{q}^{\mathrm{s}}) = \exp[-\rho^{\mathrm{s}} \Delta t / L^{\mathrm{s}}]$. Thus, L^{s} determines how quickly sediment transport returns to equilibrium. For small adaptation lengths, flow should be near equilibrium. The adaptation length can assume any of a number of values for non-equilibrium flows (*e.g.,* Armanini & di Silvio, 1988; Phillips & Sutherland, 1989; Wu *et al.*, 2004; Yalin, 1972). Of these, Phillips & Sutherland showed that the adaptation length is 0.09–0.9 m for coarse sand. Yalin suggested that the adaptation length was a function of several flow constants and the average grain jump length. van Rijn (1984a) reviewed the jump length and determined it to be approximately 0.01–0.08 m. For larger grain sizes, the adaptation length decreases such that the bed load is nearly always in equilibrium. For smaller grain sizes, the adaptation length is more uncertain and depends on the particle fall velocity and the turbulence structure of the flow (*e.g.,* van Rijn, 1984b). Wu *et al.* (2004) noted that different authors chose different values for L^{s} depending on which length scale they were interested in (*e.g.,* ripple v. dune v. bar) and whether the data was from field or flume studies. In general, adaptation lengths are shorter for flume studies and longer for field studies. Furthermore Wu *et al.* noted that short adaptation lengths increase convergence times for numerical models.

The change in bed height must be a function of the total sediment transport at the bed. Any volume of sediment lost or gained at the bed would reflect a change in the average height

of the bed. The mass of the bed is

$$M_0 = \int_s \int_W \int_{z_0}^{z^{\mathrm{s}}} \left\{ \left(1 - n_p^{\mathrm{s}}\right) \rho^{\mathrm{s}} + n_p^{\mathrm{s}} \rho^{\mathrm{w}} \right\} dz\, dy\, ds, \tag{4.5}$$

where n_p^{s} is the porosity of the sediment and M_0 is the total mass between a fixed datum z_0 and the base of the water layer z^{s}. Assuming that the bed is stationary, the pore water and sediment matrix are incompressible, and the porosity is constant, the local mass balance is

$$\left\{ \left(1 - n_p^{\mathrm{s}}\right) \rho^{\mathrm{s}} + n_p^{\mathrm{s}} \rho^{\mathrm{w}} \right\} \frac{\partial z^{\mathrm{s}}}{\partial t} = -\tilde{\Psi}^{\mathrm{s}} \left\{ 1 + \frac{n_p^{\mathrm{s}} \rho^{\mathrm{w}}}{(1 - n_p^{\mathrm{s}}) \rho^{\mathrm{s}}} \right\} \tag{4.6}$$

Equation (4.6) also assumes that water saturates the pore space. Equation (4.6) shows that rate of change of mass per unit width is equal to the supply of sediment and water from the overlying water layer. This formulation is equivalent to equations (2.13) for the porosity in the ice adjacent to the water layer. The rate of change of the bed elevation follows from equation (4.6),

$$\frac{\partial z^{\mathrm{s}}}{\partial t} = -\frac{1}{(1 - n_p^{\mathrm{s}}) \rho^{\mathrm{s}}} \tilde{\Psi}^{\mathrm{s}}. \tag{4.7}$$

If equation (4.7) is substituted directly into equation (4.3) the standard form of the Exner equation follows (Paola & Voller, 2005). The two equations are separate to draw distinction to the sediment supply, which must be defined via a semiempirical relation.

Channel

Because sediments are exposed to flowing water at the base of semicircular channels (Fig. 2.2b), the mass balance for sediments in channels pertains to this channel cross section. The total mass of sediment in a channel is similar to that of the sheet,

$$M^{\mathrm{s}} = \int_s \int_{S^{\mathrm{b}}} \lambda^{\mathrm{b}}(s, S, t)\, \rho^{\mathrm{s}}\, ds\, dS. \tag{4.8}$$

Integrating equation (4.8) over S^{b} and applying Reynolds transport theorem yields the local balance of mass in the channel,

$$\rho^{\mathrm{s}} \frac{\partial}{\partial t} \left(\lambda^{\mathrm{b}} S^{\mathrm{b}} \right) + \rho^{\mathrm{s}} \frac{\partial}{\partial s} \left(u_{s:b}^{\mathrm{b}} \lambda^{\mathrm{b}} S^{\mathrm{b}} \right) = \rho^{\mathrm{s}} \frac{\partial}{\partial t} \left(\lambda^{\mathrm{b}} S^{\mathrm{b}} \right) + \rho^{\mathrm{s}} \frac{\partial q^{\mathrm{s}}}{\partial s}, \tag{4.9a}$$

$$= 2R^{\mathrm{b}} \tilde{\Psi}^{\mathrm{s}} + \Psi^{\mathrm{i}}, \tag{4.9b}$$

where q^{s} is the volumetric flux of sediment and Ψ^{i} is the sediment mass supply from the ice. In equation (4.9b), $\tilde{\Psi}^{\mathrm{s}}$ is still defined with respect to the transport rate per unit width (eq. 4.4), which contains $\tilde{q}^{\mathrm{s}}$. For the case of a semicircular channel, $\tilde{q}^{\mathrm{s}} = q^{\mathrm{s}}/(2R^{\mathrm{b}})$. In equation (4.9b), the change to the melt rate m from the melt rate per unit width $\tilde{m}$ in equation (4.3b) corrects the units for the supply of sediment from the ice.

The global mass of the bed is similar to equation (4.5) except that the horizontal limits of integration are $(0,\, 2R^{\mathrm{b}})$. The mass rate of change per unit width is exactly the same (eqs. 4.6) as is the rate of change of the bed elevation (4.7). However, before applying Reynolds transport theorem, M_0 needs to be divided by $2R^{\mathrm{b}}$ to obtain the mass per unit width. The channel radius will vary with time.

Volumetric rate of change of sediment

From the mass balance of the sediment in the water, the volume of sediment per unit volume evolves according to

$$\frac{\partial \lambda^{\mathrm{b}}}{\partial t} = \frac{1}{\rho^{\mathrm{s}} S^{\mathrm{b}}} \left(2R^{\mathrm{b}} \tilde{\Psi}^{\mathrm{s}} + \Psi^{\mathrm{i}} - \rho^{\mathrm{s}} \lambda^{\mathrm{b}} \frac{\partial S^{\mathrm{b}}}{\partial t} - \rho^{\mathrm{s}} \frac{\partial q^{\mathrm{s}}}{\partial s} \right) \qquad \text{channel,} \tag{4.10a}$$

$$\frac{\partial \lambda^{\mathrm{b}}}{\partial t} = \frac{1}{\rho^{\mathrm{s}} H^{\mathrm{b}}} \left(\tilde{\Psi}^{\mathrm{s}} + \tilde{\Psi}^{\mathrm{i}} - \rho^{\mathrm{s}} \lambda^{\mathrm{b}} \frac{\partial H^{\mathrm{b}}}{\partial t} - \rho^{\mathrm{s}} \frac{\partial \tilde{q}^{\mathrm{s}}}{\partial s} \right) \qquad \text{sheet.} \tag{4.10b}$$

These equations are subject to the definitions of $\tilde{\Psi}^{\mathrm{s}}$ (eq. 4.4), Ψ^{i}, and $\tilde{\Psi}^{\mathrm{i}}$.

4.1.2 Fluid flow balance laws

Movement of sediments at the bed will affect the mass, momentum, and thermal energy balances at the bed. The water layer can enlarge via either the melting of ice, as previously discussed, or through the erosion of sediments. If the bed is eroding, sediment and pore water are supplied from the bed to the flow, changing the hydraulic cross-section. When the bed is aggrading, the converse is true, and the flow supplies the bed with sediment and water. In this case, there is no Darcian flow. Supply of water is only from the arrangement of grains and pores. As grains enter the flow, interstitial water also enters the flow.

For a semicircular channel, relations equivalent to equations (2.17) and (2.15) are,

$$\begin{aligned} \frac{\partial S^{\mathrm{b}}}{\partial t} =& \frac{1}{\left(1-\lambda^{\mathrm{i}}\right)\left(1-n_p^{\mathrm{i}}\right)\rho^{\mathrm{i}} + n_p^{\mathrm{i}}\rho^{\mathrm{w}} + \lambda^{\mathrm{i}}\left(1-n_p^{\mathrm{i}}\right)\rho^{\mathrm{s}}} \left\{ \left[1 + \frac{n_p^{\mathrm{i}}\rho^{\mathrm{w}}}{\left(1-\lambda^{\mathrm{i}}\right)\left(1-n_p^{\mathrm{i}}\right)\rho^{\mathrm{i}}} \right] m + \Psi^{\mathrm{i}} \right\} \\ & - 2S^{\mathrm{b}} \operatorname{sgn}(p^{\mathrm{i}} - p^{\mathrm{b}}) \left(\frac{|p^{\mathrm{i}} - p^{\mathrm{b}}|}{n\mathcal{B}} \right)^n + \frac{2R^{\mathrm{b}}\tilde{\Psi}^{\mathrm{s}}}{\left(1-n_p^{\mathrm{s}}\right)\rho^{\mathrm{s}}}. \end{aligned} \tag{4.11a}$$

$$\begin{aligned} \frac{\partial p^{\mathrm{b}}}{\partial t} =& -\frac{1}{\gamma^{\mathrm{b}} S^{\mathrm{b}}} \left(\frac{\partial S^{\mathrm{b}}}{\partial t} + \frac{\partial \left(S^{\mathrm{b}} u^{\mathrm{b}}\right)}{\partial s} - \frac{1}{\lambda^{\mathrm{b}}\rho^{\mathrm{s}} + (1-\lambda^{\mathrm{b}})\rho^{\mathrm{w}}} \left\{ -S^{\mathrm{b}} \left(\rho^{\mathrm{s}} - \rho^{\mathrm{w}}\right) \left[\frac{\partial \lambda^{\mathrm{b}}}{\partial t} + u^{\mathrm{b}} \frac{\partial \lambda^{\mathrm{b}}}{\partial s} \right] \right. \right. \\ & \left. \left. + \left[1 + \frac{n_p^{\mathrm{i}}\rho^{\mathrm{w}}}{\left(1-\lambda^{\mathrm{i}}\right)\left(1-n_p^{\mathrm{i}}\right)\rho^{\mathrm{i}}} \right] m + \Psi^{\mathrm{i}} + \left[1 + \frac{n_p^{\mathrm{s}}\rho^{\mathrm{w}}}{\left(1-n_p^{\mathrm{s}}\right)\rho^{\mathrm{s}}} \right] 2R^{\mathrm{b}}\tilde{\Psi}^{\mathrm{s}} \right\} \right), \end{aligned} \tag{4.11b}$$

where λ^{i} is the sediment concentration in the overlying ice and S^{b} represents the cross section of the sediment-fluid mixture. If there is no supply of sediment from the bed or overlying ice, and the volumetric concentration of sediment in the flow is zero, then these equations revert to equations (2.17) and (2.15). Equation (4.11a) is the sum of the instantaneous misfit balances of the ice and sediment. Equation (4.11b) is the balance of the fluid in the cross section. These equations are derived in appendix D (eqs. D.8 and D.9) with an alternative formulation for the pressure evolution equation based on the mass balance of water (eq. D.12). Similarly, relations

equivalent to equations (2.16) for the subglacial water sheet are

$$\frac{\partial H^{\mathrm{b}}}{\partial t} = \frac{1}{\left(1-\lambda^{\mathrm{i}}\right)\left(1-n_p^{\mathrm{i}}\right)\rho^{\mathrm{i}} + n_p^{\mathrm{i}}\rho^{\mathrm{w}} + \lambda^{\mathrm{i}}\left(1-n_p^{\mathrm{i}}\right)\rho^{\mathrm{s}}} \left\{ \left[1 + \frac{n_p^{\mathrm{i}}\rho^{\mathrm{w}}}{\left(1-\lambda^{\mathrm{i}}\right)\left(1-n_p^{\mathrm{i}}\right)\rho^{\mathrm{i}}} \right] \tilde{m} + \tilde{\Psi}^{\mathrm{i}} \right\} + \left(\frac{\partial H^{\mathrm{b}}}{\partial t} \right)_{\mathrm{close}} + \frac{\tilde{\Psi}^{\mathrm{s}}}{\left(1-n_p^{\mathrm{s}}\right)\rho^{\mathrm{s}}}, \tag{4.12a}$$

$$\frac{\partial p^{\mathrm{b}}}{\partial t} = -\frac{1}{\gamma^{\mathrm{b}} H^{\mathrm{b}}} \left(\frac{\partial H^{\mathrm{b}}}{\partial t} + \frac{\partial \left(H^{\mathrm{b}} u^{\mathrm{b}} \right)}{\partial s} - \frac{1}{\lambda^{\mathrm{b}}\rho^{\mathrm{s}} + (1-\lambda^{\mathrm{b}})\rho^{\mathrm{w}}} \left\{ -H^{\mathrm{b}} \left(\rho^{\mathrm{s}} - \rho^{\mathrm{w}} \right) \left[\frac{\partial \lambda^{\mathrm{b}}}{\partial t} + u^{\mathrm{b}} \frac{\partial \lambda^{\mathrm{b}}}{\partial s} \right] + \left[1 + \frac{n_p^{\mathrm{i}}\rho^{\mathrm{w}}}{\left(1-\lambda^{\mathrm{i}}\right)\left(1-n_p^{\mathrm{i}}\right)\rho^{\mathrm{i}}} \right] \tilde{m} + \tilde{\Psi}^{\mathrm{i}} + \left[1 + \frac{n_p^{\mathrm{s}}\rho^{\mathrm{w}}}{\left(1-n_p^{\mathrm{s}}\right)\rho^{\mathrm{s}}} \right] \tilde{\Psi}^{\mathrm{s}} \right\} \right). \tag{4.12b}$$

Not surprisingly, these equations are similar to the equations for the channel. Their derivation parallels the derivation in Appendix D.

The momentum equation is much more difficult to modify. The reason for this difficulty is the movement of sediment. Generally, sediment transport is correlated to the water flow using a semiempirical relationship. As a result, the sediment momentum balance becomes a semiempirical black box. There are a few manageable modifications, however. The simplest modification is to substitute the fluid density,

$$\rho^{\mathrm{f}} = \lambda^{\mathrm{b}}\rho^{\mathrm{s}} + \left(1-\lambda^{\mathrm{b}}\right)\rho^{\mathrm{w}}, \tag{4.13}$$

in place of the water density in equations (2.27). Another modification, given equations (4.11b) and (4.12b), is the scalar multiplication of production and supply terms with the velocity u^{b}. This modification creates additional impulse terms as material moves off the hydraulic boundaries. The changes to equations (2.27) yield

$$\frac{\partial u^{\mathrm{b}}}{\partial t} = -u^{\mathrm{b}}\frac{\partial u^{\mathrm{b}}}{\partial s} - \left\{ \left[1 + \frac{n_p^{\mathrm{i}}\rho^{\mathrm{w}}}{\left(1-\lambda^{\mathrm{i}}\right)\left(1-n_p^{\mathrm{i}}\right)\rho^{\mathrm{i}}} \right] m + \Psi^{\mathrm{i}} + \left[1 + \frac{n_p^{\mathrm{s}}\rho^{\mathrm{w}}}{\left(1-n_p^{\mathrm{s}}\right)\rho^{\mathrm{s}}} \right] 2R^{\mathrm{b}}\tilde{\Psi}^{\mathrm{s}} \right\} \frac{u^{\mathrm{b}}}{\rho^{\mathrm{f}} S^{\mathrm{b}}} - \frac{1}{\rho^{\mathrm{f}}}\frac{\partial p^{\mathrm{b}}}{\partial s} - g\frac{\partial z^{\mathrm{b}}}{\partial s} - \frac{P^{\mathrm{w}}\tau_0}{S^{\mathrm{b}}\rho^{\mathrm{f}}}, \tag{4.14a}$$

$$\frac{\partial u^{\mathrm{b}}}{\partial t} = -u^{\mathrm{b}}\frac{\partial u^{\mathrm{b}}}{\partial s} - \left\{ \left[1 + \frac{n_p^{\mathrm{i}}\rho^{\mathrm{w}}}{\left(1-\lambda^{\mathrm{i}}\right)\left(1-n_p^{\mathrm{i}}\right)\rho^{\mathrm{i}}} \right] \tilde{m} + \tilde{\Psi}^{\mathrm{i}} + \left[1 + \frac{n_p^{\mathrm{s}}\rho^{\mathrm{w}}}{\left(1-n_p^{\mathrm{s}}\right)\rho^{\mathrm{s}}} \right] \tilde{\Psi}^{\mathrm{s}} \right\} \frac{u^{\mathrm{b}}}{\rho^{\mathrm{f}} H^{\mathrm{b}}} - \frac{1}{\rho^{\mathrm{f}}}\frac{\partial p^{\mathrm{b}}}{\partial s} - g\frac{\partial z^{\mathrm{b}}}{\partial s} - \frac{2\tau_0}{H^{\mathrm{b}}\rho^{\mathrm{f}}}, \tag{4.14b}$$

where equation (4.14a) describes flow in a semicircular channel and equation (4.14b) describes flow in the sheet. The constitutive relationship for τ_0 could also be altered; however, the bed shear velocity used in sediment transport relationships is commonly described in terms of the water density rather than the mixture density. For the purposes here, the relationship for τ_0 is fixed by equation (2.24).

The thermal energy balance of the water is the energy balance of interest because the phase change from water to ice (or vice versa) is important. When the impulse terms are included for

the water (eqs. D.11 and D.14b), the thermal balances from equations (2.29) become

$$\frac{\partial T^{\mathrm{b}}}{\partial t} = - u^{\mathrm{b}} \frac{\partial T^{\mathrm{b}}}{\partial s} - \frac{m}{(1-\lambda^{\mathrm{b}})\,\rho^{\mathrm{w}} c_p^{\mathrm{w}} S^{\mathrm{b}}} \left(L + c_p^{\mathrm{w}} \Delta T_{\mathrm{mp}} - \left\{ \left[1 + \frac{n_p^{\mathrm{i}} \rho^{\mathrm{w}}}{(1-\lambda^{\mathrm{i}})\left(1-n_p^{\mathrm{i}}\right)\rho^{\mathrm{i}}} \right] m + \frac{n_p^{\mathrm{s}} \rho^{\mathrm{w}}}{\left(1-n_p^{\mathrm{s}}\right)\rho^{\mathrm{s}}} 2R^{\mathrm{b}} \tilde{\Psi}^{\mathrm{s}} \right\} \frac{(u^{\mathrm{b}})^2}{2} \right) + \frac{P^{\mathrm{w}}}{S^{\mathrm{b}}} \frac{\tau_0 u^{\mathrm{b}}}{(1-\lambda^{\mathrm{b}})\,\rho^{\mathrm{w}} c_p^{\mathrm{w}}}, \tag{4.15a}$$

$$\frac{\partial T^{\mathrm{b}}}{\partial t} = - u^{\mathrm{b}} \frac{\partial T^{\mathrm{b}}}{\partial s} - \frac{\tilde{m}}{(1-\lambda^{\mathrm{b}})\,\rho^{\mathrm{w}} c_p^{\mathrm{w}} H^{\mathrm{b}}} \left(L + c_p^{\mathrm{w}} \Delta T_{\mathrm{mp}} - \left\{ \left[1 + \frac{n_p^{\mathrm{i}} \rho^{\mathrm{w}}}{(1-\lambda^{\mathrm{i}})\left(1-n_p^{\mathrm{i}}\right)\rho^{\mathrm{i}}} \right] \tilde{m} + \frac{n_p^{\mathrm{s}} \rho^{\mathrm{w}}}{\left(1-n_p^{\mathrm{s}}\right)\rho^{\mathrm{s}}} \tilde{\Psi}^{\mathrm{s}} \right\} \frac{(u^{\mathrm{b}})^2}{2} \right) + \frac{2}{H^{\mathrm{b}}} \frac{\tau_0 u^{\mathrm{b}}}{(1-\lambda^{\mathrm{b}})\,\rho^{\mathrm{w}} c_p^{\mathrm{w}}}, \tag{4.15b}$$

for the channel and sheet, respectively. In these equations, the impulse from sediment motion is not included. This assumption follows Walder & Fowler (1994) who made no allowance for the work done in eroding and transporting sediment. The temperature of the subjacent pore water directly below the flowing water should be approximately at the temperature of the flowing water. As a consequence, no allowance is made for the sensible heat of the entrained pore water. Other terms, such as the sensible heat of the entrained sediment, could be included but are of secondary importance.

The thickness of the ice changes as ice is accreted or melted from the base. A simple mass balance term for overlying ice is given by

$$\frac{\partial Z^{\mathrm{i}}}{\partial t} = - \frac{1}{(1-\lambda^{\mathrm{i}})(1-n_p^{\mathrm{i}})\rho^{\mathrm{i}} + n_p^{\mathrm{i}}\rho^{\mathrm{w}} + \lambda^{\mathrm{i}}(1-n_p^{\mathrm{i}})\rho^{\mathrm{s}}} \left\{ \left[1 + \frac{n_p^{\mathrm{i}} \rho^{\mathrm{w}}}{(1-\lambda^{\mathrm{i}})(1-n_p^{\mathrm{i}})\rho^{\mathrm{i}}} \right] \tilde{m} + \tilde{\Psi}^{\mathrm{i}} \right\}, \tag{4.16a}$$

$$\frac{\partial Z^{\mathrm{i}}}{\partial t} = \frac{1}{\left(1-n_p^{\mathrm{i}}\right)\rho^{\mathrm{i}} + n_p^{\mathrm{i}}\rho^{\mathrm{w}} + 2\left(1-n_p^{\mathrm{i}}\right)\left(\rho^{\mathrm{s}}-\rho^{\mathrm{i}}\right)\lambda^{\mathrm{i}}} \left\{ \left[\left(1-n_p^{\mathrm{i}}\right)\left(1-\frac{\rho^{\mathrm{i}}}{\rho^{\mathrm{s}}}\right) - 1 \right] \tilde{\Psi}^{\mathrm{i}} - \left[1 + \frac{n_p^{\mathrm{i}} \rho^{\mathrm{w}}}{\left(1-\lambda^{\mathrm{i}}\right)\left(1-n_p^{\mathrm{i}}\right)\rho^{\mathrm{i}}} \right] \tilde{m} \right\}, \tag{4.16b}$$

where equation (4.16a) holds for $\tilde{m} > 0$ and equation (4.16b) holds for $\tilde{m} < 0$. Because I assume that the ice is static, there is no convective velocity, which is equivalent to the assumptions used in equation (2.18). If the melt rate is positive, then the supply term has a simple form (see eqs. 4.34) and equation (4.16a) simplifies to

$$\frac{\partial Z^{\mathrm{i}}}{\partial t} = - \frac{1}{(1-\lambda^{\mathrm{i}})(1-n_p^{\mathrm{i}})\rho^{\mathrm{i}}} \tilde{m}. \tag{4.17}$$

This equation has the satisfying effect of resembling equation (2.18).

4.2 Subglacial sediment characteristics

A necessary assumption is that the subglacial bed exposed to the overlying ice and water is unconsolidated sediment. While bedrock is undoubtedly exposed at the bed of many glaciers, in the ablation zones the bed is often sediment covered (*e.g.,* Clark & Walder, 1994; Lawson, 1981). In general, it is in the ablation zones where supercooling has been observed.

Typically, subglacial sediments are tills. Sediment size distributions for tills formed under shear follow a fractal distribution,

$$N^{\mathrm{s}} = N_0^{\mathrm{s}} \left(\frac{D}{D_0} \right)^{-m}, \tag{4.18}$$

such that the dimension, or fractal index m in equation (4.18), is approximately 2.9 (Hooke & Iverson, 1995). Equation (4.18) relates the number of particles N^{s}, of a characteristic diameter D, to a known number N_0^{s}, for a reference size D_0. For a fractal dimension of exactly 3, the volume occupied by each of the grain sizes will be the same. For $m < 3$, the volume of material will preferentially be in the larger grain sizes. For $m > 3$, the converse is true and more of the total volume of the till will be in the smaller grain sizes. Because the sheet closure mechanism relies on the index being 2 for the surface sediments (Fig. 3.10), I assign the volumetric distribution consistent with this and choose $m = 3$ in equation (4.18).

Khatwa *et al.* (1999) analyzed sediments in various diamictons from different glacial environments. Their results show fractal distributions ranging from 2.55 to 2.97. Supraglacial deposits in this study had a fractal dimension near 2.83, while the subglacial deposits had a fractal dimension near 2.92. Khatwa *et al.* questioned whether the fractal nature of glacial sediments is really characteristic of the erosion and sedimentation process. In particular, all of the diamictons they analyzed had a reasonable fractal dimension, but not all of the diamictons showed a shear fabric.

Benn & Gemmell (2002) demonstrated, through synthetic distributions of sediments, that the use of a fractal distribution is not an especially discerning analysis for tills. They showed superimposed Gaussian distributions with different mean values may resemble fractal distributions with $m \sim 3$. Benn & Gemmell went on to suggest that tills with a fractal distribution of about three can be formed not only from shearing as Hooke & Iverson (1995) proposed but also from mixing of tills.

A practical problem of a fractal distribution of clast sizes lies in the larger grain sizes. Most studies with field data (*e.g.,* Hooke & Iverson, 1995; Fischer & Hubbard, 1999; Khatwa *et al.*, 1999; Benn & Gemmell, 2002) truncate the fractal distribution at either 1 or 10 mm. This truncation makes it difficult to estimate the size fraction larger than fine pebbles. Estimating the larger fraction from proglacial deposits is difficult because the fines may be winnowed. Analyses of till recovered from under Ice Stream B suggest that the fraction of sediment larger than 4 mm is roughly 3% (Tulaczyk *et al.*, 1998). A drilling program at Black Rapids Glacier produced several cores of variable quality. Pebbles and cobbles were retrieved from beneath the glacier with over 20% of the recovered sediments being larger than 4 mm (Truffer *et al.*, 1999). Because of core quality problems, the Black Rapids data may provide only an upper limit to the percent of coarse material.

While a fractal distribution may not be very indicative of the genesis of a till, it does provide a starting point for approximating the texture of subglacial sediments. Because of the generality of the fractal distribution, it serves as an adequate initial condition on the parent till below the ice. For grain sizes larger than four millimeters, the fractal distribution may not hold because these grains usually are not investigated. The work of Benn & Gemmell (2002) circumvents this inadequacy of the published data, allowing for the fractal distribution to be used. By using a fractal distribution, I assign an equal volume of solids in subglacial till to all clast sizes.

Lawson (1979) performed sedimentological analyses of the accreted basal layers at Matanuska Glacier, Alaska. He found that the accreted ice had an average sediment content of 25% by volume that ranged in size from clay to pebble gravel with large fractions being medium silt to

sand. Grain size distributions of accreted sediment commonly have multiple peaks in sand to silt size particles, $0.008 < D < 2.0$ mm (Lawson, 1979, 1993). Often there is a spike in coarse silt, $D \simeq 0.05$ mm, accounting for approximately 20% of the sediment in the basal layers. However, sediment distributions may be dominated by sand or even be up to 50% gravel and larger grains. Lawson also identified a melt out till directly below the accreted ice at the margin that has the same source as the sediment entrained in the ice. He described the melt out till as a "pebbly sandy silt" (Lawson, 1979, p. 39). On the basis of these observations, it seems plausible that the smaller grain sizes may be volumetrically more important.

There are two possible source options for sediment accreted in the ice. Either the accreted ice reflects the exact composition of the subglacial layer; or the accreted ice reflects a preferential sorting of sediment. In the case of a preexisting melt-out till, the accreted sediment may match the source sediment exactly. A melt-out till is comprised of sediment that had already been accreted. In most other cases, the accreted sediment will not reflect the exact texture of the parent material. Subaerial fluvial systems readily sort sediment. Therefore, one expects flowing water at the base of a glacier to sort sediment as well. Lawson *et al.* (1998) also described individual processes such as the filtering of sediment by frazil ice flocs near the terminus of Matanuska Glacier. This filtering mechanism would tend to sort sediment as it is frozen into the accreted ice. As a consequence, it is unlikely that the accreted sediment fully represents the source.

There are no direct observations of sediments in overdeepenings. As a result, I have assumed that the subglacial material is a deformation till. Where an active subglacial hydraulic system exists, the sediments could possibly be sorted such that they resemble proglacial outwash. Lawson (1981) described a section of fluvially sorted material in front of Matanuska Glacier; however, the location of this section relative to the terminus of the glacier is unclear. In addition, data on subglacial till from Storglaciären, Sweden, suggests that this overdeepening is occupied by deformation till (Hooke *et al.*, 1997).

4.2.1 Mobile sediments

Knowledge of the grain size distribution is necessary to state what is and is not mobile subglacially. From the foregoing discussion, two issues are critical: (1) grain size distributions in overdeepenings are not well characterized, and (2) the smaller grain sizes appear to dominate subglacial sediments. The result of the first issue is that the model presented here cannot accurately reproduce any data including the grain size distributions presented by Lawson (1979). This shortcoming is beyond control; and, if necessary, a community effort will be required to more accurately characterize subglacial beds in situ.

The consequence of the second issue is that construction of a model can focus on the smaller grain sizes. Focusing on smaller grain sizes is a benefit because the number of processes occurring at the bed are limited. Armoring of a subglacial streambed, for example, does not merit consideration. Furthermore if smaller grain sizes are readily available at the bed in large quantity, this availability suggests that the source of much of the sediment in the flowing water is local. The amount of sediment in the flow is not limited by either source or upstream conditions. Sediment transport conditions are then approximately near equilibrium.

Equilibrium transport occurs when flowing water is eroding and depositing equivalent amounts of bed material simultaneously. Laboratory experiments or field measurements of equilibrium conditions require that the flow be steady, the sediment supply not limit the sediment transport, and the transport conditions be statistically steady (Bagnold, 1966). Once these conditions have

been met, relations are constructed to predict sediment transport based on flow and sediment characteristics. The equilibrium assumption pertains to flow conditions. For long time periods, flow conditions will not be steady, and it must be true that entrained sediment is preferentially eroded from or deposited on the bed. For example, daily cycles of water discharge do not meet equilibrium conditions. On a second-to-second time period, transport will be near equilibrium. Subtle changes in the equilibrium load will lead to the daily variation. The assumption implicit in this statement is that the sediment concentration always responds faster than the flow conditions. For large hydraulic cross-sections, this assumption may not be valid. However, for relatively shallow subglacial water sheets, this assumption is acceptable.

If sediment responds slower than the flow conditions or the amount of sediment available to be transported varies spatially, a correction to an equilibrium transport rule via an adaptation length (*e.g.,* Armanini & di Silvio, 1988; Wu, 2004; Yalin, 1972) or an equivalent spatial lag in sediment transport (*e.g.,* Einstein, 1968; Phillips & Sutherland, 1989) is possible (eq. 4.4). However, adaptation lengths range from a few centimeters to a few meters for coarse sand (Phillips & Sutherland, 1989). The spatial effect introduced by not applying an adaptation length is quite small especially when the longitudinal glacier sections (Figs. 1.3 and 1.5) are hundreds to thousand of meters long.

Larger grain sizes, such as gravel and coarser material, are undoubtedly mobilized by subglacial water flow. R-channels, in particular, may mobilize sediments as the cross section enlarges. If larger grain sizes are mobilized, then processes such as sorting and armoring may become important. Sorting and armoring are observed in esker cross-sections (*e.g.,* Shreve, 1985) that indicate these processes occur subglacially. To simulate armoring, the bed must be divided into vertical levels. Each of these levels contains grain size information. This type of bed discretization is referred to informally as a Hirano bed (*e.g.,* Parker & Sutherland, 1990). Sediment transport rules for a partially mobile sediment are required when multiple grain sizes may be mobile along the bed (Wilcock & McArdell, 1997, 1993; Wilcock, 1997). These processes are not beyond the scope of this thesis. However, the data available to constrain a model of subglacial water flow with multiple grain sizes using a Hirano bed is limited. The prudent course in this situation is to use a relation for total sediment transport before returning to finer details such as armoring and grain distributions. The consequence is that larger grains, primarily gravels, will not be a primary concern here.

In addition, the height of subglacial cross-sections along overdeepenings is expected to be small (Hooke, 1991; Röthlisberger & Lang, 1987) resulting in a size limitation to the material transported. In this instance, if the shear stress does cross the threshold necessary for entrainment of larger grains in the water layer, these grains will not be mobile. The grains could be rotated within the flowing water such that they touch the ice ceiling and are frozen in place along the melting perimeter.

Another mechanism that may limit sediment available to be transported is the closure relationship presented in Chapter 3. If ice rests on larger grains, these will be locally fixed. If the shear stress exceeds the critical shear necessary for entrainment, the grain will not move. Finer sediments around the fixed grain will be winnowed. Ice could then preferentially move around the larger grain, possibly entraining it (Iverson, 2000; Iverson & Semmens, 1995). Large grains with the fines winnowed do appear in the accreted basal layers at Matanuska Glacier, Alaska (Lawson *et al.*, 1998). Because of these complications the closure mechanism presented in Chapter 3 is decoupled in terms of grain size distribution from the model presented here.

4.3 Equilibrium transport rules

Sediment transport is commonly split into two categories: suspended load and bed load. This division is common within the fluvial literature and follows analyses of transport equations by Gomez & Church (1989) and Garcia & Parker (1991). Lawson (1993) and Loso *et al.* (2004) also make this distinction for sediments with a subglacial source. Suspended load consists of sediment grain sizes that are small enough to be suspended by the turbulence within the flow. Bed load is the sediment that travels in contact with or near the bed via rolling, sliding, or saltation. For most turbulent water flow, silt- and clay-sized particles ($D < 0.06$ mm), will be in the suspended load, while gravel and coarser sediments ($D > 2$ mm) will be in the bed load. The break between bed and suspended load often falls in sand-sized particles ($0.06 \leq D \leq 2$ mm); and the break is dependent on both the sediments and water flow (*e.g.,* Church, 2006). The distinction is not necessarily sharp as there is an unbroken transition from bed to suspended load.

Another sediment categorization is bed material load and wash load. Bed material load is that part of the sediment load that interacts with the bed. The sediment sizes in the bed material load can be found in the bed material. Wash load consists of the finer portion of the suspended load that rarely interact with the bed. These sediments can be held in suspension for quite a long distance and may not represent the local bed material. Komar (1989) noted that little attention has been given in the literature to wash load; and the amount of wash load in the flow is governed by its availability (Bagnold, 1966; Komar, 1989). While the sediment mass balance equations (eqs. 4.10) do not explicitly capture this feature of sediment transport, an approximate calculation of the wash load/bed material load fraction is possible based on the material transported.

From the sediment size considerations, it is clear that two transport relations are necessary: one for bed load and one for suspended load. Ideally, all grain sizes below 4 mm are of interest. However, these gravel-sized sediments are still relatively large. Avoiding gravel, the maximum size would be 2 mm. Typically, sediment enters suspension around 0.5 mm (*e.g.,* Garcia & Parker, 1991). The two relations that best account for suspended sediment are those proposed by van Rijn (1984b) and Smith & McLean (1977) (Garcia & Parker, 1991). Because there is a complementary bed load formula for van Rijn's suspended load formulation, I use both in tandem to estimate sediment transport. These relationships provide an appropriately scaled estimate of sediment transport that is preferable to simpler formulae that have less accuracy. van Rijn's (1984a; 1984b) formulae will handle sand-sized suspended load ($0.1 \leq D \leq 0.5$ mm) and sand-sized bed load ($0.2 \leq D \leq 2.0$ mm). These sand-bed formulae will determine the equilibrium sediment flux $\tilde{q}_e^s$ in equation (4.4).

At first glance, determining $\tilde{q}_e^s$ from fluvial relationships seems tenuous. These flux relationships were developed for rivers and canals that are deep relative to subglacial water flows. Nevertheless, these relationships will most likely yield the best estimates for subglacial flows. Sand-bed flume experiments often have water depths of three to 15 centimeters (*e.g.,* Abbott & Francis, 1977; Lee & Hsu, 1994) that are within the range of water depths expected along overdeepenings. Furthermore, field data suggest that sand is commonly mobilized subglacially. The bulk of accreted sediment at Matanuska Glacier is in the silt/sand regime (Lawson, 1979; Lawson *et al.*, 1998), and glaciers with larger subglacial passageways, Skeiðarárjökull for example, often discharge a significant amount of sand-sized sediment (*e.g.,* Russell *et al.*, 2006).

In what follows, I briefly review van Rijn's formulae. For clarity, only an overview appears here. The essential parts of the formulation can be found in Appendix E. Additional information

can be found in the original papers as well as the review of suspended load transport algorithms by Garcia & Parker (1991).

4.3.1 Sand formulae

van Rijn published a series of papers that explored sand movement as bed load (van Rijn, 1984a), suspended load (van Rijn, 1984b), and in creating bedforms and modifying alluvial roughness (van Rijn, 1984c). The papers build a framework for sand motion in fluvial environments. The two later papers build on the bed load paper. As a result, I briefly review the bed load before examining the suspended load.

Bed load

van Rijn developed a physical model of saltation at the bed based on first principles. He then compared model simulations against experimental data of saltation along the bed. His model reproduced observed jump lengths and jump heights of sand grains reasonably well. The jump height varies from a few millimeters to about a centimeter. The jump length varies from a few millimeters to a few centimeters (Abbott & Francis, 1977; Lee & Hsu, 1994; van Rijn, 1984a). From this physical model, van Rijn developed a bed load transport relationship. The relationship is valid for grain sizes in the range ($0.2 \leq D \leq 2.0$ mm).

The bed load transport is

$$\tilde{q}_{e:b} = u_b \delta_b \lambda^{\mathrm{b}}_{e:b}, \tag{4.19}$$

where u_b is the mean sediment velocity in the bed load layer, δ_b is the thickness of the bed load layer, and λ^{b}_b is the volumetric sediment concentration. The bed load velocity is

$$u_b = 1.5 \mathcal{T}^{0.6} \left\{ \left(\frac{\rho^{\mathrm{s}}}{\rho^{\mathrm{w}}} - 1 \right) g D_{50} \right\}^{0.5}, \tag{4.20}$$

where $\mathcal{T}$ is a transport stage parameter and D_{50} is the median grain size of the bed. The transport stage parameter is a nondimensional measure of the excess shear stress on sediments at the bed relative to the critical shear necessary for sediment entrainment. Transport occurs in the bed load layer with thickness

$$\delta_b = 0.3 D_*^{0.7} \mathcal{T}^{0.5} D_{50}, \tag{4.21}$$

where D_* is a nondimensional particle parameter. It is a ratio of the gravity forces on a particle in fluid relative to the viscous forces and can be derived from the grain Reynolds and Froude numbers. From the discussion above, δ_b should be approximately one centimeter for sand. Finally, the volumetric sediment concentration in the bed load layer is

$$\lambda^{\mathrm{b}}_{e:b} = 0.18 \lambda^{\mathrm{b}}_{b:0} \frac{\mathcal{T}}{D_*}, \tag{4.22}$$

where $\lambda^{\mathrm{b}}_{b:0}$ is a reference concentration for the bed,

$$\lambda^{\mathrm{b}}_{b:0} = n^{\mathrm{s}}_a (1 - n^{\mathrm{s}}_p). \tag{4.23}$$

van Rijn considered the entire bed mobile and gave $\lambda^{\mathrm{b}}_{b:0}$ as 0.65. Because the closure relationship presented in Chapter 3 requires larger, immobile clasts, I introduce the mobile fraction of the bed n^{s}_a. This term states what areal fraction of the bed material is mobile.

van Rijn (1984a) supported equations (4.20), (4.21), and (4.22) with examples from experimental data. Substituting equations (4.20), (4.21), and (4.22) yields the final form of the bed load flux,

$$\tilde{q}_{e:b} = 0.081\lambda^{\mathrm{b}}_{b:0}\frac{\mathcal{T}^{2.1}}{D_*^{0.3}}\left\{\left(\frac{\rho^{\mathrm{s}}}{\rho^{\mathrm{w}}}-1\right)g\right\}^{0.5}D_{50}^{1.5}. \tag{4.24}$$

van Rijn substituted $\lambda^{\mathrm{b}}_{b:0} = 0.65$ directly into equation (4.24), using equation (4.23) instead gives

$$\tilde{q}_{e:b} = 0.053n^{\mathrm{s}}_a\frac{\mathcal{T}^{2.1}}{D_*^{0.3}}\left\{\left(\frac{\rho^{\mathrm{s}}}{\rho^{\mathrm{w}}}-1\right)g\right\}^{0.5}D_{50}^{1.5} \tag{4.25}$$

as the final form of the bed load flux. If n^{s}_a=1, as would be the case for a fully mobile bed, then the coefficient is simply 0.053, which is what appears in van Rijn (1984a).

Suspended load

The formula for the suspended load is

$$\tilde{q}_{e:s} = u^{\mathrm{b}}d^{\mathrm{b}}\lambda^{\mathrm{b}}_{e:s}, \tag{4.26}$$

where u^{b} is the velocity of the subglacial water flow, d^{b} is a representative water depth, and λ^{b}_s is the volumetric suspended sediment concentration. The depth of flow in equation (4.26) is

$$d^{\mathrm{b}} = \begin{cases}\frac{\pi}{4}R^{\mathrm{b}} & \text{semicircular channel,}\\ H^{\mathrm{b}} & \text{sheet,}\end{cases} \tag{4.27}$$

where the depth of a rectangle with an equivalent cross-sectional area approximates the depth of a semicircular channel. van Rijn (1984b) noted that his relationship is valid for grain sizes in the range ($0.1 < D < 0.5$ mm). Grain sizes smaller than 0.1 mm, silt and finer particles, undoubtedly enter suspension, but van Rijn's algorithm does not account for these grain sizes because he used data for predominantly clean sands.

The volumetric concentration is,

$$\lambda^{\mathrm{b}}_{e:s} = \mathcal{F}_s\lambda^{\mathrm{b}}_{s:0} \tag{4.28}$$

where $\mathcal{F}_s$ corrects for the distribution of suspended sediment not being vertically uniform. The reference suspended sediment concentration $\lambda^{\mathrm{b}}_{s:0}$ is defined either at half the bedform height or at the Nikuradse equivalent roughness height. For a flat bed, the bed load layer height δ^{b} is the suspended sediment reference height. Together equations (4.26) and (4.28) are the equation van Rijn (1984b) wrote for the suspended load flux.

$$\mathcal{F}_s = \frac{\left(\frac{\delta_s}{d^{\mathrm{b}}}\right)^{\mathcal{Z}'} - \left(\frac{\delta_s}{d^{\mathrm{b}}}\right)^{1.2}}{\left(1-\frac{\delta_s}{d^{\mathrm{b}}}\right)^{\mathcal{Z}'}\left(1.2-\mathcal{Z}'\right)} \tag{4.29}$$

where δ_s is the suspension reference level and $\mathcal{Z}'$ is a nondimensional ratio of the momentum from a falling particle to the momentum available to keep that particle in suspension. The reference concentration is

$$\lambda^{\mathrm{b}}_{s:0} = 0.015\frac{D_{50}\mathcal{T}^{1.5}}{\delta_s D_*^{0.3}} \tag{4.30}$$

where D_{50}, D_*, and $\mathcal{T}$ were defined for bed load. All equations presented for both bed load and suspended load are subject to the supplementary relationships in Appendix E.

4.3.2 Bed shear and sediment transport

The shear stress imparted on the fraction of mobile sediments at the bed determines whether those sediments are entrained in the flow. The shear stress available to sediments is commonly broken up into a grain stress necessary to move sediment, and a form stress (*e.g.,* Yang, 1996, p. 70). Because fluid velocity and density are the same for both stresses, the friction coefficients are additive such that

$$f_d^{\mathrm{s}} = f_d' + f_d'', \tag{4.31}$$

where f_d' and f_d'' are the grain and form roughness coefficients, respectively. The boundary shear stress from equations (2.24) and (2.25) becomes

$$\tau_0 = \tau_0^{\mathrm{i}} + \left(\tau_0' + \tau_0''\right). \tag{4.32}$$

where τ_0' and τ_0'' are the grain and form shear along the bed.

Partitioning the shear stress along the bed is necessary to compute the sediment load. This partitioning is important for estimating the grain Chézy coefficient in equation (E.3). The grain Chézy coefficient is related to the grain Darcy-Weisbach friction coefficient via

$$C' = \sqrt{\frac{8g}{f_d'}} \tag{4.33}$$

As a result, estimates of f_d' are necessary.

In alluvial rivers, form resistance generally accounts for bedforms such as ripples, bars, and dunes. In rough streams, large clast sizes account for a significant portion of the form shear, with relatively little grain shear available to move smaller grain sizes (Church *et al.*, 1998). In a subglacial water system, not only are fluvial bedforms possible, but the assumed fractal nature of the grain distribution suggests that large grains bear much of the total stress available for the bed. As a result, a reasonable assumption is that the grain stress is approximately 15–20% of the total stress available to the bed. It is possible to have slightly lower or higher values depending on conditions. These percentages are only suggestive and need to be refined via field studies.

The fraction of the bed that is mobile is limited to the grain sizes less than about 2 mm in accordance with van Rijn (1984a). Furthermore, the closure relationship proposed for the bed has 18 grain sizes (Fig. F.4). Because the bed is assumed to be fractal with $m = 3$ (eq. 3.23), each of the grain sizes occupies an equivalent volume of the bed. As a result, half of the bed material is assumed to be mobile. By making this assumption, I implicitly assume that the suspended load grain sizes below $\Phi = 4$ behave as suspended sand (van Rijn, 1984b). In general, this is not true, but it does allow an expeditious procedure for simulating smaller grain sizes. Small grain sizes will be mobile, and treating them as suspended sand provides a sensible mobility criterion.

Depending on how the bed elevation evolves, the grain size distribution could also evolve. There is little data against which to check such an evolution. In consequence, I make no allowance for the erosion or deposition of fine-grained material relative to the coarse-grained material. Thus, dynamically armoring the bed via sand mining—removal of fines from space between coarse clasts—is not possible.

Measured friction coefficients are lower for mobile beds. Vanoni & Nomicos (n.d.) performed flume experiments on both mobile and immobile sand beds. Their intention was to examine the influence of roughness elements on the flow. They found that, relative to equivalent clearwater flows, bed mobility lowered the friction coefficient by 5 to 28%. Using similar experiments,

Gao & Abrahams (2004) found that the shear along the bed was lowered by up to 10%. While modulation of the friction factor with sediment concentration may occur, it is difficult to examine variations when the effective magnitudes of the friction coefficient are not known for subglacial water flow. In consequence, no modification is made to the friction coefficient to account for sediment transport.

4.4 Conceptual model of sediment and ice accretion

Sediment accretion is not well understood. Using a sediment concentration of subglacial water of 5 g L^{-1} (Lawson, 1993), then the equivalent volume of accreted sediment should be approximately 2%. Because sediment concentrations in the ice are approximately 25% by volume but can range from practically 0% to over 95%, Lawson *et al.* (1998) invoke a filtering mechanism to increase the concentration of sediment accreted. Figure 4.1c illustrates subglacial sediment transport and this filtering mechanism.

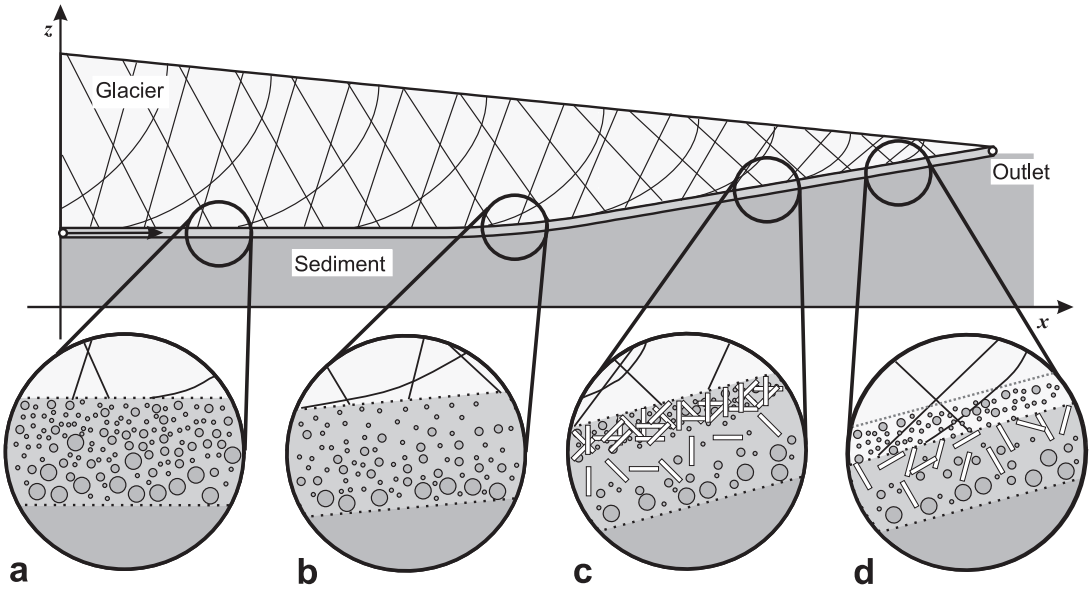

Figure 4.1: Illustration of sediment transport and accretion. Lines through the overlying glacier represent porosity in the form of fractures (Chap. 5). Filled circles represent sediment grains, and thin white rectangles represent frazil ice. (a) Sediment is eroded from the bed and transported in the flow. (b) Water begins to flow up the adverse slope and loses sediment. (c) Frazil ice forms in the flow and flocculates along the top of the water layer. Sediment is filtered through a porous lattice of frazil crystals. (d) Ice seals the porous lattice, and sediment is accreted.

Using the ideas of Alley *et al.* (2003b) and Hooke (1991) as a template, Figure 4.1 illustrates most of the ideas captured by the balance laws for sediment transport and equilibrium transport rules. In Figure 4.1a, sediment is eroded from the bed and transported in the fluid. As the fluid begins to ascend the overdeepening, water pressure increases (Hooke & Pohjola, 1994). The increased pressure forces water to distribute laterally along the ice–bed interface. Alternatively, water may escape through an englacial aquifer. The reduced flow rates along the bed imply a lessened velocity. As a result, sediment transport is diminished (Fig. 4.1b). The

fluid continues to ascend the adverse slope, and the water temperature drops below the bulk freezing temperature and supercools. Frazil ice forms in the flow and can flocculate. The flocs float to the top of the water layer. Figure 4.1c shows schematically how these flocs can trap sediment. The flocculated layer is exceptionally porous and allows water flow to pump sediment through those pores. In Figure 4.1d[12], the freezing front descends, and sediment is trapped in the ice. Obviously, all of these processes are continuous, or nearly so, but the four subfigures illustrate snapshots. Furthermore, Figures 4.1c and d would be continuous in a vertical sense, with the freezing front descending as frazil flocs are added to the base of the glacier.

Processes occurring in the flocculated layer are responsible for sediment accretion, and to model sediment accretion properly a frazil ice component is necessary. However, the nucleation, enlargement, flocculation, and eventual solidification of a frazil ice layer is a complex and demanding topic (*e.g.,* Ashton, 1982; Daly, 1984; Martin, 1981; Wettlaufer, 2001). Because incorporation of a frazil ice component into the model is beyond the scope of this thesis, Ψ^{i} and $\tilde{\Psi}^{\mathrm{i}}$ in equations (4.10) become adjustable parameters when the melt rate is negative and ice is accreting. The supply to or from the ice is

$$\Psi^{\mathrm{i}} = \begin{cases} \dfrac{\lambda^{\mathrm{i}}\rho^{\mathrm{s}}}{\left(1-\lambda^{\mathrm{i}}\right)\rho^{\mathrm{i}}} m & \text{for} \quad m > 0 \\ C_3 \lambda^{\mathrm{b}} m & \text{for} \quad m < 0 \end{cases} \qquad \text{channel} \tag{4.34a}$$

$$\tilde{\Psi}^{\mathrm{i}} = \begin{cases} \dfrac{\lambda^{\mathrm{i}}\rho^{\mathrm{s}}}{\left(1-\lambda^{\mathrm{i}}\right)\rho^{\mathrm{i}}} \tilde{m} & \text{for} \quad \tilde{m} > 0 \\ C_3 \lambda^{\mathrm{b}} \tilde{m} & \text{for} \quad \tilde{m} < 0 \end{cases} \qquad \text{sheet} \tag{4.34b}$$

where C_3 is an arbitrary constant. An assumption inherent in this mass supply term is that there is no sediment in the water in the pore space of the ice. Ideally, C_3 would be related to the degree of supercooling, the flow Reynolds number (or alternatively, the turbulence intensity which has been linked to frazil ice formation (Daly, 1984)), as well as the concentration of sediment in the water. These heuristic suggestions would make C_3 nonlinear. However, because there is no data to support these suggestions, implementation would be tenuous. As a result, I retain C_3 as an assigned parameter.

4.5 Verification of the results

The amount of sediment accretion can be tuned via the free parameter C_3. Tuning the sediment accretion can yield results that may not be related via a physical mechanism to field observations of sediment accretion. Furthermore, the equilibrium transport relations of van Rijn (1984a,b) have prediction limitations. When compared to data, van Rijn's bed load algorithm successfully predicts an amount that is 0.5 to 2 times the actual sediment transported for 77% of 600 data sets (van Rijn, 1984a). Similarly, the suspended load algorithm predicts a value that is between 0.5 and 2 times the suspended sediment concentration for 76% of 800 data sets (van Rijn, 1984b). Amounts of subglacial sediment accreted can vary substantially because of the variability associated with the equilibrium transport relations and balance laws presented here.

A fully independent assessment of subglacial sediment transported and accreted may not be possible; however, some checks are available. One of these checks is a comparison of sediment

[12]In Figure 4.1d, I have extended the fractures to symbolize the residual porosity originally introduced in equation (2.11). Obviously, the fractures will not extend to the accreted ice without incorporating a rule for fracture generation in a moving glacier.

eroded, transported, and deposited to the Hjulström diagram (Fig. 4.2). The Hjulström diagram illustrates velocities necessary to erode, transport, and deposit grains of a given diameter. While not a stringent test, the Hjulström diagram provides a viable way of checking the sediment concentration versus the flow conditions. Because the wash load can be calculated from the balance laws, the Hjulström diagram may be most stringent for smaller grain sizes in the transportation regime.

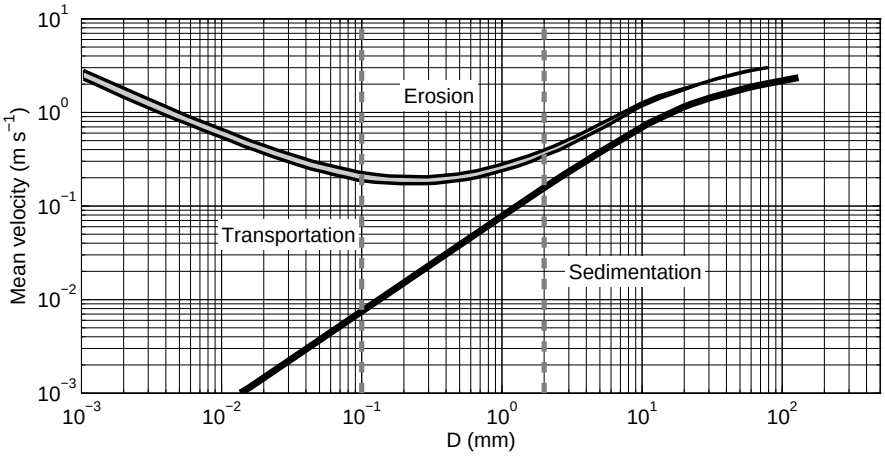

Figure 4.2: Hjulström diagram. (After Graf, 1971, p. 88). Hjulström (1935) derived these grain size–velocity relationships empirically for beds with uniform grain size. The double line separating the transportation and erosion regimes shows that this boundary is not necessarily sharp. Dashed vertical lines indicate the range of validity for equilibrium bed load and suspended load relationships (van Rijn, 1984a,b)

4.6 Summary

This chapter presents a model of subglacial sediment erosion and deposition. Using the mass balance for a continuum, rates of sediment transport per unit flow width are derived (eqs. 4.10) as well as the elevation evolution for the subglacial bed (eq. 4.7). If the subglacial fluid density changes significantly because of sediment transport (eq. 4.13), then the fluid flow balance laws take a different form for both the channel and sheet (eqs. 4.11, 4.12, 4.14, 4.15). Suspended load and bed load are common divisions of types of sediment transport. For each type of transport there is one set of equations (4.10), resulting in two equations for sediment transport in subglacial channels and two equations for sediment transport in subglacial sheets. Because sediment textures at the base of the glacier are difficult to quantify and fines seem to dominate, only equilibrium transport relationships for sand are employed (eqs. 4.24 and 4.26). These relationships are subject to a number of auxiliary equations (Appendix E). Furthermore, sediment transport in the sheet is not explicitly coupled to the closure relationship proposed in Chapter 3. In addition, sediment accretion to the base of the glacier is parameterized based on the amount of sediment in the water (eqs. 4.34). Finally, verifying the sediment load within the subglacial water system is not straightforward. One simple check is to compare results to the Hjulström curve.

Chapter 5

Englacial aquifer

5.1 Introduction

Subglacial passageways will not always be available at the ice–bed interface. In these instances, water will move through either an englacial aquifer in the overlying ice or a subglacial aquifer below the sheet. An englacial aquifer poses unique problems in that the porosity and permeability may evolve as water freezes or melts depending on local conditions. Flow then responds not only to the change in head driving the system but also to the change in permeability with time.

Glaciers with an active hydrology have several different types of aquifers based on the form of the porosity. In the glacier surface snow, there is a multigranular porosity where meltwater percolates through the snow (*e.g.,* Illangasekare *et al.*, 1990; Pfeffer *et al.*, 1990). Veins at ice-grain boundaries are another type of porosity (Nye & Frank, 1973). Veins are found throughout most glaciers and ice sheets but contribute relatively little to the overall hydrology because they have extremely small apertures. Fractures comprise a third type of porosity. Recently, Fountain *et al.* (2005a) suggested that fractures not only dominate englacial flow but may also be the dominant hydraulic pathway through glaciers. Fractures form in glaciers for any number of reasons (*e.g.,* Hambrey & Dowdeswell, 1997; Hambrey *et al.*, 2005; Lawson, 1996), but they are commonly generated as ice flows over steep bedrock. For example, crevasses develop at Storglaciären as the ice descends bedrock riegels (Fig. 1.5) (*e.g.,* Fountain *et al.*, 2005a; Stenborg, 1973). These crevasses do not completely close, creating an ubiquitous fracture network. These fractures are expected to govern water flow within an englacial system.

There are only a few existing models of englacial water flow. Nye (1976) discussed flow in veins. He provided a physical and thermodynamic formulation of water flow through veins. Hutter (1982) developed a model of ice flow and water transport within the cold and temperate portions of an ice sheet. His formulation of the temperate ice touched on the mass and momentum balances of the water and ice as well as the jump conditions at the phase boundary. Fowler (1984) added to Hutter's work by including a formal heat balance for the temperate ice. Fowler's work is particularly interesting because of this feature. Flowers & Clarke (2002a) created a vertically integrated model of englacial water flow through fractures. I expand upon Fowler's work with the intention of simulating flow in fractures. Water temperature, pore space, and permeability evolution are of particular interest. Because there may be supercooled water at the base of a glacier, this water may be able to move upward, freezing to block pore space. Alternatively, warmer englacial water may move downward, curbing subglacial supercooling. These two scenarios illustrate how the englacial hydrology may affect the subglacial hydrology or vice versa. Much of this chapter focuses on the derivation of appropriate relationships to expand previous work to be able to investigate hydrologic scenarios pertinent to glaciohydraulic supercooling.

5.2 Balance laws

Chapter 2 featured steady-state and time-dependent variations of three balance laws: mass, momentum, and thermal energy. For an englacial system, the balance laws closely parallel a subglacial water system. However, the balance of momentum is the most important because it leads to Darcy's law.

5.2.1 Momentum balance

Darcy's law governs the mass and momentum balance for flow in a porous medium,

$$\mathbf{q}^{\mathrm{w}} = -\frac{K_H^{\mathrm{w}}}{\rho^{\mathrm{w}} g}\nabla\phi^{\mathrm{w}}, \tag{5.1a}$$

$$K_H^{\mathrm{w}} = \frac{k\rho^{\mathrm{w}} g}{\mu}, \tag{5.1b}$$

where $\mathbf{q}^{\mathrm{w}}$ is the specific discharge of water vector, K_H^{w} is the hydraulic conductivity, k is the permeability, and μ is the static viscosity of water. The hydraulic potential assumes its usual form, $\phi^{\mathrm{w}} = \rho^{\mathrm{w}} g z + p^{\mathrm{w}}$ (eq. 2.23).

A melt rate term must be included in the momentum equation prior to applying the simplifying assumptions inherent in Darcy's law. Where the pore space is changing with time, equation (5.1a) may not provide a proper balance. The goal of expanding the momentum equation is to alter Darcy's law for a change in pore space via melting or freezing. Alternatively, inclusion of a melt rate may not warrant a change in Darcy's law. Either conclusion is useful.

The material derivative of linear momentum per unit volume is given by,

$$\rho^{\mathrm{w}}\frac{\partial \mathbf{u}^{\mathrm{w}}}{\partial t} + \rho^{\mathrm{w}}\mathbf{u}^{\mathrm{w}}\cdot\nabla\mathbf{u}^{\mathrm{w}} = -(m_v - d_v)\mathbf{u}^{\mathrm{w}} - \nabla\phi^{\mathrm{w}} - \frac{P^{\mathrm{w}}\tau_0}{S}, \tag{5.2}$$

where $\mathbf{u}^{\mathrm{w}}$ is the velocity vector of the water through a cross section S, m_v is a volumetric melt rate, d_v is a pore closure rate via viscous deformation of ice, τ_0 is the shear along the hydraulic perimeter P^{w}. The right hand side represents an impulse from melt $-m_v\mathbf{u}^{\mathrm{w}}$, an impulse from moving ice $d_v\mathbf{u}^{\mathrm{w}}$, a change in potential $\nabla\phi^{\mathrm{w}}$, and a loss in momentum from the water flowing within the matrix $P^{\mathrm{w}}\tau_0/S$. The hydraulic perimeter P^{w} is related to the surface area of the pore space. The melt rate m_v is positive when matrix ice melts or negative when pore water freezes.

Because flow is predominantly slow and steady and $\partial\mathbf{u}^{\mathrm{w}}/\partial t$ is usually assumed small, the left hand side of (5.2) can be neglected. Recognizing that Darcy's law is a balance between hydraulic potential and dissipation from shear, the shear term in equation (5.2) can be approximated using equation (5.1a),

$$-(m_v - d_v)\mathbf{u}^{\mathrm{w}} - \nabla\phi^{\mathrm{w}} - \frac{\rho^{\mathrm{w}} g}{K_H^{\mathrm{w}}}\mathbf{q}^{\mathrm{w}} = 0. \tag{5.3}$$

Rewriting this equation for the specific discharge gives

$$\mathbf{q}^{\mathrm{w}} = -\frac{K_H^{\mathrm{w}}}{\rho^{\mathrm{w}} g}\Big\{(m_v - d_v)\,\mathbf{u}^{\mathrm{w}} + \nabla\phi^{\mathrm{w}}\Big\}. \tag{5.4}$$

Equation (5.4) is further simplified substituting the pore water velocity with $\mathbf{q}^{\mathrm{w}}/n_p^{\mathrm{i}}$. A simplified expression for specific discharge with the momentum source terms is

$$\mathbf{q}^{\mathrm{w}} = -\frac{K_H^{\mathrm{w}}}{\rho^{\mathrm{w}} g\left\{1 + \dfrac{K_H^{\mathrm{w}}\,(m_v - d_v)}{\rho^{\mathrm{w}} g n_p^{\mathrm{i}}}\right\}}\nabla\phi^{\mathrm{w}}. \tag{5.5}$$

If the melt rate is zero, equation (5.5) reverts to Darcy's law (eq. 5.1a). In practice, the impulse term should be negligible such that the product $K_H^{\mathrm{w}}\left(m_v - d_v\right)/(\rho^{\mathrm{w}} g n_p^{\mathrm{i}}) \ll 1$, making Darcy's law in its original form a satisfactory approximation. The net result is that Darcy's law should hold for an aquifer in which the melt rate is much smaller than the flow rate. If the melt rate is much greater than the flow rate, then equation (5.2) must be used.

5.2.2 Mass balance

The total mass balance is the sum of the mass fractions of the ice and water components of the aquifer (*e.g.,* Hutter, 1982). Furthermore, balances for each of the mass fractions can be separated. In a similar form to the subglacial mass balance equations, the englacial ice balance becomes the porosity evolution equation, and the water mass balance helps to define the pressure evolution equation. The total water mass is simply the sum of the mass of water over the domain,

$$M^{\mathrm{w}} = \int_V n_p^{\mathrm{i}} \rho^{\mathrm{w}}\, dV, \tag{5.6}$$

where M^{w} is the mass of water in a volume of aquifer V. Moving equation (5.6) from a total mass to a local balance and expanding the material derivative gives

$$\frac{\partial(\rho^{\mathrm{w}} n_p^{\mathrm{i}})}{\partial t} + \nabla\cdot(\rho^{\mathrm{w}} n_p^{\mathrm{i}} \mathbf{u}^{\mathrm{w}}) \;\; = \;\; m_v - d_v, \tag{5.7}$$

where d_v is the deformation rate of the ice. Deformation acts to close the pore space, and d_v could also be called a closure rate. Because I am not interested in ice flow, the deformation rate behaves as a source term, contracting the local water volume when there is a stress difference between the water and ice. The deformation rate of the ice displaces water but at a volume equivalent to the mass of ice displaced. There is another form of equation (5.7) in which the moisture flux is included as a source term; however the moisture flux will result from the divergence term in the present formulation.

Converting equation (5.7) to an equation governing the evolution of the pore space yields

$$\frac{\partial n_p^{\mathrm{i}}}{\partial t} = \frac{(m_v - d_v)}{\rho^{\mathrm{w}}} - \frac{n_p^{\mathrm{i}}}{\rho^{\mathrm{w}}}\frac{\partial \rho^{\mathrm{w}}}{\partial t} - \frac{1}{\rho^{\mathrm{w}}}\nabla\cdot(\rho^{\mathrm{w}}\mathbf{q}^{\mathrm{w}}). \tag{5.8}$$

While the variation of density in time and space is negligible in most cases, it must be left in (5.8) until the pressure equation is developed.

The global form of the mass balance, the local balance, and the resulting equation governing the porosity evolution for ice are similar to equations (5.6), (5.7), and (5.8),

$$M^{\mathrm{i}} = \int_V \left(1 - n_p^{\mathrm{i}}\right)\rho^{\mathrm{i}}\, dV, \tag{5.9a}$$

$$\frac{\partial\left\{\rho^{\mathrm{i}}(1 - n_p^{\mathrm{i}})\right\}}{\partial t} = -\, m_v + d_v, \tag{5.9b}$$

$$\frac{\partial n_p^{\mathrm{i}}}{\partial t} = -\,\frac{1}{\rho^{\mathrm{i}}}\left\{-m_v + d_v - \left(1 - n_p^{\mathrm{i}}\right)\frac{\partial \rho^{\mathrm{i}}}{\partial t}\right\}. \tag{5.9c}$$

In this formulation, the ice is assumed to be static, with the exception of the local deformation rate on the right hand side. The production terms on the right hand side of equations (5.7) and

(5.9b) sum to zero, indicating that the local mass balance is zero for the englacial aquifer and matrix.

The change in density with pressure varies according to

$$\rho^{\mathrm{w}} = \rho_0^{\mathrm{w}} \exp\Big\{\gamma^{\mathrm{w}} \left(p^{\mathrm{w}} - p_0^{\mathrm{w}}\right)\Big\}, \tag{5.10}$$

which is an equation of state. In equation (5.10), the reference values p_0^{w} and ρ_0^{w} are taken as atmospheric pressure and the water density at atmospheric pressure, respectively. The coefficient γ^{w} is the compressibility of water. Taking the derivative of equation (5.10) gives the time evolution equation of the water density,

$$\frac{\partial \rho^{\mathrm{w}}}{\partial t} = \rho^{\mathrm{w}} \gamma^{\mathrm{w}} \frac{\partial p^{\mathrm{w}}}{\partial t}. \tag{5.11}$$

The equation of state for ice is similar and varies according to

$$\rho^{\mathrm{i}} = \rho_0^{\mathrm{i}} \exp\Big\{\gamma^{\mathrm{i}} \left(p^{\mathrm{i}} - p_0^{\mathrm{i}}\right)\Big\}, \tag{5.12a}$$

$$\frac{\partial \rho^{\mathrm{i}}}{\partial t} = \rho^{\mathrm{i}} \gamma^{\mathrm{i}} \frac{\partial p^{\mathrm{i}}}{\partial t}, \tag{5.12b}$$

where ρ_0^{i} is the reference ice density at the reference ice pressure p_0^{i}, and γ^{i} is the bulk compressibility of ice. These reference values are the density of ice at atmospheric pressure and atmospheric pressure, respectively. The pressure in this case is the stress exerted on the ice frame. Using a pressure in the equation of state necessitates that the stress state be isotropic. If the ice were deforming viscously, strictly speaking, the stress tensor would not be isotropic, but the isotropic case would provide a reasonable approximation. In addition, the compressibility of the porous ice matrix is not that of pure ice. This compressibility should be lower than that of pure ice but should converge to the value of ice as the porosity approaches zero.

Expanding equations (5.8) and (5.9c) and solving them for $(m_v - d_v)$ gives two equivalent equations. Setting these equations equal and substituting the derivatives of the equations of state for the change in water and ice density gives an evolution equation for the pressures,

$$n_p^{\mathrm{i}} \gamma^{\mathrm{w}} \frac{\partial p^{\mathrm{w}}}{\partial t} + (1 - n_p^{\mathrm{i}}) \gamma_e^{\mathrm{i}} \frac{\partial p^{\mathrm{i}}}{\partial t} = -\frac{1}{\rho^{\mathrm{w}}} \nabla \cdot (\rho^{\mathrm{w}} \mathbf{q}^{\mathrm{w}}) - \left(\rho^{\mathrm{w}} - \rho^{\mathrm{i}}\right) \frac{\partial n_p^{\mathrm{i}}}{\partial t}, \tag{5.13}$$

where γ_e^{i} is the effective compressibility of the ice matrix. While the values of the pressure in the ice and water may be different, if there are no changes in the aquifer, then locally $\partial p^{\mathrm{w}}/\partial t = \partial p^{\mathrm{i}}/\partial t$; and equation (5.13) can be solved for the water pressure,

$$\frac{\partial p^{\mathrm{w}}}{\partial t} = -\frac{1}{\rho^{\mathrm{w}} \left\{n_p^{\mathrm{i}} \gamma^{\mathrm{w}} + (1 - n_p^{\mathrm{i}}) \gamma_e^{\mathrm{i}}\right\}} \left\{\nabla \cdot (\rho^{\mathrm{w}} \mathbf{q}^{\mathrm{w}}) + \left(\rho^{\mathrm{w}} - \rho^{\mathrm{i}}\right) \frac{\partial n_p^{\mathrm{i}}}{\partial t}\right\}. \tag{5.14}$$

Bear (1988, p. 204) derived a similar form of this equation without source terms. Equation (5.14) is also reminiscent of the equation for water flow in a deforming medium (*e.g.,* Domenico & Schwartz, 1997, p. 463), but there are two large differences. In water flow in a deforming medium, the matrix has a velocity; and the material derivative is not equal to a source term. If a flowing ice matrix is also incorporated into the present formulation, then the deforming matrix and the pore space change via melt/freezing would both be necessary and the equations would be slightly different.

With both the equation for the evolution of the porosity and the evolution of pressure in hand, one final assumption can be made: that the local change in density is negligible. This assumption simplifies equations (5.9c) and (5.14) to

$$\frac{\partial n_p^{\mathrm{i}}}{\partial t} = \frac{m_v - d_v}{\rho^{\mathrm{i}}}, \tag{5.15a}$$

$$\frac{\partial p^{\mathrm{w}}}{\partial t} = -\frac{1}{n_p^{\mathrm{i}}\gamma^{\mathrm{w}} + (1 - n_p^{\mathrm{i}})\gamma_e^{\mathrm{i}}} \left\{ \nabla \cdot \mathbf{q}^{\mathrm{w}} + \left(1 - \frac{\rho^{\mathrm{i}}}{\rho^{\mathrm{w}}}\right) \frac{\partial n_p^{\mathrm{i}}}{\partial t} \right\}. \tag{5.15b}$$

The mass balance for the water is not used for the evolution of the porosity for the simple reason that the ice matrix defines the porosity. Inclusion of the divergence of the flux helps to determine the pressure and would, essentially, be double counted if used in the porosity evolution equation. While the change in the porosity is expected to be small, one weakness of this formulation is that the mass balance of the ice should be fully coupled to ice flow, especially for the viscous deformation term. This coupling is well beyond the scope of the present work, but equation (5.15b) is a reasonable approximation because the hydraulic system responds much more quickly than the ice flows.

5.2.3 Energy balance

The thermal energy balance can be broken into parts in a fashion similar to the mass balance equation. In this case, the mixture of water and ice is the sum of the constituent balances. With the porosities expected to be low, the mixture temperature T should be close to the ice temperature T^{i}. Below the water table, water content at Falljökull, Iceland, for example, is commonly 2–4% (Murray *et al.*, 2000), indicating that the bulk temperature is controlled by the temperate ice. Because neither the mixture temperature nor the ice temperature will vary significantly near the melting point, the total heat of the water must be determined independently of the mixture heat. The water sheet below the ice and the boundary condition at the surface of the glacier will affect the temperature of the water.

The temperature evolution of the ice fraction may be important, but the suspicion is that the ice temperature change is not important. Sensible heats near the freezing point are typically orders of magnitude smaller than latent heat terms. In order to simplify the problem, I assume that the ice is isothermal and at the melting point, as is commonly observed at many temperate glaciers. I thus ignore the thermal energy balance of the ice entirely. Other formulations for polythermal glaciers exist (*e.g.,* Fowler, 1984; Hutter, 1982) but are beyond the scope of the present work.

Using elements of the derivations of Fowler (1984) and Spring & Hutter (1982), the total internal energy of the water E^{w} in the pore space is

$$E^{\mathrm{w}} = \int_V \rho^{\mathrm{w}} n_p^{\mathrm{i}} \varepsilon^{\mathrm{w}} \, dV, \tag{5.16}$$

where the internal energy density can be approximated as $\varepsilon^{\mathrm{w}} = c_p^{\mathrm{w}} \Delta T_{\mathrm{mp}} + L$. This approximation neglects the kinetic energy as well as any variations in the kinetic energy. For Darcian flow, ignoring the kinetic energy is justified. Moving equation (5.16) from a total internal energy to

a local energy balance yields,

$$\rho^{\mathrm{w}} c_p^{\mathrm{w}} n_p^{\mathrm{i}} \frac{dT^{\mathrm{w}}}{dt} = \rho^{\mathrm{w}} c_p^{\mathrm{w}} n_p^{\mathrm{i}} \frac{\partial T^{\mathrm{w}}}{\partial t} + \rho^{\mathrm{w}} c_p^{\mathrm{w}} \mathbf{q}^{\mathrm{w}} \cdot \nabla T^{\mathrm{w}}, \tag{5.17a}$$

$$= -\left(m_v - d_v\right)\left(L + c_p^{\mathrm{w}} \Delta T_{\mathrm{mp}}\right) + \frac{\rho^{\mathrm{w}} g}{n_p^{\mathrm{i}} K_H^{\mathrm{w}}} \left(q^{\mathrm{w}}\right)^2, \tag{5.17b}$$

where q^{w} is the magnitude of the water flux vector. Both the momentum balance (eq. 5.1) and the mass balance (eq. 5.7) have been used to simplify these local balances. The only source term is the final term on the right hand side of equation (5.17b), which represents viscous dissipation. Because of Darcy's law, the viscous dissipation can also be written as $K_H^{\mathrm{w}}(\nabla\phi^{\mathrm{w}})^2/(n_p^{\mathrm{i}}\rho^{\mathrm{w}} g)$. Other source terms, such as diffusion of heat through the water via Fourier's law is omitted because porosity is low. Rewriting equations (5.17) as an englacial temperature evolution equation yields,

$$\frac{\partial T^{\mathrm{w}}}{\partial t} = -\frac{\mathbf{q}^{\mathrm{w}}}{n_p^{\mathrm{i}}} \cdot \nabla T^{\mathrm{w}} - \frac{m_v - d_v}{\rho^{\mathrm{w}} c_p^{\mathrm{w}} n_p^{\mathrm{i}}}\left(L + c_p^{\mathrm{w}} \Delta T_{\mathrm{mp}}\right) + \frac{g}{c_p^{\mathrm{w}} K_H^{\mathrm{w}}}\left(\frac{q^{\mathrm{w}}}{n_p^{\mathrm{i}}}\right)^2. \tag{5.18}$$

This equation is qualitatively similar to equation (2.29).

5.3 Pore geometry

Numerous attempts have been made to relate hydraulic conductivity, permeability, and porosity (*e.g.,* Bear, 1988, chap. 5). Specifically, researchers have attempted to link physical models of different pore geometries to Darcy's law. The goal is to be able to say how the hydraulic conductivity varies with a change in the pore volume. A relationship between porosity and hydraulic conductivity is necessary to close the mass balance and momentum equations.

Flowers & Clarke (2002a) chose the intersecting fracture model of Snow (1968). This model has several advantages. Snow's model is relatively simple in its treatment of both the geometry and the flow physics. In addition, because englacial hydrology is expected to be a fracture network, Snow's model is immediately relevant.

The hydraulic conductivity of a network of intersecting fractures is

$$K_H^{\mathrm{w}} = \frac{\rho^{\mathrm{w}} g}{\mu} \frac{F_\ell b^3}{12}, \tag{5.19}$$

where F_ℓ is a number of fractures per unit length, and b is an average fracture width (Snow, 1968; Flowers & Clarke, 2002a). The porosity is the average fracture width multiplied by the number density:

$$n_p^{\mathrm{i}} = F_\ell b. \tag{5.20}$$

These relationships are strictly for laminar flow between two approximately parallel-sided fracture walls. Snow (1968) originally applied this relationship to horizontal packer tests of crystalline rocks with low permeability and porosity. He suggested that the maximum fracture size be less than two millimeters. Furthermore, equation (5.19) assumes that all of the fractures are hydraulically conductive. For Storglaciären, Sweden, approximately half the fractures are hydraulically conductive with remaining fractures storing water (Fountain *et al.*, 2005b). In consequence, equation (5.19) represents an upper limit of englacial hydraulic conductivity. It is possible to reduce the hydraulic conductivity by multiplying equation (5.19) by the fraction of active fractures.

Of the three quantities in equation (5.20) that describe the hydraulic properties of the ice, F_ℓ is the most problematic. Recently, Hambrey conducted a study of fractures at Trapridge Glacier, Yukon Territory, Canada. He found that fracture densities ranged from 0.6–2.6 m^{-2} ($\simeq$0.8–1.6 m^{-1}) (pers. comm., 2006). Fracture densities for the terminus of Matanuska Glacier most likely fall at the lower end of these values, and fracture densities for the overdeepenings of Storglaciären can be significantly less. Between the other two remaining parameters n_p^{i} and b, the porosity of the ice below the water table is better constrained and can range from approximately 0.01 to 0.10 (Pettersson *et al.*, 2004, and references therein). Fracture widths are difficult to ascertain because hot water drilling often enlarges the fracture before it is measured (*e.g.,* Fountain *et al.*, 2005b). However, these are constrained to a maximum of 2 mm as noted above.

Rather than evolve the number density of fractures, which would require additional conditions for fracture opening and closing, it is preferable to continue simply with the thermal evolution of crack width. From (5.20), the time evolution of the porosity becomes,

$$\frac{dn_p^{\mathrm{i}}}{dt} = F_\ell \frac{db}{dt}, \tag{5.21}$$

where the additional $b\,dF_\ell/dt$ is intentionally absent from the right hand side. Without a change in the number density of fractures with time, this number density becomes a constant; and the change in porosity is directly linked to the change in fracture width. The evolution of the fracture width can be calculated from equations (5.15b) and (5.20).

5.3.1 Creep closure rate

Nye (1953) explored the viscous creep of isotropic ice using Glen's power law for ice rheology (Glen, 1954). Nye used these relations to show how cylindrical holes, spherical holes, and conduits in ice close. The extension to an isotropically closing fracture in ice is not necessarily straightforward given that the divergence terms in a circular, spherical, or cylindrical coordinate system lend themselves immediately to solution via separation of variables (Nye, 1953).

Assuming incompressibility and that tractions are negligible, the strain rate tensor for a crack becomes $\partial u/\partial x = -\partial u/\partial z = 0$. This relationship implies that the closure rate is independent of crack width and depends only on the pressure difference between the ice and the water. However, experience gained from conduit closure suggests that the hydraulic cross section does matter. For example, Ng (1998, chap. 3) derived a closure relationship for elliptical channels, but a complementary derivation is beyond the scope of this work. Rather, it will be more useful to parameterize both Ng and Nye's work with respect to fractures in a porous medium. Considering Nye's (1953) relationship for contraction of a tunnel in ice and rewriting it for the change in the diameter of that tunnel yields a one-dimensional closure rate,

$$\frac{db}{dt} = -b \operatorname{sgn}\left(p^{\mathrm{i}} - p^{\mathrm{w}}\right) \left(\frac{|p^{\mathrm{i}} - p^{\mathrm{w}}|}{n\mathcal{B}} \right)^n, \tag{5.22}$$

which is similar to the closure term in equation (2.17). Given that a circular aperture should close faster than a long fracture because of the circular convergence of the ice, this relationship would provide a reasonable upper bound for the closure of a fracture. Conversely, if the fractures are opening via deformation of the ice, then this relationship will overestimate the change. Arguably, a shape factor could be inserted into (5.22) to account for the change in cross section. The pressure of the ice in equation (5.22) is simply the ice overburden pressure, $p^{\mathrm{i}} = \rho^{\mathrm{w}} g \left(z^{\mathrm{i}} - z\right)$.

From equations (5.21),and (5.22) the closure rate d_v becomes,

$$d_v = \rho^{\mathrm{i}} n_p^{\mathrm{i}} \operatorname{sgn}\left(p^{\mathrm{i}} - p^{\mathrm{w}}\right) \left(\frac{|p^{\mathrm{i}} - p^{\mathrm{w}}|}{n\mathcal{B}}\right)^n, \tag{5.23}$$

where ρ^{i} corrects the units for equation (5.15a). Equation (5.23) arbitrarily takes closure to be positive when fracture apertures are decreasing (i.e., closing).

5.3.2 Volumetric melt rate

Heat transfer in laminar flow regimes has been well-studied. Analytic solutions for both the flow distribution and the temperature distribution have been derived for Hagen-Poiseuille flow through tubes and laminar flow between flat plates. Pigford (1955, eq. 32) gave the heat transfer coefficient for nonisothermal conditions for a tube,

$$h = \frac{1.27}{2R} \left(\frac{S\rho^{\mathrm{w}} c_p^{\mathrm{w}} K_T^{\mathrm{w}} u^{\mathrm{w}}}{s}\right)^{\frac{1}{2}}$$

where R is the radius of the tube, s is its length, and S is its cross-sectional area. If the transverse length of a fracture can be taken as equivalent to its height, then an equivalent relation for plane-parallel fractures is

$$h = 1.27 \left(\frac{\rho^{\mathrm{w}} c_p^{\mathrm{w}} K_T^{\mathrm{w}} q^{\mathrm{w}}}{n_p^{\mathrm{i}} b}\right)^{\frac{1}{2}}. \tag{5.24}$$

Equation (5.24) is the heat transfer coefficient for only one crack. Multiplying this equation by F_ℓ yields the heat transfer density.

Substituting the heat transfer density into equation (2.33b) yields the volumetric melt rate,

$$m_v = 1.27 \left(\frac{\rho^{\mathrm{w}} c_p^{\mathrm{w}} K_T^{\mathrm{w}} q^{\mathrm{w}}}{n_p^{\mathrm{i}} b}\right)^{\frac{1}{2}} \frac{F_\ell \Delta T_{\mathrm{mp}}}{L}. \tag{5.25}$$

The temperature difference is simply that of the interstitial water and the melting point, with the melting point governed by the Clausius-Clapeyron equation (eq. 2.8). The melting point is dependent on the interfacial pressure between the water and the ice.

5.4 Aquifer thickness evolution

At the top of the englacial aquifer, water may leave or enter the glacier, depending on the availability of water and the saturation of the ice. Water can also enter the aquifer from the sheet or conduit at the base of the glacier. These two sources of water as well as the flow of water within the englacial aquifer may cause the total thickness of the aquifer to change height. Figure (5.1) shows the conceptual configuration of the englacial aquifer where the thickness of the aquifer is defined as $Z^{\mathrm{e}} = z^{\mathrm{e}} - z^{\mathrm{b}}$. This figure complements figure (2.1) in defining the different geometrical quantities.

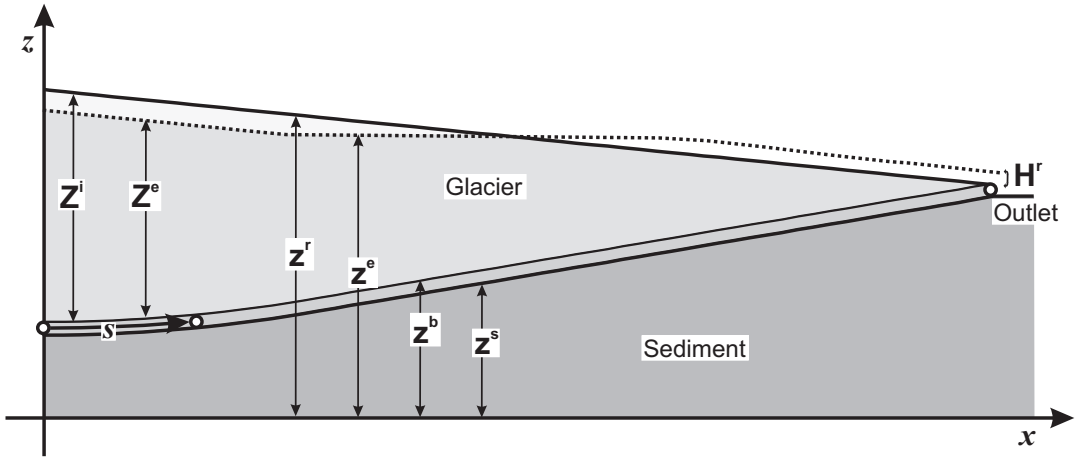

Figure 5.1: Schematic englacial aquifer. Front of the section presented in Figure 1.3. Dotted line indicates the height of the water table. From left to right: Z^{i} is the glacier thickness. Z^{e} is the englacial aquifer thickness. z^{r} is the height of the glacier surface. z^{e} is the height of the englacial water table. z^{b} is the height of the base of the glacier. z^{s} is the height of the base of the water layer. H^{r} is the thickness of water above z^{r}. If $H^{\mathrm{r}} > 0$, then $z^{\mathrm{e}} = z^{\mathrm{r}}$. In this illustration, the front of the glacier has a seepage face.

5.4.1 Water table evolution

The rate of change of englacial water table elevation z^{e}, is a kinematic boundary problem. The formulation is well known (*e.g.,* Fowler, 1997, pp. 79–80),

$$\frac{\partial z^{\mathrm{e}}}{\partial t} = q_z^{\mathrm{w}} - q_x^{\mathrm{w}} \frac{\partial z^{\mathrm{e}}}{\partial x} + q_z^{\mathrm{r}}, \tag{5.26}$$

where all values are valid on the boundary. Equation (5.26) holds for cases of the change in the water table elevation is below the surface of the glacier.

When the englacial water table reaches or exceeds the surface of the glacier, there is no condition on equation (5.26) to either keep the water table at the surface or restore the water table to the surface. As a result, there will need to be a condition that restores the water table to the surface of the glacier when it is exceeded. A penalty function forces the englacial system to monotonically approach the surface of the glacier once the water table has exceeded an arbitrary elevation,

$$\frac{\partial z^{\mathrm{e}}}{\partial t} = \frac{1}{\tau^{\mathrm{r}}} \left(z^{\mathrm{i}} - z^{\mathrm{e}} \right), \tag{5.27}$$

where τ^{r} is an arbitrary time constant. Flowers & Clarke (2002a) used a similar formulation to describe the exchange of water between the en- and supraglacial water systems instead of a form of Darcy's law (eq. 5.28). Penalty functions are a mode of mitigating inconsistencies between a physical formulation and necessary simplifications. In this instance, the physical formulation allows the water table to exceed the glacier surface, which is not realistic. Other methods of solving the confined kinematic boundary problem exist, and equation (5.27) is simply numerically expedient.

5.4.2 Surface boundary

The boundary at the glacier surface is phreatic with the fluid pressure set to atmospheric pressure, if there is no supraglacial flow at the surface of the glacier. If there is water flow at the surface then conditions are assumed for the flow of water into the ice. No attempt is made to model the capillary fringe above the phreatic surface, nor is any attempt made to capture the full physics of fluid flow in the snowpack, firn, or unsaturated zone in general.

There are two options for the surface boundary: the water table is at the surface of the glacier or the water table is below the surface of the glacier. If the water table is at the surface of the glacier, then the pressure condition on the aquifer surface is simply atmospheric if there is no surface water at the surface. If there is water on the glacier surface, then the pressure condition is taken as the height of the surface water layer. These pressure conditions affect the surface formulation of Darcy's law,

$$q^{\mathrm{w}}_{z=z^{\mathrm{e}}} = -\frac{K^{\mathrm{w}}_H}{\rho^{\mathrm{w}} g}\frac{\partial \phi^{\mathrm{r}}}{\partial z}\,, \tag{5.28}$$

where $\partial\phi^{\mathrm{r}}/\partial z$ is the hydraulic potential difference across the surface of the water table. This hydraulic potential does not have a pressure component when when there is not a supraglacial water system.

In some cases, there may be a perched aquifer on the surface of the glacier. For example, meltwater ponds form at the surface when water flows over the surface of the glacier but cannot drain through moulins, fractures, or other drainage features. If the flux of water across the surface of a glacier is greater than the flux from the surface to the englacial system, then there may be a perched aquifer feeding the englacial aquifer. In terms of the Darcian model presented here, the flux of water to the englacial system may be approximated as,

$$q^{\mathrm{r}}_z = \begin{cases} -K^{\mathrm{w}}_H \left(\dfrac{H^{\mathrm{r}}}{z^{\mathrm{i}} - z^{\mathrm{e}}} + 1 \right) & \text{for} \quad H^{\mathrm{r}} > 0, \\ 0 & \text{for} \quad H^{\mathrm{r}} = 0, \end{cases} \tag{5.29}$$

where q^{r}_z is the vertical water flux at the glacier surface and H^{r} is the thickness of the supraglacial water system. If there is no supraglacial system, there is no flux from the surface. Rather than model the unsaturated zone explicitly, I assume that water is instantaneously added to the water table with an amount governed by Darcy's law. Because the unsaturated zone has a pressure equal to atmospheric pressure, the pressure difference is approximated by the hydrostatic pressure at the base of the supraglacial water layer taken over the height of the unsaturated zone (upper condition in (5.29)). If there is no surface water layer, then this term decays to zero. If there is no unsaturated zone such that the englacial water height is equal to the surface elevation of the ice, $z^{\mathrm{e}} = z^{\mathrm{i}}$, then q^{r}_z takes the form of equation (5.28).

In groundwater applications, the hydraulic conductivity of the unsaturated zone is generally lower than that of the saturated medium. Because equation (5.19) relates flow through a parallel fracture, it is not immediately clear what part of the physics should be altered. To compensate, the unsaturated zone hydraulic conductivity will be the equivalent saturated hydraulic conductivity multiplied by an arbitrary retarding coefficient.

If water emerges at the surface of the glacier, then the water may flow supraglacially. Typically, water will form streams at the surface of the glacier in a way similar to subaerial streams. Because these streams are not of particular interest here, water flow on the glacier surface is

handled as a diffusive flux in the same fashion as Flowers & Clarke (2002a),

$$\frac{\partial H^{\mathrm{r}}}{\partial t} = -\nabla \cdot (\mathbf{u}^{\mathrm{r}} H^{\mathrm{r}}) + q_z^{\mathrm{r}}, \tag{5.30a}$$

$$\mathbf{u}^{\mathrm{r}} = -\mathbf{K}_H^{\mathrm{r}} \nabla \left(Z^{\mathrm{i}} + H^{\mathrm{r}} \right), \tag{5.30b}$$

where $\mathbf{u}^{\mathrm{r}}$ is the surface velocity, and $\mathbf{K}_H^{\mathrm{r}}$ is the surface hydraulic conductivity tensor. Surface energy balance terms and precipitation terms can be added to this balance for a more inclusive surface hydrology (Flowers & Clarke, 2002a). These terms are avoided here.

Streams preferentially move water directly downhill on glaciers, melting out supraglacial stream beds. As a consequence, the hydraulic conductivity tensor in equation (5.30b) is rarely isotropic. However, because this relationship is used only to accommodate water flow, I assume that the conductivity is isotropic in the same manner as Flowers & Clarke (2002a).

5.4.3 Subglacial boundary

The lower boundary is the water layer. Flux into the aquifer is governed by Darcy's law applied at the base of the glacier. This water flux not only provides water to the englacial aquifer, but drains water from the subglacial sheet. Obviously, water can flow from the englacial aquifer to the water layer or in the reverse direction, depending on the hydraulic potential gradient. There is no necessary flow boundary condition at the lower bound except the pressure condition, which is simply the water pressure in the sheet. The mass of water in the subglacial sheet will be governed by equation (5.31a) while the flux into the base of the aquifer is governed by its negative in equation (5.31b),

$$\frac{\partial H^{\mathrm{b}}}{\partial t} = -\frac{K_H^{\mathrm{w}}}{\rho^{\mathrm{w}} g} \frac{\partial \phi^{\mathrm{w}}}{\partial z}, \tag{5.31a}$$

$$q_z^{\mathrm{b}} = \frac{K_H^{\mathrm{w}}}{\rho^{\mathrm{w}} g} \frac{\partial \phi^{\mathrm{w}}}{\partial z}. \tag{5.31b}$$

The pressure difference governing the flux is simply the difference in pressure between the sheet and the aquifer. Similarly, temperature can be imported or exported depending on the water flux. Both the pressure and temperature are Dirichlet conditions in that they are specified at the boundary of the aquifer as the conditions in the sheet. These boundary conditions are not dependent on a transition from laminar to turbulent flow when the water leaves the aquifer and enters the sheet or the converse when water leaves the sheet and enters the aquifer.

Melting or accretion of ice by the subglacial water will either expand or contract the aquifer at its base. This accretion is described by the melt rate equation for the subglacial sheet,

$$\frac{dz^{\mathrm{b}}}{dt} = -\frac{\tilde{m}}{\left(1 - n_p^{\mathrm{i}}\right) \rho^{\mathrm{i}}}. \tag{5.32}$$

This equation is the same as equation (2.18) presented for the glacier thickness; however, here, the equation has a different function as a change in the height of the base of the glacier. The thickness of the englacial aquifer,

$$\frac{dZ^{\mathrm{e}}}{dt} = \frac{dz^{\mathrm{e}}}{dt} - \frac{dz^{\mathrm{b}}}{dt}, \tag{5.33}$$

is simply a derivative of the definition of the aquifer thickness. Either the ordinary or partial derivatives could be used in (5.33) because the convective velocities are zero for these terms because the glacier is assumed to be static.

5.4.4 Downstream and upstream boundaries

At the downstream end of the glacier, ice and water meet. If the water table is high enough englacially, then the glacier may have a seepage face. The condition on the seepage face is that the pressure is atmospheric. As a result, the hydraulic potential is simply the height at the outlet, with no pressure component. Computationally, this outlet is a simple Dirichlet condition on the seepage face.

The upstream boundary is also prescribed as a Dirichlet condition. This condition can vary with time, and as a result, requires a function to describe its evolution. An upstream condition is somewhat artificial because water would normally enter the glacier from the surface. The usual upstream condition would be a flux condition. For example, a zero flux at a glacier headwall, or an equivalent condition would be more physical. However, because I am only interested in sections of glaciers at this point, head will be the prescribed quantity.

5.5 Summary

Throughout this chapter, I have focused on the hydrologic and thermal evolution of the englacial aquifer. Together the three balance laws—momentum (eqs. 5.1), mass (eqs. 5.15), and energy (eq. 5.18)—provide a mathematical representation through which water flux, aquifer porosity, water pressure, and water temperature can be simulated. These formulations are subject to auxiliary conditions for creep closure of the pore space (eq. 5.23) and heat transfer between the ice and water (eq. 5.25). Boundary conditions at the surface of the glacier are based on Darcy's law (eq. 5.28) and on the conservation of water along a kinematic boundary (eq. 5.26). If the water reaches the surface of the glacier, a penalty function (eq. 5.27) limits the height of the aquifer to the glacier surface. However, water can leave the glacier to flow over the surface of the glacier via an enhanced diffusion scheme (eq. 5.30). At the base of the glacier, water can enter or exit the glacier from the sheet (eqs. 5.31). If ice is accreting, the englacial aquifer is also changing (eq. 5.32). Upstream and downstream boundaries have conditions on hydraulic potential. Together, all of these equations form an internally consistent scheme for simulating englacial water flow in temperate ice.

Chapter 6

Results and discussion

In this chapter, I illustrate some of the behaviors of the physical model using numerical simulations. This departs from previous chapters where the focus was the construction of a physical model. Details of the numerical formulation can be found in Appendix F. Because much of the theory in the previous chapters has either not been assembled in the present format or has not been developed for sub- and englacial water flow, I separate these into clear water flows (Chapter 2) and sediment laden flows (Chapter 4), but I omit water flow through an englacial aquifer (Chapter 5).

The relative importance of the terms in several of the governing equations need to be illustrated. For example, the relative importance of the energy balance terms in equations (2.29) governing the thermal evolution of the water are important. Furthermore, for parameters that require careful selection, an exhaustive search is not possible. Fortunately, an exhaustive search is also not warranted. Glaciers such as those discussed in Chapter 1 have a finite range of physical characteristics. Numerical simulations presented here capture relevant processes and rates for these physical characteristics.

6.0.1 Longitudinal sections

The subglacial water flow model is not designed to give prognostications for any particular glacier. Rather, the model is intended to diagnose and elucidate controlling processes. Ideally, simulations should capture relevant features of the physical model. Because the ice-surface slope and the bed slope are of first-order importance, suitable longitudinal sections are necessary.

Longitudinal sections from the terminal overdeepening at Matanuska Glacier are shown in Figure 6.1. Lawson *et al.* (1998) published these sections as approximate hydraulic sections. Each has a water vent emerging at its downstream end. These sections display much information, both in the surface and bed structure and also in the supercooling ratios plotted below the sections. The bed slope in these sections is often -3 to -5 times the surface slope, where negative values imply that the bed slope is adverse to flow (Figs. 6.1b,d). Therefore, these bed slopes are well-above the steady-state supercooling threshold. Surprisingly, at 50 m from the terminus, Figure 6.1c displays a ratio that is below the steady-state subglacial lake criterion of -11.0 (Clarke *et al.*, 2005, using values from Table 6.2). Obviously, simulating these sections is useful if local process-based results are desired for Matanuska Glacier.

However, the level of information in the Matanuska sections is unwarranted for elucidating the behavior of the governing equations. As an alternative, any number of parameters can be chosen for synthetic sections, and these sections have the benefit of being spatially smooth. Smoothness in space aids in the convergence of the numerical solver. Four relevant sections are shown in Figure 6.2. These sections are meant to mimic some of the features of Matanuska Glacier and other glaciers while retaining an uncomplicated structure. Relevant parameters for each of these sections appear in Table 6.1. Of these, the surface-to-bedslope ratio is the most telling. The section in Figure 6.2a has a threshold bed and surface slope ratio, -1.70, for the

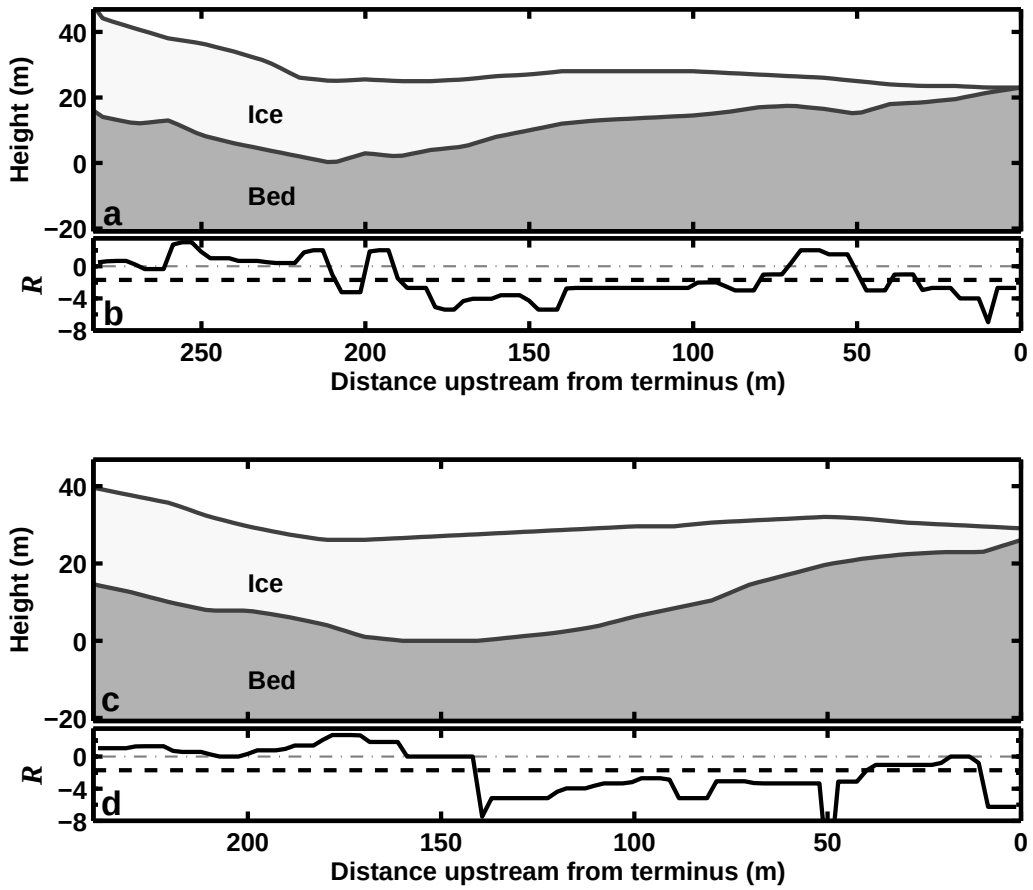

Figure 6.1: Interpreted longitudinal sections from Lawson *et al.* (1998). (a) Figure 9a from Lawson *et al.* (1998). Height=0 m is the minimum ice elevation in this figure. The aspect ratio is 1 : 1. (b) Supercooling ratio derived from bed and surface data in Fig. 6.1a. Thick dashed line is the steady-state supercooling threshold ($\mathcal{R} = -1.70$, eq. (2.44)). Values below this line indicate locations of supercooling for steady-state hydraulic conditions. Thin dot-dashed line is $\mathcal{R} = 0$. (c) Figure 9b from Lawson *et al.* (1998). Height=0 m is the minimum ice elevation in this figure. The aspect ratio is 1 : 1, but the x-axis is not the same scale as (a). (d) Same as (b) but data from Fig. 6.1b. Minimum value at 50 m is $\mathcal{R} = -15.6$.

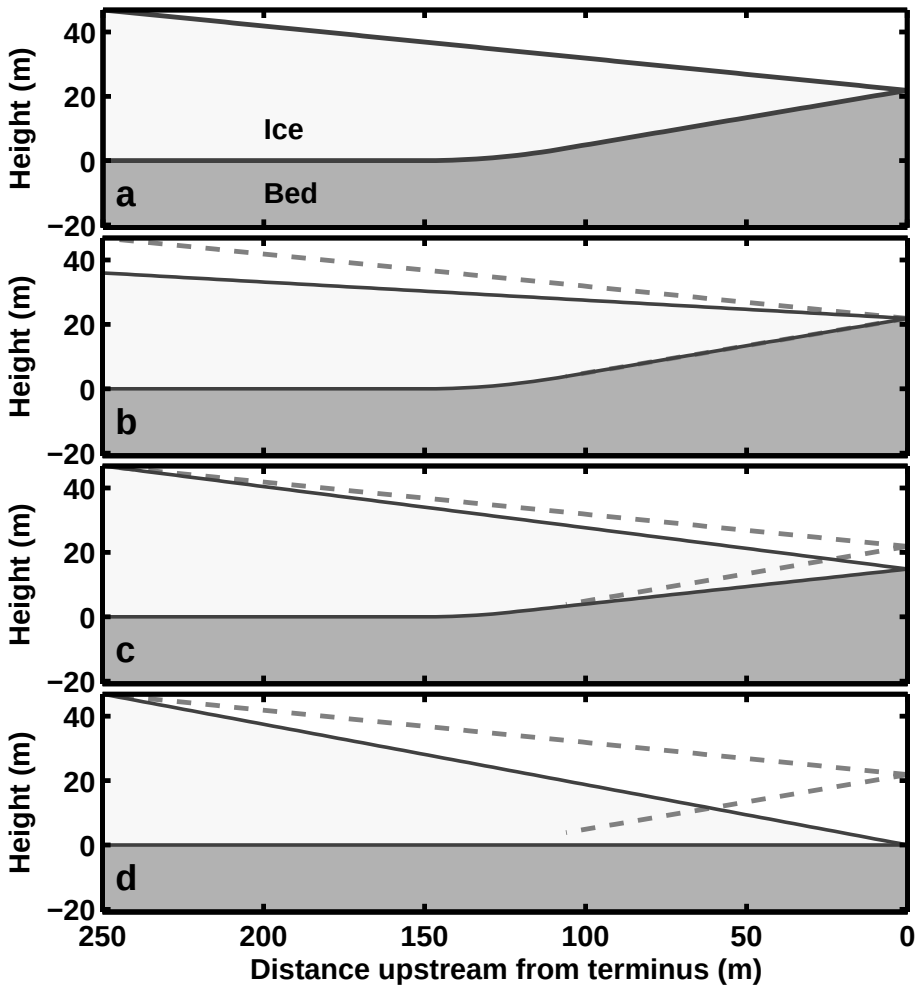

Figure 6.2: Simulated synthetic glacier sections. Subglacial water flows from left to right along the line at the interface of the ice and bed. (a) Threshold-overdeepened case with $\mathcal{R} = -1.70$ (Figs. 1.3 and A.1). (b) Overdeepened case with $\mathcal{R} = -3$, which is above the steady-state supercooling threshold.. (c) Overdeepened case with $\mathcal{R} = -0.85$, which is below the steady-state supercooling threshold. (d) Flat-bedded case. Dashed lines in (b), (c), and (d) are the surface and bed in (a). The aspect ratio is 1 : 1.

parameters listed in Table 6.2. The section in Figure 6.2b has a surface to bed slope ratio of −3.00 and a maximum ice thickness of 35.99 m. Both sections in 6.2c and 6.2d have surface to bed slope ratios that are below the steady-state threshold necessary for supercooling. These non-supercooled cases will be used to illustrate several key points. None of the synthetic sections is meant to illustrate entire glaciers. Rather, these are meant to illustrate processes occurring near a glacier terminus.

Table 6.1: Parameters used to create the synthetic glacier sections in Figure 6.2

		Threshold	Above-threshold	Below-threshold	Flat-bedded
Figure		6.2a	6.2b	6.2c	6.2d
Start of overdeepening:	x_u	150.00	150.00	150.00	n/a
Start of wedge:	x_w	107.59	107.59	122.84	n/a
Elevation at outlet:	z_0^{b}	21.85	21.85	14.82	0.00
Upstream ice thickness:	Z_l^{i}	46.86	35.99	46.86	46.86
Bed to surface slope ratio:	$\mathcal{R}$	-1.70	-3.00	-0.85	0.00
Surface slope:	$\tan\alpha^{\mathrm{r}}$	0.10	0.06	0.13	0.19
Bed slope:	$\tan\alpha^{\mathrm{b}}$	0.17	0.17	0.11	0.00

Values of x, z, and Z have units of meters. The other parameters are unitless. For all sections, the coefficient $C_x = 0.002$ m$^{1-2o_x}$, ice thickness at the outlet $Z_0^{\mathrm{i}} = 0.00$ m, the transition coefficient $o_x = 1$, the location of the downstream water outlet $x_0 = 0.00$ m, the location of the upstream water boundary $x_l = 250.00$ m, and the elevation of the upstream water boundary $z_l^{\mathrm{b}} = 0.00$ m. See Appendix A for a more detailed explanation.

6.0.2 Model details

Parameters and constants that are applicable to all model runs are presented in Table 6.2. Many of these values are well-established in the literature and need no further clarification. However, several require additional clarification. The natural variability of the pressure melting coefficient β, lies between -7.4×10^{-8} and -9.8×10^{-8} K Pa^{-1} depending on whether the water is pure or air-saturated, respectively. Alley *et al.* (1998) investigated effects of applying different values and found that the accretion rate is sensitive to β when water flux is high. More ice accretes when water is air-saturated. I thus choose a value of β that corresponds to pure water to yield conservative estimates of accretion. This value is consistent with the densities in Table 6.2 and equation (2.7).

Another parameter that deserves attention is the compressibility of the subglacial hydraulic system γ^{b}. Its physical limit is the compressibility of the mixture of water, ice, and sediment in the flowing water and should be close to the compressibility of water, 4.5×10^{-10} Pa^{-1}. Clarke (2003) noted that this parameter is essentially numerical and governs the rate of convergence of the computational scheme. However, γ^{b} does not govern accuracy. I have tested numerous values for this parameter over several orders of magnitude using the sheet version of the code, with no noticeable difference in the results. As a result, I assign γ^{b} to the value of 1.0×10^{-7} Pa^{-1} (Clarke, 2003).

The flow-law exponent n also deserves some discussion. There is evidence that n is commonly less than 2 at low driving stresses (*e.g.,* Duval *et al.*, 2000). Low effective stresses are often found

subglacially. For most examples contained within this thesis, closure is not dominated by creep. Rather, sheet closure is predominantly regelation, and creep is less important (Fig. F.5). In the case of negative effective pressures, $n = 3$ will overestimate the rate of opening for faster changes in sheet thickness. In this case, $n = 3$ provides conservative estimates of pressure response from ice closure. Thus, a higher value of n is not problematic in terms of the model. Furthermore, smaller values of n can be substituted easily into the formulation presented in Chapter 3.

Table 6.2: Model parameters

Parameter	Value	Units	Notes
Physical constants:			
$\mathcal{A}$	6.8×10^{-24}	$\text{Pa}^{-n}\ \text{s}^{-1}$	Flow law coefficient (Paterson, 1994, p. 97)
c_p^{w}	4217.6	$\text{J kg}^{-1}\ \text{K}^{-1}$	Specific heat of water at constant pressure
g	9.81	m s^{-2}	Gravitational acceleration
K_T^{w}	0.5610	$\text{W m}^{-1}\ \text{K}^{-1}$	Thermal conductivity of water
L	3.336×10^5	J kg^{-1}	Latent heat of water
n	3.0	[unitless]	Flow exponent (Nye, 1953; Paterson, 1994)
ρ^{w}	1000.0	kg m^{-3}	Mass density of water at 0 °C
ρ^{i}	916.7	kg m^{-3}	Mass density of ice
μ	1.781×10^{-3}	N s m^{-2}	Viscosity of water
Derived constants:			
$\mathcal{B}$	5.28×10^7	$\text{Pa s}^{1/n}$	Flow law coefficient ($= \mathcal{A}^{1/n}$)
Pr	13.39	[unitless]	Prandtl number
β	-7.44×10^{-8}	K Pa^{-1}	Pressure melting coefficient (eqs. 2.7, 2.8)
$\mathcal{R}$	-1.70	[unitless]	Threshold bed to surface slope ratio (eq. 2.44)
Numerical parameters:			
γ^{b}	1×10^{-7}	Pa^{-1}	Subglacial water compressibility
Δx	2.5–5	m	Longitudinal grid spacing
Δt	30	s	Maximum forward time step
$Z_0^{\text{b:e}}$	0	m	Minimum accreted ice thickness

The grid spacing Δx is relatively arbitrary. Essentially, Δx needs to be small enough to capture the relevant processes. However, if Δx is too small, then the matrix inversions necessary to advance in time for the numerical differentiation formula become prohibitively expensive. In the limit of an extremely tight spatial discretization, time stepping is not possible because the matrices have high condition numbers. Knowledge of a horizontal length scale of any of the processes discussed in previous chapters would limit Δx. The most conspicuous of these is the ice–bed configuration of the longitudinal section to be simulated. For the synthetic sections, I take Δx as 5 meters unless otherwise noted. I have tested other discretizations and found the results presented here to be largely independent of the grid spacing

In addition to parameter choices listed in 6.2, other parameters are also necessary. These are given in Table 6.3. The crevasse-cross sectional area is relatively small. This low value provides little buffering in terms of the response time of the subglacial system to the recharge rate. In terms of a simple geometry, the crevasse cross-sectional area corresponds to circular moulin of approximately 3.6 m diameter. The Darcy-Weisbach friction coefficient is high relative to subaerial streams. However, Clarke (2003) showed that appropriate flood discharge hydrographs for Steele Glacier, Yukon Territory, Canada can be reconstructed using values of f_d in the

range 0.12–0.20. I take 0.16 as the mean value. The crevasse recharge rate is taken to be 0.1 $m^3\ s^{-1}$. This value corresponds to a maximum summertime discharge for Matanuska Glacier, as described above. Finally, I explicitly state that the width of the sheet is 1 m. Thus, all simulations are per unit glacier width. Values of width-averaged parameters discussed in Chapter 2 are returned to their usual dimensions using this value.

Table 6.3: Additional model parameters

	Parameter	Value	Units
Crevasse cross-sectional area	A^c	10	m^2
Darcy-Weisbach friction coefficient (eq. 2.24)	f_d	0.16	[unitless]
Crevasse recharge rate	Q_{melt}	0.1	$m^3\ s^{-1}$
Unit glacier width	W	1	m

Boundary conditions

Meltwater from the glacier surface can flow into the subglacial water system through fractures, moulins, or crevasses. Because there is no surface component to the model, a feeder crevasse is constructed at the upstream end of the longitudinal section. The feeder crevasse acts as a reservoir. This reservoir is a simplification of upstream hydrology and is meant to loosely approximate upstream conditions. The crevasse has a cross sectional area normal to z, and a recharge rate feeds into the crevasse. The pressure difference between the crevasse and the subglacial water system determines the flux of water into the subglacial system. Upstream crevasse water temperature is assumed to be at the equilibrium melting point. If instead sensible heat were imported from the surface, the subglacial hydraulic system would melt open. Because the upstream crevasse is a simplification of upstream hydrology, I make the expedient assumption that there is no sensible heat; and water enters the subglacial system at the melting temperature. Details of the crevasse formulation appear in Appendix F.1.2 and are illustrated in Figure F.2.

While the crevasse condition is a useful addition to the model, the selection of the crevasse cross-sectional area and the recharge rate are arbitrary. A large upstream crevasse buffers the evolution of the hydrostatic pressure at its base. Large crevasses represent an upstream hydraulic system with much storage while small crevasses represent the opposite. Given these representations, the cross sectional area of the upstream crevasse need not be physically exact but only justifiable for the simulation.

Surface melt water flows through a glacier for only a fraction of a year. Opening and closing of the subglacial system are not treated here because they are extremely difficult to simulate. To simplify, I assume that the subglacial water system is capable of accepting water at the time that water flows into the crevasse. Furthermore, time integration is limited to a melt season. Duration and intensity of the melt season depends on climatic and geographical parameters which are not treated here. For simplicity, I make the expedient assumption that a melt season is approximately 100 days long (*e.g.,* Pearce *et al.*, 2003).

There are two limits for steady state solutions for the height of water in the crevasse: (1) either the water height is at the glacier surface, or (2) the water is at the height of maximum bed elevation downstream of the crevasse. For long time intervals, the recharge rate will determine if and when the crevasse water elevation approaches either of these limits. If the crevasse water level is below the maximum downstream bed elevation, then water will flow in reverse from

the subglacial system to the crevasse. In this case, recharge will also play an important role in returning the crevasse water elevation to a permissible level. In sum, the crevasse water height must be between these two limiting elevations in order for water to flow through the subglacial water system.

For longer times, the numerical model seeks an equilibrium among crevasse water pressure, storage, and subglacial discharge. If the recharge rate is high relative to discharge to the subglacial system, then the crevasse height can rise to the glacier surface. Discharge through the subglacial system increases until a critical subglacial cross-section is reached. The crevasse then drains to a steady level. This decay often takes tens to hundreds of hours depending on the crevasse size and water recharge rate. If the converse is true, and the recharge rate is low, then the crevasse water elevation can approach its minimum value. Generally, long integration times are necessary for the water system to creep closed in this case.

Depending on the simulation, recharge into the crevasse can take a value of 0.001–0.3 $m^3\ s^{-1}\ m^{-1}$ based on field data. Discharge data from Matanuska Glacier and Storglaciären are relatively important because glaciohydraulic supercooling at these locales is relatively well-described and the width-averaged water fluxes constrain upstream model conditions. At Matanuska Glacier, summer discharge measured approximately 200 m downstream of the terminus can exceed 80 $m^3\ s^{-1}$ (Lawson *et al.*, 1998). The width at the terminus is approximately 5 km, giving a width averaged discharge of about 0.02 $m^3\ s^{-1}\ m^{-1}$. However, a large portion of the terminus is not active. Therefore, Alley *et al.* (1998) suggested that summertime discharge may meet or exceed 0.1 $m^3\ s^{-1}\ m^{-1}$. In addition the subglacial system may leak water to an englacial or subglacial aquifer (Alley *et al.*, 1998; Hooke *et al.*, 1988), which then discharges to the hydrologic system downstream of the overdeepening. Consequently, the width-averaged discharge at the ice–bed interface is most likely lower than 0.1 $m^3\ s^{-1}\ m^{-1}$. During winter, proglacial water discharge continues at a rate of approximately 1 $m^3\ s^{-1}$, either from water stored sub- or englacially. Accretion occurs but is slow relative to summertime conditions.

At Storglaciären, two streams, Nordjokk and Sydjokk, drain the glacier. These two streams have maximum summer discharges of approximately 2.5 and 1.5 $m^3\ s^{-1}$, respectively (estimated from Hooke *et al.*, 1988; Hooke & Pohjola, 1994; Seaberg *et al.*, 1988). The width of the glacier at the riegel is approximately 850 m (Fig. 1.4). The width-averaged discharge is therefore approximately 0.005 $m^3\ s^{-1}\ m^{-1}$, which is considerably lower than the equivalent value for Matanuska Glacier. This is not surprising given that Storglaciären is in a drier climate and is a small fraction of the size of Matanuska Glacier.

Other glaciers have similar width-averaged discharges. Width-averaged discharge on Columbia Glacier, Alaska, approach 0.1 $m^3\ s^{-1}\ m^{-1}$, but the water pathways are not well known (R.A. Walters *et al.* as cited in Alley *et al.*, 1998). Bering Glacier, one of the largest glaciers in the Chugach Mountains, Alaska, has width averaged discharges that can exceed 0.3 $m^3\ s^{-1}\ m^{-1}$ in the glacier's non-surge phase (Fleisher *et al.*, 1998). Findelengletscher, Switzerland has width averaged discharges of approximately 0.001–0.01 $m^3\ s^{-1}\ m^{-1}$ and the water there travels through a subglacial cavity system (Iken & Bindschadler, 1986). Haut Glacier d'Arolla, Switzerland has a peak summer discharge of approximately 7 $m^3\ s^{-1}\ m^{-1}$ and a width near the terminus of 1 km (Swift *et al.*, 2005) leading to a maximum width averaged discharge of approximately 0.007 $m^3\ s^{-1}\ m^{-1}$. Bench Glacier is a relatively small glacier ($\sim$7.5 km^2) in the Chugach Mountains. Maximum summer discharge is approximately 7 $m^3\ s^{-1}$ and the width is approximately 0.9 km (Riihimaki *et al.*, 2005). These numbers yield a maximum width-averaged discharge of 0.008 $m^3\ s^{-1}\ m^{-1}$. There are no overdeepenings at Bench Glacier, and probably none at Haut Glacier d'Arolla and Findelengletscher; however, these glaciers are nearly the same size as Storglaciären

and provide roughly equivalent width-averaged discharges in the range 0.001–0.01 $m^3\ s^{-1}\ m^{-1}$. Columbia and Bering Glaciers are closer to the same size and have similar climatic conditions to Matanuska Glacier.

Because the recharge rate is arbitrary, selection of the direction is largely by trial and error within the bounds of the physical system. However, Alley *et al.* (1998) showed that accretion is favored for higher discharge systems. In response to their estimates, I take 0.1 $m^3\ s^{-1}\ m^{-1}$ as a baseline discharge in an attempt to reproduce their accretion rates.

At the outlet end of the longitudinal section, water pressure must be prescribed. Two simple options are either atmospheric pressure or ice overburden pressure at the terminus. Numerous field studies of supercooled vents demonstrate that water flow is artesian (*e.g.,* Lawson *et al.*, 1998; Pearce *et al.*, 2003; Tweed *et al.*, 2005). Consequently, a value of pressure slightly above atmospheric or ice overburden can also be used. However, the degree of overpressure is difficult to estimate *a priori*. Unless otherwise noted, pressure is prescribed as atmospheric.

Initial conditions

Nonzero initial values are necessary for p^b, u^b, T^b, and, depending on cross-section, either H^b or S^b. Initial conditions are discussed in Appendix F.1.3. A reasonable initial assumption for the water pressure is the ice overburden pressure. The water velocity can be assumed to be the velocity of steady state via equation (2.26). Initial temperature can be set via the Clausius-Clapeyron relationship (eq. 2.8). Values of p^b, u^b, and T^b are readily purged in numerical simulations provided that initial values are reasonably close to an expected solution.

The values of H^b or S^b are more difficult to initialize because there are no accepted values of either for overdeepenings. Moreover, these values should vary through the overdeepening and depend on the mass balance of the water layer. In previous studies, Clarke (2003) and Ng (1998) chose S^b to match data from jökulhlaups. However, matching data from outburst floods is not a goal of this study. Alley *et al.* (1998) posited that distributed water systems in overdeepenings were cavities and used a value of 0.1 m taken from field studies (Walder & Hallet, 1979). For the sheet model, H^b values of 0.1 m are possible but high, and I thus choose 0.1 m as a default initial maximum water depth. This value translates into an average water depth of 0.087 m (see Appendix F.4.1).

6.1 Steady flow: simple hydraulic sheets

The basic model presented in Chapter 2 with auxiliary relationships presented in Chapter 3 governs clear water flow. In this case, the subglacial hydraulic system is opened via a high melt rate. Closure occurs through accretion via freezing or a combination of creep and regelation. One important scenario for the clear water model is a steady forcing where the recharge to the upstream crevasse is kept constant. This boundary condition represents the simplest forcing function for the subglacial water system. Responses among terms within the governing equations and different geometries are most easily illustrated for steady forcing because the subglacial water system is forced to find a configuration that matches input conditions. Illustrated configurations may not be attainable in reality because of diurnal, seasonal, and other variations. I discuss the effects of these fluctuations later in this chapter. This boundary condition is meant to illustrate governing processes rather than give site- or scenario-specific information.

Furthermore, discharge is included in the steady state accretion rate (eq. 2.42a). However, there is not a steady state as is implied in this equation because the melt rate must either be

positive or negative for flowing water. Only for the trivial case of no water discharge is there an obvious steady state. It is thus useful to explore the behavior of the accretion rate under steady forcing.

Unless otherwise noted, these simulations are specifically for hydraulically conductive sheets. I contrast conduits later in this chapter.

6.1.1 Constant recharge simulations

Overdeepened case: Threshold section

Clear water results for sheet thickness H^{b}, water pressure p^{b}, water velocity u^{b}, and water temperature T^{b} are plotted in Figure 6.3 from the model presented in Chapter 2. In Figure 6.3a, from approximately 250–175 m from the terminus, the water depth decreases. From approximately 175–60 m, the water sheet bulges; and from 60–0 m, the water sheet thins below its initial value. In Figure 6.3b, the water pressure is smooth throughout the section, with a relatively smooth bend in the contours at approximately 25 d and farther than 150 m from the terminus. Water pressure decreases smoothly from the inlet pressure to the outlet. The water velocity in Figure 6.3c, shows variations similar in overall form to Figure 6.3a, but opposite in sign. Values for the velocity are high—approximately 1 m s^{-1} (Fig 6.3c). Where the water sheet is relatively thick, velocity is slow relative to areas where the water sheet is thin and vice versa. The water temperature illustrated is Figure 6.3d and bears some resemblance to Figure 6.3b; but there is additional structure in the plot for water temperature that is not evident in the water pressure.

From the four basic output variables a working hypothesis appears. Water sheet depth and water velocity are related to each other via a simple continuity relationship such that $Q^{\mathrm{b}} = WH^{\mathrm{b}}u^{\mathrm{b}}$. Thus, as the water sheet thickness increases, the water velocity must decrease to maintain a constant discharge. Furthermore, water pressure and water temperature appear to be related to one another via the Clausius-Clapeyron relationship. However, additional effects appear in the results for the temperature that are not clearly evident in the water pressure results.

Discharge results shown in Figure 6.4 point to the monotonous nature of inlet and along-path discharge. In Figure 6.4a, the water height of the crevasse, a surrogate for inlet pressure head, (solid black line) is plotted against the left axis, and discharge from the crevasse to the subglacial sheet (solid gray line) is plotted against the right axis. The pressure head has a strong transient response for approximately the first 10 d before relaxing to a constant pressure head of 34.3 m. This value is well below the maximum allowable value of 46.86 m which is the upstream ice thickness. Furthermore, the inlet pressure head is less than the flotation height of 42.96 m. Discharge to the subglacial sheet is constant after approximately three hours of integration.

The along-path discharge is plotted in Figure 6.4b with time on the vertical axis. Approximately 0.2% of the array values fall out of the range 0.1 ± 0.0001 m^3 s^{-1}, and most of this variation occurs within the first 10 d. Once inlet pressure variations subside, the variations in water discharge also subside.

The Reynolds number varies directly with discharge for sheet water flow (eq. 2.35a). Because discharge does not vary significantly, Figure 6.4 only shows small variations in Reynolds number. The consequence is that the Reynolds number does not appear to be very telling in this case. For example, there are no large variations from the non-overdeepened portion of the section to the overdeepened portion. The important result is that water discharge is fully turbulent because the Reynolds number exceeds 2100. Key results from the discharge information are (1) sheet water discharge attempts to mimic the crevasse recharge rate, (2) the discharge is roughly

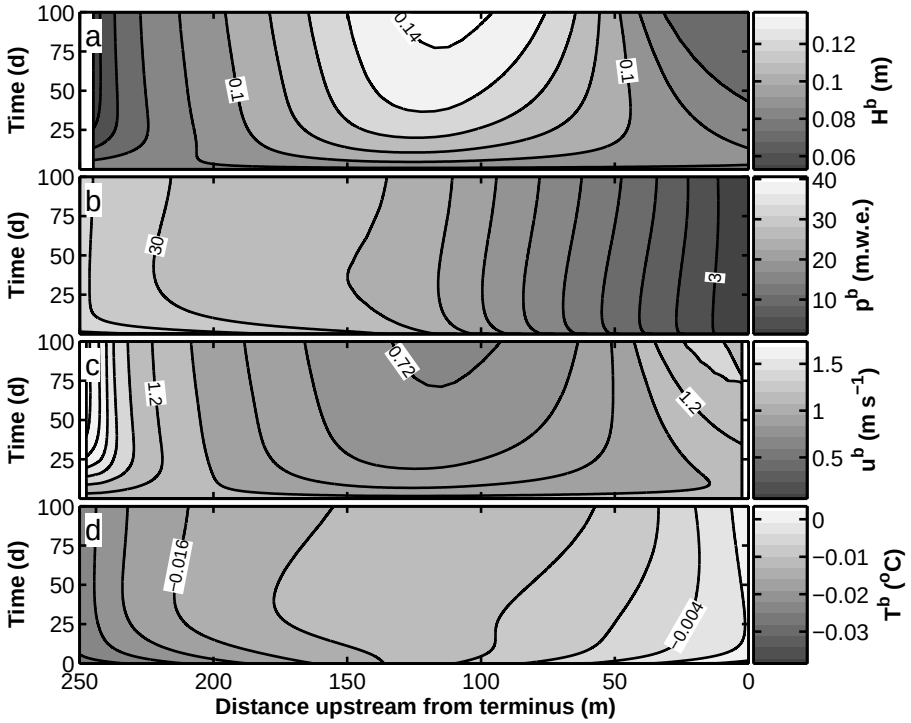

Figure 6.3: Threshold section output for a 100-day simulation under constant recharge conditions. Water flows from left to right along the line at the interface of the ice and bed. Time is along the vertical axis. (a) Water depth. Contour interval is 0.01 m. (b) Water pressure. Contour interval is 3 m. (c) Water velocity. Contour interval is 0.12 m s^{-1}. (d) Water temperature. Contour interval is 0.003 °C.

constant over the section such that $Q^{\mathrm{b}} = WH^{\mathrm{b}}u^{\mathrm{b}}$ where $W \equiv 1$ m, and (3) Reynolds numbers are fully turbulent.

In Figure 6.5a, the difference in temperature over the course of the model simulation ranges from about −0.001 to approximately 0.010 °C. The temperature depression shows that most of the flow path is above the melting point except for a small fraction that lies up the overdeepening. The area bounded by the zero degree isotherm is of particular interest. This swath starts approximately 20 d from the onset of the simulation. Eventually, it steps back to approximately 50 m from the terminus over the course of the simulation. Simultaneously, water upon exit from the terminus is not supercooled at 100 d. A similar feature in the same area also exists in the velocity simulation (Fig. 6.3c). This swath is more clearly evident in longer simulations (not shown), and the swath steps upstream to the onset of supercooling at about 107 m, which is the start of the wedge (Table 6.1).

The net accretion from this area of supercooling is shown in Figure 6.5b. A total of approximately 0.017 m ice accretes near the terminus. The maximum accretion is nearly 0.015 m at the terminus at approximately 75 d. Because the supercooled swath is stepping upstream (Fig. 6.5a), accretion is not monotonic or sustained throughout the simulation; and some accreted ice is melted in the final days of the simulation. However, this simulation is a threshold simulation. The expectation is that there will be no or very little supercooling, which is evident in the amount of accretion.

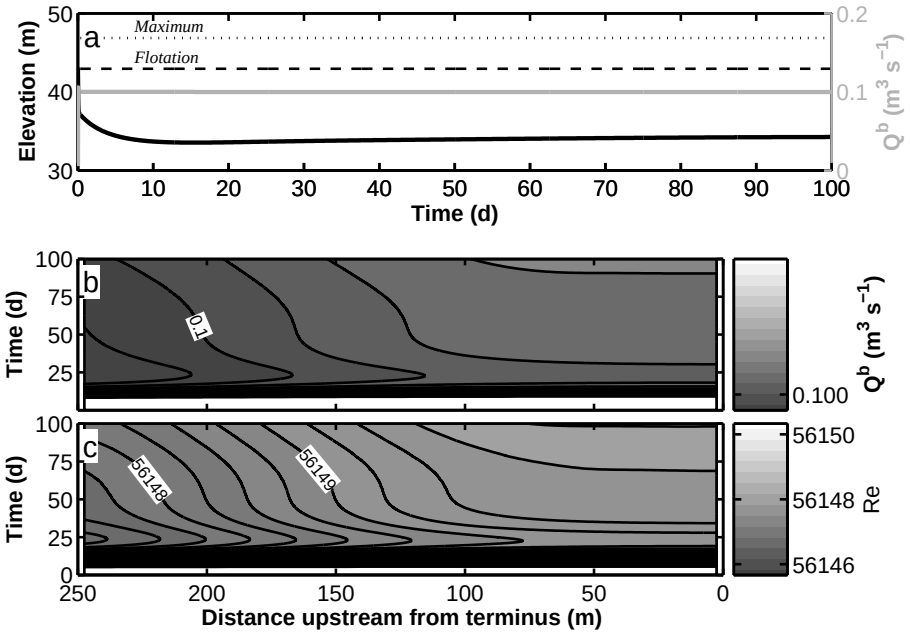

Figure 6.4: Discharge and Reynolds numbers in Figure 6.3. (a) *Left axis:* Elevation of water in the crevasse (black line). Black dotted line is the maximum water height and corresponds to the ice surface elevation. Black dashed line is the flotation limit. *Right axis:* Water discharge from the crevasse into the subglacial sheet (gray line). (b) Subglacial water discharge. Contour interval is 1×10^{-6} m^3 s^{-1}. Approximately 0.2 % of the array is not in the range 0.1 ± 0.0001 m^3 s^{-1}. The colorbar has only one tick owing to its small range (0.099995, 0.100003). (c) Reynolds numbers corresponding to (a). The precision is indicative of the lack of variability and does not reflect additional knowledge of subglacial water flow. Contour interval is 0.25.

Relevant melt rates are shown in Figure 6.6. Figure 6.6a shows the model melt rate computed using the Dittus-Boelter semiempirical relationship (eq. 2.38b). Rates vary from about -0.6×10^{-5} to slightly over 8×10^{-5} kg m^{-2} s^{-1}. The swath of negative melt rates corresponds directly to the swath of temperature depression (Fig. 6.5a). This feature is a result of the melt rate being directly dependent on the temperature depression. There is a secondary dependence on $(u^{\mathrm{b}})^{4/5}$ and $(H^{\mathrm{b}})^{-1/5}$.

It is possible to compute alternative melt rates based on the output variables. Specifically, the approximate melt rates based on the steady state assumptions are useful for comparison (eqs. 2.9) (*e.g.,* Röthlisberger & Lang, 1987). Figure 6.6b shows a melt rate using ice overburden pressure as an approximation from equation (2.42b). In this case the melt rate varies from about -0.4×10^{-5} to slightly over 21×10^{-5} kg m^{-2} s^{-1}. The pattern results from the small variation in the overall glacier ice thickness during the model run. High melt rates occur where ice is thickest. Tight contours from 150 to 100 m occur because of the onset of the overdeepening. Generally, the approximate melt rate is a factor of ±2–3 greater than the model melt rate. Furthermore the pattern is starkly different.

Instead of approximating the water pressure as the ice overburden pressure in the steady state melt rate, it is possible to use the water pressure directly. Figure 6.6c shows the approximate melt rate using this substitution. Instead of being a better fit to the model melt rate, the result is worse. Average misfit melt rates are closer to ±5–20 times the model rate along the adverse slope. However, locally the misfit can be much greater.

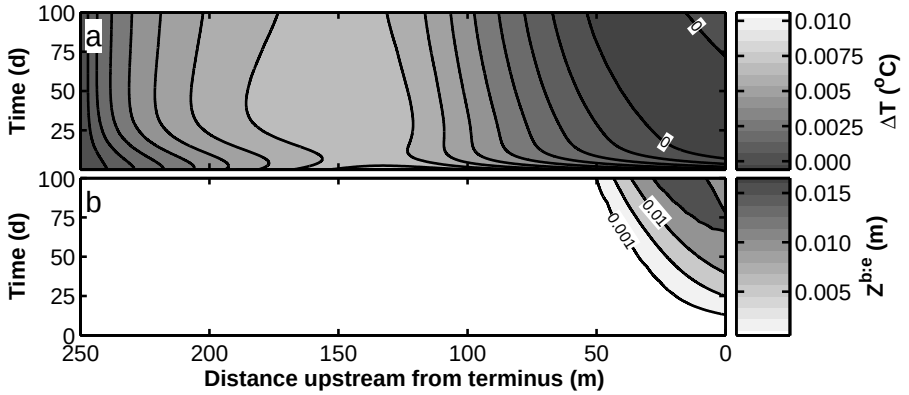

Figure 6.5: Temperature depression and ice accretion for the threshold case in Figure 6.3. (a) Temperature relative to freezing. Positive values indicate melt. Contour interval is 0.001 °C. (b) Amount of ice accreted. At $t = 100$ d, the maximum ice accreted is not at the terminus, but is approximately 5 m from the terminus. Contours indicate 0.001, 0.005, 0.010, and 0.015 m.

Overdeepened case: Above-threshold section

The above-threshold section fully activates the glaciohydraulic supercooling phenomenon. In Figure 6.7a, the water depth shallows along the adverse slope from about 100 m to the terminus. The darkened curved contours are the area of supercooling; and it steps upstream towards the onset of the wedge at about 107 m. The minimum water depth is below 0.07 m. Beneath the flat-bedded portion, the sheet expands to above 0.18 m at 150 m and 100 d.

The pressure evolution displayed in Figure 6.7b has a strong upstream contour from approximately 0–50 d. This feature results from the input pressure taking a much longer time to approach a steady value (Fig. 6.8, left axis). The input pressure head evolves to a value of approximately 32 m, which is below ice flotation. However, the pressure head only reaches a steady value after 200 d (not shown). As a result, the pressure evolution in Figure 6.7b has not equilibrated after 100 d.

For the first four days, the crevasse water elevation is at the glacier surface and above flotation. These first four days are clear in all of the plots for the above-threshold overdeepened section. After approximately 4 d, the water system has reorganized, and the upstream crevasse pressure evolution follows a damped decay pattern. For the threshold case, the damping takes 30 d (Fig. 6.4a, left axis). For the above-threshold case, the damping to a steady value takes more than 200 d. In both instances, the discharge into the subglacial system from the crevasse equilibrates relatively rapidly to the recharge rate (Figs. 6.4a, 6.8, left axes).

Because water discharge is nearly constant across the overdeepening (Fig. 6.8, right axis), the velocity increases where the water depth decreases. This behavior is illustrated in Figure 6.7c. Water velocities up the adverse slope exceed 1.4 m s^{-1} where the water depth is shallow. Where the sheet bulges, water velocities are lower.

From Figure 6.7d, water temperature again varies in a fashion very similar to water pressure. However, water temperature relative to the melting point appears to be more closely related to the water depth and velocity (Fig. 6.9a). The maximum amount of ice accreted is slightly above 0.039 m at 100 d and 70 m (Fig 6.9b). This ice thickness is over double the maximum ice accreted ice thickness for the threshold case.

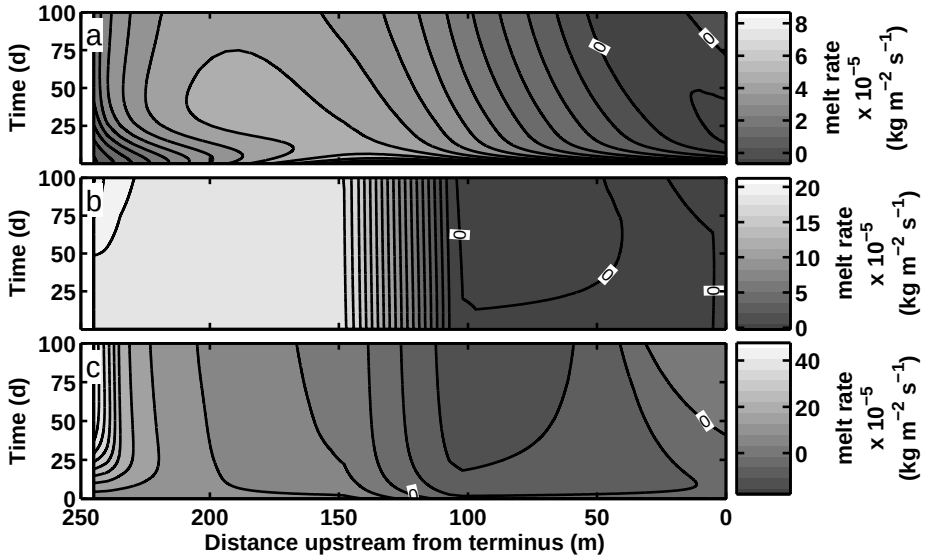

Figure 6.6: Melt rates for the threshold case in Figure 6.3. (a) Melt rate using equation (2.38b). Contour interval is 0.5×10^{-5} kg m^{-2} s^{-1}. (b) Approximate melt rate using ice overburden pressure from equation (2.42b). Contour interval is 1×10^{-5} kg m^{-2} s^{-1}. (c) Approximate melt rate using water pressure from equation (2.32b) Contour interval is 5×10^{-5} kg m^{-2} s^{-1}.

Furthermore, the area of accreted ice extends along most of the adverse slope by 100 d. There is a drop in the accreted ice thickness near the terminus with time because the water temperature drops below freezing, rises above freezing, and then drops below freezing again. This feature is shown in the location of the zero degree isotherms in Figure 6.9a with a swath that is slightly above zero separating the two zero degree isotherms that are farthest right.

In Figure 6.10a, the modeled melt rate follows the temperature depression inasmuch as the zero degree isotherms are also the zero-values for the melt rate. The patterns for both the temperature depression and melt rate are similar. The steady state melt rate shown in Figure 6.10b appears to be governed more by the ice overburden pressure than the actual flow. The approximate melt rates are approximately ±2–3 times the modeled melt rates along the adverse slope.

Results are plotted in Figure 6.10c for the case when water pressure is used in the approximate melt rate instead of ice overburden pressure. This plot resembles many of the others inasmuch as there is a swath. However, the melt rates do not come close to giving the proper rates or areas of melt. Except for the obvious statement that water freezes along the adverse slope, it is clear that this approximation does not capture the areas or rates very well relative to the model melt rate.

Reconstructing the time-dependent local balance of temperature is useful because it is possible to discern the governing terms in the heat balance. From equation (2.29b), the local balance

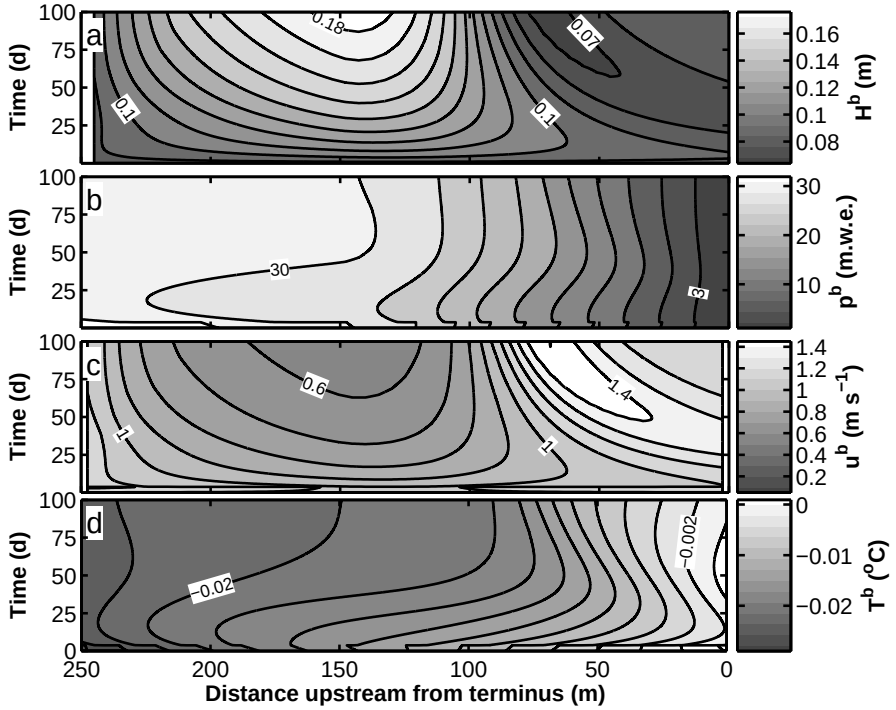

Figure 6.7: Above-threshold section output for a 100-day simulation under constant recharge conditions. Water flows from left to right along the line at the interface of the ice and bed. Time is along the vertical axis. (a) Water depth. Contour interval is 0.01 m. (b) Water pressure. Contour interval is 3 m. (c) Water velocity. Contour interval is 0.1 m s^{-1}. (d) Water temperature. Contour interval is 0.002 °C.

is

$$\frac{\partial T^{\mathrm{b}}}{\partial t} = \underbrace{-u^{\mathrm{b}}\frac{\partial T^{\mathrm{b}}}{\partial s}}_{\text{Divergence term}} - \frac{\tilde{m}}{\rho^{\mathrm{w}} c_p^{\mathrm{w}} H^{\mathrm{b}}} \left\{ \underbrace{L}_{\text{Latent heat}} \underbrace{+c_p^{\mathrm{w}} \Delta T_{\mathrm{mp}}}_{\text{Sensible heat}} \underbrace{- \frac{\left(1-n_p^{\mathrm{i}}\right)\rho^{\mathrm{i}} + n_p^{\mathrm{i}}\rho^{\mathrm{w}}}{\left(1-n_p^{\mathrm{i}}\right)\rho^{\mathrm{i}}} \frac{(u^{\mathrm{b}})^2}{2}}_{\text{Specific kinetic energy}} \right\} + \underbrace{\frac{2}{H^{\mathrm{b}}} \frac{\tau_0 u^{\mathrm{b}}}{\rho^{\mathrm{w}} c_p^{\mathrm{w}}}}_{\text{Viscous dissipation}} \quad . \tag{6.1}$$

The latent heat, sensible heat, and kinetic energy terms all have the same melt rate prefactor outside the left, vertical brace.

The actual values for each of these five terms is not necessarily important, but the relative magnitudes and patterns are important. These are plotted in order of appearance in Figure 6.11. Immediately apparent from Figure 6.11 is that the divergence and viscous dissipation terms (Fig. 6.11a and e, respectively) are clearly dominant and nearly balance each other with ranges up to $\pm 50 \times 10^{-5}$ °C s^{-1}. In Figure 6.11b, the latent heat term is the next largest term. The specific kinetic energy term is surprisingly large in Figure 6.11d. The sensible heat in Figure 6.11c is negligible because it is approximately five orders of magnitude smaller than the largest terms.

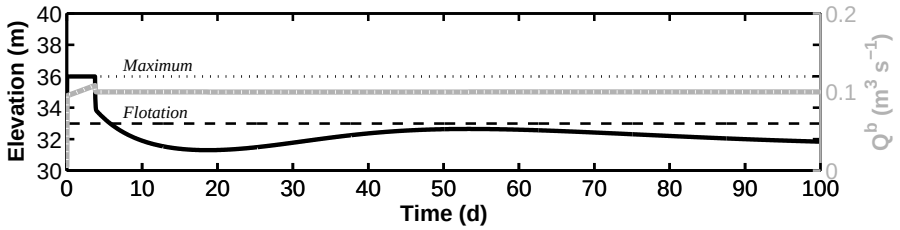

Figure 6.8: Boundary conditions for the above-threshold case (Fig. 6.7). *Left axis:* Elevation of water in the crevasse. Black dotted line is the maximum water height and corresponds to the ice surface elevation. Black dashed line is the flotation limit. *Right axis:* Water discharge. Gray line is the input into the subglacial water system. Light gray dotted line contained within the gray line is the effluent subglacial water discharge.

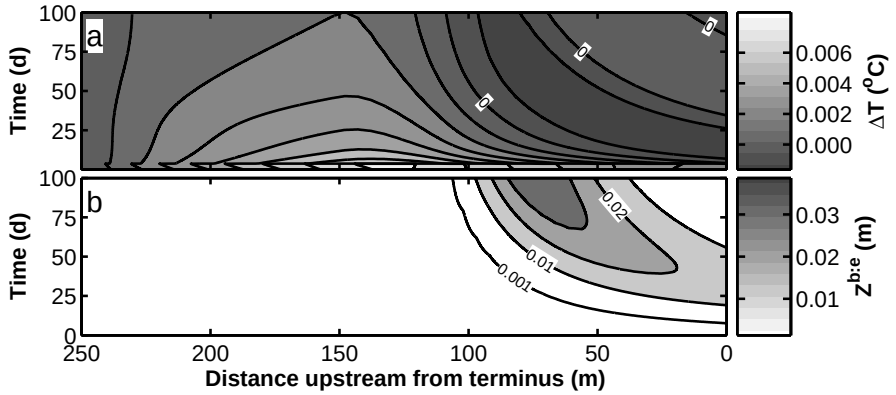

Figure 6.9: Temperature depression and ice accretion for the above-threshold case in Figure 6.7. (a) Temperature relative to freezing. Positive values indicate melt. Contour interval is 0.001 °C. (b) Amount of ice accreted. At $t = 100$ d, the maximum ice accreted is not at the terminus, but is approximately 75 m from the terminus. Contours are 0.001, 0.01, 0.02, and 0.03 m.

Both the viscous dissipation and specific kinetic energy terms depend on the water velocity. From equation (2.24), the viscous dissipation goes as $(u^{\mathrm{b}})^3$ while the kinetic energy term goes as $(u^{\mathrm{b}})^2$. In consequence, it is not surprising that these two terms bear a resemblance to Figure 6.7c. Furthermore, because the velocity is closely coupled to the change in water thickness via $Q^{\mathrm{b}} = WH^{\mathrm{b}}u^{\mathrm{b}}$ when discharge is constant, it is not surprising that these terms are coupled to the ice accretion rate. In addition, the latent heat term is coupled directly to the ice accretion because this term is directly linked to the phase change.

In Figure 6.7a, the heat divergence term is more difficult to interpret as-is because it relates how much heat is available to move through the subglacial water system. Substituting the Clausius-Clapeyron relationship (eq. 2.8) gives $-u^{\mathrm{b}}\partial T^{\mathrm{b}}/\partial s \sim -u^{\mathrm{b}}\beta\partial p^{\mathrm{b}}/\partial s$. The result is that an approximate heat divergence follows from the subglacial water pressure gradient. This approximation appears in Figure 6.12a, and the residual appears in Figure 6.12b. The residual has a similar pattern to the approximate melt rate in Figure 6.10 which is not a coincidence given that the same approximation appears in both figures. The obvious conclusion is that there is enough heat in the subglacial system that the pressure-melting assumption does not unequivocally hold in order to recover the location or rate of accretion.

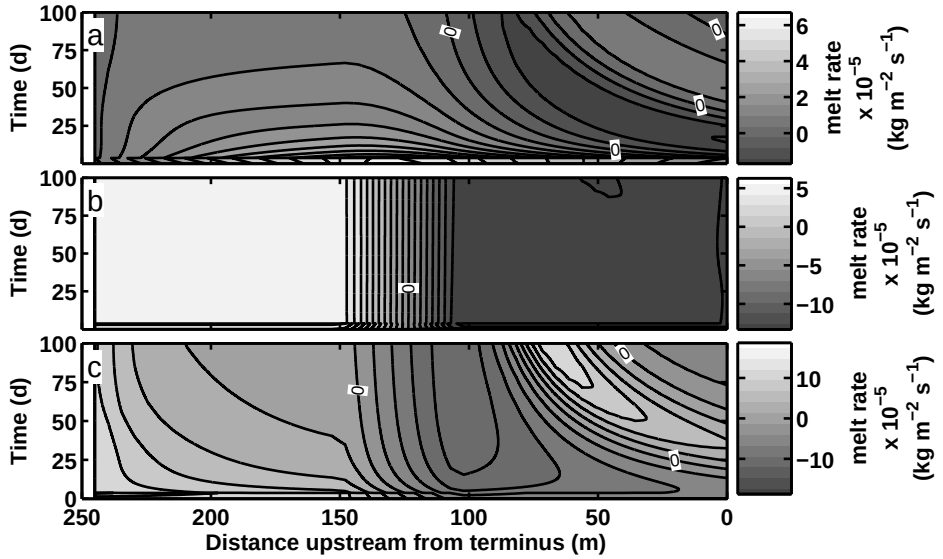

Figure 6.10: Melt rates for the above-threshold case presented in Figure 6.7. (a) Melt rate using equation (2.38b). Contour interval is 0.5×10^{-5} kg m^{-2} s^{-1}. (b) Approximate melt rate using ice overburden pressure from equation (2.42b). Contour interval is 1×10^{-5} kg m^{-2} s^{-1}. (c) Approximate melt rate using water pressure from equation (2.32b) Contour interval is 2.5×10^{-5} kg m^{-2} s^{-1}.

Overdeepened case: Below-threshold section

The below-threshold overdeepened section shown in Figure 6.2c is different from the previous two synthetic sections because supercooling should not occur. This will also be true of the flat-bedded case presented in the next section.

Figure 6.13a shows that the water depth is low at the upstream end, and grows through time at the terminus. At the upstream end, the water depth at 100 d is approximately 0.047 m. Because the melt rate must be positive, only the combination of creep and regelation closure under the thicker ice contracts the sheet thickness at the upstream boundary. Closure occurs more readily where there is lower water pressure and higher ice overburden stress. The water depth at the terminus at 100 d approaches 0.19 m, which is indicative of vigorous melting with a small closure rate.

The water pressure head varies smoothly and appears to be approaching a steady state near 100 d. The values at the upstream crevasse are near 29 m w.e., which are about 14 m below the flotation pressure head (Fig. 6.14a, left axis). Water velocities are also monotonic. At the upstream end, these exceed 2 m s^{-1}. At the downstream end, these are 0.55 m s^{-1} at 100 d.

As is common with the previous examples, discharge to the subglacial system is constant throughout much of the simulation (Fig. 6.14a, right axis). Furthermore, the effluent discharge (light dotted line) at the terminus plots directly over the upstream discharge (gray solid line). The water level in the crevasse stabilizes at about 18 d. After 18 d, the Reynolds numbers in Figure 6.14b increase towards the outlet. This increase results from water added to the flow because of melt.

In Figure 6.13c, the water temperature is relatively monotonic after 18 d. In general, the water temperature is warmer than the freezing point (Fig. 6.15a). The temperature difference

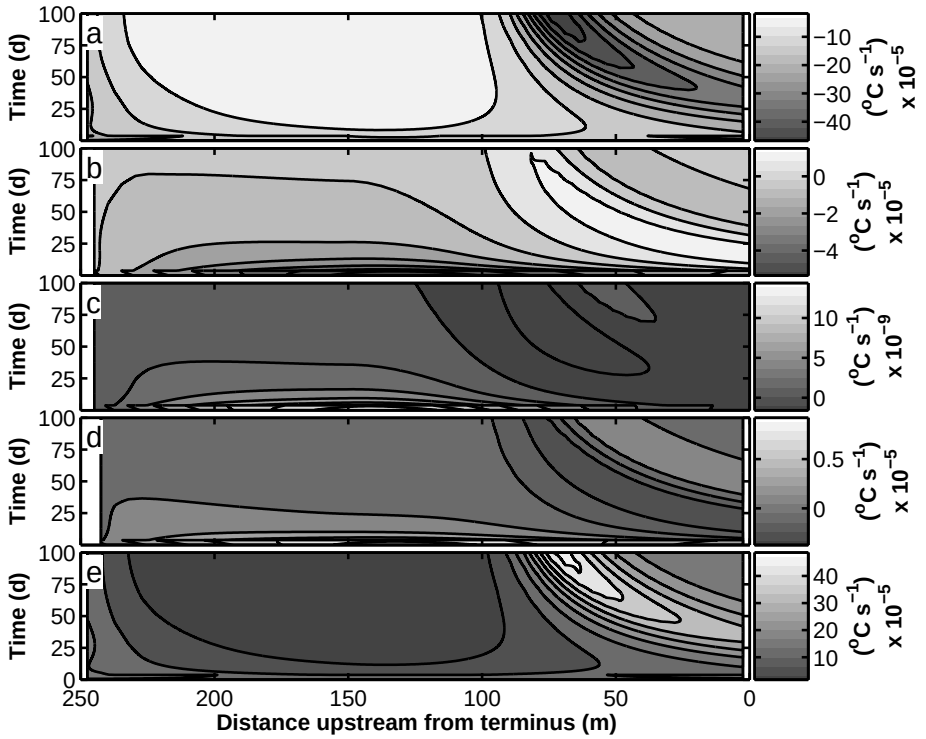

Figure 6.11: Components of the local internal energy balance for the above threshold case. All colorbars are independent. Each colorbar has a different scale. (a) Heat divergence term. Contour interval is 5.4×10^{-5} °C s^{-1}. (b) Latent heat term. Contour interval is 0.76×10^{-5} °C s^{-1}. (c) Sensible heat term. Colorbar is scaled to 10^{-9} °C s^{-1}. Contour interval is 1.6×10^{-9} °C s^{-1}. (d) Specific kinetic energy term. Contour interval is 0.15×10^{-5} °C s^{-1}. (e) Viscous dissipation term. Contour interval is 5.5×10^{-5} °C s^{-1}.

is greatest along the flat portion of the section and decreases as the water ascends the overdeepening. In Figure 6.15b, the melt rate follows the pattern of the temperature difference relatively closely with the highest melt rates lying over the flat portion of the section.

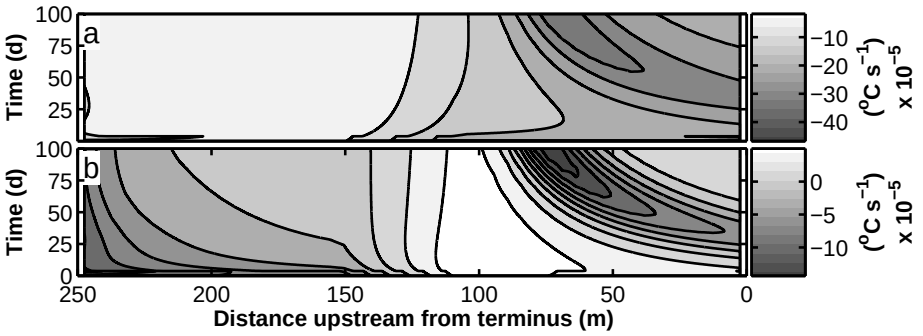

Figure 6.12: Components of the local internal energy balance for the above-threshold section. Each colorbar has a different scale. (a) Approximate temperature divergence (pressure melting) term scaled to Fig. 6.11a's colorbar. Contour interval is 5.4×10^{-5} °C s^{-1}. (b) Difference between Fig. 6.11a and Fig. 6.12a. Contour interval is 2.3×10^{-5} °C s^{-1}.

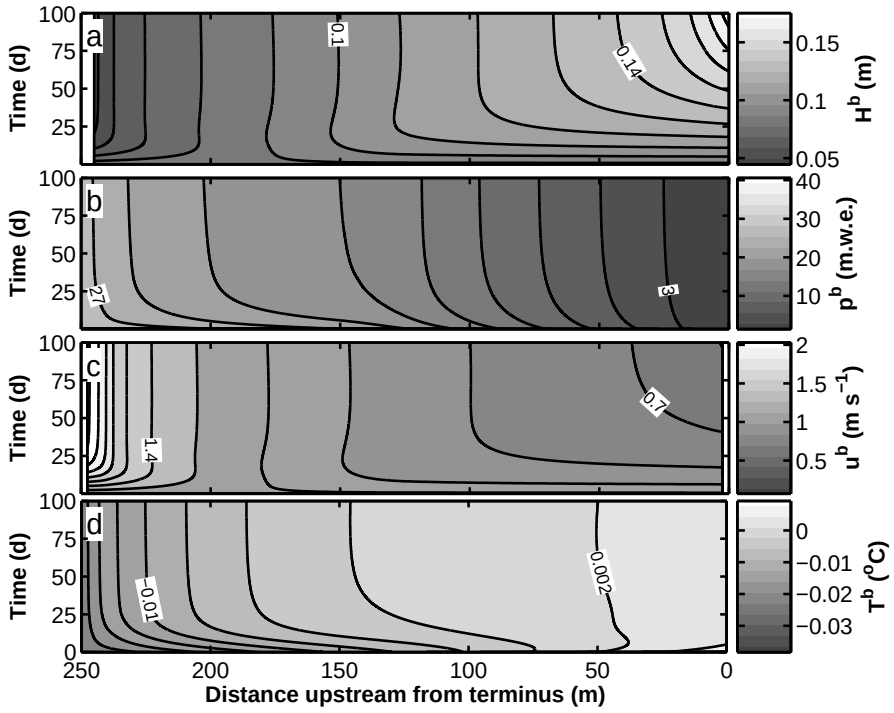

Figure 6.13: Below-threshold section output for a 100-day simulation under constant recharge conditions. Water flows from left to right along the line at the interface of the ice and bed. Time is along the vertical axis. (a) Water depth. Contour interval is 0.01 m. (b) Water pressure in meters of water equivalent. Contour interval is 3 m. (c) Water velocity. Contour interval is 0.14 m s^{-1}. (d) Water temperature. Contour interval is 0.003 °C.

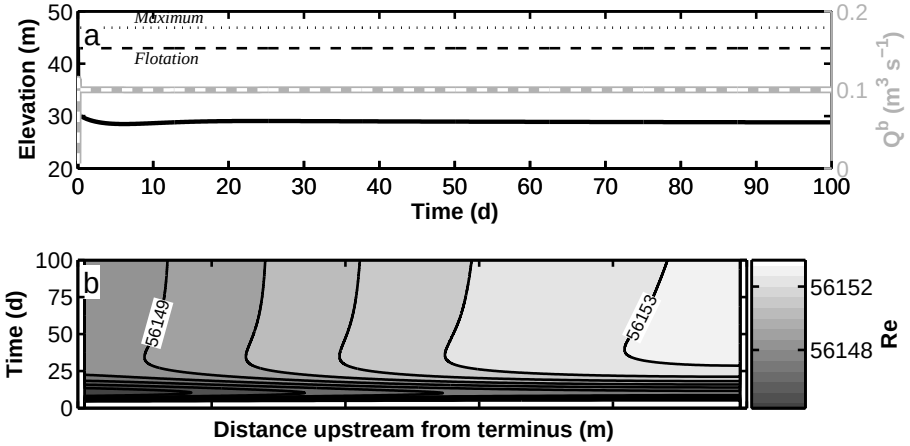

Figure 6.14: Discharge and Reynolds numbers in Figure for the below-threshold output presented in 6.13. (a) *Left axis:* Elevation of water in the crevasse. Black dotted line is the maximum water height and corresponds to the ice surface elevation. Black dashed line is the flotation limit. *Right axis:* Water discharge. Gray line is the input into the subglacial water system. Light dashed line contained within the gray line is the effluent subglacial water discharge. (b) Reynolds numbers corresponding to (a). The precision is indicative of the lack of variability and does not reflect additional knowledge of subglacial water flow. Contour interval is 1.

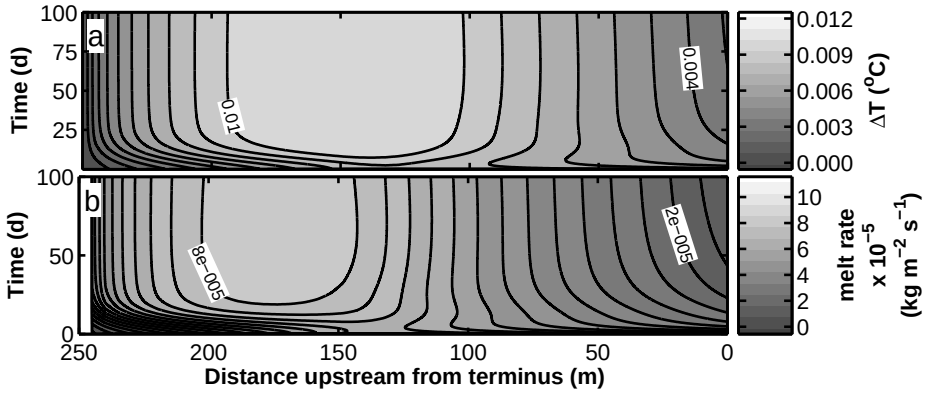

Figure 6.15: Temperature depression and melt rate from Figure 6.13. (a) Temperature depression. Contour interval is 0.001 °C. (b) Modeled melt rate using equation (2.38b). Contour interval is 0.5×10^{-5} kg m^{-2} s^{-1}.

Flat-bedded case

The flat-bedded case displays many of the same features as the below-threshold overdeepened case. In Figure 6.16a, the water depth increases monotonically to the terminus. In this case, the water depth maximum, 0.255 m, is reached at approximately 42 d. Because I have not incorporated a closure scheme when the maximum height of the largest size class is exceeded in Chapter 3, the numerical integration ceases. The net result is that this simulation takes about 42 d to lift off the bed for this case.

Within those 42 d, the sheet grows rapidly at the terminus, but the upstream sheet thickness does not evolve significantly after the first 10 d. The pressure, velocity, and temperature output in Figures 6.16b–d is also nearly constant at a given upstream location after 10 d. Upstream water velocities are high, exceeding 2 m s^{-1}.

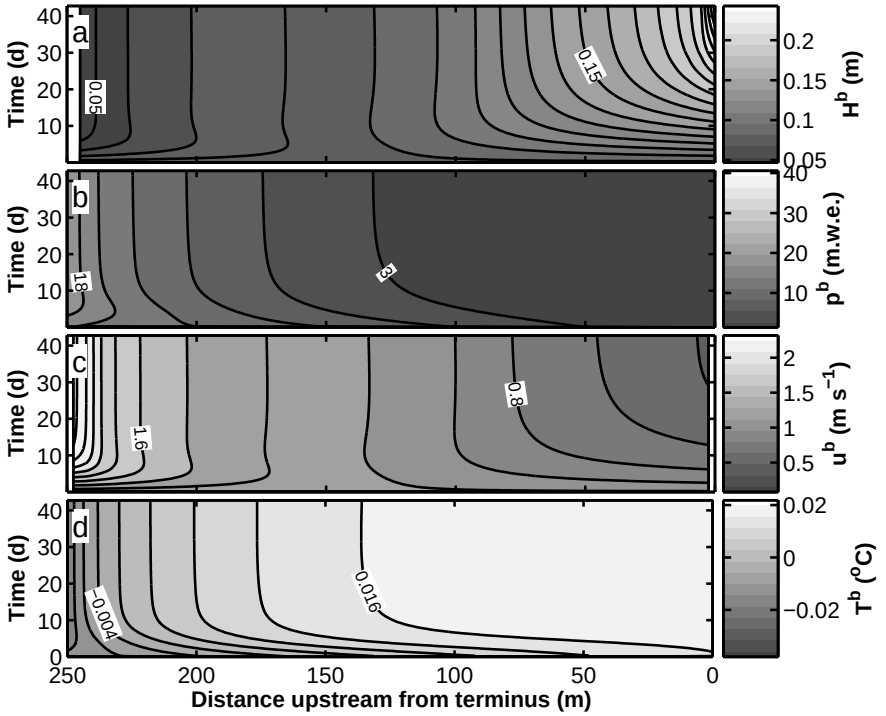

Figure 6.16: Flat-bedded section output for a 100-day simulation under constant recharge conditions. Water flows from left to right along the line at the interface of the ice and bed. Time is along the vertical axis. (a) Water depth. Contour interval is 0.01 m. (b) Water pressure in meters of water equivalent. Contour interval is 3 m. (c) Water velocity. Contour interval is 0.16 m s^{-1}. (d) Water temperature. Contour interval is 0.004 °C.

Surprisingly, the crevasse does not drain completely, but drains to approximately 21 m (Fig. 6.17a, left axis). Approximately 15 m of pressure head are dispersed in the first 150 m of flow, where most of the gradients in the other output are steady. Discharge, however, has a constant value throughout the 42 d (Fig. 6.17a, right axis), matching the recharge condition. Reynolds numbers in Figure 6.17b increase slightly from left to right, indicating that the ice ceiling is melting and adding water to subglacial water flow.

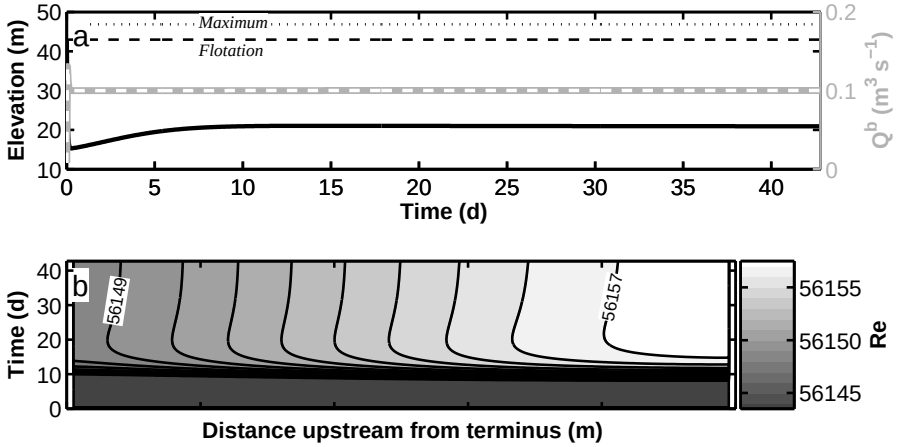

Figure 6.17: Discharge and Reynolds numbers in Figure 6.16. (a) Elevation of water in the crevasse. Dotted line is the maximum water height and corresponds to the ice surface elevation. Dashed line is the flotation limit. (b) Reynolds numbers corresponding to (a). The precision is indicative of the lack of variability and does not reflect additional knowledge of subglacial water flow. Contour interval is 1.

The output temperature in Figure 6.16 is warm, with values near the terminus exceeding 0 °C. The temperature difference in Figure 6.18a shows that the water is only at the melting point at the upstream boundary where it is prescribed. The remainder of the section is above zero. As a result, the melt rates in Figure 6.18b are fairly high. The contour patterns of Figures 6.18a and 6.18b do not align near the terminus. The flat bedded case is the first of the examples that has not aligned.

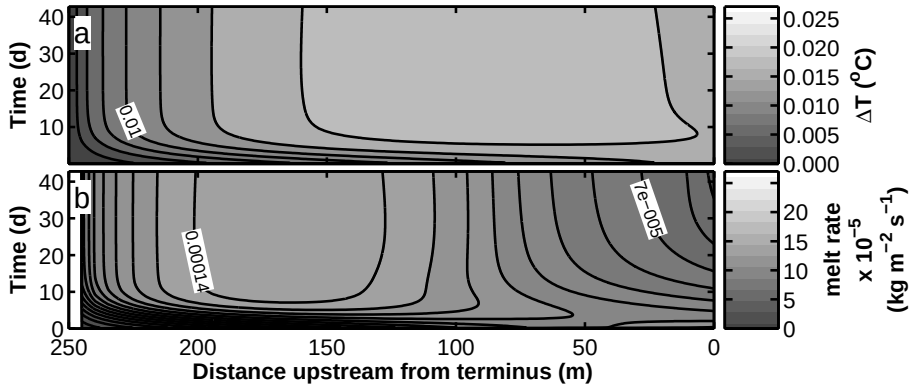

Figure 6.18: Temperature depression and melt rate from Figure 6.16. (a) Temperature depression. Contour interval is 0.0025 °C. (b) Modeled melt rate using equation (2.38b). Contour interval is 1.0×10^{-5} kg m^{-2} s^{-1}.

The terms of the local internal energy balance are presented in Figure 6.19. All terms, with the exception of the sensible heat term, are approximately 10 times greater in the flat-bedded case, with viscous dissipation dominating the heat balance. The divergence term almost balances viscous dissipation, and the sensible heat term is negligible. In Figure 6.19b, the latent heat component is lowest upstream.

In contrast to Figure 6.11 for the above-threshold section, the heat balance terms are generally quite different for the flat-bedded section. Velocities are much higher for the flat-bedded section, increasing viscous dissipation. Furthermore, a feature that dominates the above-threshold section, the area of ice accretion, is absent for the flat-bedded section.

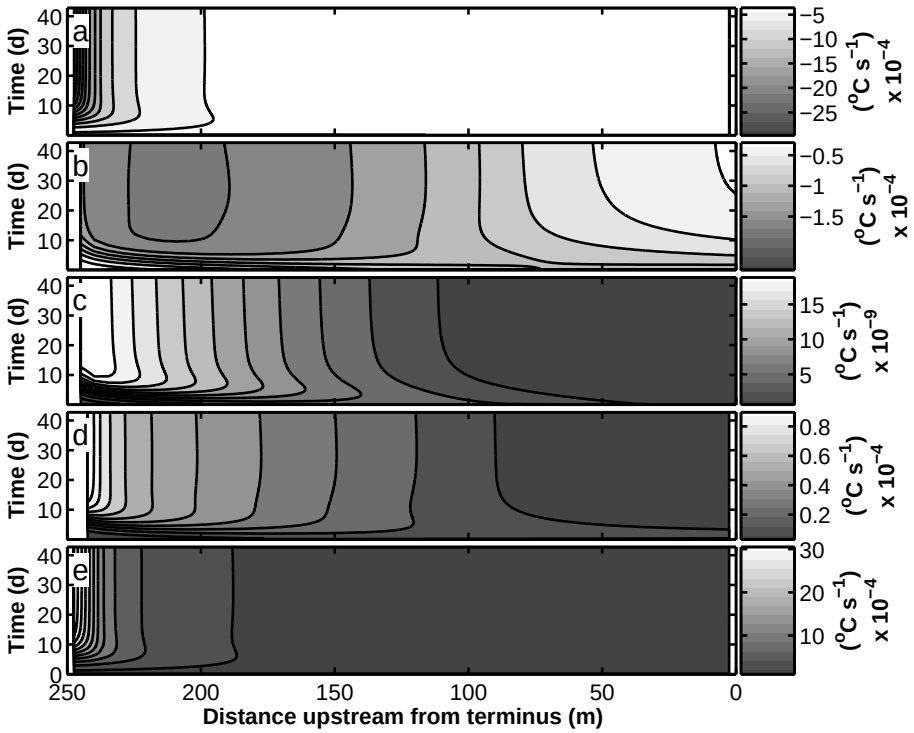

Figure 6.19: Components of the local internal energy balance in Figure 6.16. All figures have 10 contours for the individual colorbar range. Each colorbar has a different scale. (a) Temperature divergence (pressure melting) term. (b) Latent heat term. (c) Sensible heat term. Colorbar is scaled to 10^{-9} °C s^{-1}. (d) Specific kinetic energy term. (e) Viscous dissipation term.

Discussion

One of the most important characteristics of all simulations is that discharge is approximately constant along the section. Water velocity and sheet thickness are closely coupled. The only explicit source or sink of water is melt. Variations in melt are small, and even the overdeepened sections for which ice accretes experience net melting over the entire base of the glacier. Because water discharge is constant, where the sheet bulges, velocity is low and vice versa. Along the sections with ice accretion, sheet thickness drops along the adverse slope, and velocities increase. Upstream of the overdeepening, melt increases the sheet thickness and velocities are lower.

Because discharge is constant, the hydraulic system seeks an equilibrium with the recharge rate. As a result, the upstream crevasse water elevation varies to accommodate a constant discharge. Crevasse water elevation decays to a level that is below ice flotation. Only in the case of the above-threshold overdeepening are there significant damped oscillations of crevasse water elevation. These oscillations are revealed in the structure of the pressure evolution for the above-threshold section.

Pressure and temperature are coupled as well via the Clausius-Clapeyron equation. However, this coupling is significantly weaker because the balance of internal energy equation dynamically smoothes the temperature variation. The result is that there is a spatial lag associated with the latent heat in the subglacial system. This lag can be seen clearly in that the accretion for the threshold and above-threshold sections does not begin exactly at the onset of the overdeepening. For these sections, the accretion steps backward towards the onset of the overdeepening from the outlet point.

The areas of accretion correspond directly to areas where the temperature is below the freezing point. This observation is clear in comparing melt rates and temperature differences. These areas vary based upon the internal energy balance, and appear to undulate along the adverse slope based on where accretion is occurring and how water accelerates to get through constricted cross-sections.

Water flow along each section is fully turbulent, enabling use of the turbulent heat transfer relation. The turbulent Nusselt number gives melt rates that are a fraction of the equilibrium melt rates calculated using either ice overburden pressure or water pressure. Estimates of accretion, therefore, are biased high when using equilibrium estimates. Conversely, it is possible to state that the Nusselt number approach underestimates accretion. One argument against this, though, is that discharge is constant, and viscous dissipation will increase where velocity increases—where accretion occurs. However, I do not suggest that the accretion rate is correct using the turbulent Nusselt number because there are other formulations that undoubtedly give different estimates (*e.g.,* eq. 2.36 v. eq. 2.37).

The below-threshold and flat-bedded case exhibit few of the intricacies as the other sections. Because water is not forced back to the pressure melting point by the bed slope, these sections show that the hydraulic systems simply melt open under constant discharge conditions. The below-threshold case melts open less aggressively than the flat-bedded case because some energy is needed for the change in the pressure melting point.

Maximum accretion for the threshold and above-threshold sections is in the range 0.02–0.05 cm for the 100 d simulations. If 100 days sufficiently approximates a melt season, then there would be about 2–5 m of accretion per century. This rate is less than half the rate seen at Matanuska Glacier (Lawson *et al.*, 1998), but is certainly reasonable given the simplifying assumptions inherent in this model. Moreover, Matanuska Glacier has adverse slopes with larger potential for supercooling (Fig. 6.1) such that estimates presented here would most likely be lower than field estimates.

6.1.2 Energy Balance

The two largest fractions of the internal energy balance are the divergence term and the viscous dissipation term. Figures 6.11 and 6.19 show that the heat balance boils down to trade-offs among latent heat released through melting, heat divergence in the flow, and viscous dissipation. A smaller component is borne by the specific kinetic energy, and the sensible heat component is negligible as noted above. Because the degree of glaciohydraulic supercooling is sensitive to the friction coefficient, I explore this sensitivity in this section.

The friction coefficient f_d requires careful attention because the heat balance depends on the viscous dissipation term. This coefficient is not clearly defined relative for overdeepened environments. For outburst floods of the Steele Glacier, (Clarke, 2003) determined that reasonable values of the friction coefficient lie in the range 0.12–0.2. For the case of glacier lake outbursts, Clarke tuned the friction coefficient by matching the measured flood hydrograph to the modeled hydrograph. This is possible because both accurate flood hydrographs and water flowpaths are known. The friction coefficient is tuned via the momentum equation. In the case of glaciohydraulic supercooling, both flow paths and hydrographs are not well constrained. Thus, tuning via the momentum equation is not possible. It would be possible to tune the equations to effluent water temperatures if discharge was known. However, these data are sparse and not known with great accuracy despite high-spirited studies (*e.g.,* Lawson *et al.*, 1998; Tweed *et al.*, 2005).

Only the above-threshold section is illustrated. Results are broadly applicable to other sections. For these examples, I have chosen two different friction coefficients, $f_d = 0.20$ and $f_d = 0.12$ that bracket the value of $f_d = 0.16$ used in simulations discussed previously. All other parameters in Table 6.2 remain the same.

Results

Figures 6.20 and 6.21 illustrate discharge variables for $f_d = 0.20$ and $f_d = 0.12$, respectively. Figures 6.20a and 6.21a show the sheet thickness results. Overall, the plots are similar. Upstream thicknesses are dominated by the growth of the sheet as water passes through the flat-bedded area of the section. Along the adverse slope, the water sheet thickness drops in both cases because ice forms and constricts the flow. Because discharge is constant (Figs. 6.20c and 6.21c), velocity results shown in Figures 6.20b and 6.21b vary inversely to the sheet thickness results. Upstream, velocity is slow relative to flow along the adverse slope, where water velocity increases.

Finer structure of the results results from the difference in the friction coefficient. Maximum values of the sheet thickness are approximately 0.2 m and 0.18 m at about 150 m from the terminus for $f_d = 0.20$ and $f_d = 0.12$, respectively. Along the adverse slope, water sheet depths are also greater for the case of $f_d = 0.20$, owing to the increase friction and higher melt rate. In the case with higher viscous dissipation, more melt is produced (Fig. 6.22b), enlarging the sheet. Along the overdeepening, the case of $f_d = 0.20$ has clear gentle undulation in water thickness. These undulations in water depth yield accompanying undulations in output velocity. Although undulations also exist in the case of lower friction, the undulations are subdued. The velocity results show that increased friction lowers the velocity by about 0.1 m s^{-1} along the flat-bedded portion of the section and by about 0.2 m s^{-1} along the adverse slope.

In Figures (c), both simulations match input and outlet water discharge (0.1 m^3 s^{-1}), and the water elevation in the crevasse decays to approximately 32 m for each simulation. In Figure 6.20,

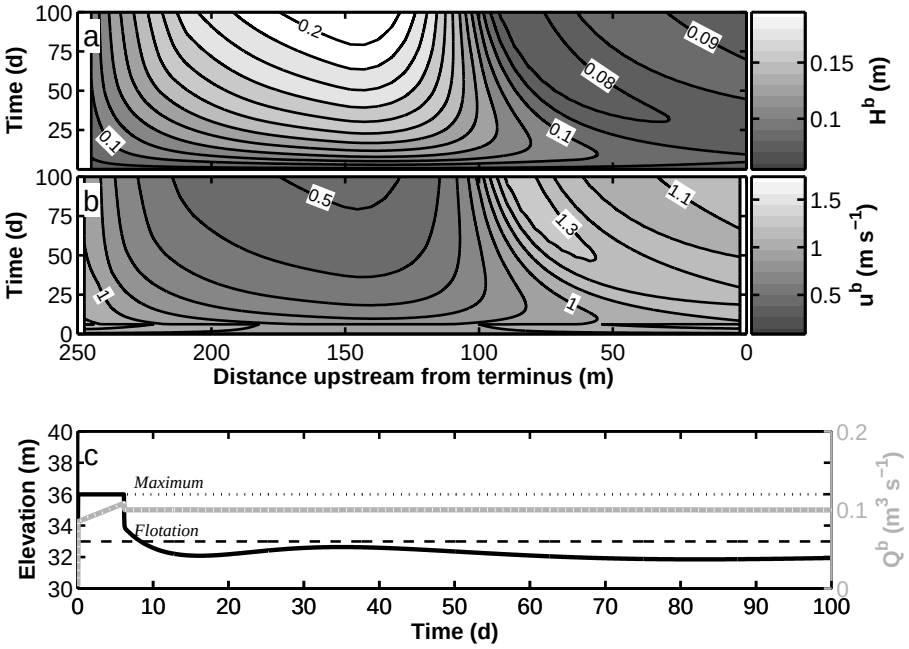

Figure 6.20: Above-threshold discharge output for $f_d = 0.20$. In (a) and (b), each colorbar has a different scale. (a) Water sheet thickness. Contour interval is 0.01 m. (b) Water velocity. Contour interval is 0.01 m s^{-1} (c) *Left axis:* Elevation of water in the crevasse. Black dotted line is the maximum water height and corresponds to the ice surface elevation. Black dashed line is the flotation limit. *Right axis:* Water discharge. Gray line is the input into the subglacial water system. Light gray dotted line contained within the gray line is the effluent subglacial water discharge.

the crevasse water elevation reaches flotation before the water drains rapidly after six days. This threshold behavior is also shown in Figure 6.8; however it is absent from Figure 6.21c.

With all other candidate processes removed, it is clear that this threshold feature is related to viscous dissipation. In Figures 6.8 and Figure 6.20c, the friction is high enough that the crevasse cannot drain. Because the friction coefficient is high, the sheet melts open rapidly over the first six days, as shown in Figure 6.20a. The latent heat released is strongly negative over those first six days, indicating much melt (Fig. 6.23b).

The comparison of accretion characteristics in Figure 6.22 illustrates many similar characteristics to the discharge results. Aside from the undulations previously discussed, the form of both temperature differences and both melt rates are similar. For the high-friction case, the temperature difference is less than 0.001 °C higher than that of the low-friction case. Furthermore, the melt rates are quite similar with the exception of the first six days in the high friction case. The largest differences are in the accreted ice thickness, which is nearly a centimeter greater for the low-friction case than that of the high friction case.

Figure 6.23 shows each of the heat balance terms for both cases. In general, each of the figures on the right hand side for $f_d = 0.12$ are greater in absolute magnitude than the equivalent plot for $f_d = 0.20$. This contrast is a direct result of the velocity being greater for the low-friction case. For example, because the viscous dissipation term goes as $(u^{\mathrm{b}})^3$ but is only linear in f_d, the shear heating term is higher for the low-friction case. This additional heat is then available to be moved in the flow by the divergence term, which also has a dependence on velocity.

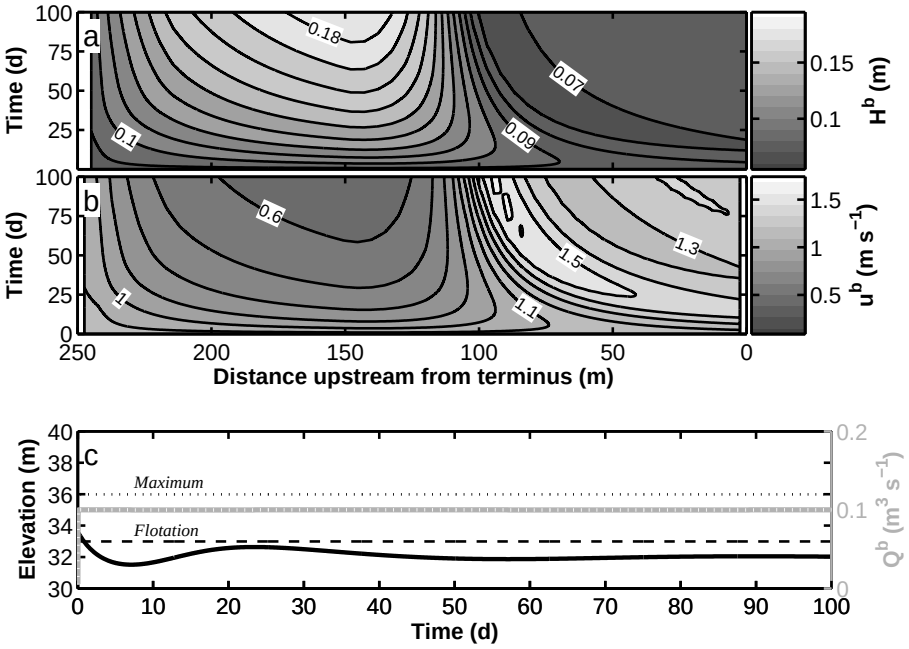

Figure 6.21: Above-threshold discharge output for $f_d = 0.12$. In (a) and (b), each colorbar has a different scale. (a) Water sheet thickness. Contour interval is 0.01 m. (b) Water velocity. Contour interval is 0.01 m s^{-1}. (c) *Left axis:* Elevation of water in the crevasse. Black dotted line is the maximum water height and corresponds to the upstream ice surface elevation. Black dashed line is the flotation limit. *Right axis:* Water discharge. Gray line is the input into the subglacial water system. Light gray dotted line contained within the gray line is the effluent subglacial water discharge.

Discussion

Because the melt rate is sublinearly dependent on velocity via the Reynolds number, melt is slightly higher for the high-friction case. This observation is seemingly inconsistent with the available heat terms presented in Figure 6.23. However, because of the form in which the heat balance is presented in equation (6.1), the latent heat, sensible heat, and specific kinetic energy terms are lower for a higher sheet thickness. Thus, the only necessary condition for an increased melt rate is that the Reynolds number be higher. The net result is that larger magnitudes of heat balance terms do not yield greater melt.

Another key aspect of the friction coefficient is that it controls the forced opening and closing of the subglacial system during the first few days of the simulation for $f_d = 0.20$ and $f_d = 0.16$ presented in the last section. The case of $f_d = 0.12$ does not show the same threshold. This threshold is exceptional in that it suggests that the pressure driving flow may be above ice overburden for short time periods to force the entire system to melt open. The water system reorganizes during this period and then returns to conditions where the input water pressure is below flotation. Only during these periods does subglacial discharge not match the recharge rate for a steady forcing.

The range of friction coefficients suggested by Clarke (2003) and explored here does not alter the subglacial water flow significantly. Water depths, velocities, pressures, and temperatures are quite similar. The result is that other quantities, such as melt rate, are very similar. For

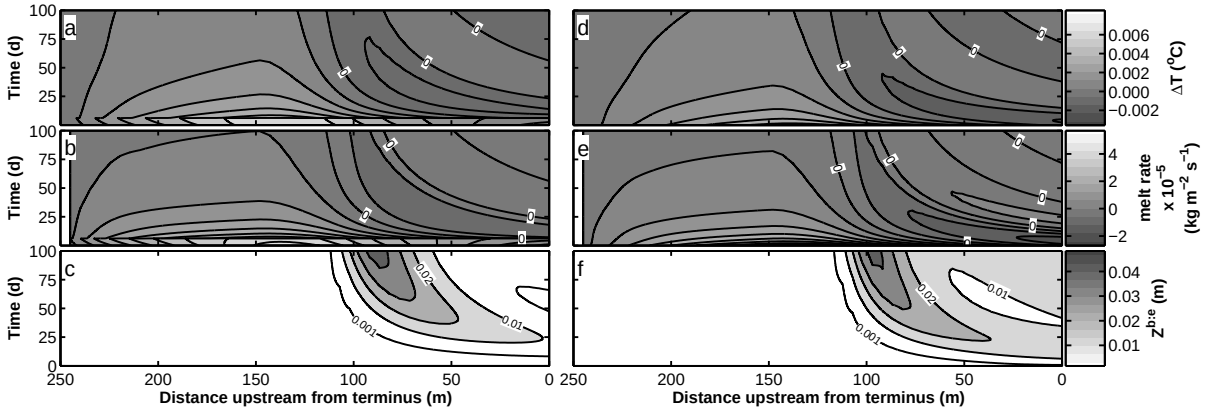

Figure 6.22: Accretion characteristics for different friction factors. Figures (a–c) are for $f_d = 0.20$. Figures (d–f) are for $f_d = 0.12$. Each colorbar has a different scale. Contour values are the same for each pair of figures. (a,d) Temperature depression. Contour interval is 0.001 °C. (b,e) Melt rate. Contour interval is 5×10^{-6} kg m^{-2} s^{-1}. (c,f) Accreted ice thickness. Contours are 0.001, 0.01, 0.02, 0.03, and 0.04 m.

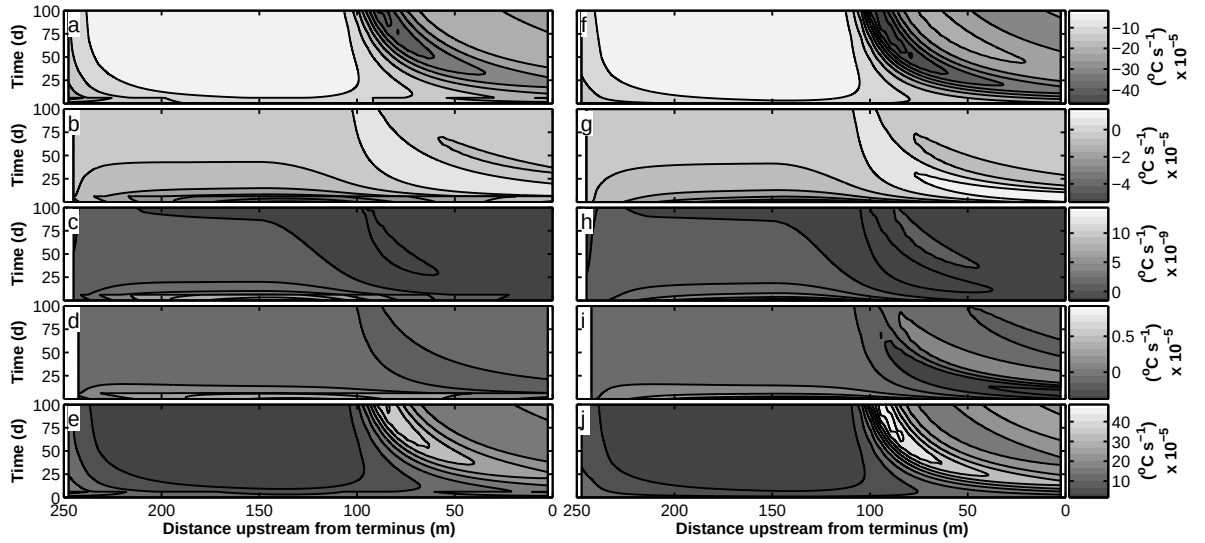

Figure 6.23: Components of the local internal energy balance for different friction factors. Figures (a–e) are for $f_d = 0.20$. Figures (f–i) are for $f_d = 0.12$. Each colorbar has a different scale. Contour values are the same for each pair of figures. (a,f) Heat divergence term. Contour interval is 5.4×10^{-5} °C s^{-1}. (b,g) Latent heat term. Contour interval is 0.76×10^{-5} °C s^{-1}. (c,h) Sensible heat term. Colorbar is scaled to 10^{-9} °C s^{-1}. Contour interval is 1.6×10^{-9} °C s^{-1}. (d,i) Specific kinetic energy term. Contour interval is 0.15×10^{-5} °C s^{-1}. (e,j) Viscous dissipation term. Contour interval is 5.5×10^{-5} °C s^{-1}.

significantly different friction coefficients, the water system does behave differently. A calibrated bed roughness, or friction coefficient, would be extremely useful but is not possible with present data sets.

6.1.3 Effect of porosity of the accreted ice

In Chapter 2, I augmented the original theory of Spring & Hutter to include the porosity of the accreted ice. Because different selections of ice porosity may change subglacial water flow it is important to illustrate this modification. In the present formulation, the ice porosity is constant and needs to be assumed based on field data and experimental analogues. Generally, an increase in the accreted ice porosity will block flow, and change flow conditions. In this case, I test two different values: a high porosity case with $n_p^{\mathrm{i}} = 0.10$ and a low porosity case with $n_p^{\mathrm{i}} = 0.01$. Each of these simulations relies on the above-threshold longitudinal section and the same model parameters used in the previous sections. The recharge rate is held constant at 0.1 $\mathrm{m}^3\ \mathrm{s}^{-1}$.

Results

Flow variable results presented for $n_p^{\mathrm{i}} = 0.05$ in Figure 6.7 are almost identical to those each of these simulations. In consequence, those results are not presented. Figure 6.24 presents results for the temperature difference, melt rate, and accreted ice thickness. Overall, the two figures are almost identical. The simplest point of reference is the amount of ice accreted from 75–100 d. More ice accreted for the high porosity case. However, the difference is almost negligible. The only numerical result that is quite different is that specific kinetic energy for the low porosity case (not shown) is negligible to the overall heat balance.

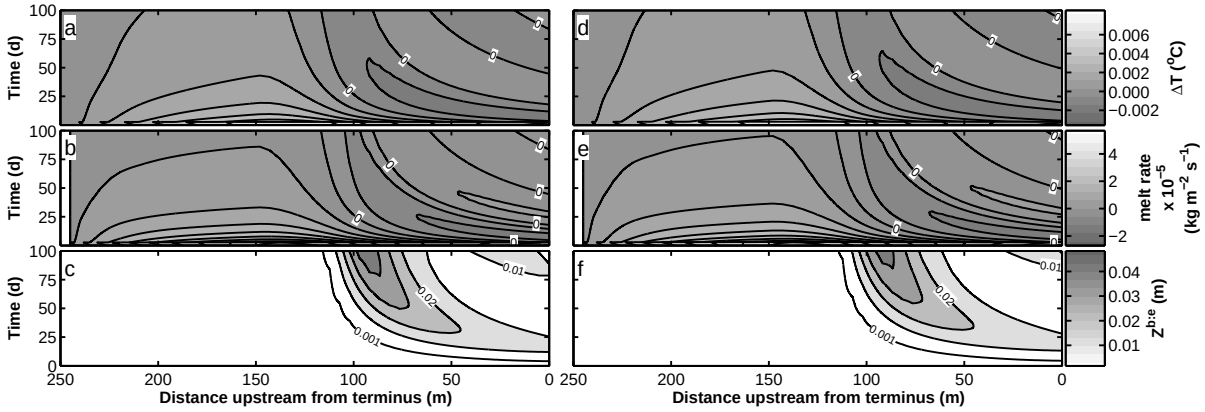

Figure 6.24: Accretion characteristics for different ice porosities. Figures (a–c) are for $n_p^{\mathrm{i}} = 0.10$. Figures (d–f) are for $n_p^{\mathrm{i}} = 0.01$. Each colorbar has a different scale. Contour values are the same for each pair of figures. (a,d) Temperature depression. Contour interval is 0.001 °C. (b,e) Melt rate. Contour interval is 5×10^{-6} kg m^{-2} s^{-1}. (c,f) Accreted ice thickness. Contours are 0.001, 0.01, 0.02, 0.03, and 0.04 m.

Discussion

Overall, the change in porosity is not significant to clear water flows. Trade-offs within the discharge relationship and the internal energy balance prevent large changes in flow structure.

Higher porosities yield slightly more accretion and lower sheet thickness. However, these changes are largely negligible.

Inclusion of porosity in the formulation provides a starting point for any type of porosity evolution. The flocculation and solidification of subglacial frazil ice is a parallel problem that will rely on such a formulation. These contribute to the trapping of sediment of sediment at the glacier bed. Furthermore, if water is to flow from the subglacial system to the englacial system (*e.g.,* Chapter 5), some porosity is necessary to conduct water between the two systems.

6.2 Comparison of channels and sheets

One area of interest is the cross-section that is favored by the hydraulic system. Data indicate that a fast-flowing distributed water sheet is preferred. Observations include continuous layers of sediment-rich accreted ice at the front of Matanuska Glacier (Lawson *et al.*, 1998). However, because the large body of theory on R-channels makes them a default model of subglacial flow, and channel cross sections that have been choked with ice and frozen are observed in these basal layers, it is necessary to illustrate how a distributed sheet differs from a subglacial channel in overdeepenings.

Subglacial hydraulic cross-sections can and do dynamically switch. The classic example of this is morphological switching when cavities changing morphologically into channels (*e.g.,* Kamb, 1987; Walder, 1986), (see Fig. 1.1). Sheet to conduit transitions have been modeled successfully (Flowers *et al.*, 2004). However, both spatial and temporal morphological switching is a formidable topic. Indeed, even in his lengthy treatise, Kamb (1987) made simplifying assumptions about the melt rate that are not inherent in the formulation presented in Chapter 2. As a logical consequence, I avoid switching altogether. Instead, I compare and contrast sheet and R-channel models in order to discern where switches may occur, if ever.

There are simple metrics to estimate when sheets and conduits would be favored. These chiefly rest with the subglacial water pressure evolution. If water pressures are below the ice overburden pressure, channelization should occur (*e.g.,* Röthlisberger, 1972; Walder, 1982). On the contrary, if water pressures are at or above the ice overburden pressure, then water distributes along the ice-bed interface (Hooke & Pohjola, 1994). Other phenomenological criteria exist for sheet–conduit transitions for water pressures below ice overburden, but these criteria rest on configuration and/or sliding assumptions at the ice–bed interface. However, no criterion is more durable than the relationship of water pressure to ice overburden. These concepts are readily distinguishable through simulations of longitudinal sections because glacier geometry exerts the strongest governing constraint on water flow beneath glaciers.

Simulations are presented for semicircular channels. The grid spacing is 2.5 m. All other parameters are the same as for the sheet simulations. The upstream recharge rate is held at 0.1 $m^3\ s^{-1}$. Initial conduit radii are calculated using equation (2.28b). In general, output variables for channels closely resemble the equivalent figures for sheets. I therefore omit presenting those results.

6.2.1 Results

Figures 6.25 and 6.26 show the effective pressures for the sheet and channel simulations, respectively. Within these figures areas of negative effective pressure are of particular interest. For the threshold section and sheet simulation (Fig. 6.25a), areas of negative effective pressure correspond relatively closely to areas of accretion. However, there are only negative effective pressures for approximately the final 52 d of the simulation that reach back to approximately 50 m from the terminus at 100 d. The equivalent plot for the channel (Fig. 6.26a) illustrates a much more complex evolution of channel pressures where the terminus is overpressured between approximately days 20 and 48. From 48 d to 100 d, the terminus has weakly positive effective pressures, and the region of negative effective pressures has migrated upstream.

Figures 6.25b and 6.26b illustrate the effective pressures for the above-threshold case. These two figures largely coincide with one another both temporally and spatially. Most of the section

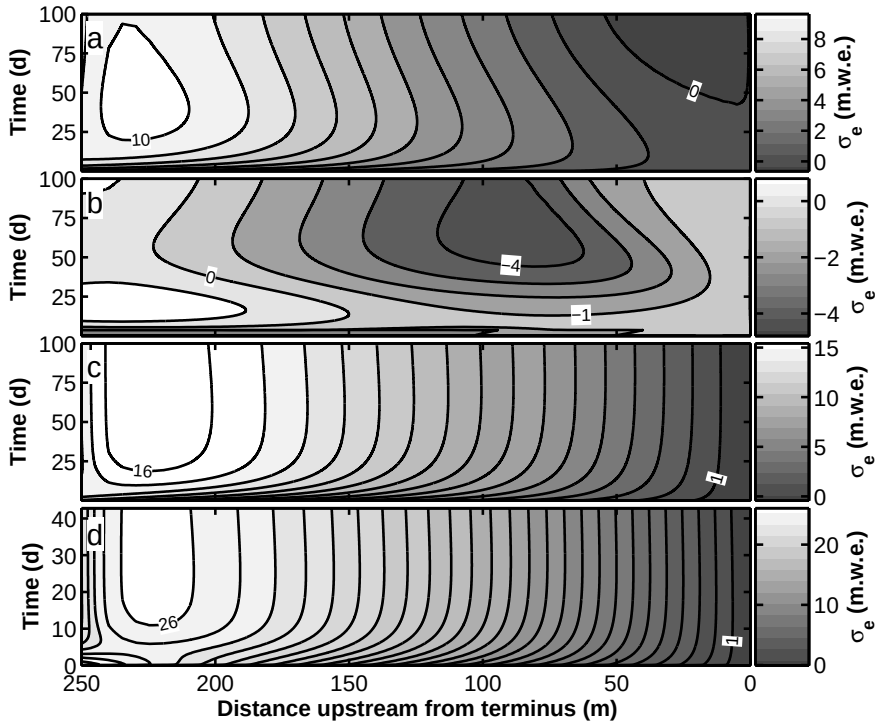

Figure 6.25: Effective pressure in meters of water equivalent for subglacial sheets. All colorbars have different axes. Contour interval is 1 m w.e. (a) Threshold case. (b) Above-threshold case. (c) Below-threshold case. (d) Flat-bedded case. The time axis ends at approximately 42 d.

is overpressured from the start of the simulation. The smooth curves around 50 d correspond to oscillations in the crevasse water height at those times.

The remaining figures (Figs. 6.25c,d and 6.26c,d) show that both the below-threshold and flat-bedded sections have positive effective pressures. Conduit results indicate that they run at lower pressures than the equivalent sheets and that upstream crevasse water elevations are lower.

Relative to Figures 6.5b and 6.9b, Figures 6.27a and b indicate that total accretion over the 100 d is higher in the case of channels. For the threshold section, sheet water flow accreted little more than a centimeter near the terminus. However, for the same section, total accretion reaches a maximum of approximately 6 cm after 100 d but is less than a centimeter at the terminus. For the above-threshold section, total accretion is only slightly higher (∼2 cm) and follows the same general pattern.

One surprising result is that ice accretes along the below-threshold section as shown in Figure 6.27. Not only is there accretion, but it is also in comparable amounts to the other two sections in the figures directly above. Obviously, this case is different from the equivalent sheet flow because that simulation experiences net melting along the entire length.

According to the steady-state theory presented in Chapter 2, accretion is not possible in the case of below-threshold section conduits. The bed-to-surface slope criterion depends on water pressure gradients being comparable to ice pressure gradients. However, in this case, water pressure is only loosely related to ice overburden pressure. The pressure gradient driving flow is shallower than the ice overburden gradient. As a result, supercooling and ice accretion occur.

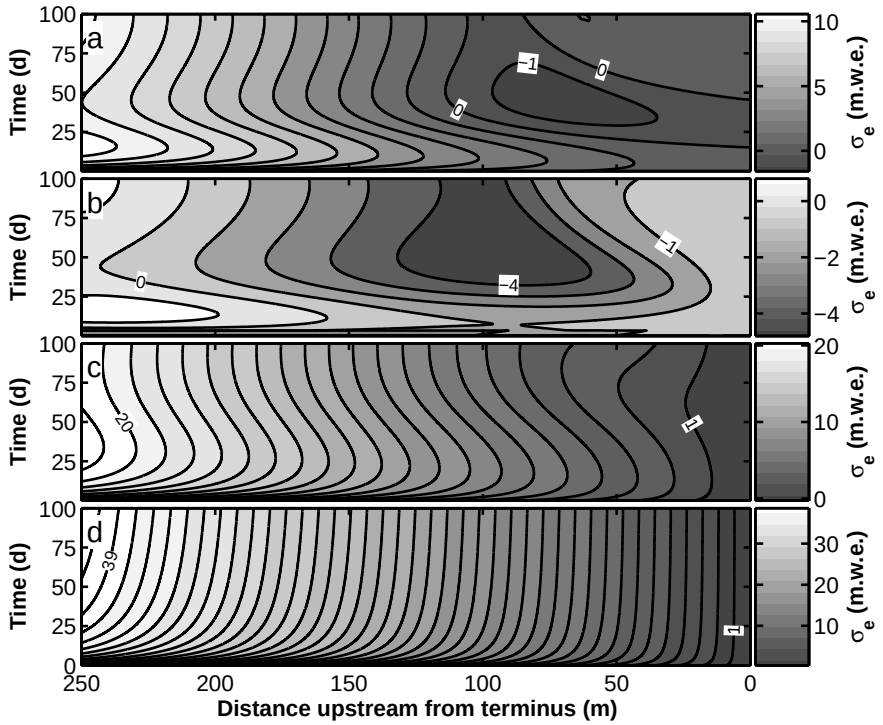

Figure 6.26: Effective pressure in meters of water equivalent for subglacial channels. All colorbars have different axes. Contour interval is 1 m w.e. (a) Threshold case. (b) Above-threshold case. (c) Below-threshold case. (d) Flat-bedded case.

6.2.2 Discussion

Broadly, sheets operate at higher pressures (lower effective pressures) and dissipate more heat than channels. Channels flow faster and move water more effectively than sheets. The generation of heat along both the ice ceiling and the sediment floor in the case of sheets means that supercooling is less dramatic.

For the flat-bedded case, it is clear that, barring microtopography or unusual water input from the surface, water must flow in conduits. There would not be an impetus for water to remain in a sheet. The arguments of Walder (1982) hold such that melt concentrates locally, pressures drop where there is melt, and water flows towards the melting zones. This feedback continues until a channel forms.

The below-threshold overdeepened simulations are less clear. These simulations show that a conduit preferentially freezes closed, but that a sheet melts open. Water flows at lower pressure in the conduit, and these cross-sections will be favored. However, a conduit will slowly constrict along an adverse slope. This situation may be one where an intermediate cross-sectional form such as a broad-and-flat channel is favored (Hooke *et al.*, 1990). In addition, some ice-choked conduits appear in basal ice at Matanuska Glacier (Lawson *et al.*, 1998) that are broader than they are thick. While it is not certain that these ice-choked channels are below-threshold, wide channels, their genesis is consistent with results from the model.

Furthermore, these simulations indicate that intermediate bedslopes exist that are below the steady-state supercooling threshold but still permit water to freeze. This possibility exists when the upstream pressure driving flow is free to drop well below ice overburden pressure. Pressure

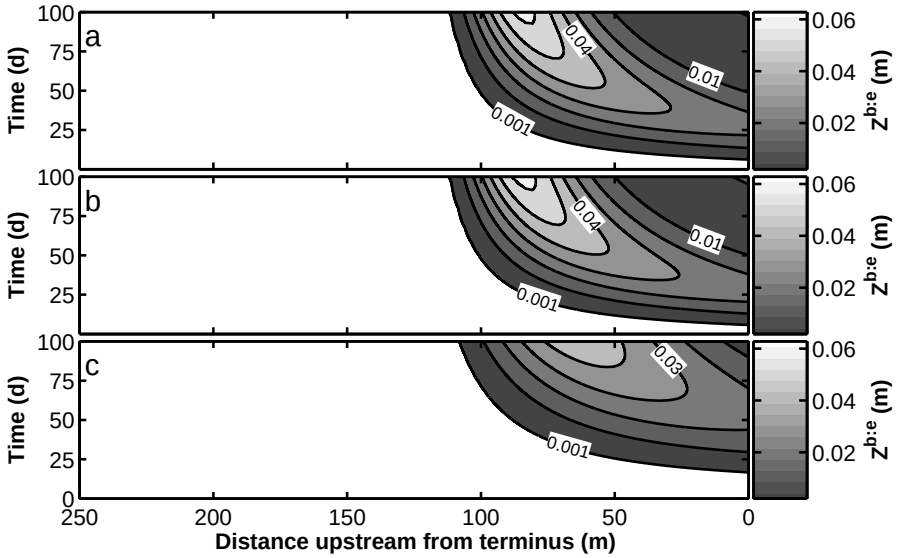

Figure 6.27: Effective pressure in meters of water equivalent for subglacial channels. All colorbars have different axes. Contour interval is 1 m w.e. (a) Threshold case. (b) Above-threshold case. (c) Below-threshold case.

most readily drops in the subglacial system when the system is connected to the surface (*e.g.,* Murray & Clarke, 1995). Water pressure can also be lower on the lee side of subglacial bumps (*e.g.,* Kamb, 1987; Schoof, 2005; Walder, 1986). This case may require additional constraints on the hydraulic potential (eq. 2.23) to include compressive, longitudinal stresses in the direction of ice flow (C. Schoof, pers. comm., 2007). Results such as these signify that research into below-threshold glaciohydraulic thermodynamics may provide additional insight into the subglacial hydraulic system.

For the above-threshold case, water pressure exceeds ice overburden pressure along most of the longitudinal section. In this case, water distributes laterally over the bed into a sheet. Alternatively, water can move into an englacial or subglacial aquifer. For high englacial hydraulic conductivity, enough water can leave the bed that subglacial pathways are flux-limited (see eqs. 5.1). Presumably, in this case, water flux lowers and intermediate channels are favored, such as those discussed above. However, englacial hydraulic conductivities can be orders of magnitude smaller than either subglacial conductivities. In the case of low englacial hydrualic conductivity, water must distribute laterally along the bed into subglacial sheets or equivalent hydraulic cross-sections.

Not surprisingly, the threshold section falls between below-threshold and above-threshold sections in terms of its behavior. For sheets, only flow along the upper portion adverse slope is overpressured. Conduits, however, can be overpressured along any part of the adverse slope, and the pressure changes its spatial distribution throughout the simulation. Based on the effective pressure, these simulations suggest that there can be along-path changes in hydraulic cross-section. Along the flat-bedded portion of the section, conduits are favored. Water that ascends the adverse slope distributes to a subglacial sheet. The location of this change is not necessarily static in time. Depending on circumstances, it may be possible that the sheet can change back into a conduit. However, once the conduit transforms into a sheet, it is unlikely that the sheet will transform back into conduit because the water flows through a sheet at higher pressure.

In summary, simulations of each type of cross-section reveal negative effective pressures. These negative effective pressures can determine where switching between cross-sections can occur (Hooke, 1991). Moreover, there may be intermediate cross-sections that have an intermediate behavior to both a laterally distributed sheet and a semicircular conduit. Locations of transitions between sheets and conduits vary depending on the surface-to-bedslope ratio. Furthermore, these locations of transitions can vary through time. For high surface-to-bedslope ratios, distributed systems are clearly favored, provided sub- and superjacent aquifers have low hydraulic conductivity.

6.3 Diurnal forcing

Glaciers commonly exhibit diurnal variations in surface meltwater production that yield variations in sub- and englacial drainage characteristics. Meltwater input to crevasses and moulins that act to recharge the subglacial water system varies principally with glacier surface temperature and solar insolation (Hock, 1999). Other factors, such as snowpack thickness and proximity of melt sources, also affect meltwater recharge to an individual crevasse.

Figure 6.28 captures several features of meltwater recharge and approximates field data from boreholes (*e.g.,* Flowers & Clarke, 2002b; Hubbard *et al.*, 1995). This synthetic forcing is a truncated daily sine curve with a peak at 1500h. This peak mimics peaks in glacier melt that commonly fall in mid- to late afternoon. Melt commonly ceases at night when temperatures drop below freezing, and borehole water levels respond to various drainage mechanisms. Recharge and melt are not synonymous inasmuch as water that does not refreeze at night can still recharge a borehole or crevasse. In addition, a crevasse may be recharged by englacial or subglacial water flow from up-glacier. However, I ignore this inconsistency and assume that recharge occurs only during the day and ignore en- and subglacial recharge entirely as these are of secondary importance.

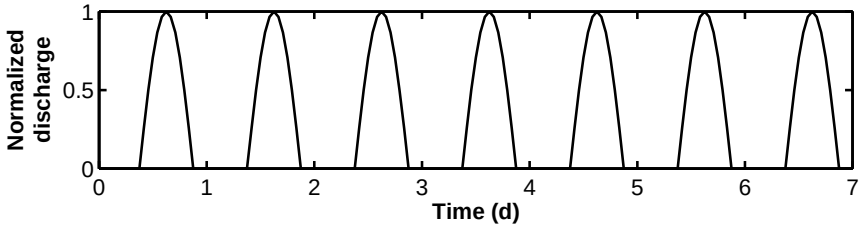

Figure 6.28: Synthetic diurnal forcing

I multiply the synthetic diurnal forcing by a background recharge rate, say 0.1 $m^3\ m^{-1}\ s^{-1}$ for example, to obtain an actual recharge value. Because the peak is set at 1500h, melt begins recharging the crevasse at 0900h and ceases at 2100h. Each of these simulations is also run for 100 days, starting at 0000h with a crevasse filled such that hydrostatic pressure at its base is equivalent to ice overburden pressure. Aside from the recharge rate, the only difference between the clear water and diurnally-forced simulations is that the grid spacing is reduced to 2.5 m for these simulations from the previous 5 m.

6.3.1 Results

Overdeepened case: threshold section

Based on Figure 6.5b, the threshold case does not accrete much ice. However, as a counterpoint example, I present the threshold case when forced with diurnal recharge.

Obvious structure appears in the evolution of the daily cycles (not shown). After approximately 20 d, the daily maximum crevasse water elevation reaches the glacier surface for approximately one hour each day. Within the 12 hour recharge cycle for the remaining 80 days, recharge raises the water level during the first seven hours. Maximum water elevation in the crevasse peaks at flotation approximately one hour after the discharge into the crevasse peaks. The water level then decreases between 1600h and 2200h. Over the course of the simulation, the daily cycles evolve slightly such that the subglacial system accepts less water, but this effect is

subdued relative to the magnitude of diurnal oscillations. Maximum discharge from the crevasse to the sheet decreases from by approximately 0.004 $m^3\ s^{-1}$.

Figure 6.29 depicts the final five days of the simulation. Figures 6.29a, b, and c show the prescribed crevasse recharge rate, the resultant crevasse water height, and the resultant discharge to the subglacial sheet, respectively. From left to right, each of these figures helps to generate the next figure. During the middle of the day, the crevasse water height maxima are blunted because water reaches the surface of the glacier. From approximately 1400h to nearly 1800h the crevasse water elevation is above the flotation level.

Discharge to the subglacial sheet (6.29c, thicker, solid line) skews to later time and indicates that the subglacial system is not symmetric with respect to recharge and draining. The downstream outlet discharge (thinner, dashed line) overprints the inlet discharge and indicates that even though the subglacial water system does not have constant discharge in time, it has nearly constant discharge in space. Obviously, the discharge changes some small amount as ice is melted off or accreted to the overlying glacier. This variability is contained within the line thicknesses.

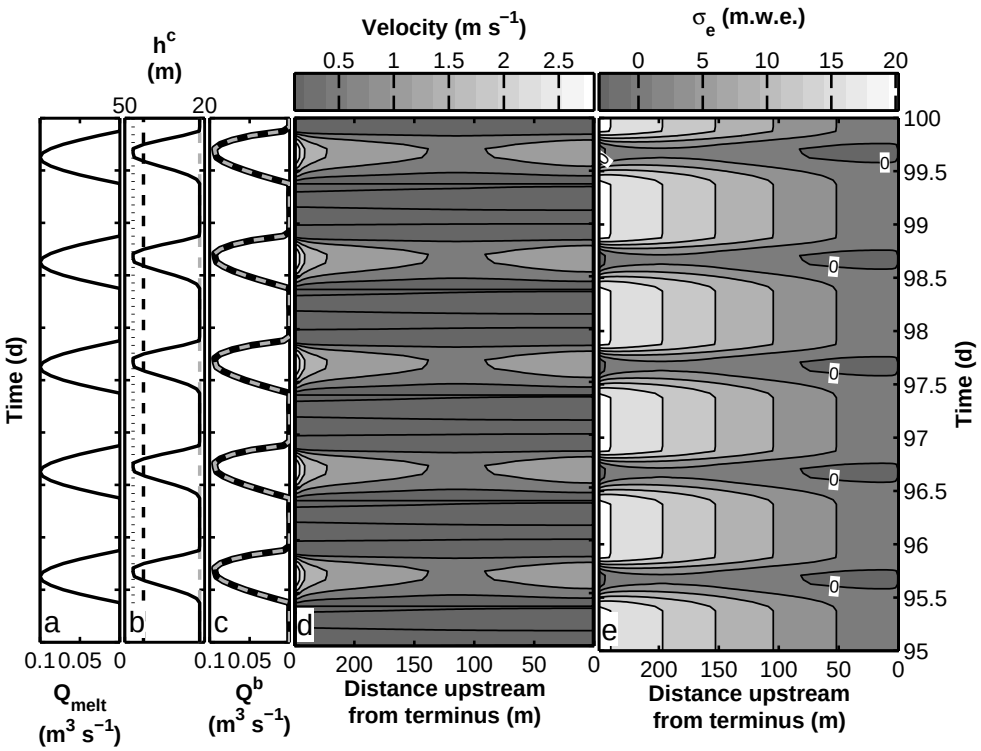

Figure 6.29: Final five daily cycles for the threshold case. (a) Discharge into the crevasse from the surface. (b) Water elevation in the upstream crevasse. Outlet elevation is given by the dotted line. (c) The thick line is discharge from the upstream crevasse to the water sheet. Dotted line within the thick line is water discharge at the terminus of the section. (d) Water velocity. Contour interval is 0.5 m s^{-1}. (e) Effective pressure. Contour interval is 4 m w.e.

Water velocities plotted in Figure 6.29d show the diurnal cycles. During daytime conditions, water velocities peak at about 2.9 m s^{-1} near the entrance to the water sheet. This maximum reflects a change in pressure gradient driving flow. There is also a maximum velocity during the

day of about 1.3 m s^{-1} near the terminus that results from a decrease in sheet thickness. Velocities during nighttime conditions hover near 0 m s^{-1} and can be slightly negative. Maximum nightly negative values for the 100 d simulation are approximately 10^{-3}–10^{-4} m s^{-1}. Overall, the negative velocity values are not especially significant because there is little discharge.

Figure 6.29e delineates the times and locations for changes in the effective pressures. The effective pressures are dominated by large temporal and spatial swaths of positive values. These indicate that the water pressure is below the ice overburden pressure. Negative effective pressures occur from about 1400h to 1900h along the adverse slope. During all other times, effective pressures are positive along the adverse slope. Spatially, the negative effective pressures occur from about 80 m upstream from the terminus, which is roughly 27 m from the start of the overdeepened wedge (Table 6.1). Other negative effective pressures occur within the first six meters from the upstream crevasse during the daily maximum in crevasse water elevation.

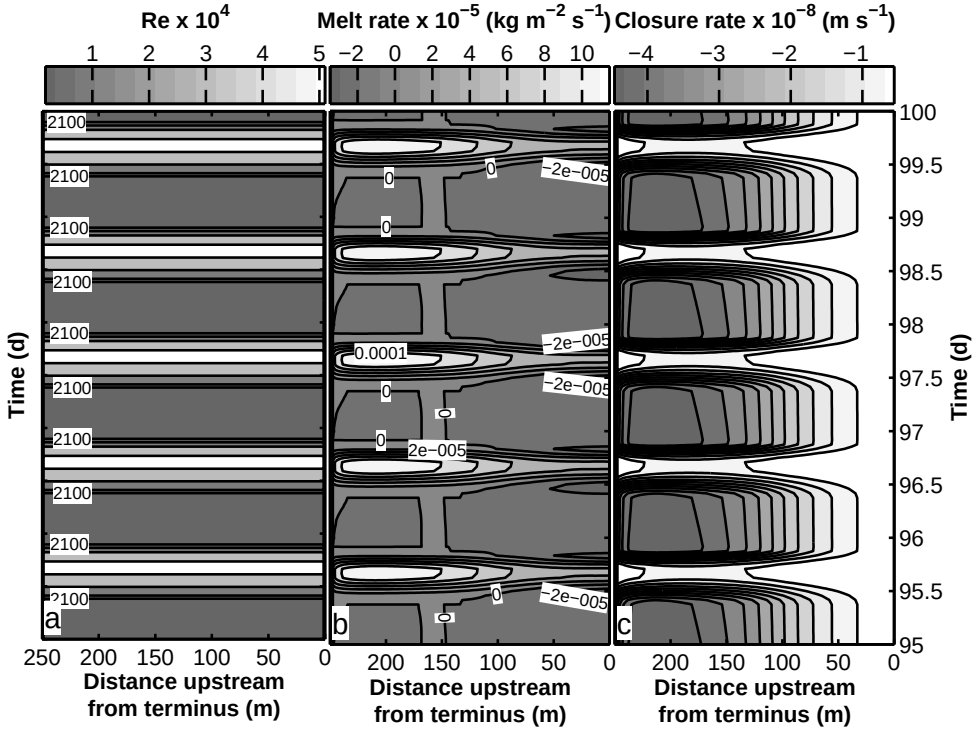

Figure 6.30: Final five daily cycles for the threshold case. These figures have the same input conditions as Figure 6.29. (a) Reynolds numbers. Contours are 2100, 10000, 30000, and 50000. (b) Melt rate. Contour interval is 2×10^{-5} kg m^{-2} s^{-1}. (c) Closure rate. Contour interval is 5.2×10^{-1} m s^{-1}.

The variability in the Reynolds numbers is subdued. Daily maxima are reached at approximately 1600h. During the night phase, Reynolds numbers are in the laminar range. Between 0900h and 1000h, flow becomes turbulent as meltwater infiltrates the upstream crevasse. Similarly, between 2100h and 2200h, flow becomes laminar as the crevasse drains to its minimum elevation. These changes mean that during nighttime conditions the melt rate (Fig. 6.30b) switches from the regular turbulent Nusselt number (eq. 2.36) to the laminar formulation (eq. 2.40b). The melt rate is approximately 0 kg m^{-2} s^{-1} during the nighttime.

Melt rates during daytime conditions contain much structure. Along the flat-bedded portion of the section, melt dominates in a fashion similar to Figure 6.6a. These melt rates increase as both the Reynolds number and temperature change increase and subsequently decrease during the day. Along the adverse slope, melt rates are initially near zero and decrease to a minimum at approximately 1100h. Melt rates then increase and maintain positive values between about 1330h and 1900h. Melt rates then return to negative values before entering the nighttime phase.

Closure rates are dependent on the effective stress. Therefore, the highly negative closure rates mimic the effective stresses. There is a juxtaposition of process in the daily cycles. Days are dominated by melting and freezing with very little closure. At night, closure dominates the evolution of the subglacial water sheet.

The net results of the cycles are plotted in Figure 6.31. Qualitatively, the water sheet thickness looks very much like the results for the steady flows (Fig. 6.3). However, the bulge around 100 m from the terminus is about 0.05 m shallower for the case of the daily cycles. In addition, there are daily variations in sheet thickness because of nightly closure and daily melt cycles. Total closure acts most effectively on the upstream portion of the sheet (Fig. 6.31c). Ice accretes at the terminus in this case (Fig. 6.31b). Maximum values are approximately 0.015 m at the terminus.

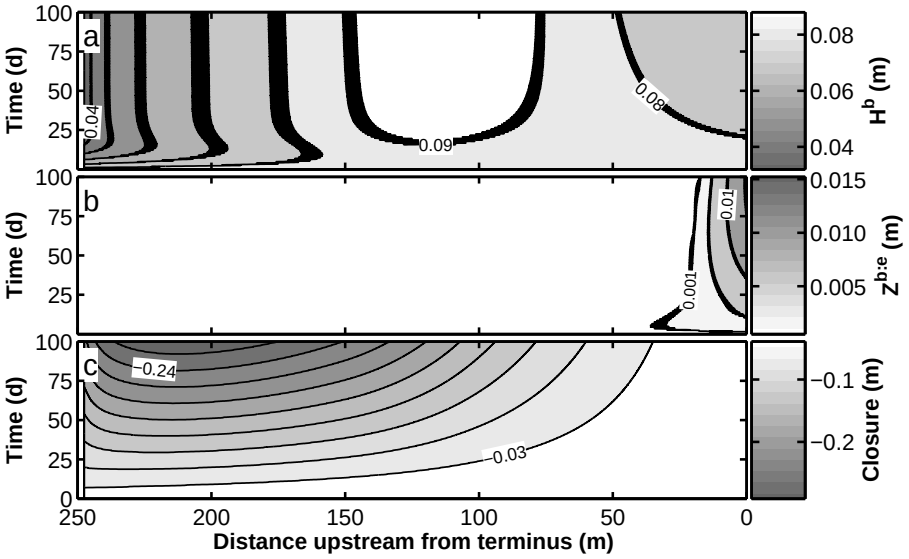

Figure 6.31: Results for the threshold case with daily cycles. Variability of the thickness of the contour lines is indicative of movement of the contours over the daily cycles. (a) Water sheet thickness. Contour interval is 0.01 m. (b) Accreted ice thickness. Contours represent 0.001, 0.05, 0.1, and 0.15 m. (c) Reconstructed total closure. Negative values indicate ice intrusion into the sheet. Contour interval is 0.03 m.

Overdeepened case: above-threshold section

Simulations for the above-threshold overdeepened section have many characteristics that are similar either to above-threshold simulations with a constant recharge rate or to the threshold case with diurnal forcing. Other characteristics bear a stark contrast to either of those simulations.

Figure 6.32a shows the exact same recharge condition as Figure 6.29a. However, the resultant crevasse water elevation and subglacial discharge have truncated peaks. Furthermore, the above-threshold case develops continuously over the course of the simulation. Structure is clearly visible in the evolution of the daily cycles (not shown). In the first day, the daily maximum crevasse water elevation reaches the glacier surface between 1500h and 1700h. By the end of the simulation, the crevasse water elevation reaches the surface between 1300h and 1900h (Fig. 6.32b).

Evolution of crevasse water elevations are driven by the decrease in discharge from the crevasse to the subglacial sheet over 100 d. Maximum discharge evolves from approximately 0.095 $m^3\ s^{-1}$ on the first model day to 0.053 $m^3\ s^{-1}$ on model day 100 (Fig. 6.32b). Discharge at the terminus closely mimics input discharge such that the maximum difference is approximately $2 \times 10^{-5}\ m^3\ s^{-1}$.

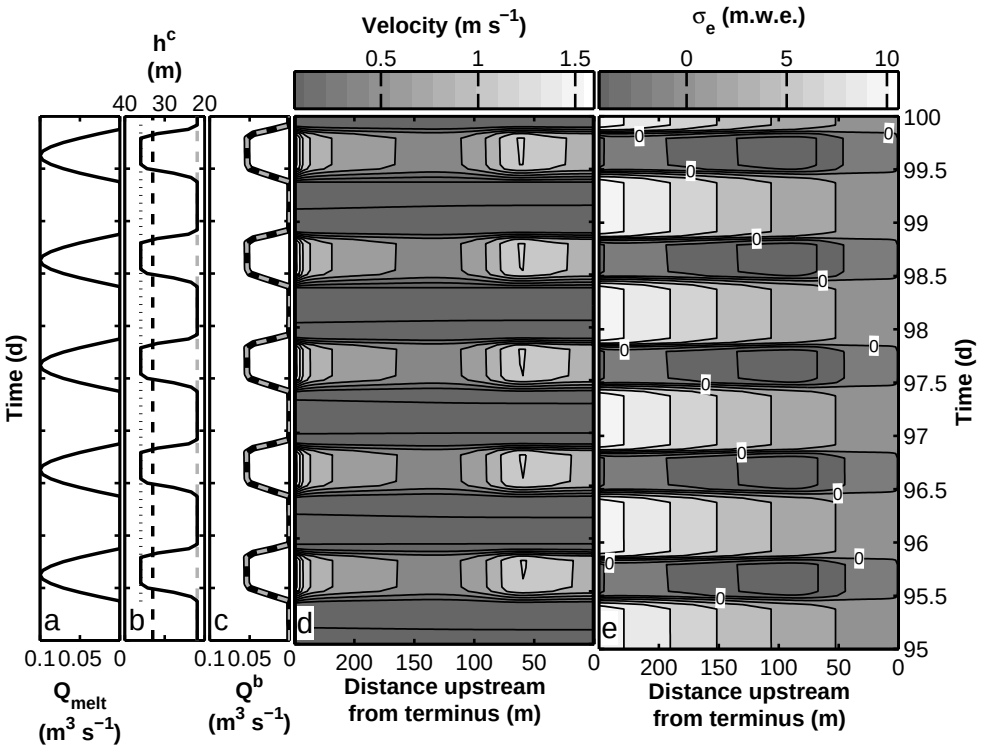

Figure 6.32: Final five daily cycles for the above-threshold case. (a) Discharge into the crevasse from the surface. (b) Water elevation in the upstream crevasse. Outlet elevation is given by the dotted line. (c) The thick line is discharge from the upstream crevasse to the water sheet. Dotted line within the thick line is water discharge at the terminus of the section. (d) Water velocity. Contour interval is 0.2 m s^{-1}. (e) Effective pressure. Contour interval is 2 m w.e.

The result of the conspicuous evolution of the input discharge is that transitions from the low-discharge, nocturnal portion of the cycle the high-discharge, diurnal portion of the cycle become progressively more rapid. Figures 6.32d and e illustrate these transitions for the velocity and effective pressure for the final five days.

For these five days, daily maximum velocities of about 1.7 m s^{-1} occur near the upstream entrance. Throughout the simulation, the location of the daily maximum is steady, but its magnitude evolves smoothly over the first 40 d from a minimum value of about 1.1 m s^{-1}. There is also a strong velocity maximum along the adverse slope approximately 60 m from the terminus. This feature is not constant, but begins at the terminus at approximately 20 d and moves upstream over the final 80 d.

Figure 6.32e illustrates that effective pressures during the day are negative along the the length of section. Morning and evening transitions are also abrupt. Because upstream crevasse water elevations reach the surface during much of the day, inlet conditions suggest that effective pressures are negative.

The temperature relative to the freezing point shows several interesting features (Fig. 6.33). Upstream, daily maximum temperature differences are near 2.5×10^{-3} °C, but nightly temperature differences drop to 0 °C. Along the adverse slope, daily maximum temperature differences are approximately 1.6×10^{-3} °C. These drop sharply with the evening transition to about -6×10^{-3} °C before recovering to values near zero. With the onset of the daily cycle, temperatures again drop well below freezing before climbing to the daily maximum.

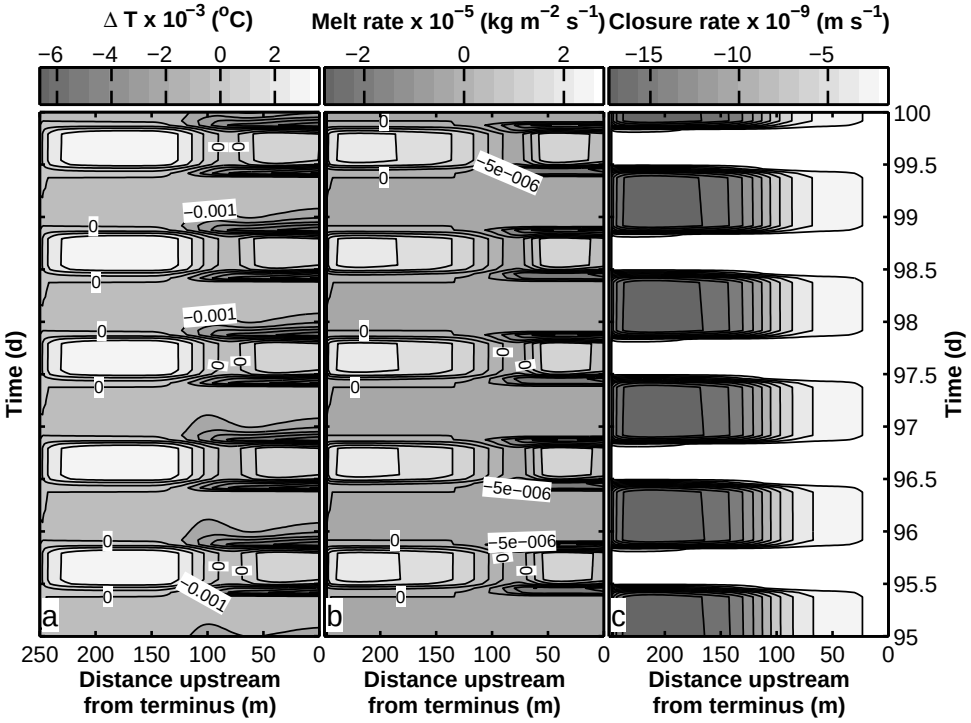

Figure 6.33: Final five daily cycles for the above-threshold case. (a) Difference between the water temperature and the melting point. Contour interval is 0.001 °C. (b) Melt rate. Contour interval is 5×10^{-6} kg m^{-2} s^{-1}. (c) Closure rate. Contour interval is 2.1×10^{-1} m s^{-1}.

The result of these temperature swings is that the melt rate is largely positive during the day, with the exception of about 60–90 m upstream from the terminus where they are slightly negative. During the morning and evening transitions, the melt rate along the adverse slope is strongly negative. Despite the temperature difference being fairly large during the night phase, water discharge is low. The result is that the melt rate is small and negative. Thus, accretion largely occurs during the morning and evening transitions. During the day, ice melts along the adverse slope. During the night, little happens via melt.

Closure of the water system is dependent on effective pressure. Because effective pressures are large at night, closure proceeds almost entirely at night (Fig. 6.33c). Therefore, during the morning and evening transitions, the subglacial sheet along the adverse slope is dominated by freezing. During the daytime, the sheet melts open. At night, ice intrudes into the sheet. Along the flat-bedded portion of the section, the sheet melts open during the day. At night, the ice intrudes vigorously into the flat-bedded portion.

The net result of these processes is shown in Figure 6.34. The sheet decreases on input owing to the high amount of closure. From about 100 m from the terminus to the terminus, closure of the sheet mainly occurs through accretion of ice. Maximum values are upwards of 0.03 m. This value is roughly the same as that of the steady flow (Fig. 6.9b).

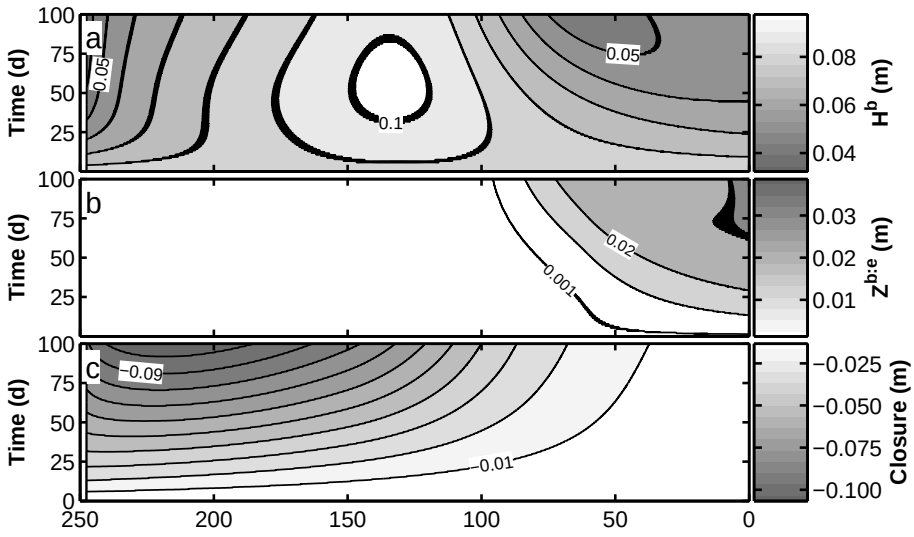

Figure 6.34: Results for the above-threshold case with daily cycles. Variability of the thickness of the contour lines is indicative of movement of the contours over the daily cycles. (a) Water sheet thickness. Contour interval is 0.01 m. (b) Accreted ice thickness. Contours represent 0.001, 0.1, 0.2, and 0.3 m. (c) Reconstructed total closure. Negative values indicate ice intrusion into the sheet. Contour interval is 0.01 m.

Overdeepened case: below-threshold section

Not surprisingly, the below-threshold section closes upstream, where ice thickness is greatest, and melts open near the terminus (Fig. 6.35). Upstream, relatively steady water depths are reached after approximately 20 d. Downstream, the water sheet dilates from melt throughout the integration time.

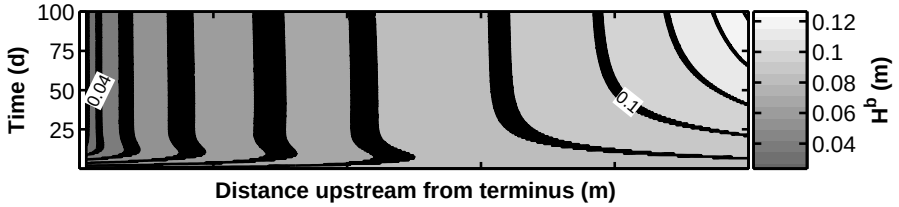

Figure 6.35: Water sheet thickness results for the above-threshold case with daily cycles. Variability of the thickness of the contour lines is indicative of movement of the contours over the daily cycles. Contour interval is 0.01 m.

Figures 6.36a, b, c show the recharge into the crevasse, the crevasse water elevation, and subglacial discharge, respectively for the last five days of the one hundred-day simulation. Relative to the recharge rate, crevasse water elevation and subglacial discharge are skewed to later times. This result is consistent with previous examples of daily cycles. The water pressure in the crevasse is above flotation for approximately two hours starting at 1515h, but does not reach the ice surface elevation. Figure 6.36b is the only diurnal example where this is true. Both the discharge into the subglacial water system and discharge at the terminus closely match each other and the recharge rate, which is consistent with the subglacial system accepting all water that feeds the upstream crevasse. Furthermore, the water system has similar peak discharge for the final 80 d of the simulation. Thus, these results are largely indicative of the system as for those days.

Figures 6.36d and e illustrate several important features of the heat-transfer of the below-threshold section. Temperature differences are mainly positive throughout the day, as would be expected for a system that melts open. However, along the adverse slope from 80 m to the terminus, accretion occurs during the morning and evening hours. Melt rates are largely negative along the adverse slope during the morning, evening, and night. However, these melt rates are small. Viscous dissipation overwhelms the other terms in the heat balance during the day. Thus, there is no accretion.

Lower discharge. If the peak recharge rate is lower, say 0.05 $m^3\ s^{-1}$, then it is possible to accrete ice along the below-threshold section. Figure 6.37a illustrates the water depth evolution. All other simulation parameters are the exact same as for Figure 6.35. Contrasting these to figures, it is clear that the evolution of the sheet is quite different for both. Sheet thickness decreases along the adverse slope for the lower recharge rate with a maximum accretion over 0.02 m (Fig. 6.37b). Upstream, the sheet thickness is lower for the low recharge rate because less water passes through the system. Thus, less melting occurs upstream.

For the lower-recharge case, Figure 6.38 is equivalent to Figure 6.36 for the higher-recharge case. Clear differences exist because the discharges are approximately half (Fig. 6.38a, c). Crevasse water elevation is quite similar for both cases, but the lower-discharge case only has values over flotation for about one half hour around 1700h each day.

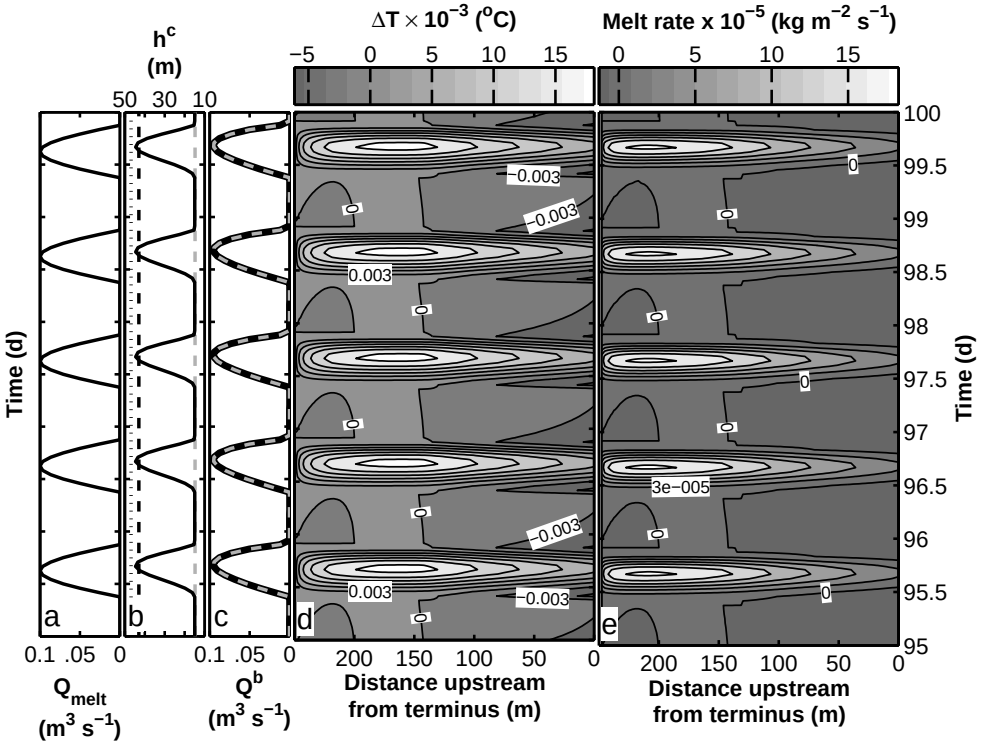

Figure 6.36: Final five daily cycles for the below-threshold case. (a) Discharge into the crevasse from the surface. (b) Water elevation in the upstream crevasse. Outlet elevation is given by the gray dashed line. Maximum water elevation is given by the black dotted line. The black dashed line indicates the flotation level. (c) The thick line is discharge from the upstream crevasse to the water sheet. Dashed line within the thick line is water discharge at the terminus of the section. (d) Temperature depression. Contour interval is -0.003 °C. (e) Melt rate. Contour interval is 3×10^{-5} kg m^{-2} s^{-1}.

More telling are the temperature depressions and melt rates. Figure 6.38d shows that temperature depressions are lower during the day for all areas of the sheet. During the evening and morning the temperature depressions are higher along the adverse slope, indicating that there is less accretion for this case relative to the higher-recharge rate case. Figure 6.38e illustrates that the melt rates are less by about 4 kg m^{-2} s^{-1}.

For both cases, during the morning and evening, accretion occurs along the adverse slope. Nighttime is insignificant in terms of the accretion because discharge is low. Even with negative temperature differences, the lack of discharge drives the melt rate to zero. During the day, for the higher-recharge case, viscous dissipation overwhelms the other terms in the heat balance because the velocity is relatively high. The total daytime melt exceeds the morning and evening accretion. In contrast, daytime melt does not exceed morning and evening accretion for the lower-recharge case.

The effective pressures for the lower-discharge case are positive (Fig. 6.39a). This result suggests that even with accretion, the below-threshold case favors a conduit. However, after significant accretion, the conduit may give way to a hybrid conduit–sheet form such as broad- and flat-channels (*e.g.,* Hooke *et al.*, 1990). Furthermore, closure rates are strongly positive at night (Fig. 6.39b) and positive, but near zero during the day.

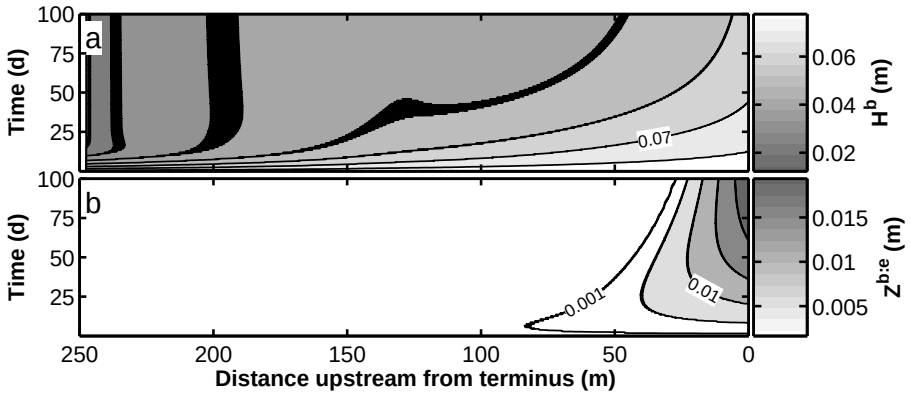

Figure 6.37: Results for the below-threshold case with diurnal forcing and lower recharge rate. Variability of the thickness of the contour lines is indicative of movement of the contours over the daily cycles. (a) Water sheet thickness. Contour interval is 0.01 m. (b) Accreted ice thickness. Contours represent 0.001, 0.05, 0.1, 0.15, and 0.2 m.

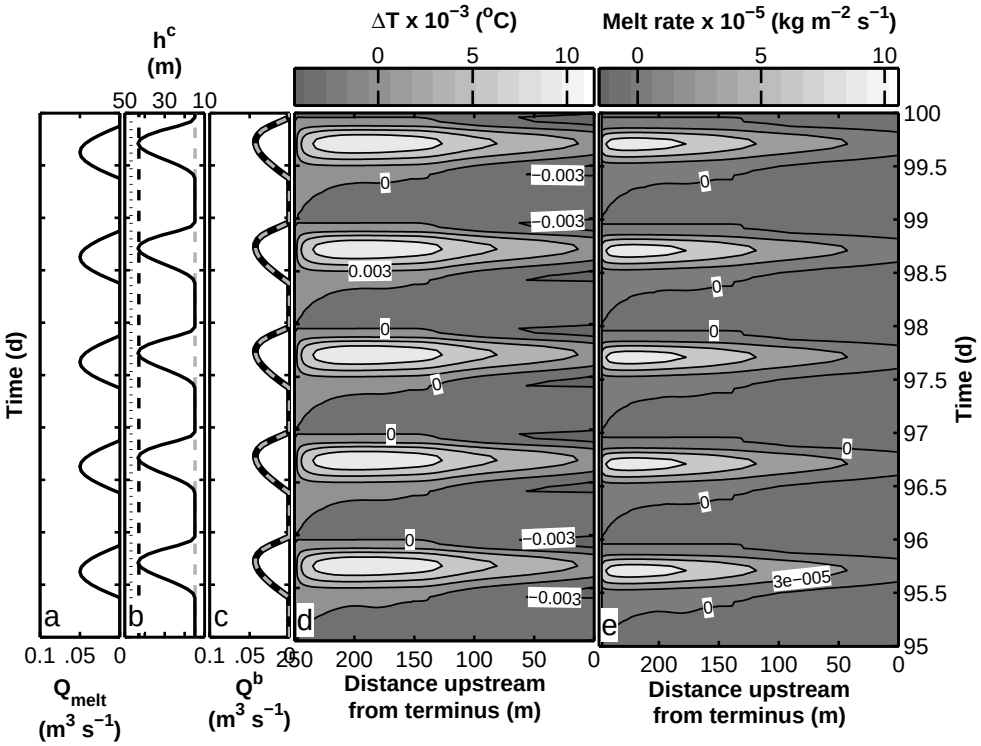

Figure 6.38: Final five daily cycles for the below-threshold case with lower discharge. (a) Discharge into the crevasse from the surface. (b) Water elevation in the upstream crevasse. Outlet elevation is given by the gray dashed line. Maximum water elevation is given by the black dotted line. The black dashed line indicates the flotation level. (c) The thick line is discharge from the upstream crevasse to the water sheet. Dashed line within the thick line is water discharge at the terminus of the section. (d) Temperature depression. Contour interval is -0.003 °C. (e) Melt rate. Contour interval is 3×10^{-5} kg m^{-2} s^{-1}.

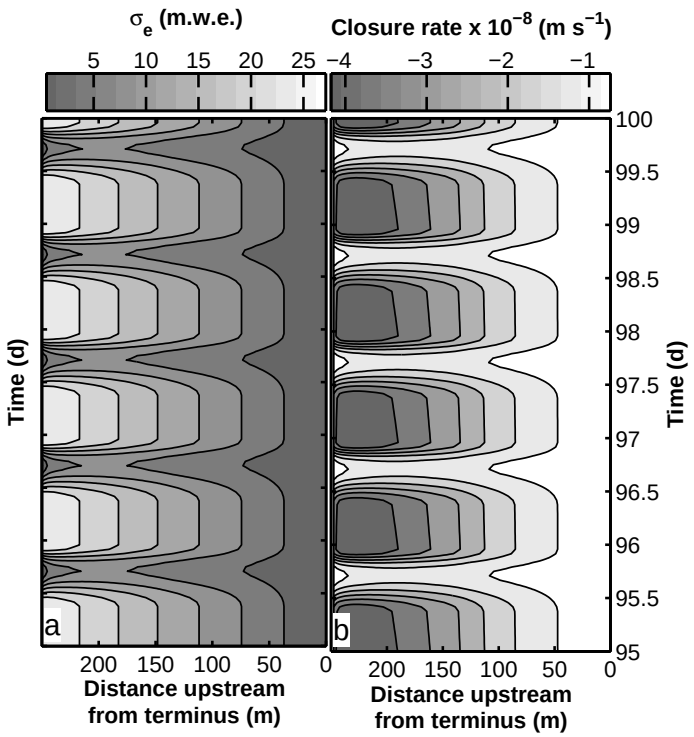

Figure 6.39: Final five daily cycles for the below-threshold case with diurnal forcing and lower recharge rate. (a) Effective pressure. Contour interval is 4 m w.e. (b) Closure rate. Contour interval is 6.1×10^{-9} m s^{-1}.

6.3.2 Discussion

The diurnally forced simulations suggest that there are several fundamental time periods for water flow. I break these up into morning, daytime, evening and nighttime. Morning and evening conditions are similar but opposite in sign and are shoulder or transition periods between daytime and nighttime conditions.

1. During morning, crevasse water elevation rises from its nightly minimum. Water discharge rises in concert with the input water elevation. Reynolds numbers indicate an almost immediate onset of turbulence with the beginning of the daily cycle. Ice accretes to the glacier base. Effective pressures decrease, and sheet closure occurs but is low.

2. During daytime, crevasse water elevation rises above the flotation limit. In some cases, crevasse water elevation reaches the glacier surface. Water flow reaches its peak discharge, and viscous dissipation melts ice from the base of the glacier. Effective pressure reaches its maximum and sheet closure ceases or is very low. Accretion is possible, but it is low.

3. During evening, crevasse water elevation and subglacial water discharge fall. Ice accretion occurs. Effective pressures decrease. Sheet closure occurs, but is low. The evening extends up to one hour beyond the cessation of recharge into the crevasse, indicating that there is a lag caused by the subglacial drainage system.

4. Through the night, crevasse water elevation drops to its nightly minimum, and water discharge is low to zero. Effective pressures are high, and sheet closure accelerates. Temperature depressions are largely below freezing; however, the lack of discharge precludes significant accretion. The nighttime ends punctually with the onset of melt.

In conjunction with subglacial discharge, ice-bed configuration determines how daily cycles behave. Upstream ice thickness limits maximum water pressure to approximately 110% of flotation pressure. Maximum water pressure at inlet and atmospheric pressure at water outlet help to determine along-path pressure gradients that drive water flow. The speed at which the water system passes through the shoulder periods is determined by the pressure gradients and the bed-to-surface slope ratios. For example, the above-threshold section has rapid transitions in less than a few hours. In contrast, the lower discharge simulations for the below-threshold section vary gently throughout the diurnal cycle.

In the case of steady recharge, maximum accretion focuses some distance back from the terminus. In the case of diurnally varying recharge, maximum accretion occurs at the downstream terminus. Studies at discharge vents at Matanuska Glacier (Lawson *et al.*, 1998), water outlets at Bering Glacier (Fleisher *et al.*, 1998), and at various locations in Iceland (Roberts *et al.*, 2002), indicate that much accretion can occur near the outlet. However, glaciers with exposed basal ice possibly accrete ice upstream and transport these accreted layers through glacier movement. Radar profiles at Matanuska Glacier indicate that the basal ice thickness is nearly constant through the overdeepening and suggest that net accretion occurs upstream (Lawson *et al.*, 1998). However, where this accretion occurs along the adverse slope is not clear, but it most likely occurs at the farthest downstream extent of the adverse slope.

Net accretion for the longitudinal sections is in the range 0.01–0.04 m. If a hundred days

accurately represents a melt season, then net accretion is 1–4 m per century. This amount of accretion is one quarter to one half of an equivalent amount at Matanuska Glacier (Lawson *et al.*, 1998). However, bed-to-surface slope ratios are less aggressive in the simulations presented here than at Matanuska Glacier. Modeled accretion rates are compatible with field data for results presented here.

In terms of sheet to conduit transitions, there may be both spatial and temporal transitions based on the effective pressure criterion discussed in Section 6.2. These transitions can occur for either threshold or above-threshold longitudinal sections. During nighttime, effective pressures are high, and closure dominates the subglacial water system. There is very little water flux during the night, and as a result, there would be little water to channelize. However, if there are incipient channels either melted into the ice or eroded out of the bed, then water would retreat to these hydraulic lows during the night.

During daytime, an incipient channel would flood laterally into a subglacial floodplain to create a sheet. For the above-threshold section, the entire subglacial system would transform into a sheet system for the entire overdeepening illustrated here. For the threshold section, only part of the area along the adverse slope transforms to a sheet. Broadly speaking, there is most likely a range of intermediate behaviors between these two, whereby different extents of the overdeepening transform between sheets and conduits. More extreme morphological switching behaviors may exist for higher bed-to-surface slope ratios.

Below-threshold section effective pressure results are complementary to similar results discussed in Section 6.2. Effective pressures are positive, but accretion occurs. A typical channel might not be favored by the hydraulic system, but water cannot spread into a sheet. Again, a logical conclusion is that there is an intermediate channel-like form that can conduct water. In addition, these intermediate cross-sections may be dependent on discharge. For the lower-discharge case, net accretion occurs, but for the higher-discharge case, there is no net accretion. Therefore, an intermediate channel cross-section may be favored by lower discharge flows. It is worth noting, however, that R-channels are only a default cross-section. Other forms undoubtedly exist subglacially.

6.4 Sediment transport

By extending the governing equations to include sediment transport, one can examine numerous other questions of glacier hydrology and erosion. The two questions that are most pertinent to glaciohydraulic supercooling are: (1) Under what conditions does the bed aggrade or erode? and (2) How much sediment can be accreted to the base of the glacier? The first question pertains to how the configuration of the ice and bed evolves. Specifically, Alley *et al.* (2003b) hypothesized that alluvial glacier beds should tend toward threshold bed-to-surface slope conditions. Answering the second question gives insight into how glaciers entrain sediment. In particular, the amount of entrainment can be used to bound both processes and rates along a glacier bed.

The sediment transport equations build upon the clear water equations.[13] Additional terms are introduced to account for erosion and sedimentation along the bed. When there is no sediment present in the flow, the sediment transport equations collapse to the clear water equations.

[13]I designate the equations in Chapter 2 as "clear water" equations. However, an alternative but equally valid designation is "non-erosive" or "hard bed" equations for the situation when the bedrock is immobile.

6.4.1 Model details

In order to implement sediment transport, several parameters are necessary. These parameters are summarized in Table 6.4. The sediment density could take a range of values, but I assume a value of 2500 kg m^{-3}, which is close to the density of quartz sand (∼2650 kg m^{-3}). von Karman's constant is a constant of proportionality for the turbulent mixing length. Its value presented here is in ordinary usage in the sediment transport literature.

Table 6.4: Model parameters specific to sediment transport.

	Parameter	Value	Units	Notes
Sediment entrainment coefficient	C_3	1	[unitless]	see eq. (4.4)
Median grain diameter	D_{50}	0.001	m	see eqs. (4.20), (4.21), (4.30)
Grain diameter of the 90th percentile	D_{90}	0.0018	m	see eq. (E.17)
Friction coefficient	f_d	0.16	[unitless]	see eq. (2.24)
Grain friction coefficient	f'_d	0.0176	[unitless]	see eq. (4.31)
Adaptation length	L^s	10	m	see eq. (4.4)
Porosity of the bed	n_p^s	0.35	[unitless]	see eq. (4.7)
Active fraction of the bed	n_a^s	0.5	[unitless]	see eq. (4.23)
Maximum crevasse recharge rate	Q_{melt}	0.05	$m^3\ s^{-1}$	see eq. (F.10)
Sediment mass density	ρ^s	2500	kg m^{-3}	
von Karman's constant	κ^s	0.4	[unitless]	see eq. (E.12)

Other parameters are related to the semiempirical sediment transport formulae of van Rijn (1984a,b). The bed porosity is exactly the value put forth in these papers. In addition, median and 90th percentile grain sizes are meant to coincide with the sand-bed equations. The median grain size represents coarse sand, and the 90th percentile represents very coarse sand. Other grain size choices would be acceptable; however, I weight these choices on the large size of sand to account for the poorly sorted nature of glacial sediments. Because I assume that the silt and finer sizes behave as fine sand, these are accounted for in the suspended load calculations. The active fraction of the bed n_a^s, is based on the sediment distribution used in the closure relationship. Exactly half the bed is composed of sand and smaller grain sizes. All of these sizes are assumed to be mobile. Data from Matanuska Glacier corroborate these assumptions where sand and silt appear to be the dominant grain sizes discharged (Lawson, 1979).

With the sediment entrainment coefficient set as unity, the concentration of sediment entrained in the ice is assumed to be exactly the same as the concentration of sediment in the flow. When the sediment entrainment coefficient is set greater than unity, the assumption is that the sediment entrainment processes are efficient at extracting sediment from the water. Processes, such as frazil ice filtering of sediments, are acknowledged from field studies (*e.g.,* Lawson *et al.*, 1998). Without baseline studies, it is impossible to know what value is acceptable for the sediment entrainment coefficient. I make the conservative assumption that this factor is unity.

The adaptation length L^s, is the distance over which nonequilibrium flow becomes an equilibrium flow. For bed load, this value should be low (∼1 m). For suspended load, this value can be higher. Furthermore, as reviewed in Chapter 4, the adaptation length governs numerical convergence. Smaller values require longer times to converge. The value of 10 m strikes a bal-

ance between physical definition of L^s and the computational difficulty of simulating sediment transport. In addition, I have tested lower values of L^s but have found little overall difference in the results.

In Table 6.4, I assign the grain roughness coefficient f'_d as 0.0176. This value accounts for 11% of the overall friction along the bed. Even though this value is lower than the value of 15–20% discussed in Chapter 4, it still allows sufficient sediment motion. The reason the grain roughness can be set at such a low value is that the friction coefficient f_d, is set high relative to subaerial fluvial values. In addition, I choose this value based on numerical tests that suggest that values at 15–20% of overall friction are excessive.

6.4.2 Initial and boundary conditions

In Table 6.4, I lower the maximum crevasse recharge rate to 0.05 $m^3\ s^{-1}$. While lower than the value of 0.1 $m^3\ s^{-1}$ used in the previous simulations, it is within the range of 0.001–0.3 $m^3\ s^{-1}$ observed at field locations and discussed previously. Lower discharge aids in numerical solution of the governing equations. The evolution of the subglacial discharge is important to sediment transport, and I discuss how the recharge rate is relevant to the subglacial system later in this chapter. Finally, the upstream recharge rate follows the diurnal cycle illustrated in Figure 6.28.

Suspended and bed load sediment concentrations in the subglacial water system are initialized to equilibrium conditions using the semiempirical sediment transport relationships. The initial water velocity is calculated as a steady state velocity. Sediment concentrations in the accreted ice are assumed to be zero.

Upstream boundary conditions on sediment transport are set such that there is no upstream gradient in sediment concentration: $\partial\lambda_s^s/\partial s = \partial\lambda_b^b/\partial s = 0$. Another acceptable boundary condition would be that $\lambda_b^b = \lambda_b^b = 0$, implying that influent water contains no sediment. The trouble with specifying concentrations is that the subglacial water is probably not clear prior to entering the longitudinal section. Even though water that recharges a subglacial hydraulic system is commonly sediment-free, the upstream crevasse in the present scenario is simplified representation of the upstream water supply. While neither sediment boundary condition is ideal, the condition on the concentration gradient more closely describes the subglacial system.

All other initial and boundary conditions are those for the clear water simulations. In addition, these simulations are only for subglacial hydraulic sheets.

6.4.3 Results

Overdeepened case: Threshold section

The crevasse water elevation evolves such that the water elevation reaches the surface on day 12 during the daytime (Fig. 6.40a). For the first 37 d, the nightly water elevation returns to approximately 22 m, which is the elevation of the terminus. The subglacial system remains saturated at all times. After day 37, the minimum nightly crevasse water elevation rises over the remainder of the simulation to about 32 m. This nighttime rise indicates that the crevasse is not draining completely.

The crevasse does not drain completely during the nighttime because the subglacial discharge is decreasing over the course of the model run. Figure 6.40b shows that the maximum daily discharge is exactly the recharge condition, 0.05 $m^3\ s^{-1}$. Over the course of the simulation, discharge decreases to approximately 0.004 $m^3\ s^{-1}$ during daytime and 0.003 $m^3\ s^{-1}$ during

nighttime. Nighttime discharge is coincident with nonzero crevasse pressure gradients driving water flow.

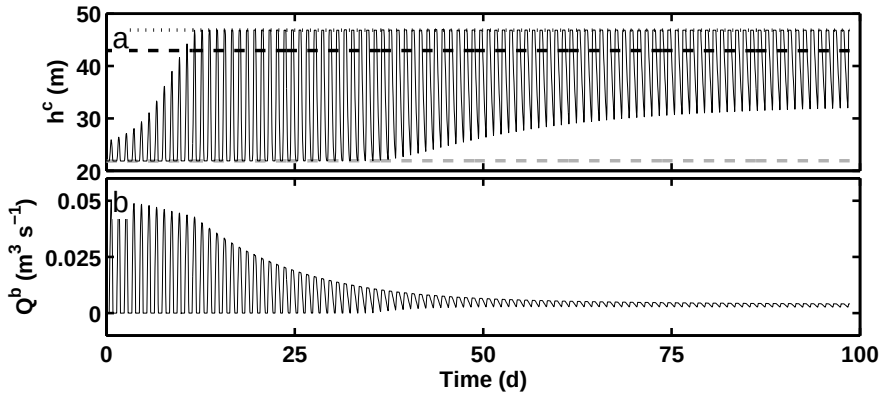

Figure 6.40: Daily cycles with erosion: Threshold case. (a) Water elevation in the upstream crevasse. Uppermost dotted line is the elevation of the glacier surface. Dark dashed line indicates the equivalent flotation elevation. Lowermost, gray dashed line is the elevation of the terminus. (b) Discharge from the crevasse to the subglacial water system.

Discharge falls over the course of the simulation because the water sheet decreases in thickness. Figure 6.41a illustrates the decreases of the water depth from its starting value near 0.1 m to below 0.01 m. This occurs over the first 85 d of the simulation. After about 88.7 d, low water discharge and water depth cause the bedload equations to produce inaccuracies in the numerical integration. However, the numerical solver is able to integrate until 98.7 d. In consequence, I show only up until day 85. Failure of the numerical integration scheme is a consequence of the limited degrees of freedom of the modeled physical system, as I discuss below.

Candidate processes for closing the water sheet are ice intrusion, sedimentation, and accretion. Figure 6.41b rules out ice intrusion because closure is extremely small over the 85 d. Sedimentation is clearly a factor in the decrease of water depth (Fig. 6.41c). Much sedimentation (>0.1 m) occurs at the upstream end of the adverse slope. At the upper end of the adverse slope, sedimentation occurs, but is slow relative to the upstream end, especially after day 40, when little sedimentation occurs.

Figure 6.42a illustrates that accretion is low for the threshold case. Total accretion is slightly above 0.01 m near terminus. This result is consistent with all other simulations of threshold sections, where the accreted ice thickness is near zero. Furthermore, accretion begins downstream of the onset of the adverse slope. After 25 d, accretion begins at 55 m from the terminus, which is downstream of the onset of the supercooled slope at about 107 m.

The total volumetric concentration of sediment in the ice varies near the terminus but is low. Relatively high concentrations occur for low accreted ice thicknesses. These concentrations occur prior to 37 d. After 37 d, concentration drops off in the accreted ice.

The daily cycles illustrated in Figures 6.43a–c detail the relationship of crevasse recharge, crevasse water elevation, and subglacial discharge for days 80–85. Despite large variations in the recharge, there is little variation in the discharge to the subglacial system from the upstream crevasse. Downstream discharge mimics upstream discharge in the same manner as all previous simulations. In addition, the crevasse water elevation lags the recharge rate by about three hours. During nighttime, the crevasse water elevation drops nearly linearly because the subglacial discharge is approximately constant.

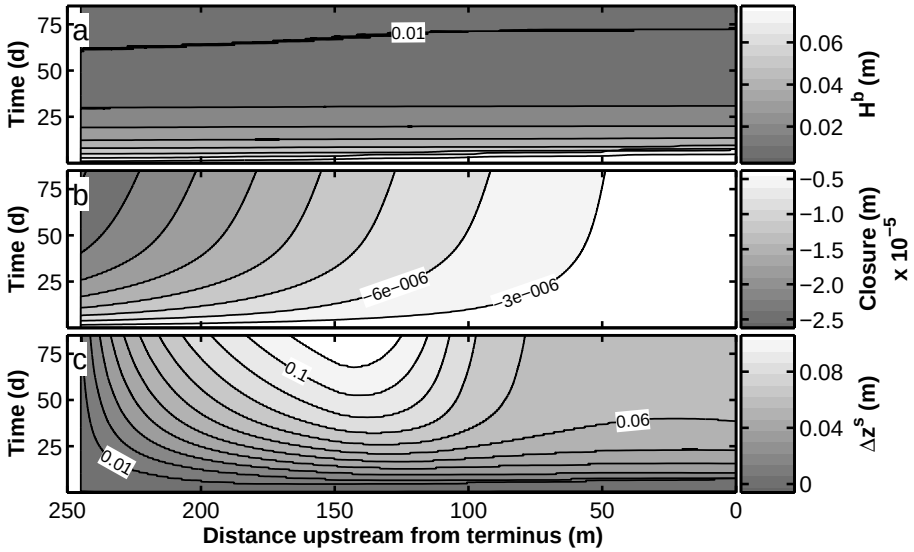

Figure 6.41: Daily cycles with erosion: Threshold case. (a) Thickness of the subglacial water sheet. Contour interval is 0.01 m. (b) Total ice closure. Contour interval is 3×10^{-6} m. (c) Change in bed elevation. Positive values indicate sedimentation. Contour interval is 0.01 m.

The daily variations in melt rate illustrated in Figure 6.43c show that accretion occurs from about midnight to noon. Melt occurs during the remainder of the day. Along the flat-bedded portion, melt occurs at all times but is highest from 1600h to 1700h. Accretion occurs only on the adverse slope. Because water discharge is constant, the system is able to sustain accretion at night. This result contrasts with the clear water case where discharge was zero and accretion was negligible at night.

Figure 6.43e shows the total sediment supply, both bed load and suspended load, from the bed. Where the supply is negative, sedimentation occurs. During nighttime, there is little sedimentation. During the day, there is much sedimentation with most of it occurring in the early part of the afternoon along the flat-bedded portion of the section. Sedimentation drops off sharply from 140 to 75 m from the terminus as the water loses its sediment load. Because the water is losing its sediment load, there is little sediment that can be accreted. Thus, in Figure 6.42b, the drop in sediment concentration occurs because accretion happens at night while sediment transport occurs during the day.

Prior to day 37, sediment transport and accretion occur at nearly the same time (not shown). During the early part of the simulation, accretion still occurs during the shoulder times of morning and evening, but there is enough sediment in the flow that elevated concentrations are captured by the accreted ice.

Figures 6.44a–c show the total sediment load in the subglacial system, the suspended load, and the bed load, respectively. Sediment load is largely dependent on the daily discharge being relatively high. Even though the discharge varies by only about 0.001 $m^3\ s^{-1}$ from daytime to nighttime, this is enough to stimulate sediment transport. In addition, concentration in the water exceeds concentration in the ice by two orders of magnitude. Both suspended and bed load sediment concentrations are low. These are approximately factors of 5–10 lower than concentrations observed at Matanuska Glacier (Lawson *et al.*, 1998).

Water velocities range from 0.3 to 0.5 m s^{-1}. In terms of the Hjulström diagram (Fig. 4.2), these velocities should imply erosion. However, the Hjulström diagram was developed for rivers

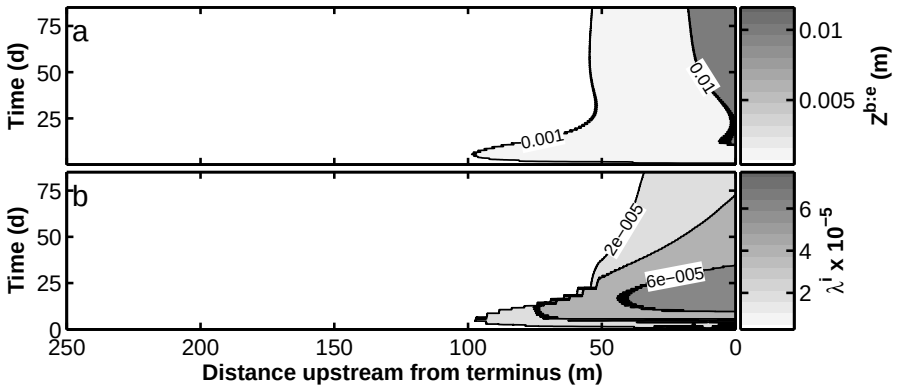

Figure 6.42: Daily cycles with erosion: Threshold case. (a) Accreted ice thickness. Except for the first contour at 0.001 m, the contour interval is 0.01 m. (b) Concentration of sediment in the basal ice. Contour interval is 2×10^{-5}. Blocky contours upstream prior to day 25 are a numerical artifact and result from low accretion ice thickness.

with higher hydraulic radii than simulated subglacial sheets. For comparison, Reynolds numbers have a daytime peak at about Re=2700 during days 80 to 85. At night, Reynolds numbers drop to about 1600. In consequence, the subglacial system is tending toward a low-flow state that is not accurately captured by the Hjulström diagram.

In sum, the hydraulic system becomes choked with sediment over the course of the simulation. Silting of the hydraulic system prevents significant drainage of water. Because of the blockage, the numerical solver eventually fails because there is no optional routing for the discharge. Sediment choking is compatible with field observations. Furthermore, as the subglacial system chokes with sediment, accretion switches from occurring during morning and evening to occurring at nighttime. As a result, ice that accretes at nighttime has low sediment concentrations. Overall, ice accretion is low when the hydraulic system chokes.

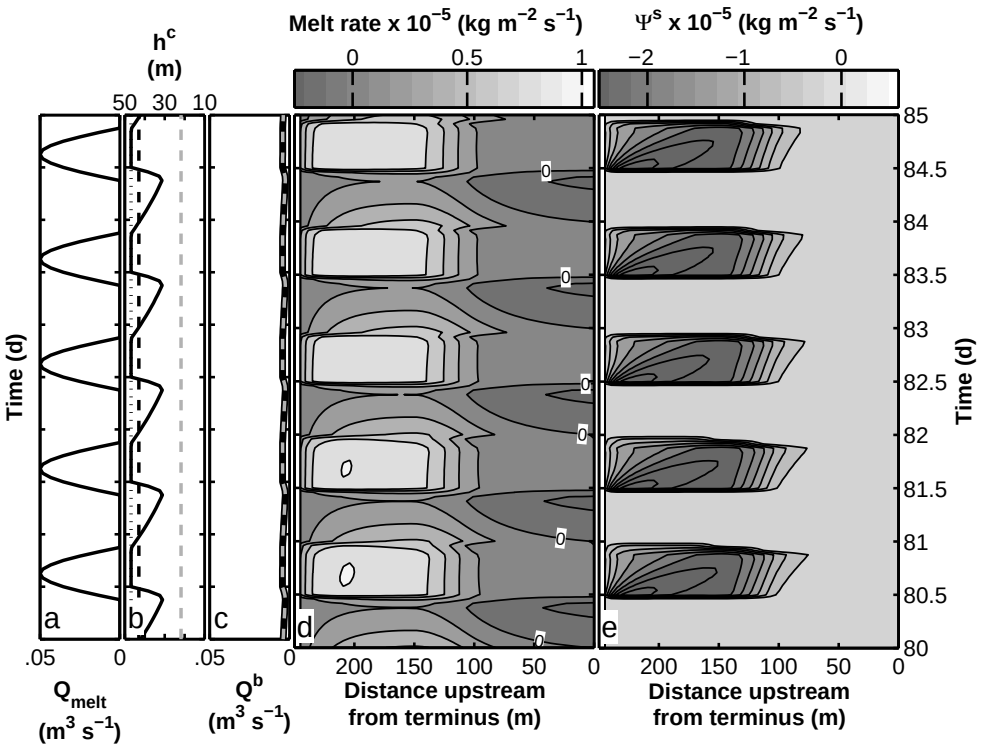

Figure 6.43: Daily cycles with erosion: Threshold case. (a) Recharge into the subglacial water system. (b) Water elevation in the upstream crevasse. Dark dotted line is the glacier surface elevation. Dark dashed line is the flotation elevation. Light dashed line is the elevation of the glacier terminus. (c) Water discharge. Dark line denotes water discharge into the subglacial water system. Light dashed line overlying the dark line denotes water discharge at the terminus. (d) Melt rate. Contour interval is 2×10^{-6} kg m^{-2} s^{-1}. (e) Sediment supply from the bed. Positive values indicate erosion. Contour interval is 3.6×10^{-6} kg m^{-2} s^{-1}.

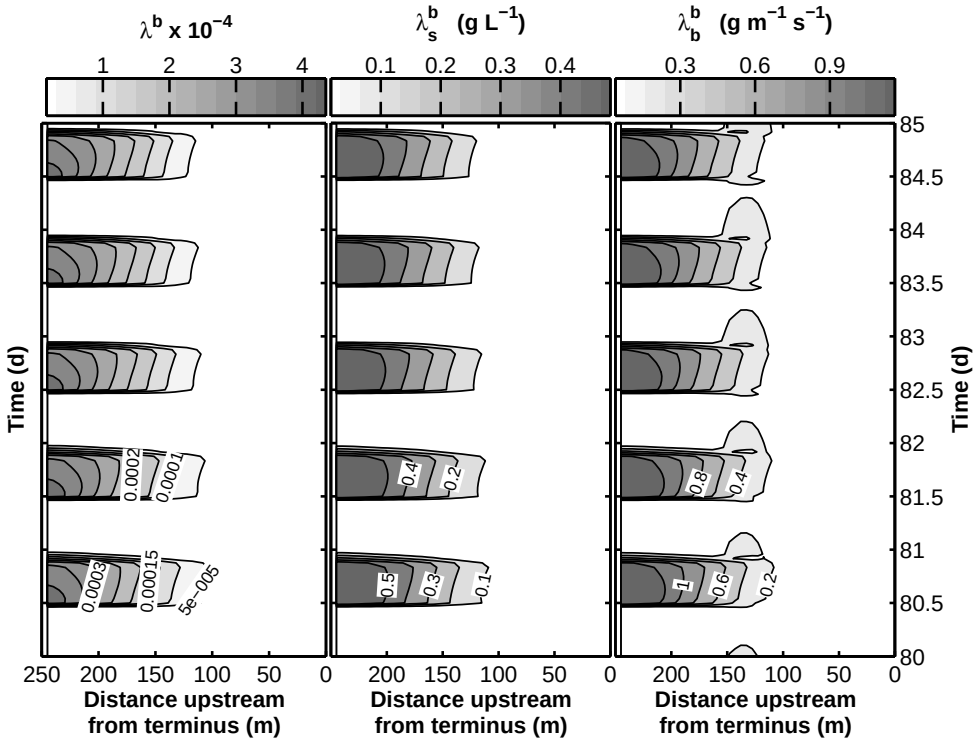

Figure 6.44: Daily cycles with erosion: Threshold case. (a) Total concentration of sediment in subglacial water. Contour interval is 5×10^{-5}. (b) Concentration of suspended sediment in subglacial water. Contour interval is 0.1 g L^{-1}. (c) Bed load transport rate in subglacial water (converted from volume concentration and velocity). Contour interval is 0.2 g m^{-1} s^{-1}.

Overdeepened case: Above-threshold section

The crevasse water elevation reaches the surface of the glacier after 21 d (Fig. 6.45a). During the remaining days of the simulation, crevasse water elevation reaches the surface of the glacier during the daytime. In contrast to the threshold section, the above-threshold section is able to drain completely at night. The crevasse is able to drain in the above-threshold case because the ice thickness is about 11 m thinner than the threshold case.

After 21 d, the maximum daily discharge to the subglacial hydrology from the crevasse decreases from 0.05 to about 0.008 $m^3\ s^{-1}$. Minimum nighttime discharge is negligible. There is not a particular discharge that the above-threshold case strives to maintain; however, the subglacial discharge decreases significantly.

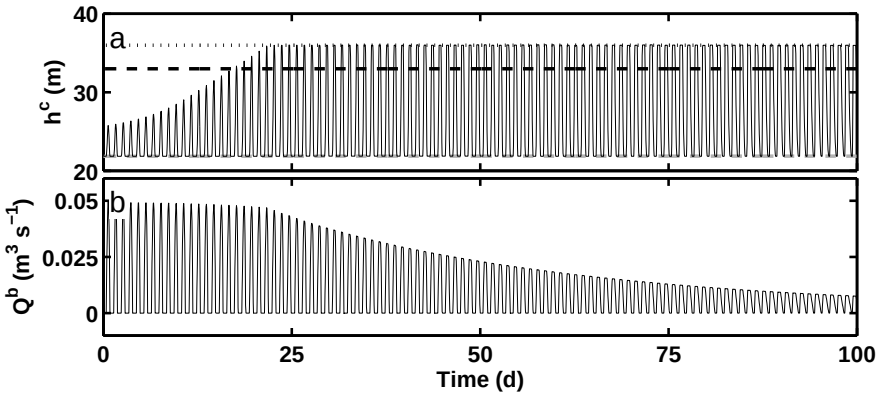

Figure 6.45: Daily cycles with erosion: Above-threshold case. (a) Water elevation in the upstream crevasse. Uppermost dotted line is the elevation of the glacier surface. Dark dashed line indicates the equivalent flotation elevation. Lowermost, gray dashed line is the elevation of the terminus. (b) Discharge from the crevasse to the subglacial water system.

Minimum water depths are below 0.02 m but above 0.01 m after 80 d (Fig. 6.46). The water depth responds nearly in unison over the entire length. Downstream water depth evolution precedes the upstream end by a day or two. Much of the evolution of the water sheet occurs within the first 21 d when the sheet drops over 0.03 m. Figure 6.46b illustrates that ice intrusion into the sheet is negligible. Maximum intrusion occurs upstream and is about 2×10^{-5} m. In terms of water depth, ice intrusion is almost irrelevant.

However, sedimentation is not negligible. Figure 6.46c shows that over the course of 100 d, maximum sedimentation of about 0.1 m occurs at the start of the adverse slope. Sedimentation also occurs along the adverse slope for most of the first 50 d. During the final 50 d, the erosion steps upstream from the terminus to about 100 m from the terminus by the end of the simulation.

Ice accretion is also important in reducing water depth over the course of 100 d. Figure 6.47 shows that maximum accretion is at the terminus and is over 0.06 m at 100 d. This amount of accretion is roughly double the amount for daily water cycles with clear water flows. The spatial lag between the onset of the adverse slope and the onset of accretion is also smaller for the case with sediment motion.

The volume concentration of sediment in the ice varies but is greatest near the terminus. Maximum values are about 1.3×10^{-4}. After about 60 d, the concentration of sediment in the ice begins to decrease.

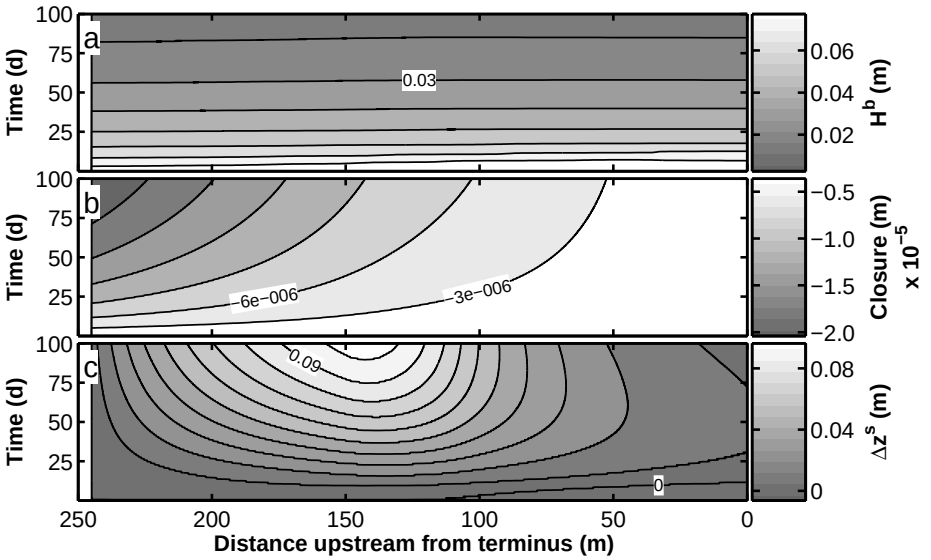

Figure 6.46: Daily cycles with erosion: Above-threshold case. (a) Thickness of the subglacial water sheet. Contour interval is 0.01 m. (b) Total ice closure. Contour interval is 3×10^{-6} m. (c) Change in bed elevation. Positive values indicate sedimentation. Contour interval is 0.01 m.

Meltwater recharge to the upstream crevasse, crevasse water elevation, and discharge in the subglacial water system are illustrated in Figures 6.48a–c, respectively. Response of the crevasse water elevation follows the onset of daytime conditions at 0900h. Maximum crevasse water elevation is reached by noon, and crevasse water elevation begins to drop at 2000h. The system has a time lag such that the minimum water elevation is reached at about 0700h. The daily cycle then repeats.

Over the last five days of the simulation (Fig. 6.48d), the melt rate is largely negative, indicating of accretion. During the morning, daytime, and evening, melt rates are strongly positive along the flat-bedded portion of the section. From 0700h to 0900h, during the end of the night phase, melt rates are negative along the flat-bedded portion. However, the lack of discharge precludes accretion. Downstream, accretion occurs from about 100 m to the terminus and is strongest during the morning and evening. This result is consistent with results from clear water diurnal forcing for the above-threshold section.

Figure 6.48e reveals that sediment supply from the bed is negative upstream for most of the day. Along the final 75–100 m from the terminus, erosion occurs during the daytime. Little sediment is available to the hydraulic system during the morning, evening, or night portions of the diurnal cycle. Small amounts of sediment are present throughout the night, and these are deposited nearly uniformly along the section.

Sediment concentrations illustrated in Figures 6.49a–c, show that sediment transport decreases over the final five days during the daytime. Total sediment concentrations are highest upstream. As water flows downstream, sediment is deposited along flat-bedded portion of the section. Suspended sediment load and bed load are lower than field studies, but are higher than the concentration of sediment accreted in the ice. This result corresponds to sediment transport occurring largely within the daytime portion of the diurnal cycle. Very little sediment is mobilized during the morning or evening when accretion rates are higher.

Maximum daily discharge, therefore, crosses a threshold at approximately 60 d when less

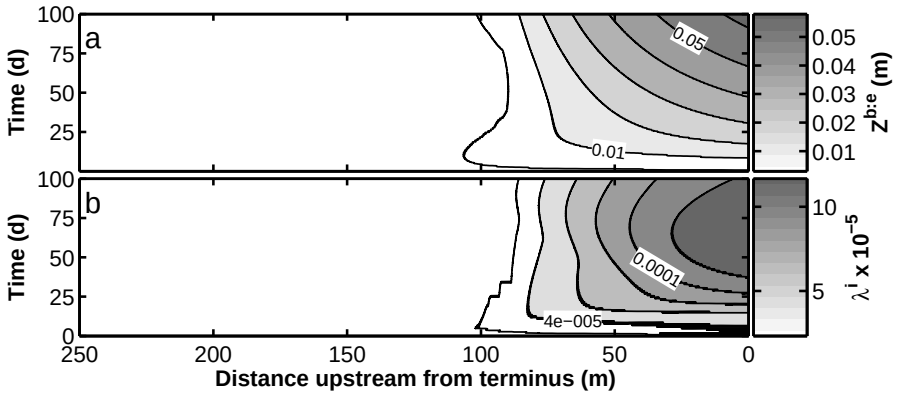

Figure 6.47: Daily cycles with erosion: Above-threshold case. (a) Accreted ice thickness. Except for the first contour at 0.001 m, the contour interval is 0.01 m. (b) Volume concentration of sediment in the basal ice. Contour interval is 2×10^{-5}.

sediment is mobilized. As a result, less sediment is captured by the accreted ice, and the accreted ice becomes cleaner over the final 40 d of the simulation.

Maximum daily water velocities over the final five days of the simulation reach 0.5 m s^{-1}. In terms of the Hjulström diagram (Fig. 4.2), these velocities should produce erosion albeit by a nominal amount given a D_{50} of 0.001 m. Maximum daytime Reynolds numbers for the final five days peak at about 5000, which is a consequence of shallow water depths. As a result, the Hjulström diagram is not necessarily a valuable tool for estimating whether subglacial water sheets will erode or deposit sediment because the diagram is intended for use with higher hydraulic radii and higher Reynolds numbers. Still, the Hjulström diagram does indicate that the erosion–transportation–sedimentation thresholds are bunched together, which is what the above-threshold simulations indicate. In sum, the Hjulström diagram is loosely analogous to what occurs in the subglacial alluvial system but is not particularly revealing.

The above-threshold system also chokes with sediment. However, this choking takes longer to accomplish because the system moves less sediment than the threshold section by about a factor of two. The net result is that the hydraulic system is able to evacuate water more effectively despite the additional effect of accretion during along the adverse slope.

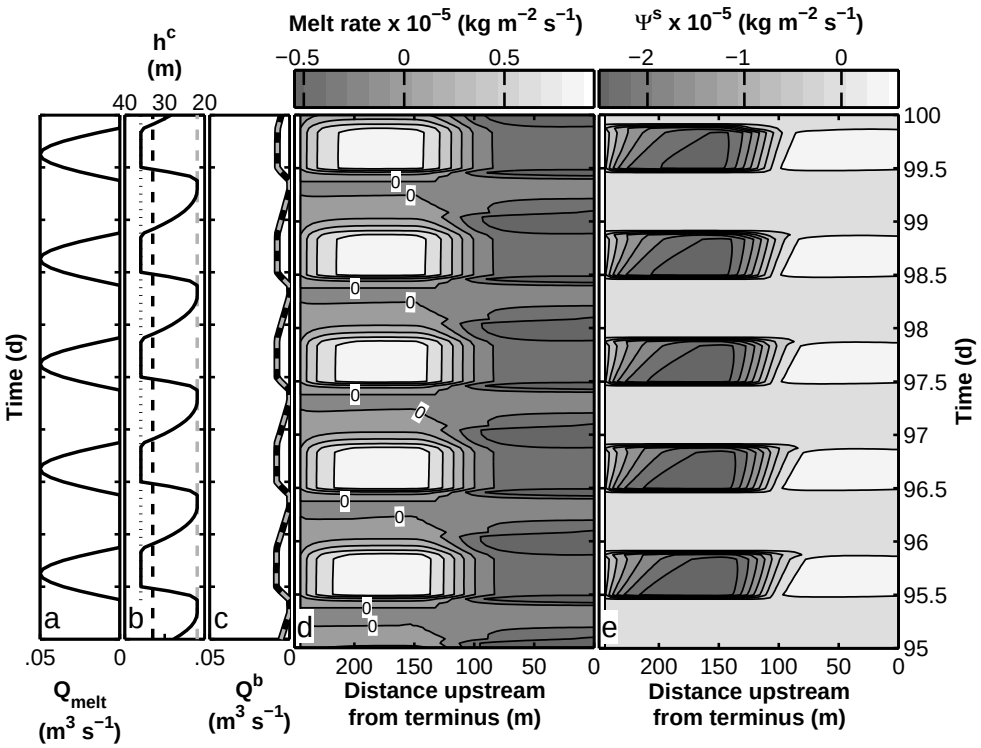

Figure 6.48: Daily cycles with erosion: Above-threshold case. (a) Recharge into the subglacial water system. (b) Water elevation in the upstream crevasse. Dark dotted line is the glacier surface elevation. Dark dashed line is the flotation elevation. Light dashed line is the elevation of the glacier terminus. (c) Water discharge. Dark line denotes water discharge into the subglacial water system. Light dashed line overlying the dark line denotes water discharge at the terminus. (d) Melt rate. Contour interval is 2×10^{-6} kg m^{-2} s^{-1}. (e) Sediment supply from the bed. Positive values indicate erosion. Contour interval is 3.6×10^{-6} kg m^{-2} s^{-1}.

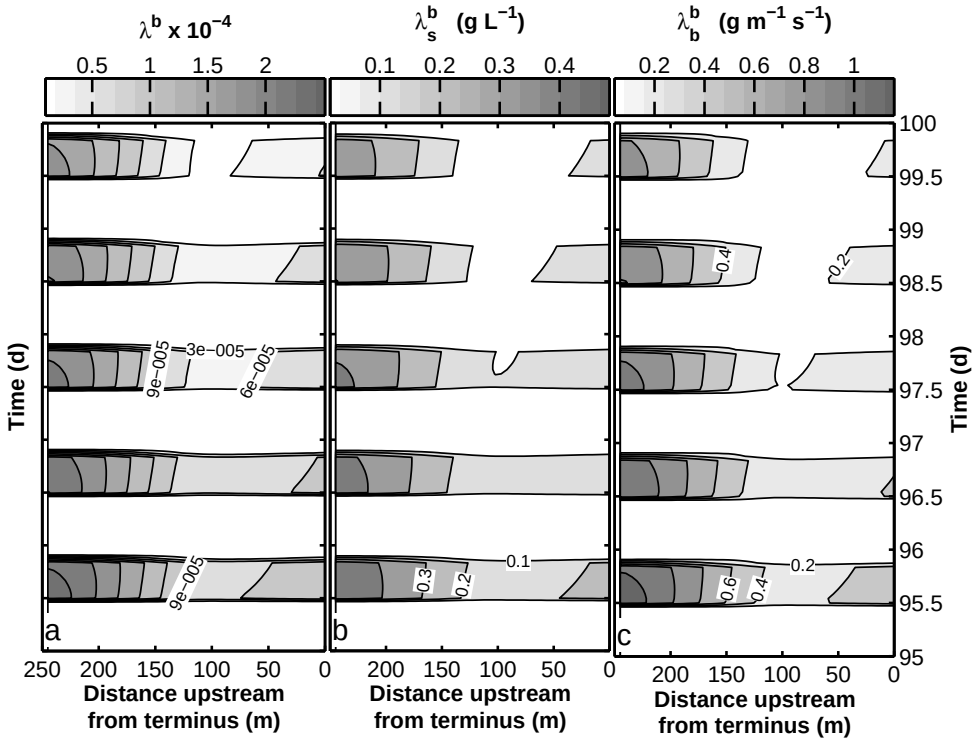

Figure 6.49: Daily cycles with erosion: Above-threshold case. (a) Total volume concentration of sediment in subglacial water. Contour interval is 3×10^{-5}. (b) Concentration of suspended sediment in subglacial water. Contour interval is 0.1 g L^{-1}. (c) Bed load transport rate in subglacial water (converted from volume concentration and velocity). Contour interval is 0.2 g m^{-1} s^{-1}.

Overdeepened case: Below-threshold section

Crevasse water elevation for the below-threshold section rises to the surface of the glacier by simulation day 9 (Fig. 6.50a). After 21 d, the crevasse water elevation rises from the minimum value of the terminus elevation. This result parallels the threshold section where the crevasse also did not drain to its minimum value.

As shown in Figure 6.50b, maximum daytime discharge for the below-threshold section decreases over the course of the simulation. Nighttime discharge rises above zero beginning on day 21. This result is consistent with the upstream crevasse retaining additional water at night. By the end of the simulation, subglacial discharge varies between 0.003 and 0.005 $m^3\ s^{-1}$. This variation is greater than that of the threshold section and adds to the numerical stability of the below-threshold section for the course of the entire 100 days.

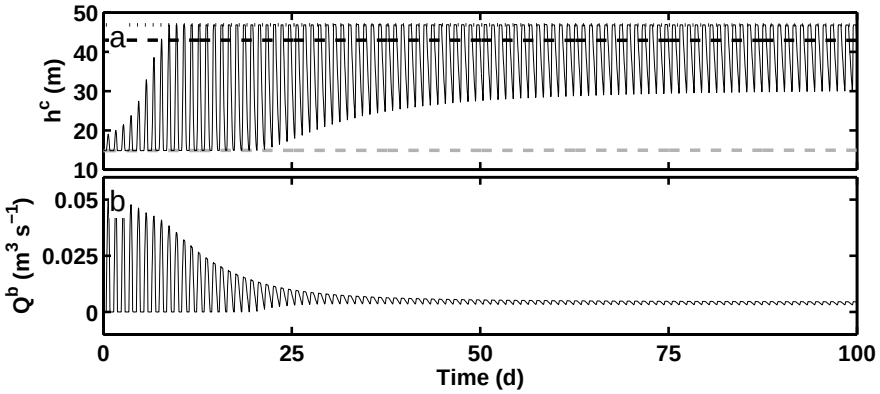

Figure 6.50: Daily cycles with erosion: Below-threshold case. (a) Water elevation in the upstream crevasse. Uppermost dotted line is the elevation of the glacier surface. Dark dashed line indicates the equivalent flotation elevation. Lowermost, gray dashed line is the elevation of the terminus. (b) Discharge from the crevasse to the subglacial water system.

Most of the evolution of the subglacial sheet is complete by day 21, as illustrated in Figure 6.51a. For the final 79 days of the simulation, the sheet shallows by less than 0.01 m. In this instance, ice intrusion is negligible because the total closure over 100 days is tens of microns (Fig. 6.51b).

The shallowing of the water depth primarily results from deposition of sediments along the section (Fig. 6.51c). Maximum sedimentation is about 0.15 m and occurs at the upstream end of the adverse slope. Along the adverse slope, there is a subdued pattern where additional sedimentation occurs approximately 75 m from the terminus.

Figure 6.52 illustrates the components of the mass balance of the sheet for the final five days of the simulation. The melt rate is always moderately positive in both space and time. Only during the late night part of the diurnal cycle does the melt rate approach zero. This observation draws sharp contrast to the clear water example where accretion was possible during the morning and evening parts of the diurnal cycle. Melt during the day opens the water system at about double that of the nighttime closure rate (Fig. 6.52b).

Sediment supply from the bed is roughly twice the magnitude of the melt during the daytime (Fig. 6.52c). There is no sedimentation at night when water velocity is too low to move sediment. Sedimentation concentrates during the morning portion of the daily cycle along the flat-bedded portion of the section. During nighttime, competition between the closure and melt rates acts

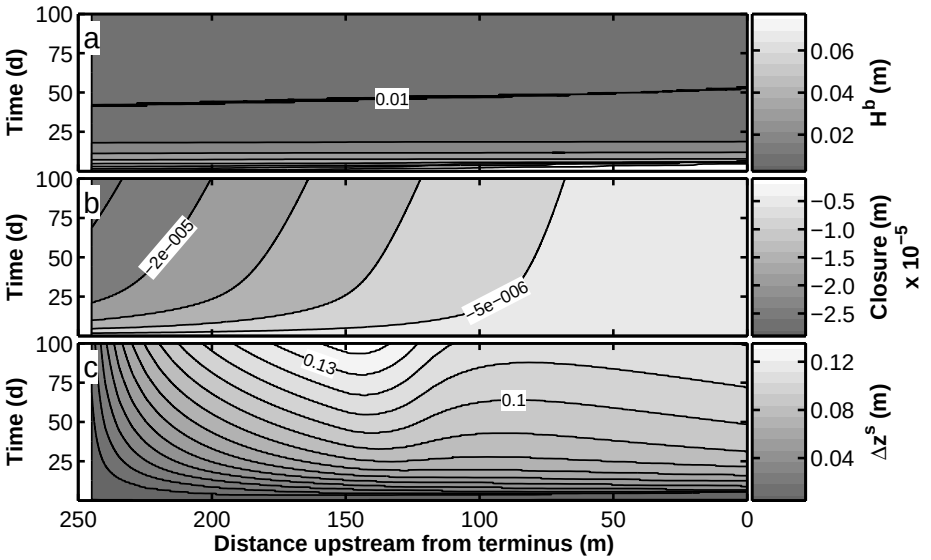

Figure 6.51: Daily cycles with erosion: Below-threshold case. (a) Thickness of the subglacial water sheet. Contour interval is 0.01 m. (b) Total ice closure. Contour interval is 5×10^{-6} m. (c) Change in bed elevation. Positive values indicate sedimentation. Contour interval is 0.01 m.

to close the sheet. However, onset of melt and cessation of closure during the morning open the sheet. Accommodation space created by melt is quickly filled in by the movement of sediment during the morning.

As Figure 6.53a illustrates, the below threshold case carries much sediment. Maximum daily total volumetric sediment concentration is approximately 0.001 near the inlet. During daytime conditions, the concentration decreases along the section. This drop increases along the adverse slope. At night, sediment transport is negligible. The evening transition from sediment-laden to low-sediment conditions occurs over a few hours and is not as sharp as the morning transition from low to high sediment load.

Relative to the threshold section, water flow in the below-threshold section carries significantly more sediment up the adverse slope. Along the flat-bedded portion of the section, bed load is approximately three times greater in the case of the below-threshold section (Fig. 6.53b). Suspended load along the flat-bedded portion of the below-threshold section is also about three times greater (Fig. 6.53c).

Despite the fact that the below-threshold section flushes more sediment through the system, the water system chokes with sediment. The added sediment reduces the water depth considerably during the first part of the simulation. Nighttime melt opens the channel enough to create accommodation space which is then filled with sediment during daytime conditions.

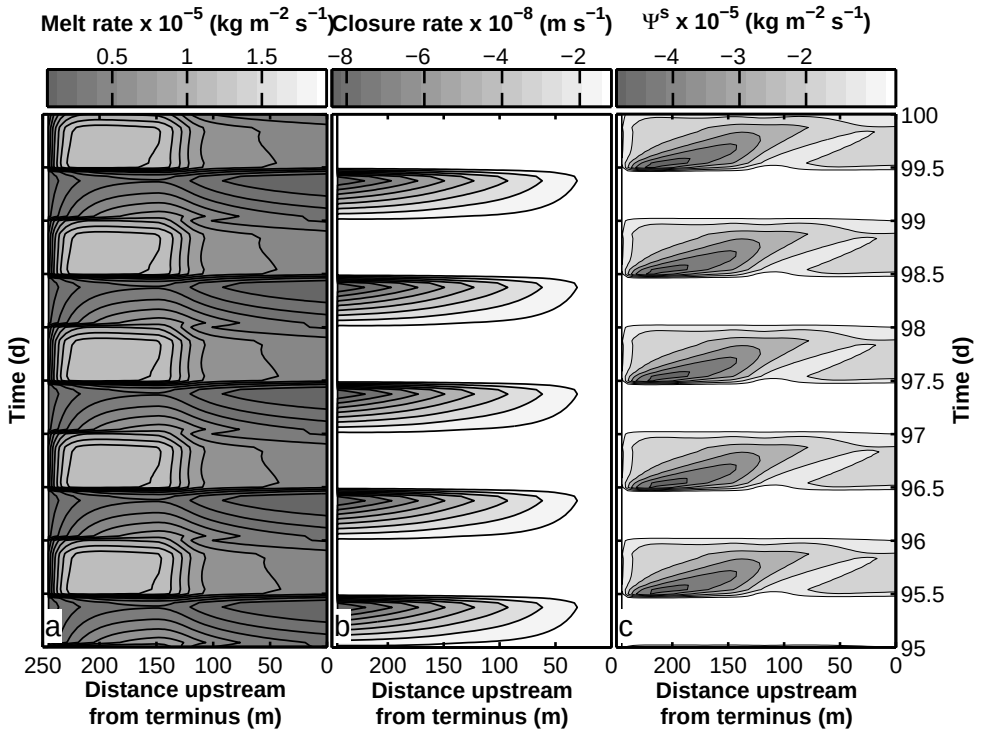

Figure 6.52: Daily cycles with erosion: Below-threshold case. (a) Melt rate. Contour interval is 1.16×10^{-6} kg m^{-2} s^{-1}. (b) Closure rate. Contour interval is 1×10^{-10} m s^{-1}. (c) Sediment supply from the bed. Contour interval is 0.75×10^{-5} kg m^{-2} s^{-1}.

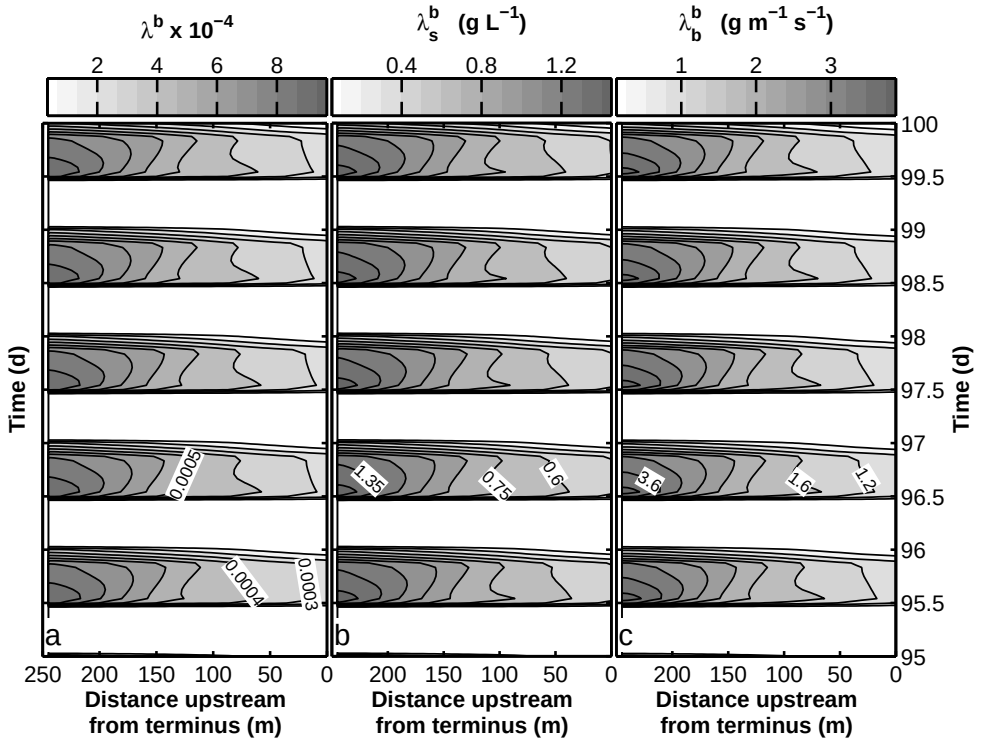

Figure 6.53: Daily cycles with erosion: Below-threshold case. (a) Total concentration of sediment in subglacial water. Contour interval is 1×10^{-4}. (b) Concentration of suspended sediment in subglacial water. Contour interval is 0.15 g L^{-1}. (c) Bed load transport rate in subglacial water (converted from volume concentration and velocity). Contour interval is 0.4 g m^{-1} s^{-1}.

6.4.4 Discussion

One of the most important observations of these numerical simulations is that the threshold and below-threshold sections effectively choke with sediment. The threshold section chokes so severely that numerical solution of the governing equations eventually ceases. Both of these longitudinal sections seek nighttime water velocities that are below the sediment transport threshold. Daytime water velocities cross the transport threshold, and sediment is mobilized. For the choice of parameters presented here, the threshold lies in the range 0.003–0.004 $m^3\ s^{-1}$.

The above-threshold section also chokes with sediment but not as sharply as the other two sections. Nighttime water discharge is able to lower to zero for the above threshold section. In this case, shallower pressure gradients drive water flow. Therefore, water velocities are lower and not as much sediment is mobilized. Consequentially, less sediment is available to choke the water system.

Another key observation is the timing of accretion. For the threshold section, accretion shifts to the nighttime once the system has choked. However, sediment is available to be accreted only during daytime conditions when discharge is higher. The net result is that cleaner ice is accreted. This scenario is one that has not been considered in the literature. Field studies support low water and sediment discharge at night; but the timing of accretion of clear ice in the diurnal cycle has not been discussed. Clear ice lenses are observed at Matanuska Glacier (Lawson *et al.*, 1998), and these lenses can form at nighttime based on threshold simulation results.

For the above-threshold section, maximum sediment concentrations occur during daytime. Accretion, however, is favored during the morning and evening portions of the diurnal cycle. Sediment concentrations in the accreted ice are thus lower than daily maximum concentrations. For ice and sediment to accrete simultaneously, low viscous dissipation combined with mobile sediment are necessary but not sufficient. A mechanism not captured in the model physics must also act to concentrate sediment in the accretion ice. Frazil floc filters, for example, could be sufficient to concentrate the sediment at many times the transport concentration (*e.g.,* Lawson *et al.*, 1998).

For all sections, sedimentation occurs primarily at the base of the adverse slope. In this case, $\partial^2\phi/\partial s^2$ is highest at the start of the adverse slope. The result is that velocity slows considerably at this location. Because sediment transport has a velocity threshold, sedimentation occurs when the velocity drops. Once the water depth has stabilized around 0.01 m, the above-threshold and threshold sections erode a small amount along the adverse slope. The below-threshold section deposits sediment here. Sediment transport smoothes bed topography for all of these sections because the curvature of the hydraulic potential is highest at the onset of the adverse slope.

In light of the hypothesis that alluvial glacier beds should tend toward threshold conditions proposed by Alley *et al.* (2003b), simulations presented here do not support this hypothesis. Simulations show much more sedimentation at the upstream end of the adverse slope than along it. The important difference between simulations presented here and the theory proposed by Alley *et al.* is that much sedimentation occurs in the simulations before water reaches the area of supercooling and ice accretion. In this case, the sedimentation and supercooling are fairly well decoupled; whereas in the theory of Alley *et al.* (2003b) they are coupled. In addition, these simulations suggest that glaciers tend toward slopes where the subglacial system can discharge its upstream water supply efficiently. The sedimentary response tends to mute topography rather than create it.

Model results can be compared and contrasted to results from dye tracing studies at Matanuska Glacier. Lawson *et al.* (1998) determined the water depth to be about 0.03 m for

conduit-like cross-sections. Results from simulations with sediment transport show much shallower water depths than those for clear water flows that are comparable to Lawson *et al.*'s (1998) results. The compatibility of this result comes as no surprise because Matanuska Glacier is actively transporting sediment along its base. Maximum daily model velocities are in the range 0.4–0.5 m s^{-1}, which is much faster than dye-tracing studies. However, the one dimensional model does not capture the lateral variations in hydraulic cross-sections that most likely exist (*e.g.,* Lappegard *et al.*, 2006). Dye can either enter areas of lateral storage. In addition, velocities of 0.04 m s^{-1} inferred from travel times are low relative to threshold sediment transport criteria (see Appendix E).

In two-dimensions, the model would yield lateral migration of flow paths as sediment is deposited. Water most likely would move from one area to another to minimize resistance. Lateral migration would be on the order of the sedimentation rate ($\sim 10^{-8}$ m s^{-1}). This hypothesis is supported by observations of basal ice, where cross-stratification may indicate hydraulic cross section migration (Lawson *et al.*, 1998).

Temporal evolution of the cross-section during the diurnal cycle is justified via model results. The cross section for all longitudinal profiles is a distributed sheet during the day as indicated by water pressures above flotation. At night, however, the water system operates at pressures below ice overburden pressure. Therefore, nightly cross-sections would be more like a Röthlisberger channel. During the day, the channels flood into a distributed, sheet-like cross section. Moreover, there are probably temporal switches between between sheets and R-channels, and intermediate forms, such as the broad-and-flat channel, may appear during these switches.

6.5 Summary

Simulations presented throughout this chapter highlight the variability and complexity of the subglacial hydraulic system. Because of the level of detail in Matanuska Glacier sections, I present results from simplified synthetic longitudinal sections. Results from the synthetic sections help to diagnose accretion rates, accretion locations, variability of daily cycles, sediment transport, and other phenomena associated with glaciohydraulic supercooling. Simulated subglacial hydraulic systems display many behaviors that are thresholded, periodic, and/or counter-intuitive. These results are broadly applicable to glaciers where supercooling occurs. Reasonable assumptions yield intriguing results, many of which are directly compatible with field data and observations.

Chapter 7

Conclusions

7.1 Summary

This thesis focuses on subglacial hydrology, specifically on glaciohydraulic supercooling. Glaciohydraulic supercooling is a natural process whereby water that flows en- or subglacially freezes spontaneously because of depressurization without equilibration of internal energy.

7.1.1 Model

Evidence from field sites indicates that water disperses into a broad, distributed water system. To this end, I reformulate the model of Spring & Hutter (1981) to account for subglacial sheets that are much wider than high (Chap. 2). This theory rests on the mass balances of ice and water, the balance of linear momentum, and the balance of internal energy of the water. These balances ultimately yield four equations: one for the water sheet height, or water depth, water pressure, water velocity, and water temperature. Equivalent formulations exist for subglacial channels (Clarke, 2003), and I present these for completeness. Water flow in sheets and channels is turbulent. In addition, I include ice porosity in the mass balance equations that govern the evolution of the water sheet. The turbulent melt rate affects supercooling; but with common assumptions, the theory presented here reduces to the bed-to-surface slope ratio criterion discussed by others (Alley *et al.*, 1998; Hooke, 1991; Röthlisberger & Lang, 1987).

Because the mathematical description of turbulent sheets is new, a suitable closure relationship for ice intrusion into the sheet is necessary. I formulate the closure relationship based on ideas taken from subglacial cavities where stress is partitioned based on areal fractions (*e.g.,* Fowler, 1987; Lliboutry, 1979; Schoof, 2005, see Chap. 3). The basic idea of these sheets is that a fraction of the ice rests on sediments. The remainder of the ice rests on the water sheet, pressurizing it. This idea departs from the formulation of Walder (1982) who envisioned a water sheet that everywhere separated ice from bed. When the effective pressure is negative, water floods the bed and distributes laterally. This conceptualization is based on the ideas of Hooke & Pohjola (1994), where they suggest that water distributes over the bed when water pressure is greater than ice overburden pressure.

Field observations demonstrate that effluent water and accreted ice can contain much sediment. Chapter 4 expands the form of the equations governing water flow to include sediment. In this case, I modify the commonly used Exner equation (*e.g.,* Paola & Voller, 2005) to suit the subglacial system. This expansion results in equations for the evolution of subglacial bed elevation and sediment concentrations for both water and accreted ice. Erosion via the spatial adaptation length (*e.g.,* Einstein, 1968) provides a way of formulating sediment supply from the bed. Finally, the semiempirical sand-bed equations of van Rijn (1984a,b) close the system. With the sand-bed equations, the model accounts for both suspended and bed load.

Because water flow up adverse slopes can be above ice overburden pressure and because accretion ice is observed in crevasses and fractures, Chapter 5 presents an englacial aquifer

model. This model rests on the balance laws of mass, momentum, and internal energy. The local forms of these laws yield equations for the evolution of englacial porosity, water pressure, water temperature. Linear momentum is governed by Darcy's law, implying that water flow must be laminar. Two relationships close the governing equations: (1) a semiempirical formulation for creep closure of pore space, and (2) a formulation of the melt rate for laminar flow. Pore space volume is assumed to be in the form of englacial fractures (Flowers & Clarke, 2002a; Snow, 1968). Features of the englacial aquifer model that make it unique relative to previous work include local formulation of the model (*i.e.,* not vertically integrated) and evolution of pore space via creep and melt.

7.1.2 Simulations

In Chapter 6, I present results from numerical simulations of the governing equations. These simulations are primarily for subglacial sheets. Both clear water and sediment laden flows are included, but I omit englacial aquifer simulations for brevity and simplicity. Through the use of different synthetic sections, simulations reveal many interesting phenomena within the subglacial system. Within the accompanying assumptions, these simulations are broadly applicable to glaciers that have overdeepenings. Here, I summarize some of the results.

For steady recharge rates, several key points are important. Discharge along the hydraulic section is nearly constant. Variations in discharge occur primarily because ice melts from or accretes to the overlying glacier. Subglacial discharge is almost exactly equal to the upstream crevasse recharge rate. Upstream crevasse water pressure that determines discharge can take longer to equilibrate. Specifically, the above-threshold section does not equilibrate over a 100 d melt season. In this case, upstream pressure also responds to the crevasse filling completely to the glacier surface. The water system then dramatically reorganizes when this overpressure forces melt to occur along the entire length of the section. This reorganization is linked to viscous dissipation and specifically the choice of friction coefficient.

Model melt rates and approximate melt rates from steady state theory yield starkly different accretion patterns and rates. The different between the two varies by factors of ± 2 to over 20 and can be locally two orders of magnitude higher. Approximate melt rates overestimate accretion along adverse slopes. For steady recharge rate, areas of accretion propagate upstream along the adverse slope. For overdeepened simulations with diurnal forcing, accretion is greatest at the terminus. However, there is a spatial lag between the onset of the adverse slope and the onset of supercooling. This spatial lag is not captured by the approximate melt rates.

Comparisons between conduits and sheets reveal several features. Longitudinal sections that are above threshold conditions invariably favor sheets during periods of high discharge. In the overdeepening, water pressure is above ice overburden pressure and can force water to disperse laterally. For threshold conditions, upstream and downstream may not behave in unison such that an upstream conduit can spatially change into a sheet along an adverse slope. Conduits are favored for cross-sections that are below threshold conditions, but accretion occurs because heat generation from viscous dissipation is low. Accretion would act to diminish the channel, and an intermediate hydraulic cross section probably forms.

Nighttime and daytime conditions offer a temporal glimpse of sheet–conduit behavior. During the day, water pressures are above flotation and suggest that sheets dominate the drainage system. At night, water pressures fall below flotation and ice intrusion dominates. If the bed floods during the daytime, simulations suggest that channels may be favored at night as water flux decreases and flooded areas drain to deeper areas of flow. In the case of clear water flows,

there is little nightly water flux despite the hydraulic system being fully saturated. If there is no lateral variation in water depth, then nighttime will still be dominated by a stagnant or slowly flowing sheet. The implication that these are channels may thus be dubious. For sediment-laden flows, discharge does not cease at nighttime for the threshold case and channelization can occur. In the case of sediment transport, the above-threshold section drains completely at night; however, this results from ice at the terminus being relatively thin. For other parameter choices, it is possible that the hydraulic system does not fully drain, and conduits could be favored.

Portions of diurnal cycles—morning, daytime, evening, and nighttime—each have a different effect on subglacial hydrology. For sections where ice forms, accretion commonly occurs during morning and evening. Ice intrudes into the subglacial drainage system at night. The combination of melt, accretion, and intrusion yield a sheet that evolves not for maximum water flow but for some intermediate discharge. Maximum daily discharge cannot be conducted by the sheet for most subglacial sections, and water pressure is above flotation. An exception occurs when water sheets are thick and discharge is low, as in the case of the below-threshold section with lower discharge. Sedimentation occurs solely during the daytime and adds additional features to the daily hydrograph.

Ice accretion is compatible with field estimates. For diurnally-forced clear water simulations, accretion is about 1–4 m per century. For diurnally-forced flows with sediment transport, accretion is in the range 1–6 m per century. These values are low relative to Matanuska Glacier, but bed-to-surface slope ratios are higher there than in the simulations. In consequence, the low values are not surprising. For threshold sections, accretion is nominal, as would be expected. Because conduits have lower viscous dissipation, they accrete slightly more ice than sheets. For the case of the below-threshold section, parameter choices exist that produce water pressure gradients that are below ice overburden pressure gradients. These low gradients permit ice accretion. Thus, for certain hydrologic systems, the bed-to-surface slope criterion may not hold. In general, however, this criterion is useful.

Sediment concentrations in accreted ice are below daily maximum discharge sediment concentrations. This result stems from accretion occurring during morning, evening, and nighttime when sediment concentrations are low when ice accretes. Because sediment transport has a shear stress criterion governing incipient motion, transport only occurs during daytime. The result is that concentrations are low. Furthermore, a mechanism must exist that enhances sediment capture during accretion because field observations of accreted sediments are often higher than results from simulations.

Sedimentation occurs during daytime conditions. Over the course of the simulations, sediment chokes the hydraulic system. Sedimentation is greatest at the base of the adverse slope and subdues topography at the glacier base. The above-threshold and threshold sections erode a moderate amount along the downstream end of the adverse slope. The below-threshold section deposits a moderate amount of sediment near the end of the adverse slope. In consequence, the base of the section tends to smooth to permit both sediment transport during the day and water discharge throughout the diurnal cycle. Sediment transport also drops off dramatically as pressure gradients shallow.

7.2 Directions for future work

Because much of the material is new, the thesis also provides an opportunity to examine directions for future work. Future work falls into two broad and often intermingled areas: technical directions and topical directions.

7.2.1 Technical directions

From a technical perspective of the model there are several parameters that are not defined sufficiently. Chief among these is the friction coefficient, f_d. This coefficient governs the magnitude of viscous dissipation in sheets and channels. Lower values allow greater velocities that yield more heat generation. Higher values slow velocities and yield less heat generation. The values I choose in Chapter 6 are based on estimates for outburst floods. Better estimates from field and laboratory studies would help to constrain the model more effectively.

Similarly, the grain friction coefficient f'_d, is not well-constrained. I have assumed that subglacial sheets have high form friction and low grain friction based on analogous mountain streams. Without field or laboratory studies of subglacial sediment transport that are geared to finding these terms, it is difficult to constrain sediment transport effectively. These numbers should be obtainable via flume experiments.

Spatial lags in the accretion rate are the result of the form of the Nusselt number (eq. 2.34). Where the Nusselt number is more highly dependent on Reynolds number, the spatial lag increases. The Dittus-Boelter relationship was originally developed for smooth flow in pipes. It would thus be useful to construct experiments or design field studies to constrain this parameterization of the melt rate to examine spatial lags. In general, though, it is notable that results presented here show that the thermal balance is able to adapt for parameter changes.

A broader technical direction of interest is sheet–channel transitions. Walder (1982) presented the general idea for these transitions: when melt is greater than ice intrusion, channels dominate subglacial drainage. Using the theory presented in Chapter 3, it would be stimulating to see how channels develop along beds with large clast sizes and other bed obstacles.

In terms of sediment transport, exploring two dimensional water flow would be very interesting. How channels and sheets transform in the presence of sedimentation may be compelling and useful for other areas of glaciology and geomorphology. Furthermore, subglacial meandering or other similar processes may become more apparent with a two-dimensional model. The equations presented in this thesis are easily transformed into two dimensions.

7.2.2 Topical directions

Large ice sheets create their own overdeepenings via isostatic depression. Glaciohydraulic supercooling plays a role in hydrology and sediment transport beneath these ice sheets. For example, water flow up the sill at the end of Hudson Strait may have supercooled and accreted sediment to the base of the ice sheet. The accreted ice was later discharged to the North Atlantic during Heinrich Events (*e.g.,* Dowdeswell *et al.*, 1995; Hemming, 2004). Exploring accretion and sedimentation beneath the Laurentide Ice Sheet may yield interesting results.

Other topical directions involve the geomorphological features associated with the margins of former ice sheets. Shreve (1985) noted that size in eskers was dependent on the hydraulic gradient and the relationship to supercooling. Revisiting this work with the sediment transport model might provide additional insight into the formation of eskers. In addition, sediment transport plays a role in the development of some types tunnel valleys, which are elongate overdeepenings cut into the substrate near the margins of former ice sheets (*e.g.,* Ó Cofaigh, 1996). Examining these features from a numerical perspective may yield additional information about their genesis.

Recently, satellite measurements of vertical ice motion in Antarctica indicate that water flows subglacially (Gray *et al.*, 2005; Fricker *et al.*, 2007; Wingham *et al.*, 2006). The work by Wingham *et al.* that examines the draining of subglacial lakes is especially interesting because

the authors published both surface and bed topography. In comparing the bed and surface slopes it is clear that glaciohydraulic supercooling occurs along their hydraulic profile. What effect, if any, supercooling plays in the draining of the lakes is difficult to ascertain without further study. Their work opens the idea that glaciohydraulic supercooling may seal or diminish lake drainage. In sum, water flow beneath Antarctica will be a fruitful area of study in the coming years.

7.3 Outlook

This thesis presents a first look at dynamic simulations of glaciohydraulic supercooling and close examination of the water–ice phase change in subglacial systems. The thesis also presents a fresh look at how glaciers move sediment in the context of hydraulic equations that govern flow. Englacial and subglacial hydrology is presently a highly topical field and investigations such as this thesis will help to constrain and identify glaciohydraulic processes.

Bibliography

Abbott, J. E., & Francis, J. R. D. 1977. Saltation and suspension trajectories of solid grains in a water stream. *Proc. Roy. Soc. Lond. A Mat.*, **284**(1321), 225–254.

Alley, R. B., Cuffey, K. M., Evenson, E. B., Strasser, J. C., Lawson, D. E., & Larson, G. J. 1997. How glaciers entrain and transport basal sediment: physical constraints. *Quaternary Sci. Rev.*, **16**, 1017–1038.

Alley, R. B., Lawson, D. E., Evenson, E. B., Strasser, J. C., & Larson, G. J. 1998. Glaciohydraulic supercooling: a freeze-on mechanism to create stratified, debris-rich basal ice: II. Theory. *J. Glaciol.*, **44**(148), 563–569.

Alley, R. B., Lawson, D. E., Evenson, E. B., & Larson, G. J. 2003a. Sediment, glaciohydraulic supercooling, and fast glacier flow. *Ann. Glaciol.*, **36**, 135–141.

Alley, R. B., Lawson, D. E., Larson, G. J., Evenson, E. B., & Baker, G. S. 2003b. Stabilizing feedbacks in glacier-bed erosion. *Nature*, **424**, 758–760.

Arcone, S. A., Lawson, D. E., & Delaney, A. J. 1995. Short-pulse radar wavelet recovery and resolution of dielectric contrasts within englacial and basal ice of Matanuska Glacier, Alaska U.S.A. *J. Glaciol.*, **41**(137), 68–86.

Armanini, A., & di Silvio, G. 1988. A one-dimensional model for the transport of a sediment mixture in non-equilibrium conditions. *J. Hydraul. Res.*, **26**(3), 275–292.

Arnold, N., & Sharp, M. 2002. Flow variability in the Scandinavian ice sheet: modelling the coupling between ice sheet and hydrology. *Quaternary Sci. Rev.*, **21**(4–6), 485–502.

Ascher, U. M., & Petzold, L. R. 1998. *Computer methods for ordinary differential equations and differential-algebraic equations.* Philadelphia: Society for Industrial and Applied Mathematics.

Aschwanden, A., & Blatter, H. 2005. Meltwater production due to strain heating in Storglaciären, Sweden. *J. Geophys. Res.*, **110**(F4), F04024.

Ashton, G. D. 1982. Frazil ice. *Pages 271–289 of:* Meyer, R. E. (ed), *Theory of dispersed multiphase flow.* New York: Academic Press.

Bagnold, R. A. 1966. An approach to the sediment transport problem from general physics. *U.S. Geological Survey Professional Paper*, **422-I**, 1–37.

Bagnold, R. A. 1973. The nature of saltation and of 'bed load' transport in water. *Proc. Roy. Soc. Lond. A Mat.*, **332**, 473–504.

Bates, P., Siegert, M., Lee, V., Hubbard, B., & Nienow, P. 2003. Numerical simulation of three-dimensional velocity fields in pressurised and non-pressurised Nye channels. *Ann. Glaciol.*, **37**, 281–285.

Bear, J. 1988. *Dynamics of fluids in porous media*. reprint, 1st edn. New York: Dover.

Benn, D. I., & Evans, D. J. A. 1998. *Glaciers and glaciation*. London: Arnold.

Benn, D. I., & Gemmell, A. M.D. 2002. Fractal dimensions of diamictic particle-size distributions: Simulations and evaluation. *Geol. Soc. Am. Bull.*, **114**(5), 528–532.

Bird, R. B., Stewart, W. E., & Lightfoot, E. N. 1960. *Transport phenomena*. 1st edn. New York: John Wiley and Sons.

Björnsson, H. 2002. Subglacial lakes and jökulhlaups in Iceland. *Global Planet. Change*, **35**, 255–271.

Bougamont, M., & Tulaczyk, S. 2003. Glacial erosion beneath ice streams and ice-stream tributaries: constraints on temporal and spatial distribution of erosion from numerical simulations of a West Antarctic ice stream. *Boreas*, **32**(1), 178–190.

Braun, J., Zwartz, D., & Tomkin, J. H. 1999. A new surface-processes model combining glacial and fluvial erosion. *Ann. Glaciol.*, **28**, 282–290.

Bridge, J. S., & Bennett, S. J. 1992. A model for the entrainment and transport of sediment grains of mixed sizes, shapes, and densities. *Water Resour. Res.*, **28**(2), 337–363.

Chen, C., & Millero, F. J. 1977. The use and misuse of pure water PVT properties for lake waters. *Nature*, **266**(5604), 707–708.

Chen, C. A., & Millero, F. J. 1986. Precise Thermodynamic properties for natural waters covering only the limnological range. *Limnol. Oceanogr.*, **31**(3), 657–662.

Church, M. 2006. Bed material transport and the morphology of alluvial river channels. *Annu. Rev. Earth Planet. Sci.*, **34**, 325–354.

Church, M., Hassan, M. A., & Wolcott, J. F. 1998. Stabilizing self-organized structures in gravel-bed stream channels: Field and experimental observations. *Water Resour. Res.*, **34**(11), 3169–3179.

Clark, P. U., & Walder, J. S. 1994. Subglacial drainage, eskers, and deforming beds beneath the Laurentide and Eurasian ice sheets. *Geol. Soc. Am. Bull.*, **106**, 304–314.

Clarke, G. K. C. 1986. Professor Mathews, outburst floods, and other glaciological disasters. *Can. J. Earth Sci.*, **23**(6), 859–868.

Clarke, G. K. C. 2003. Hydraulics of subglacial outburst floods: new insights from the Spring-Hutter formulation. *J. Glaciol.*, **49**(165), 299–313.

Clarke, G. K. C. 2005. Subglacial processes. *Annu. Rev. Earth Planet. Sci.*, **33**, 247–276.

Clarke, G. K. C., Leverington, D. W., Teller, J. T., & Dyke, A. S. 2005. Fresh arguments against the Shaw megaflood hypothesis. A reply to comments by David Sharpe on "Paleohydraulics of the last outburst flood from glacial Lake Agassiz and the 8200 BP cold event". *Quaternary Sci. Rev.*, **24**(12–13), 1533–1541.

Correia, L. R. P., Krishnappan, B. G., & Graf, W. H. 1992. Fully coupled unsteady mobile boundary flow model. *J. Hydraul. Eng., ASCE*, **118**(3), 476–494.

Cui, Y., Parker, G., & Paola, C. 1996. Numerical simulation of aggradation and dowstream fining. *J. Hydraul. Res.*, **34**(2), 185–204.

Daly, S. F. 1984. *Frazil ice dynamics.* Tech. rept. 84-1. U.S. Army CRREL, Hanover, N.H.

Domenico, P. A., & Schwartz, F. W. 1997. *Physical and chemical hydrogeology.* 2nd edn. New York: John Wiley & Sons.

Dowdeswell, J. A., Maslin, M. A., Andrews, J. T., & McCave, I. N. 1995. Iceberg production, debris rafting, and the extent and thickness of Heinrich layers (H-1, H-2) in North Atlantic sediments. *Geology*, **23**(4), 301–304.

Duval, P., Arnaud, L., Brissaud, O., Montagnat, M., & de la Chappelle, S. 2000. Deformation and recrystallization processes of ice from polar ice sheets. *Ann. Glaciol.*, **30**, 83–87.

Einstein, H. A. 1968. Deposition of suspended particles in a gravel bed. *J. Hydraul. Eng., ASCE*, **95**(5), 1197–1205.

Evenson, E. B., Lawson, D. E., Strasser, J., Larson, G. J., Alley, R. B., Ensminger, S. L., & Stevenson, W. E. 1999. Field evidence for the recognition of glaciohydraulic supercooling. *Pages 23–35 of:* Mickelson, D., & Attig, J. (eds), *Glacial processes past and present.* Special Paper 337. Boulder, CO: Geological Society of America.

Fischer, U. H., & Hubbard, B. 1999. Subglacial sediment textures: character and evolution at Haut Glacier d'Arolla, Switzerland. *Ann. Glaciol.*, **28**, 241–246.

Fisher, T. G., Jol, H. M., & Boudreau, A. M. 2005. Saginaw Lobe tunnel channels (Laurentide Ice Sheet) and their significance in south-central Michigan, USA. *Quaternary Sci. Rev.*, **24**, 2375–2391.

Fleisher, P. J., Cadwell, D. H., & Muller, E. H. 1998. Tsivat basin conduit system persists through two surges, Bering Piedmont Glacier, Alaska. *Geol. Soc. Am. Bull.*, **110**(7), 877–887.

Flowers, G. E. 2000. *A multicomponent coupled model of glacier hydrology.* Ph.D. thesis, Univ. of B.C., Vancouver, B.C., Canada.

Flowers, G. E., & Clarke, G. K. C. 2002a. A multicomponent coupled model of glacier hydrology, 1. Theory and examples. *J. Geophys. Res.*, **107**(B11).

Flowers, G. E., & Clarke, G. K. C. 2002b. A multicomponent coupled model of glacier hydrology, 2. Application to Trapridge Glacier, Yukon, Canada. *J. Geophys. Res.*, **107**(B11).

Flowers, G. E., Björnsson, H., Pálsson, F., & Clarke, G. K. C. 2004. A coupled sheet–conduit mechanism for jökulhlaup propagation. *Geophys. Res. Lett.*, **31**.

Fountain, A. G., & Walder, J. S. 1998. Water flow through glaciers. *Rev. Geophys.*, **36**(3), 299–328.

Fountain, A. G., Jacobel, R. W., Schlichting, R., & Jansson, P. 2005a. Fractures as the main pathways of water flow in temperate glaciers. *Nature*, **433**(7026), 618–621.

Fountain, A. G., Schlichting, R., Jansson, P., & Jacobel, R. W. 2005b. Observations of englacial water passages: a fracture-dominated system. *Ann. Glaciol.*, **40**, 25–30.

Fowler, A. C. 1984. On the transport of moisture in polythermal glaciers. *Geophys. Astro. Fluid*, **28**(2), 99–140.

Fowler, A. C. 1987. Sliding with cavity formation. *J. Glaciol.*, **33**(115), 255–267.

Fowler, A. C. 1997. *Mathematical models in the applied sciences*. Cambridge: Cambridge University Press.

Fowler, A. C. 1999. Breaking the seal at Grímsvötn, Iceland. *J. Glaciol.*, **45**(151), 506–516.

Fricker, H. A., Scambos, T., Bindschadler, R., & Padman, L. 2007. An active subglacial water system in West Antarctica mapped from space. *Science*, **315**, 1544–1548.

Gao, P., & Abrahams, A. D. 2004. Bedload transport resistance in rough open-channel flows. *Earth Surf. Process. Landforms*, **29**, 423–435.

Garcia, M., & Parker, G. 1991. Entrainment of bed sediment into suspension. *J. Hydraul. Eng., ASCE*, **117**(4), 414–435.

Gilpin, R. R. 1981. Ice formation in a pipe containing flows in the transition and turbulent regimes. *J. Heat Transf.*, **117**(2), 363–368.

Glen, J. W. 1952. Experiments on the deformation of ice. *J. Glaciol.*, **2**, 111–114.

Glen, J. W. 1954. The stability of ice-dammed lakes and other water-filled holes in glaciers. *J. Glaciol.*, **2**(15), 316–318.

Gomez, B., & Church, M. 1989. An assessment of bed load sediment transport formulae for gravel bed rivers. *Water Resour. Res.*, **25**(6), 1161–1186.

Graf, W. H. 1971. *Hydraulics of sediment transport*. New York: McGraw-Hill.

Gray, L., Joughin, I., Tulaczyk, S., Spikes, V. B., Bindschadler, R., & Jezek, K. 2005. Evidence for subglacial water transport in the West Antarctic Ice Sheet through three-dimensional satellite radar interferometry. *Geophys. Res. Lett.*, **32**(L03501).

Haltiner, G. J., & Williams, R. T. 1980. *Numerical prediction and dynamic meteorology*. 2nd edn. New York, NY: John Wiley & Sons.

Hambrey, M. J., & Dowdeswell, J. A. 1997. Structural evolution of a surge-type polythermal glacier: Hessbreen, Svalbard. *Ann. Glaciol.*, **24**, 375–381.

Hambrey, M. J., Murray, T., Glasser, N. F., Hubbard, A., Hubbard, B., Stuart, G., Hansen, S., & Kohler, J. 2005. Structure and changing dynamics of a polythermal valley glacier on a centennial timescale: Midre Lovénbreen, Svalbard. *J. Geophys. Res.*, **110**, F01006.

Harbor, J. M. 1992. Numerical modeling of the development of U-shaped valleys by glacial erosion. *Geol. Soc. Am. Bull.*, **104**(10), 1364–1375.

Harper, J. T., Humphrey, N. F., & Greenwood, M. C. 2002. Basal conditions and glacier motion during the winter/spring transition, Worthington Glacier, Alaska, USA. *J. Glaciol.*, **48**(160), 42–50.

Hemming, S. R. 2004. Heinrich Events: massive Late Pleistocene detritus layers of the North Atlantic and their global climate imprint. *Rev. Geophys.*, **42**, 43.

Henderson, F. M. 1966. *Open channel flow*. New York: MacMillan.

Hildes, D. H. D. 2001. *Modelling subglacial erosion and englacial sediment transport of the North American Ice Sheets*. Ph.D. thesis, Univ. of B.C., Vancouver, B.C., Canada.

Hildes, D. H. D., Clarke, G. K. C., Flowers, G. E., & Marshall, S. J. 2004. Subglacial erosion and englacial sediment transport modelled for North American ice sheets. *Quaternary Sci. Rev.*, **23**(3–4), 409–430.

Hinze, J. O. 1975. *Turbulence*. second edn. New York: McGraw-Hill.

Hjulström, F. 1935. The morphological activity of rivers as illustrated by Rivers Fyris. *Bull. Geol. Inst. Uppsala*, **25**, 221–527.

Hobbs, P. V. 1974. *Ice physics*. Oxford: Clarendon Press.

Hock, R. 1999. A distributed temperature-index ice- and snowmelt model including potential direct solar radiation. *J. Glaciol.*, **45**, 101–111.

Hoey, T. B., & Ferguson, R. 1994. Numerical simulation of downstream fining by selective transport in gravel bed rivers: Model development and illustration. *Water Resour. Res.*, **30**(7), 2251–2260.

Hooke, R. L. 1991. Positive feedbacks associated with erosion of glacial cirques and overdeepenings. *Geol. Soc. Am. Bull.*, **103**(8), 1104–1108.

Hooke, R. L., & Iverson, N. R. 1995. Grain-size distribution in deforming subglacial tills: role of grain fracture. *Geology*, **23**(1), 57–60.

Hooke, R. L., & Pohjola, V. 1994. Hydrology of a segment of a glacier situated in an overdeepening, Storglaciären, Sweden. *J. Glaciol*, **40**(134), 140–148.

Hooke, R. L., Miller, S. B., & Kohler, J. 1988. Character of the englacial and subglacial drainage system in the upper part of the ablation area of Storglaciären, Sweden. *J. Glaciol*, **34**(117), 228–231.

Hooke, R. L., Laumann, T., & Kohler, J. 1990. Subglacial water pressures and the shape of subglacial conduits. *J. Glaciol*, **35**(122), 67–71.

Hooke, R. L., Hanson, B., Iverson, N. R., Jansson, P., & Fischer, U. H. 1997. Rheology of till beneath Storglaciären, Sweden. *J. Glaciol.*, **43**, 172–179.

Hubbard, B., & Nienow, P. 1997. Alpine subglacial hydrology. *Quaternary Sci. Rev.*, **16**, 939–955.

Hubbard, B. P., Sharp, M. J., Willis, I. C., Nielsen, M. K., & Smart, C. C. 1995. Borehole water-level variations and the structure of the subglacial hydrological system of Haut Glacier d'Arolla, Valais, Switzerland. *J. Glaciol.*, **41**, 572–583.

Hulbe, C. L., MacAyeal, D. R., Denton, G. H., Kleman, J., & Lowell, T. V. 2004. Catastrophic ice shelf breakup as the source of Heinrich event icebergs. *Paleoceanography*, **19**(1), PA1004.

Hutter, K. 1982. A mathematical model of polythermal glaciers and ice sheets. *Geophys. Astro. Fluid*, **21**(3–4), 201–224.

Iken, A., & Bindschadler, R. A. 1986. Combined measurements of subglacial water pressure and surface velocity of Findenlengletscher, Switzerland: conclusions about drainage system and sliding mechanism. *J. Glaciol.*, **32**(110), 101–119.

Illangasekare, T. H., Walter, R. J., Meier, M. F., & Pfeffer, W. T. 1990. Modeling of meltwater infiltration in subfreezing snow. *Water Resour. Res.*, **26**(5), 1001–1012.

Isenko, E., Naruse, R., & Mavlyudov, B. 2005. Water temperature in englacial and supraglacial channels: change along the flow and contribution to ice melting on the channel wall. *Cold Reg. Sci. Technol.*, **42**(1), 53–62.

Iverson, N. R. 2000. Sediment entrainment by a soft-bedded glacier: a model based on regelation into the bed. *Earth Surf. Process. Landforms*, **25**, 881–893.

Iverson, N. R., & Semmens, D. J. 1995. Intrusion of ice into porous media by regelation: a mechanism of sediment entrainment by glaciers. *J. Geophys. Res.*, **100**(B4), 10219–10230.

Johnson, J., & Fastook, J. L. 2002. Northern Hemisphere glaciation and its sensitivity to basal melt water. *Quatern. Int.*, **95–96**, 65–74.

Kamb, B. 1970. Sliding motion of glaciers: theory and observation. *Rev. Geophys. Space Phys.*, **8**(4), 673–728.

Kamb, B. 1987. Glacier surge mechanism based on linked cavity configuration of the basal water conduit system. *J. Geophys. Res.*, **92**(B9), 9083–9100.

Kellerhals, R., & Bray, D. I. 1971. Sampling procedures for coarse fluvial sediments. *J. Hydr. Eng. Div., A.S.C.E.*, **97**(HY8), 1165–1180.

Kerr, D. J., Shen, H. T., & Daly, S. F. 2002. Evolution and hydraulic resistance of anchor ice on gravel bed. *Cold Reg. Sci. Technol.*, **35**(2), 101–114.

Khatwa, A., Hart, J. K., & Payne, A. J. 1999. Grain textural analysis across a range of glacial facies. *Ann. Glaciol.*, **28**, 111–117.

Kohler, J. 1995. Determining the extent of pressurised flow beneath Storglaciären, Sweden using results of tracer experiments and measurements of input and output discharge. *J. Glaciol.*, **41**, 217–231.

Komar, P. D. 1989. Sediment transport by floods. *Pages 97–111 of:* Baker, V. R., Kochel, R. C., & Patton, P. C. (eds), *Flood geomorphology*, vol. 77. New York, NY: John Wiley and Sons.

Krauskopf, K. B., & Bird, D. K. 1995. *Introduction to geochemistry.* New York: McGraw-Hill.

Kulessa, B., Hubbard, B., Williamson, M., & Brown, G. H. 2005. Hydrogeological analysis of slug tests in glacier boreholes. *J. Glaciol.*, **51**(173), 269–280.

Lappegard, G., Kohler, J., Jackson, M., & Hagen, J. O. 2006. Characteristics of subglacial drainage systems deduced from load-cell measurements. *J. Glaciol.*, **52**(176), 137–148.

Lawson, D. E. 1979. *Sedimentological analysis of the western terminus region of the Matanuska Glacier, Alaska.* Tech. rept. 79-9. U.S. Army CRREL, Hanover, N.H.

Lawson, D. E. 1981. *Sedimentological characteristics and classification of depositional processes and deposits in the glacial environment.* Tech. rept. 81-27. U.S. Army CRREL, Hanover, N.H.

Lawson, D. E. 1993. *Glaciohydrologic and glaciohydraulic effects on runoff and sediment yield in glacierized basins.* Tech. rept. 93-2. U.S. Army CRREL, Hanover, N.H.

Lawson, D. E., Strasser, J. C., Evenson, E. B., Alley, R. B., Larson, G. J., & Arcone, S. A. 1998. Glaciohydraulic supercooling: a freeze-on mechanism to create stratified, debris-rich basal ice: I. Field evidence. *J. Glaciol.*, **44**(148), 547–562.

Lawson, W. 1996. Structural evolution of Variegated Glacier, Alaska, U.S.A., since 1948. *J. Glaciol.*, **42**(141), 261–270.

Lee, H. Y., & Hsu, I. S. 1994. Investigation of saltating particle motions. *J. Hydraul. Eng., ASCE*, **120**(7), 831–845.

Lliboutry, L. 1979. Local friction laws for glaciers: a critical review and new opinions. *J. Glaciol.*, **23**(89), 67–95.

Lliboutry, L. 1993. Internal melting and ice accretion at the bottom of temperate glaciers. *J. Glaciol.*, **39**(131), 50–64.

Loso, M. G., Anderson, R. S., & Anderson, S. P. 2004. Post-Little Ice Age record of coarse and fine clastic sedimentation in an Alaskan proglacial lake. *Geology*, **32**(12), 1065–1068.

MacGregor, K. R., Anderson, R. S., Anderson, S. P., & Waddington, E. D. 2000. Numerical simulations of glacial-valley longitudinal profile evolution. *Geology*, **28**(11), 1031–1034.

Marshall, S. J. 1996. *Modelling Laurentide Ice Sheet thermomechanics.* Ph.D. thesis, Univ. of B.C., Vancouver, B.C., Canada.

Martin, S. 1981. Frazil ice in rivers and oceans. *Ann. Rev. Fluid Mech.*, **13**, 379–397.

Mathews, W. H. 1973. Record of two jökullhlaups. *Pages 99–110 of: International Association of Scientific Hydrology Publication 95.* IASH.

McAdams, W. H. 1954. *Heat transmission.* 3rd edn. New York: McGraw-Hill.

Motyka, R. J., & Echelmeyer, K. A. 2003. Taku Glacier (Alaska, U.S.A.) on the move again: active deformation of proglacial sediments. *J. Glaciol.*, **49**(164), 50–58.

Murray, T., & Clarke, G. K. C. 1995. Black-box modeling of the subglacial water system. *J. Geophys. Res.*, **100**(B7), 10231–10245.

Murray, T., Stuart, G. W., Fry, M., Gamble, N. H., & Crabtree, M. D. 2000. Englacial water distribution in a temperate glacier from surface and borehole radar velocity analysis. *J. Glaciol.*, **46**(154), 389–398.

Ng, F., & Björnsson, H. 2003. On the Clague–Mathews relation for jökulhlaups. *J. Glaciol.*, **49**(165), 161–172.

Ng, F. S. L. 1998. *Mathematical modelling of subglacial drainage and erosion.* Ph.D. thesis, Oxford Univ., Oxford, U.K.

Ng, F. S. L. 2000. Canals under sediment-based ice sheets. *Ann. Glaciol.*, **30**, 146–152.

Nolan, M., Motyka, R. J., Echelmeyer, K., & Trabant, D. C. 1995. Ice thickness measurements of Taku Glacier, Alaska, U.S.A., and their relevance to its recent behavior. *J. Glaciol.*, **41**(139), 541–553.

Nunn, K. R., & Rowell, D. M . 1967. Regelation experiments with wires. *Philos. Mag.*, **16**(144), 1281–1283.

Nye, J. F. 1953. The flow law of ice from measurements in glacier tunnels, laboratory experiments and the Jungfraufirn. *Proc. Roy. Soc. Lond. A Mat.*, **219**, 477–489.

Nye, J. F. 1967. Theory of regelation. *Philos. Mag.*, **16**(144), 1249–1266.

Nye, J. F. 1969. A calculation of the sliding of ice over a wavy surface using a Newtonian viscous approximation. *Proc. Roy. Soc. Lond. A Mat.*, **311**(1506), 445–467.

Nye, J. F. 1970. Glacier sliding without cavitation in a linear viscous approximation. *Proc. Roy. Soc. Lond. A Mat.*, **315**(1522), 381–403.

Nye, J. F. 1973a. The motion of ice past obstacles. *Pages 387–394 of:* Whalley, E., Jones, S. J., & Gold, L. W. (eds), *Physics and chemistry of ice.* Ottawa: Royal Society of Canada.

Nye, J. F. 1973b. Water at the bed of a glacier. *Pages 189–194 of: International Association of Scientific Hydrology Publication 95.* IASH.

Nye, J. F. 1976. Water flow in glaciers: jökulhlaups, tunnels, and veins. *J. Glaciol.*, **17**(76), 181–207.

Nye, J. F., & Frank, F. C. 1973. Hydrology of the intergranular veins in a temperate glacier. *Pages 159–161 of: International Association of Scientific Hydrology Publication 95.* IASH.

Ó Cofaigh, C. 1996. Tunnel valley genesis. *Prog. Phys. Geog.*, **20**(1), 1–19.

Osterkamp, T. E., & Gilfillian, R. E. 1975. Nucleation characteristics of stream water and frazil ice nucleation. *Water Resour. Res.*, **11**(6), 926–928.

Osterkamp, T. E., & Gosink, J. P. 1983. Frazil ice formation and ice cover development in interior Alaska streams. *Cold Reg. Sci. Technol.*, **8**(1), 43–56.

Paola, C., & Voller, V. R. 2005. A generalized Exner equation for sediment mass balance. *J. Geophys. Res.*, **110**(F4), F04014.

Park, I., & Jain, S. C. 1987. Numerical simulation of degradation of alluvial channel beds. *J. Hydraul. Eng., ASCE*, **113**(7), 845–859.

Parker, G., & Sutherland, A. J. 1990. Fluvial armor. *J. Hydraul. Res.*, **28**(5), 529–544.

Patankar, S. V. 1980. *Numerical heat transfer and fluid flow.* Washington: Hemisphere Pub. Corp.

Paterson, W. S. B. 1994. *The physics of glaciers*. 3rd edn. Tarrytown, NY: Pergamon.

Pearce, J. T., Pazzaglia, F. J., Evenson, E. B., Lawson, D. E., Alley, R. B., Germanoski, D., & Denner, J. D. 2003. Bedload component of glacially discharged sediment: insights from the Matanuska Glacier, Alaska. *Geology*, **31**(1), 7–10.

Pettersson, R., Jansson, P., & Blatter, H. 2004. Spatial variability in water content at the cold-temperate transition surface of the polythermal Storglaciären, Sweden. *J. Geophys. Res.*, **109**(F2), F02009.

Pfeffer, W. T., Illangasekare, T. H., & Meier, M. F. 1990. Analysis and modeling of melt-water refreezing in dry snow. *J. Glaciol.*, **36**(123), 238–246.

Philip, J. R. 1980. Thermal fields during regelation. *Cold Reg. Sci. Technol.*, **3**, 193–203.

Phillips, B. C., & Sutherland, A. J. 1989. Spatial lag effects in bed load sediment transport. *J. Hydraul. Res.*, **27**(1), 115–203.

Pigford, R. L. 1955. Nonisothermal flow and heat transfer inside vertical tubes. *C.E.P. Symposium Series*, **51**(17), 79–92.

Prest, V. K., Grandt, D. R., & Rampton, V. N. 1968. *Glacial map of Canada*. Geological Survey of Canada. Map 1253A, scale 1:5,000,000.

Pruppacher, H. R., & Klett, J. D. 1997. *Microphysics of clouds and precipitation*. 2nd edn. Dordrecht, The Netherlands: Kluwer.

Rempel, A. W., Wettlaufer, J. S., & Worster, M. G. 2004. Premelting dynamics in a continuum model of frost heave. *J. Fluid Mech.*, **498**, 227–244.

Riihimaki, C. A., MacGregor, K. R., Anderson, R. S., Anderson, S. P., & Loso, M. G. 2005. Sediment evacuation and glacial erosion rates at a small alpine glacier. *J. Geophys. Res.*, **110**(F3), F03003.

Roberts, M. J., Tweed, F. S., Russell, A. J., Knudsen, Ó., Lawson, D. E., Larson, G. J., Evenson, E. B., & Björnsson, H. 2002. Glaciohydraulic supercooling in Iceland. *Geology*, **30**(5), 439–442.

Röthlisberger, H. 1968. Erosive processes which are likely to accentuate or reduce the bottom relief of valley glaciers. *Pages 87–97 of: International Association of Scientific Hydrology Publication 79*, vol. 79. General Assembly of Bern 1967 — Snow and Ice.

Röthlisberger, H. 1972. Water pressure in intra- and subglacial channels. *J. Glaciol.*, **11**, 177–203.

Röthlisberger, H., & Lang, H. 1987. Glacial hydrology. *Pages 207–284 of:* Gurnell, A. M., & Clark, M. J. (eds), *Glacio-fluvial sediment transfer: an alpine perspective*. New York: John Wiley and Sons.

Russell, A. J., Roberts, M. J., Fay, H., Marren, P. M., Cassidy, N. J., Tweed, F. S., & Harris, T. 2006. Icelandic jökulhlaups: Implications for ice-sheet hydrology, sediment transfer and geomorphology. *Geomorphology*, **75**(1–2), 33–64.

Schiesser, W. E. 1991. *The numerical method of lines, integration of partial differential equations.* New York: Academic Press.

Schlichting, H. 1979. *Boundary Layer Theory.* 7th edn. New York: McGraw-Hill.

Schoof, C. 2005. The effect of cavitation on glacier sliding. *Proc. Roy. Soc. Lond. A Mat.*, **461**, 609–627.

Seaberg, S. Z., Seaberg, J. Z., Hooke, R. L., & Wiberg, D. W. 1988. Character of the englacial and subglacial drainage system in the lower part of the ablation area of Storglaciären, Sweden, as revealed by dye-trace studies. *J. Glaciol.*, **34**(117), 217–227.

Shampine, L. F., & Reichelt, M. W. 1997. The MATLAB ODE suite. *SIAM J. Sci. Comput.*, **18**(1), 1–22.

Shoemaker, E. M. 1987. Pressure and temperature effects in Röthlisberger channels. *Cold Reg. Sci. Technol.*, **14**(2), 121–127.

Shreve, R. L. 1972. Movement of water in glaciers. *J. Glaciol.*, **11**(62), 205–214.

Shreve, R. L. 1985. Esker characteristics in terms of glacier physics, Katahdin esker system, Maine. *Geol. Soc. Am. Bull.*, **96**, 639–646.

Smith, J. Dungan, & McLean, S. R. 1977. Spatially averaged flow over a wavy surface. *J. Geophys. Res.*, **82**(12), 1735–1746.

Snow, D. T. 1968. Rock fracture spacings, openings and porosities. *J. Soil Mech. Found. Div. Am. Soc. Civ. Eng.*, **94**(1), 73–91.

Spedding, N., & Evans, D. J. A. 2002. Sediments and lanforms at Kvíárjökull, south Iceland: a reappraisal of the glaciated valley landsystem. *Sediment. Geol.*, **149**(1–3), 21–42.

Spring, U., & Hutter, K. 1981. Numerical-studies of jökuhlhaups. *Cold Reg. Sci. Technol.*, **4**(3), 227–244.

Spring, U., & Hutter, K. 1982. Conduit flow of a fluid through its solid phase and its application to intraglacial channel flow. *Int. J. Eng. Sci.*, **20**(2), 327–363.

Staniforth, A., & Côté, J. 1991. Semi-Lagrangian integration schemes for atmospheric models—A review. *Mon. Wea. Rev.*, **119**(9), 2206–2223.

Stenborg, T. 1973. Some viewpoints on the internal drainage of glaciers. *Pages 117–129 of: International Association of Scientific Hydrology Publication 95.* IASH.

Stone, D. B., & Clarke, G. K. C. 1993. Estimation of subglacial hydraulic properties from induced changes in basal water pressure: a theoretical framework for borehole–response tests. *J. Glaciol.*, **39**(132), 327–340.

Swift, D. A., Nienow, P. W., Hoey, T. B., & Mair, D. W. F. 2005. Seasonal evolution of runoff from Haut Glacier d'Arolla, Switzerland and implications for glacial geomorphic processes. *J. Hydrol.*, **309**(1–4), 133–148.

Townsend, D. W., & Vickery, R. P. 1967. An experiment in regelation. *Philos. Mag.*, **16**(144), 1275–1280.

Truffer, M., Motyka, R. J., Harrison, W. D., Echelmeyer, K. A., Fisk, B., & Tulaczyk, S. 1999. Subglacial drilling at Black Rapids Glacier, Alaska, U.S.A.: drilling method and sample descriptions. *J. Glaciol.*, **45**(151), 495–505.

Tulaczyk, S., Kamb, B., Scherer, R. P., & Engelhardt, H. F. 1998. Sedimentary processes at the base of a West Antarctic ice stream: Constraints from textural and compositional properties of subglacial debris. *J. Sediment. Res. A*, **68**(108), 487–496.

Tweed, F. S., Roberts, M. J., & Russell, A. J. 2005. Hydrologic monitoring of supercooled meltwater from Icelandic glaciers. *Quaternary Sci. Rev.*, **24**, 2308–2318.

van Niekerk, A., Vogel, K. R., Slingerland, R. L., & Bridge, J. S. 1992. Routing of heterogeneous sediments over movable bed: model development. *J. Hydraul. Eng., ASCE*, **118**(2), 246–262.

van Rijn, L. C. 1984a. Sediment transport, Part I: Bed load transport. *J. Hydraul. Eng., ASCE*, **110**(10), 1431–1456.

van Rijn, L. C. 1984b. Sediment transport, Part II: Suspended load transport. *J. Hydraul. Eng., ASCE*, **110**(11), 1613–1641.

van Rijn, L. C. 1984c. Sediment transport, Part III: Bed forms and alluvial roughness. *J. Hydraul. Eng., ASCE*, **110**(12), 1733–1754.

Vanoni, V. A., & Nomicos, G. N. Resistance properties of sediment-laden streams. *Trans. Amer. Soc. Civil Eng.*

Vogel, S. W., Tulaczyk, S., Kamb, B., Engelhardt, H., Carsey, F. D., Behar, A. E., Lane, A. L., & Joughin, I. 2005. Subglacial conditions during and after stoppage of an Antarctic Ice Stream: Is reactivation imminent? *Geophys. Res. Lett.*, **32**, L14502.

Wagner, W., & Pruss, A. 1993. International equations for the saturation properties of ordinary water substance. Revised according to the International Temperature Scale of 1990. *J. Phys. Chem. Ref. Data*, **22**(3), 783–787.

Wagner, W., Saul, A., & Pruß, A. 1994. International equations for the pressure along the melting and along the sublimation curve of ordinary water substance. *J. Phys. Chem. Ref. Data*, **23**(3), 515–525.

Walder, J. 1982. Stability of sheet flow of water beneath temperate glaciers and implications for glacier sliding. *J. Glaciol.*, **28**(99), 273–293.

Walder, J., & Hallet, B. 1979. Geometry of former subglacial water channels and cavities. *J. Glaciol.*, **23**(89), 335–346.

Walder, J. S. 1986. Hydraulics of subglacial cavities. *J. Glaciol.*, **32**(112), 439–445.

Walder, J. S., & Fowler, A. 1994. Channelized subglacial drainage over a deformable bed. *J. Glaciol.*, **40**(134), 3–15.

Weertman, J. 1964. The theory of glacier sliding. *J. Glaciol.*, **5**(39), 287–303.

Weertman, J. 1972. General theory of water flow at the base of a glaciaeier or ice sheet. *Rev. Geophys. Space*, **10**(1), 287–333.

Weertman, J. 1986. Basal water and high pressure basal ice. *J. Glaciol.*, **32**(112), 455–463.

Weertman, J., & Birchfield, G. E. 1983. Stability of sheet water flow under a glacier. *J. Glaciol.*, **29**(103), 374–382.

Wettlaufer, J. S. 2001. Introduction to crystallization phenomena in natural and artificial sea ice. *Pages 105–194 of:* Leppäranta, M. (ed), *Physics of ice–covered seas*, vol. 1. Helsinki: Helsinki University Printing House.

Wilcock, P. R. 1997. Partial transport of a sand/gravel sediment. *Water Resour. Res.*, **33**(1), 235–245.

Wilcock, P. R., & McArdell, B. W. 1993. Surface-based fractional transport rates: mobilization thresholds and partial transport of a sand-gravel sediment. *Water Resour. Res.*, **29**(4), 1297–1312.

Wilcock, P. R., & McArdell, B. W. 1997. The components of fractional transport rate. *Water Resour. Res.*, **33**(1), 246–258.

Wingham, D. J., Siegert, M. J., Shepherd, A., & Muir, A. S. 2006. Rapid discharge connects Antarctic subglacial lakes. *Nature*, **440**, 1033–1036.

Worster, M. G. 1997. Convection in mushy layers. *Annu. Rev. Fluid Mech.*, **29**, 91–122.

Wu, W. 2004. Depth-averaged two-dimensional numerical modeling of unsteady flow and nonuniform sediment transport in open channels. *J. Hydraul. Eng., ASCE*, **130**(10), 1013–1024.

Wu, W., Vieira, D., & Wang, S. S. Y. 2004. One-dimensional numerical model for nonuniform sediment transport under unsteady flows in channel networks. *J. Hydraul. Eng., ASCE*, **130**(9), 914–923.

Yalin, M. S. 1972. *Mechanics of sediment transport.* New York: Pergamon.

Yang, C. T. 1996. *Sediment transport: theory and practice.* New York: McGraw-Hill.

Appendix A

Synthetic glacier section

Synthetic examples of glacier sections provide idealized situations for understanding englacial and subglacial water systems. These synthetics provide useful visual elucidation of ice–bed configurations and surface to bed slope ratios. Sections of glaciers interpreted from radar, seismic, and other investigations provide structure that is not necessarily attributable to hydrology; therefore, these are not used when introducing hydraulic concepts. Furthermore, longitudinal sections of real glaciers may not necessarily be representative of a glacier's hydraulic section. Ideally, a hydraulic section would be derived from a three-dimensional digital database of a glacier's bed and surface topography, but these datasets are often unavailable.

Consider a horizontal coordinate x, where the downstream end of the glacier is located at $x = x_0$. At some upstream value $x = x_l$, the section terminates. Subglacial water may flow from x_l to x_0. The vertical coordinate z, is a height above an arbitrary datum. The thickness of the glacier is

$$Z^{\mathrm{i}} = z^{\mathrm{r}} - z^{\mathrm{b}}, \tag{A.1}$$

where Z^{i} is the glacier ice thickness, z^{b} is the height of the ice–bed interface, and z^{r} is the height of the surface of the glacier.

As shown in Figure A.1, the base of the glacier is divided among three regimes. These three regimes are given by

$$z^{\mathrm{b}} = \begin{cases} z_l^{\mathrm{b}} & \text{for} \quad x_u < x \leq x_l, \\ C_x \left(x - x_u\right)^{2o_x} + z_l^{\mathrm{b}} & \text{for} \quad x_w < x \leq x_u, \\ 2C_x o_x \left(x_w - x_u\right)^{2o_x - 1} \left(x - x_w\right) + C_x \left(x_w - x_u\right)^{2o_x} + z_l^{\mathrm{b}} & \text{for} \quad x_0 \leq x \leq x_w. \end{cases} \tag{A.2}$$

where the coefficient C_x is an arbitrary real number and o_x is an arbitrary positive integer that determines how rapidly a transition occurs. The first regime is a horizontal entrance of the water from x_l to x_u at height $z^{\mathrm{b}} = z_l$. From x_u to x_w, there is a transition where the base turns upwards from horizontal to sloped. Because water flow along this horizon is dependent on the first derivative of the hydraulic potential, the derivative dz^{b}/dx should be smooth. The slope is chosen to ensure that the first derivative of z^{b} is smooth at x_w. Finally, from x_w to x_0, the slope of the subglacial horizon is again constant, making the final portion a wedge. The surface of a synthetic section has a constant slope where the elevation of the surface is

$$z^{\mathrm{r}} = \frac{\left(Z_l^{\mathrm{i}} + z_l^{\mathrm{b}}\right) - \left(Z_0^{\mathrm{i}} + z_0\right)}{x_l - x_0} x + z_0^{\mathrm{b}} + Z_0^{\mathrm{i}}, \tag{A.3}$$

where Z_l^{i} and Z_0^{i} are the ice thicknesses at x_l and x_0, respectively. If z_l^{b}, x_u, and Z_0^{i} are known, then one of x_w, z_w^{b} or Z_l^{i} is necessary to solve equations (A.2) and (A.3) for the longitudinal profile.

If a specific ratio is required between the surface slope and the slope of the wedge such that $\tan \alpha^{\mathrm{b}} = -\mathcal{R} \tan \alpha^{\mathrm{r}}$, then the location of x_w needs to be found with respect to the third equation

in (A.2). For $o_x = 1$ and a known z_0^{b}, x_w takes the value

$$x_w = x_0 + \left\{ (x_u - x_0)^2 + \frac{1}{C_x} \left(z_l - z_0^{\mathrm{b}} \right) \right\}^{\frac{1}{2}}. \tag{A.4}$$

Substituting this equation into the second equation of (A.2) gives z_w^{b}. Rewriting equation (A.3) with the ratio $\mathcal{R}$ yields

$$z^{\mathrm{r}} = \frac{1}{\mathcal{R}} \left(\frac{z_0^{\mathrm{b}} - z_w^{\mathrm{b}}}{x_0 - x_w} \right) x + z_0^{\mathrm{b}} + Z_0^{\mathrm{i}}. \tag{A.5}$$

If the upstream ice thickness Z_0^{i} is known and $o_x = 1$, then x_w takes the value

$$x_w \quad = \quad x_0 + \frac{x_0 - x_l}{\mathcal{R}} + \frac{1}{\mathcal{R}} \left\{ (x_l - x_0 (\mathcal{R} + 1) + \mathcal{R} x_u)^2 + \frac{\mathcal{R}^2}{C_x} \left(Z_0^{\mathrm{i}} - Z_l^{\mathrm{i}} \right) \right\}^{1/2}. \tag{A.6}$$

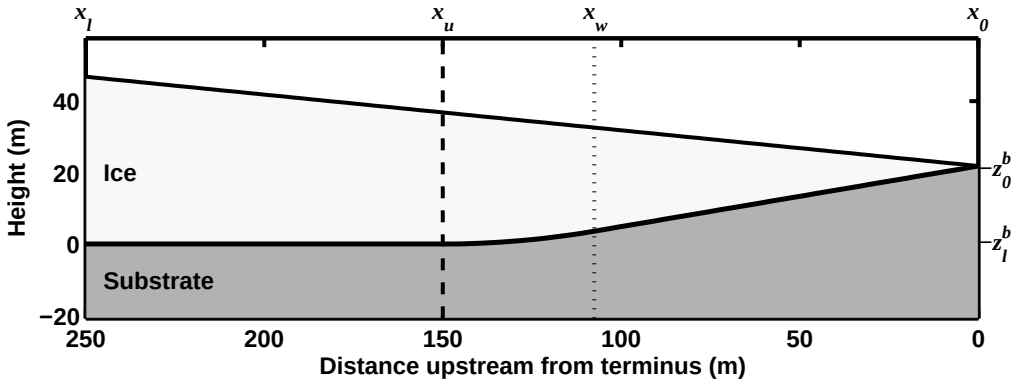

Figure A.1: A synthetic glacier section. Subglacial water flows from left to right along the line at the interface of the ice and substrate. Parameters are given in Table A.1. The aspect ratio is 1 : 1.

Table A.1: Parameters used to create Figure A.1

Parameter	Value	Units
x_0	0.00	m
x_w	107.59	m
x_u	150.00	m
x_l	250.00	m
z_0^{b}	21.85	m
z_l^{b}	0.00	m
Z_0^{i}	0.00	m
Z_l^{i}	46.86	m
C_x	0.002	m^{1-2o_x}
o_x	1	[unitless]
$\mathcal{R}$	-1.70	[unitless]
$\tan\alpha^{\mathrm{r}}$	0.10	[unitless]
$\tan\alpha_w^{\mathrm{b}}$	0.17	[unitless]

Appendix B

Grain parameterization for ice intrusion

For spheres that are intersected by a plane above their equator, the volume above that plane is a spherical section less the volume of the inscribed cone below it. The cone is inverted with its vertex at the center of the sphere and its base along H^{b}. The spherical section plus the cone is below the plane, and the spherical cap is above the plane. The plane intersects the sphere at a height H^{b} which is greater than the sphere radius r_i.

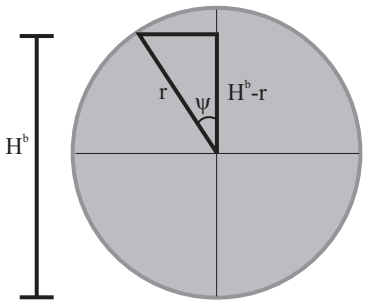

Figure B.1: Figure illustrating the relationship of r_i, H^{b}, and ψ

For $H^{\mathrm{b}} > r_i$, the volume is that of the spherical cap. The cap is the volume of the spherical segment through a polar angle ψ minus the inscribed cone below the cap,

$$\begin{aligned} V_{e:i} &= \int_{\theta=0}^{2\pi}\int_{R=0}^{r_i}\int_{\psi=0}^{\cos^{-1}\left(\left(H^{\mathrm{b}}-r_i\right)/r_i\right)} R^2\sin\psi\, d\psi\, dR\, d\theta - \frac{\pi}{3}\left(H^{\mathrm{b}}-r_i\right)\left(2r_iH^{\mathrm{b}}-\left(H^{\mathrm{b}}\right)^2\right), \\ &= \frac{\pi}{3}\left(2r_i-H^{\mathrm{b}}\right)\left(2r_i^2+r_iH^{\mathrm{b}}-\left(H^{\mathrm{b}}\right)^2\right), \end{aligned} \tag{B.1}$$

where $V_{e:i}$ is the effective volume, R is a radius, and ψ and θ are angles. The effective area is simply the area of the base of the cone,

$$a_{e:i} = \pi\left(2H^{\mathrm{b}}r_i-\left(H^{\mathrm{b}}\right)^2\right). \tag{B.2}$$

For spheres intersected by a plane below their equator, the relationship takes a similar form. The spherical cap is the bulk of the sphere when $H^{\mathrm{b}} < r_i$. In this case, the section of interest is the spherical section plus the inscribed cone. The cone has its vertex at the center of the sphere

and its base along H^{b}. A similar integration that yielded equation (B.1) yields,

$$\begin{aligned} V_{e:i} &= \int_{\theta=0}^{2\pi}\int_{R=0}^{r_i}\int_{\psi=0}^{\pi-\cos^{-1}\left(\left(r_i-H^{\mathrm{b}}\right)/r_i\right)} R^2\sin\psi\, d\psi\, dR\, d\theta + \frac{\pi}{3}\left(r_i - H^{\mathrm{b}}\right)\left(\left(H^{\mathrm{b}}\right)^2 - 2r_i H^{\mathrm{b}}\right) \\ &= \frac{\pi}{3}\left(2r_i - H^{\mathrm{b}}\right)\left(2r_i^2 + r_i H^{\mathrm{b}} - \left(H^{\mathrm{b}}\right)^2\right). \end{aligned} \tag{B.3}$$

It is not surprising that equations (B.1) and (B.3) are exactly equal. Once the ice has passed the equator, the area normal to the force is simply the area of the equator. The effective area is then that of the maximum cross section of the sphere,

$$a_{e:i} = \pi r_i^2. \tag{B.4}$$

If the geometry is a hemisphere resting on the same datum as H^{b}, then the spherical cap takes a similar form to equation (B.1),

$$\begin{aligned} V_{e:i} &= \int_{\theta=0}^{2\pi}\int_{R=0}^{r_i}\int_{\psi=0}^{\cos^{-1}\left(H^{\mathrm{b}}/r_i\right)} R^2\sin\psi\, d\psi\, dR\, d\theta - \frac{\pi}{3}H^{\mathrm{b}}\left(r_i^2 - \left(H^{\mathrm{b}}\right)^2\right) \\ &= \frac{\pi}{3}\left(2r_i^3 - 3H^{\mathrm{b}}r_i^2 + \left(H^{\mathrm{b}}\right)^3\right). \end{aligned} \tag{B.5}$$

Without an extra length of radius, the effective area is similar to equation (B.2),

$$a_{e:i} = \pi\left(r_i^2 - \left(H^{\mathrm{b}}\right)^2\right). \tag{B.6}$$

Appendix C

Solution of the equations governing ice intrusion

Because the closure relationship is dependent on the number of grain sizes and the closure velocity, the solution must be simultaneous for all of the variables. Solving for the bed closure velocity and the relevant stress terms requires a nonlinear, iterative solver. In this case, I employ a Newton scheme. The Newton solver requires error estimates G, on the functions as well as the Jacobian terms.

C.1 Three equation model

One method is direct solution of the $2N+1$ equations (3.17), (3.12), and either (3.13) or (3.14b) for the $2N+1$ variables: σ_i^{s}, σ_i, and v. The first two conditions and their accompanying Jacobian terms ($\partial \mathrm{G}_i / \partial\{\sigma_j^{\mathrm{s}}, \sigma_j, v\}$) are straightforward,

$$
\begin{aligned}
\mathrm{G}_1(v, \sigma_1^{\mathrm{s}} \dots \sigma_N^{\mathrm{s}}, \sigma_1 \dots \sigma_N) &= -\frac{\beta K_e}{\rho^{\mathrm{i}} L} \left(\frac{A_e}{V_e}\right)_i \left(\frac{A_{i-1}}{A_i^{\mathrm{s}}} \sigma_{e:i}\right) + \mathcal{A} l_{e:i} \operatorname{sgn}(-\sigma_{e:i}) \left|\sigma_{e:i}\right|^n - v, && \text{(C.1a)} \\
\frac{\partial \mathrm{G}_1}{\partial v} &= -1 \,, \\
\frac{\partial \mathrm{G}_1}{\partial \sigma_j^{\mathrm{s}}} &= \delta_{ij} \left\{ -\frac{\beta K_e}{\rho^{\mathrm{i}} L} \left(\frac{A_e}{V_e}\right)_i \frac{A_{i-1}}{A_i^{\mathrm{s}}} + n \mathcal{A} l_{e:i} \frac{A_i^{\mathrm{s}}}{A_{i-1}} \operatorname{sgn}(-\sigma_{e:i}) \left|\sigma_{e:i}\right|^{n-1} \right\}, \\
\frac{\partial \mathrm{G}_1}{\partial \sigma_j} &= \delta_{ij} \left\{ \frac{\beta K_e}{\rho^{\mathrm{i}} L} \left(\frac{A_e}{V_e}\right)_i \frac{A_{i-1}}{A_i^{\mathrm{s}}} - n \mathcal{A} l_{e:i} \frac{A_i^{\mathrm{s}}}{A_{i-1}} \operatorname{sgn}(-\sigma_{e:i}) \left|\sigma_{e:i}\right|^{n-1} \right\} \,, \\
\mathrm{G}_2(v, \sigma_1^{\mathrm{s}} \dots \sigma_N^{\mathrm{s}}, \sigma_1 \dots \sigma_N) &= \sigma^{\mathrm{i}} - p^{\mathrm{w}} - \sum_{i=1}^{N} \frac{A_i^{\mathrm{s}}}{A_{i-1}} \left(\sigma_i^{\mathrm{s}} - \sigma_i\right), && \text{(C.1b)} \\
\frac{\partial \mathrm{G}_2}{\partial v} &= 0 \,, \\
\frac{\partial \mathrm{G}_2}{\partial \sigma_i^{\mathrm{s}}} &= -\frac{A_i^{\mathrm{s}}}{A_{i-1}}, \\
\frac{\partial \mathrm{G}_2}{\partial \sigma_i} &= \frac{A_i^{\mathrm{s}}}{A_{i-1}}.
\end{aligned}
$$

In equation (C.1a) and its derivatives, the effective stress $\sigma_{e:i}$ should be replaced by its definition $A_i^{\mathrm{s}}/A_{i-1}(\sigma_i^{\mathrm{s}} - \sigma_i)$. Equation (C.1a) is the misfit for the relationship governing the closure velocity. Equation (C.1b) is the misfit for the total effective stress equation.

The third condition is not specific but must relate the intermediate stresses to one another or the intermediate stresses to the grain stress. These relationships arise from the definition of

the effective stress for the ith grain size.

$$\begin{aligned} \mathrm{G}_3(v, \sigma_1^{\mathrm{s}} \dots \sigma_N^{\mathrm{s}}, \sigma_1 \dots \sigma_N) &= \frac{A_i^{\mathrm{s}}}{A_{i-1}} \left(\sigma_i^{\mathrm{s}} - \sigma_i\right) - \sigma_{i-1} + \sigma_i, \\ \frac{\partial \mathrm{G}_3}{\partial v} &= 0\ , \\ \frac{\partial \mathrm{G}_3}{\partial \sigma_j^{\mathrm{s}}} &= \delta_{ij} \frac{A_i^{\mathrm{s}}}{A_{i-1}}, \\ \frac{\partial \mathrm{G}_3}{\partial \sigma_j} &= \delta_{ij} \left(-\frac{A_i^{\mathrm{s}}}{A_{i-1}} + 1\right). \end{aligned} \tag{C.2}$$

An alternative third condition is that the stresses must locally sum from equation (3.13).

$$\begin{aligned} \mathrm{G}_3(v_i, \sigma_1^{\mathrm{s}} \dots \sigma_N^{\mathrm{s}}, \sigma_1 \dots \sigma_N) &= A_{i-1}\sigma_{i-1} - \left(A_i^{\mathrm{s}}\sigma_i^{\mathrm{s}} + A_i\sigma_i\right), \\ \frac{\partial \mathrm{G}_3}{\partial v} &= 0\ , \\ \frac{\partial \mathrm{G}_3}{\partial \sigma_j^{\mathrm{s}}} &= -\delta_{ij} A_i^{\mathrm{s}}, \\ \frac{\partial \mathrm{G}_3}{\partial \sigma_j} &= -\delta_{ij} A_i. \end{aligned} \tag{C.3}$$

There are other variations on equations (C.2) and (C.3), but these formulations contain the same information relating the effective stress to the grain stresses and intermediate stresses.

C.2 Two equation model

Because the entire system is driven by the effective stress, there is not a need to calculate the stress on the sediments and the intermediate stress in a numerical solver. These stresses can be calculated recursively starting with either the water pressure or ice overburden pressure.

$$\mathrm{G}_1(v, \sigma_{e:1} \dots \sigma_{e:N}) = -\frac{\beta K_e}{\rho^{\mathrm{i}} L} \left(\frac{A_e}{V_e}\right)_i \frac{A_{i-1}}{A_i^{\mathrm{s}}} \sigma_{e:i} + \mathcal{A} l_{e:i} \operatorname{sgn}\left(-\sigma_{e:i}\right) \left|\sigma_{e:i}\right|^n - v, \tag{C.4a}$$

$$\begin{aligned} \frac{\partial \mathrm{G}_1}{\partial v} &= -1, \\ \frac{\partial \mathrm{G}_1}{\partial \sigma_{e:j}} &= \delta_{ij} \left\{ -\frac{\beta K_e}{\rho^{\mathrm{i}} L} \left(\frac{A_e}{V_e}\right)_i \frac{A_{i-1}}{A_i^{\mathrm{s}}} + n\mathcal{A} l_{e:i} \operatorname{sgn}\left(-\sigma_{e:i}\right) \left|\sigma_{e:i}\right|^{n-1} \right\}, \end{aligned}$$

$$\mathrm{G}_2(v, \sigma_{e:1} \dots \sigma_{e:N}) = \sigma^{\mathrm{i}} - p^{\mathrm{w}} - \sum_{i=1}^{N} \sigma_{e:i}, \tag{C.4b}$$

$$\begin{aligned} \frac{\partial \mathrm{G}_2}{\partial v} &= 0, \\ \frac{\partial \mathrm{G}_2}{\partial \sigma_{e:i}} &= -1. \end{aligned}$$

Equation (C.4a) is the misfit to the closure velocity relationship, while equation (C.4b) is the misfit for the total effective stress. In this system of equations, there are $N + 1$ variables that

need to be found: N values of $\sigma_{e:j}$ and one value of v. As a result, there are N simultaneous versions of equation (C.4a) and N derivatives in σ_e. Equation (C.4b) completes the system.

In general, the three-equation version of the solution is less desirable. The third misfit equation, either (C.2) or (C.3), does not add much information. As a result, the condition numbers for the Jacobian matrix are considerably lower for the two-equation model. The consequence of this condition number is that the number of iterations required for convergence of the two-equation model is one to two orders of magnitude smaller than that of the three-equation model.

Appendix D

Sediment mass balances

D.1 Basal water mass balance

Chapter 4 requires four equations for the mass balance of the basal water layer: two each for the channel and sheet cross sections. Sediment and ice are assumed to be incompressible. The water is slightly compressible, which yields the pressure evolution equations. Sediment can be in the flowing water, on the bed, or in the ice. However, sediment is not permitted to be in the pore space of the ice. This assumption is consistent with Snow's (1968) model of flow through fracture networks where laminar flow occurs in fractures less than 2 mm wide. On the contrary, this assumption is inconsistent with the hypothesis of Lawson *et al.* (1998) whereby the ice filters sediment out of the water. The assumption can be changed; but it would not be consistent with englacial aquifer model[14].

The balance of mass follows a similar form to that presented in Chapter 2. The form presented there follows Spring & Hutter (1982). In addition, elements of the derivation presented by Walder & Fowler (1994) appear here.

D.1.1 Channel

Both constituents

I begin with the mass of the fluid,

$$M^{\mathrm{f}} = \int_s \int_{S^{\mathrm{b}}} \left\{ \lambda^{\mathrm{b}} \rho^{\mathrm{s}} + (1 - \lambda^{\mathrm{b}}) \rho^{\mathrm{w}} \right\} dS \, ds, \tag{D.1}$$

where the superscript $^{\mathrm{f}}$ denotes the fluid, or sediment–water mixture, such that M^{f} is the mass of the fluid and S^{b} is the subglacial cross sectional area of the fluid. The global and local rates of change of the sediment mass are

$$\frac{dM^{\mathrm{f}}}{dt} = \frac{d}{dt} \left[\int_s \left\{ \lambda^{\mathrm{b}} \rho^{\mathrm{s}} + \left(1 - \lambda^{\mathrm{b}} \right) \rho^{\mathrm{w}} \right\} S^{\mathrm{b}} ds \right], \tag{D.2a}$$

$$\frac{d}{dt} \left[\left\{ \lambda^{\mathrm{b}} \rho^{\mathrm{s}} + \left(1 - \lambda^{\mathrm{b}} \right) \rho^{\mathrm{w}} \right\} S^{\mathrm{b}} \right] = \left[1 + \frac{n_p^{\mathrm{i}} \rho^{\mathrm{w}}}{\left(1 - \lambda^{\mathrm{i}} \right) \left(1 - n_p^{\mathrm{i}} \right) \rho^{\mathrm{i}}} \right] m + \Psi^{\mathrm{i}} + \left[1 + \frac{n_p^{\mathrm{s}} \rho^{\mathrm{w}}}{\left(1 - n_p^{\mathrm{s}} \right) \rho^{\mathrm{s}}} \right] 2R^{\mathrm{b}} \tilde{\Psi}^{\mathrm{s}}, \tag{D.2b}$$

[14] Alternatively, a small layer could be defined above the flow but below the ice that has a high porosity. Water could then flow through the pore space. Cases such as these are beyond the scope of this thesis but merit attention.

where the source terms in equation (D.2b) originate in equations (2.13a) and (4.9b). Equation (D.2b) can be rewritten for a rate of change of the cross section,

$$\frac{\partial S^{\mathrm{b}}}{\partial t} = -\frac{\partial\left(S^{\mathrm{b}}u^{\mathrm{b}}\right)}{\partial s} + \frac{1}{\lambda^{\mathrm{b}}\rho^{\mathrm{s}} + (1-\lambda^{\mathrm{b}})\rho^{\mathrm{w}}}\left\{-S^{\mathrm{b}}\left(\rho^{\mathrm{s}}-\rho^{\mathrm{w}}\right)\left[\frac{\partial\lambda^{\mathrm{b}}}{\partial t} + u^{\mathrm{b}}\frac{\partial\lambda^{\mathrm{b}}}{\partial s}\right] + \left[1+\frac{n_p^{\mathrm{i}}\rho^{\mathrm{w}}}{\left(1-\lambda^{\mathrm{i}}\right)\left(1-n_p^{\mathrm{i}}\right)\rho^{\mathrm{i}}}\right]m + \Psi^{\mathrm{i}} + \left[1+\frac{n_p^{\mathrm{s}}\rho^{\mathrm{w}}}{\left(1-n_p^{\mathrm{s}}\right)\rho^{\mathrm{s}}}\right]2R^{\mathrm{b}}\tilde{\Psi}^{\mathrm{s}}\right\} \tag{D.3}$$

The change in the cross section resulting from the amount of ice melted per unit time and the amount of sediment removed per unit time is the sum of those two components. From the misfit equation for ice, the change in cross section is equivalent to equations (2.14b) and (2.17) with the sediment in the ice included,

$$\left.\frac{\partial S^{\mathrm{b}}}{\partial t}\right|_{\mathrm{ice}} = \frac{1}{\left(1-\lambda^{\mathrm{i}}\right)\left(1-n_p^{\mathrm{i}}\right)\rho^{\mathrm{i}} + n_p^{\mathrm{i}}\rho^{\mathrm{w}} + \lambda^{\mathrm{i}}\left(1-n_p^{\mathrm{i}}\right)\rho^{\mathrm{s}}}\left\{\left[1+\frac{n_p^{\mathrm{i}}\rho^{\mathrm{w}}}{\left(1-\lambda^{\mathrm{i}}\right)\left(1-n_p^{\mathrm{i}}\right)\rho^{\mathrm{i}}}\right]m + \Psi^{\mathrm{i}}\right\} - 2S^{\mathrm{b}}\operatorname{sgn}(p^{\mathrm{i}}-p^{\mathrm{b}})\left(\frac{|p^{\mathrm{i}}-p^{\mathrm{b}}|}{n\mathcal{B}}\right)^{n}. \tag{D.4}$$

In this equation, λ^{i} is assumed constant. This is a small approximation because the bulk of the material that is removed from the channel walls is ice rather than sediment. The change in λ^{i} is handled by equation (D.19).

The portion of sediment removed per unit time can be treated similarly to equation (2.11) where the cross section that contains the sediment removed per unit time is

$$\widehat{S} = S^{\mathrm{s}} - S^{\mathrm{b}}. \tag{D.5}$$

This equation only applies to the bed exposed to the flow and not to the overlying ice. Applying the mass balance to equation (D.5) in a similar fashion to equation (2.13b) yields,

$$\left\{\left(1-n_p^{\mathrm{s}}\right)\rho^{\mathrm{s}} + n_p^{\mathrm{s}}\rho^{\mathrm{w}}\right\}\left\{\frac{\partial\widehat{S}}{\partial t} + \frac{\partial}{\partial s}\left(u_s^{\mathrm{s}}\widehat{S}\right)\right\} = -\left\{1+\frac{n_p^{\mathrm{s}}\rho^{\mathrm{w}}}{\left(1-n_p^{\mathrm{s}}\right)\rho^{\mathrm{s}}}\right\}2R^{\mathrm{b}}\tilde{\Psi}^{\mathrm{s}}. \tag{D.6}$$

Because the bed is not flowing, the convective velocity in the s-direction u_s^{s} is zero. Rewriting this equation in terms of the change in the fluid cross section gives,

$$\left.\frac{\partial S^{\mathrm{b}}}{\partial t}\right|_{\mathrm{bed}} = \frac{\partial S^{\mathrm{s}}}{\partial t} + \frac{2R^{\mathrm{b}}\tilde{\Psi}^{\mathrm{s}}}{\left(1-n_p^{\mathrm{s}}\right)\rho^{\mathrm{s}}}, \tag{D.7}$$

where $\partial S^{\mathrm{s}}/\partial t$ is the rate of change of the sediment. If the sediment were allowed to deform to close the fluid cross-section, then this rate of change would be the deformation of the sediment into the channel (*e.g.,* Walder & Fowler, 1994). However, in this case, $\partial S^{\mathrm{s}}/\partial t$ is exactly zero. From equations (D.4) and (D.7), the change of the cross section from misfit considerations is

$$\frac{\partial S^{\mathrm{b}}}{\partial t} = \frac{1}{\left(1-\lambda^{\mathrm{i}}\right)\left(1-n_p^{\mathrm{i}}\right)\rho^{\mathrm{i}} + n_p^{\mathrm{i}}\rho^{\mathrm{w}} + \lambda^{\mathrm{i}}\left(1-n_p^{\mathrm{i}}\right)\rho^{\mathrm{s}}}\left\{\left[1+\frac{n_p^{\mathrm{i}}\rho^{\mathrm{w}}}{\left(1-\lambda^{\mathrm{i}}\right)\left(1-n_p^{\mathrm{i}}\right)\rho^{\mathrm{i}}}\right]m + \Psi^{\mathrm{i}}\right\} - 2S^{\mathrm{b}}\operatorname{sgn}(p^{\mathrm{i}}-p^{\mathrm{b}})\left(\frac{|p^{\mathrm{i}}-p^{\mathrm{b}}|}{n\mathcal{B}}\right)^{n} + \frac{2R^{\mathrm{b}}\tilde{\Psi}^{\mathrm{s}}}{\left(1-n_p^{\mathrm{s}}\right)\rho^{\mathrm{s}}}. \tag{D.8}$$

Using equation (D.3), the change in pressure via the compressibility assumption becomes

$$\frac{\partial p^{\mathrm{b}}}{\partial t} = -\frac{1}{\gamma^{\mathrm{b}} S^{\mathrm{b}}}\left(\frac{\partial S^{\mathrm{b}}}{\partial t} + \frac{\partial\left(S^{\mathrm{b}} u^{\mathrm{b}}\right)}{\partial s} - \frac{1}{\lambda^{\mathrm{b}}\rho^{\mathrm{s}} + (1-\lambda^{\mathrm{b}})\rho^{\mathrm{w}}}\left\{ - S^{\mathrm{b}}\left(\rho^{\mathrm{s}} - \rho^{\mathrm{w}}\right)\left[\frac{\partial \lambda^{\mathrm{b}}}{\partial t} + u^{\mathrm{b}}\frac{\partial \lambda^{\mathrm{b}}}{\partial s}\right]\right.\right.$$
$$\left.\left. + \left[1 + \frac{n_p^{\mathrm{i}}\rho^{\mathrm{w}}}{\left(1-\lambda^{\mathrm{i}}\right)\left(1-n_p^{\mathrm{i}}\right)\rho^{\mathrm{i}}}\right] m + \Psi^{\mathrm{i}} + \left[1 + \frac{n_p^{\mathrm{s}}\rho^{\mathrm{w}}}{\left(1-n_p^{\mathrm{s}}\right)\rho^{\mathrm{s}}}\right] 2R^{\mathrm{b}}\tilde{\Psi}^{\mathrm{s}}\right\}\right). \tag{D.9}$$

Qualitatively, equation (D.8) is extremely close to equation (2.17). Differences between these two equations stem from the source of sediment in the ice and the supply term for sediment from the bed. The coefficient preceding the melt rate in equation (D.8) is large relative to the equivalent coefficient in equation (2.17). Substituting Ψ^{i} (eq. 4.34a, $m > 0$) into equation (D.8) yields a coefficient of $1/\left\{(1-\lambda^{\mathrm{i}})(1-n_p^{\mathrm{i}})\rho^{\mathrm{i}}\right\}$, which is similar to the equivalent coefficient in equation (2.17). On the surface, equations (D.9) and (2.15) look quite different. However, both equations are essentially the same with the exception of the space created by the supply of sediment from the bed. The small corrections for sediments in the flow could largely be ignored without sacrificing accuracy in the pressure solution. These corrections include: eliminate the derivatives of the sediment concentration in the flow, and eliminate the supply of sediment as ice melts. If the bed were aggressively aggrading or eroding, it would be difficult to eliminate either of the bed sediment supply terms. However, if the bed was fairly stable, then these terms could also be eliminated.

An alternative formulation

The balance of mass for the water,

$$M^{\mathrm{w}} = \int_s \int_{S^{\mathrm{b}}} (1-\lambda^{\mathrm{b}})\rho^{\mathrm{w}} dS\, ds, \tag{D.10}$$

can be drawn separately from equation (D.1). Carrying out the same steps above, the rate of change of the cross section is

$$\frac{\partial S^{\mathrm{b}}}{\partial t} = -\frac{\partial\left(S^{\mathrm{b}} u^{\mathrm{b}}\right)}{\partial s} + \frac{1}{\left(1-\lambda^{\mathrm{b}}\right)\rho^{\mathrm{w}}}\left\{ S^{\mathrm{b}}\rho^{\mathrm{w}}\left[\frac{\partial \lambda^{\mathrm{b}}}{\partial t} + u^{\mathrm{b}}\frac{\partial \lambda^{\mathrm{b}}}{\partial s}\right]\right.$$
$$\left. + \left[1 + \frac{n_p^{\mathrm{i}}\rho^{\mathrm{w}}}{\left(1-\lambda^{\mathrm{i}}\right)\left(1-n_p^{\mathrm{i}}\right)\rho^{\mathrm{i}}}\right] m + \frac{n_p^{\mathrm{s}}\rho^{\mathrm{w}}}{\left(1-n_p^{\mathrm{s}}\right)\rho^{\mathrm{s}}} 2R^{\mathrm{b}}\tilde{\Psi}^{\mathrm{s}}\right\}. \tag{D.11}$$

Rewriting this equation in the spirit of equation (D.9) gives

$$\frac{\partial p^{\mathrm{b}}}{\partial t} = -\frac{1}{\gamma^{\mathrm{b}} S^{\mathrm{b}}}\left(\frac{\partial S^{\mathrm{b}}}{\partial t} + \frac{\partial\left(S^{\mathrm{b}} u^{\mathrm{b}}\right)}{\partial s} - \frac{1}{\left(1-\lambda^{\mathrm{b}}\right)\rho^{\mathrm{w}}}\left\{ S^{\mathrm{b}}\rho^{\mathrm{w}}\left[\frac{\partial \lambda^{\mathrm{b}}}{\partial t} + u^{\mathrm{b}}\frac{\partial \lambda^{\mathrm{b}}}{\partial s}\right]\right.\right.$$
$$\left.\left. + \left[1 + \frac{n_p^{\mathrm{i}}\rho^{\mathrm{w}}}{\left(1-\lambda^{\mathrm{i}}\right)\left(1-n_p^{\mathrm{i}}\right)\rho^{\mathrm{i}}}\right] m + \frac{n_p^{\mathrm{s}}\rho^{\mathrm{w}}}{\left(1-n_p^{\mathrm{s}}\right)\rho^{\mathrm{s}}} 2R^{\mathrm{b}}\tilde{\Psi}^{\mathrm{s}}\right\}\right). \tag{D.12}$$

This equation bears more similarity to the clear water equation (2.15) than equation (D.9) does. As an addition simplification, the derivatives of λ^{b} could be eliminated without affecting the rate of change of the pressure.

D.1.2 Sheet

Writing the equations for the sheet is a matter of converting the relevant equations from the foregoing discussion. The evolution of the height of the sheet is

$$\begin{aligned}\frac{\partial H^{\mathrm{b}}}{\partial t} =& \frac{1}{\left(1-\lambda^{\mathrm{i}}\right)\left(1-n_p^{\mathrm{i}}\right)\rho^{\mathrm{i}} + n_p^{\mathrm{i}}\rho^{\mathrm{w}} + \lambda^{\mathrm{i}}\left(1-n_p^{\mathrm{i}}\right)\rho^{\mathrm{s}}} \left\{ \left[1 + \frac{n_p^{\mathrm{i}}\rho^{\mathrm{w}}}{\left(1-\lambda^{\mathrm{i}}\right)\left(1-n_p^{\mathrm{i}}\right)\rho^{\mathrm{i}}} \right] \tilde{m} + \tilde{\Psi}^{\mathrm{i}} \right\} \\ &+ \left(\frac{\partial H^{\mathrm{b}}}{\partial t} \right)_{\mathrm{close}} + \frac{\tilde{\Psi}^{\mathrm{s}}}{\left(1-n_p^{\mathrm{s}}\right)\rho^{\mathrm{s}}}, \end{aligned} \tag{D.13}$$

where the closure relationship is derived in Chapter 3. The pressure equation can also be appropriated from the discussion above,

$$\begin{aligned}\frac{\partial p^{\mathrm{b}}}{\partial t} =& -\frac{1}{\gamma^{\mathrm{b}} H^{\mathrm{b}}} \left(\frac{\partial H^{\mathrm{b}}}{\partial t} + \frac{\partial \left(H^{\mathrm{b}} u^{\mathrm{b}} \right)}{\partial s} - \frac{1}{\lambda^{\mathrm{b}}\rho^{\mathrm{s}} + (1-\lambda^{\mathrm{b}})\rho^{\mathrm{w}}} \left\{ -H^{\mathrm{b}} \left(\rho^{\mathrm{s}} - \rho^{\mathrm{w}} \right) \left[\frac{\partial \lambda^{\mathrm{b}}}{\partial t} + u^{\mathrm{b}} \frac{\partial \lambda^{\mathrm{b}}}{\partial s} \right] \right. \right. \\ &\left. \left. + \left[1 + \frac{n_p^{\mathrm{i}}\rho^{\mathrm{w}}}{\left(1-\lambda^{\mathrm{i}}\right)\left(1-n_p^{\mathrm{i}}\right)\rho^{\mathrm{i}}} \right] \tilde{m} + \tilde{\Psi}^{\mathrm{i}} + \left[1 + \frac{n_p^{\mathrm{s}}\rho^{\mathrm{w}}}{\left(1-n_p^{\mathrm{s}}\right)\rho^{\mathrm{s}}} \right] \tilde{\Psi}^{\mathrm{s}} \right\} \right), \end{aligned} \tag{D.14a}$$

$$\begin{aligned}\frac{\partial p^{\mathrm{b}}}{\partial t} =& -\frac{1}{\gamma^{\mathrm{b}} H^{\mathrm{b}}} \left(\frac{\partial H^{\mathrm{b}}}{\partial t} + \frac{\partial \left(H^{\mathrm{b}} u^{\mathrm{b}} \right)}{\partial s} - \frac{1}{\left(1-\lambda^{\mathrm{b}}\right)\rho^{\mathrm{w}}} \left\{ H^{\mathrm{b}} \rho^{\mathrm{w}} \left[\frac{\partial \lambda^{\mathrm{b}}}{\partial t} + u^{\mathrm{b}} \frac{\partial \lambda^{\mathrm{b}}}{\partial s} \right] \right. \right. \\ &\left. \left. + \left[1 + \frac{n_p^{\mathrm{i}}\rho^{\mathrm{w}}}{\left(1-\lambda^{\mathrm{i}}\right)\left(1-n_p^{\mathrm{i}}\right)\rho^{\mathrm{i}}} \right] \tilde{m} + \frac{n_p^{\mathrm{s}}\rho^{\mathrm{w}}}{\left(1-n_p^{\mathrm{s}}\right)\rho^{\mathrm{s}}} \tilde{\Psi}^{\mathrm{s}} \right\} \right), \end{aligned} \tag{D.14b}$$

where equation (D.14a) comes from the total mass balance and equation (D.14b) comes from the mass balance of the water. These equations are subject to the same discussion of approximation that applied to equations (D.9) and (D.12) as far as eliminating terms.

D.2 Basal ice sediment concentration

Chapter 4 requires equations that govern the thickness of the accreted ice and the sediment concentration in the ice. Sediment can accrete to the base of the glacier when water freezes there. Alternatively, sediment can be lost from the glacier when ice melts to enter the water flow. The result of this jump condition is that there is an asymmetrical condition on the concentration of sediment in the ice. The asymmetry appears in the mass balance for the accreted ice layer.

I make the expedient assumption that the basal ice layer has a constant vertical sediment concentration. Field evidence shows that this is not the case with various grain size distributions and stratigraphic relationships (*e.g.,* Lawson, 1979; Lawson *et al.*, 1998; Roberts *et al.*, 2002). However, to accurately reproduce these features, it would be necessary to record the sediment concentrations more accurately via a tracing algorithm (*e.g.,* Staniforth & Côté, 1991) or a stretched grid (*e.g.,* Hildes, 2001). Both of these methods are beyond the scope of this thesis for the simple reason that it is imperative that the scientific questions are well-posed, both in specific goal and mathematical formulation. For tracing methods to be accurate, the scalar to be traced would need to be smooth, which is not the case with the melt condition. Stretched grids have the limitation that numerical diffusion can occur and they do not necessarily conserve mass. As a result, I avoid both in favor of an average concentration in the accreted basal layer.

Another assumption inherent in the derivations presented here is that the along-path ice velocity is neglected. This assumption is consistent with the mass balance equations presented in Chapter 2.

D.2.1 Sheet

For a subglacial water sheet, the mass of an accreted layer at the glacier base is

$$M^{\mathrm{b:e}} = \int_s \int_y \int_{z^{\mathrm{b}}}^{z^{\mathrm{b:e}}} \left\{ \left(1 - n_p^{\mathrm{i}}\right) \left(1 - \lambda^{\mathrm{i}}\right) \rho^{\mathrm{i}} + \left(1 - n_p^{\mathrm{i}}\right) \lambda^{\mathrm{i}} \rho^{\mathrm{s}} + n_p^{\mathrm{i}} \rho^{\mathrm{w}} \right\} dz\, dy\, ds, \tag{D.15}$$

where $z^{\mathrm{b:e}}$ is the elevation of the englacial transition between accreted ice and overlying meteoric ice. In equation (D.15), $n_p^{\mathrm{i}}(x, y, z)$ and $\lambda^{\mathrm{i}}(x, y, z, t)$ are spatially varying quantities.[15] Throughout the remainder of this exposition, these quantities are local averages, but I avoid the tedium of creating extra notation for these averages.

Melting conditions: mass loss

When the melt rate is positive and melting is occurring, then there is no change in the sediment concentration in the basal ice. The local form of the rate of change of mass and the change in accreted ice thickness are, respectively,

$$\left\{ \left(1 - n_p^{\mathrm{i}}\right) \left(1 - \lambda^{\mathrm{i}}\right) \rho^{\mathrm{i}} + \left(1 - n_p^{\mathrm{i}}\right) \lambda^{\mathrm{i}} \rho^{\mathrm{s}} + n_p^{\mathrm{i}} \rho^{\mathrm{w}} \right\} \left\{ \frac{\partial z^{\mathrm{b:e}}}{\partial t} - \frac{\partial z^{\mathrm{b}}}{\partial t} \right\} = - \left\{ \left[1 + \frac{n_p^{\mathrm{i}} \rho^{\mathrm{w}}}{(1 - \lambda^{\mathrm{i}})(1 - n_p^{\mathrm{i}}) \rho^{\mathrm{i}}} \right] \tilde{m} + \tilde{\Psi}^{\mathrm{i}} \right\}, \tag{D.16a}$$

$$\frac{\partial Z^{\mathrm{b:e}}}{\partial t} = - \frac{1}{\left(1 - n_p^{\mathrm{i}}\right) \left(1 - \lambda^{\mathrm{i}}\right) \rho^{\mathrm{i}} + \left(1 - n_p^{\mathrm{i}}\right) \lambda^{\mathrm{i}} \rho^{\mathrm{s}} + n_p^{\mathrm{i}} \rho^{\mathrm{w}}} \left\{ \left[1 + \frac{n_p^{\mathrm{i}} \rho^{\mathrm{w}}}{(1 - \lambda^{\mathrm{i}})(1 - n_p^{\mathrm{i}}) \rho^{\mathrm{i}}} \right] \tilde{m} + \tilde{\Psi}^{\mathrm{i}} \right\}, \tag{D.16b}$$

where $Z^{\mathrm{b:e}} = z^{\mathrm{b:e}} - z^{\mathrm{b}}$. Physically, $Z^{\mathrm{b:e}}$ is the thickness of the basal ice layer. Equation (D.16b) is equivalent to equation (4.16). If the right hand side of equation (D.16b) is negative and $Z^{\mathrm{b:e}}$ is less than an arbitrary height, then

$$\frac{\partial Z^{\mathrm{b:e}}}{\partial t} = \frac{1}{\tau^{\mathrm{b:e}}} \left(Z_0^{\mathrm{b:e}} - Z^{\mathrm{b:e}} \right), \tag{D.17}$$

where $Z_0^{\mathrm{b:e}}$ is a minimum thickness and $\tau^{\mathrm{b:e}}$ is a time constant. Equation (D.17) is a penalty function that converges to $Z_0^{\mathrm{b:e}}$.

Freezing conditions: mass gain

When ice is accreting, both the concentration of sediment in the ice and the thickness of the basal ice can change simultaneously. In consequence, two simultaneous equations are necessary:

[15] An argument also exists that ρ^{i}, ρ^{w}, and ρ^{s} are spatially varying quantities. However, at no other point in the thesis do I suggest this. The densities are taken as constant.

one for the basal ice thickness, and one for the englacial sediment concentration. The local balance from equation (D.15) is

$$\left\{\left(1-n_p^{\mathrm{i}}\right)\left(1-\lambda^{\mathrm{i}}\right)\rho^{\mathrm{i}}+\left(1-n_p^{\mathrm{i}}\right)\lambda^{\mathrm{i}}\rho^{\mathrm{s}}+n_p^{\mathrm{i}}\rho^{\mathrm{w}}\right\}\frac{\partial Z^{\mathrm{b:e}}}{\partial t}+\left(1-n_p^{\mathrm{i}}\right)\left(\rho^{\mathrm{s}}-\rho^{\mathrm{i}}\right)Z^{\mathrm{b:e}}\frac{\partial\lambda^{\mathrm{i}}}{\partial t}= -\left\{\left[1+\frac{n_p^{\mathrm{i}}\rho^{\mathrm{w}}}{(1-\lambda^{\mathrm{i}})(1-n_p^{\mathrm{i}})\rho^{\mathrm{i}}}\right]\tilde{m}+\tilde{\Psi}^{\mathrm{i}}\right\}. \quad \text{(D.18)}$$

Because there are two time derivatives in equation (D.18), the local form of the mass of the sediment in the ice is also necessary,

$$\frac{\partial\left(\rho^{\mathrm{s}}\lambda^{\mathrm{i}}Z^{\mathrm{b:e}}\right)}{\partial t}=-\tilde{\Psi}^{\mathrm{i}},$$
$$\frac{\partial\lambda^{\mathrm{i}}}{\partial t}=-\frac{1}{Z^{\mathrm{b:e}}}\left(\lambda^{\mathrm{i}}\frac{\partial Z^{\mathrm{b:e}}}{\partial t}+\frac{\tilde{\Psi}^{\mathrm{i}}}{\rho^{\mathrm{s}}}\right). \quad \text{(D.19)}$$

Substituting equation (D.19) into equation (D.18) gives

$$\frac{\partial Z^{\mathrm{b:e}}}{\partial t}=\frac{1}{\left(1-n_p^{\mathrm{i}}\right)\rho^{\mathrm{i}}+n_p^{\mathrm{i}}\rho^{\mathrm{w}}}\left\{\left[\left(1-n_p^{\mathrm{i}}\right)\left(1-\frac{\rho^{\mathrm{i}}}{\rho^{\mathrm{s}}}\right)-1\right]\tilde{\Psi}^{\mathrm{i}}-\left[1+\frac{n_p^{\mathrm{i}}\rho^{\mathrm{w}}}{(1-\lambda^{\mathrm{i}})(1-n_p^{\mathrm{i}})\rho^{\mathrm{i}}}\right]\tilde{m}\right\}. \quad \text{(D.20)}$$

D.2.2 Channel

For a subglacial semicircular channel, the mass of an accreted layer at the glacier base is

$$M^{\mathrm{b:e}}=\int_s\int_0^{\pi}\int_{R^{\mathrm{b}}}^{R^{\mathrm{b}}+Z^{\mathrm{b:e}}}\left\{\left(1-n_p^{\mathrm{i}}\right)\left(1-\lambda^{\mathrm{i}}\right)\rho^{\mathrm{i}}+\left(1-n_p^{\mathrm{i}}\right)\lambda^{\mathrm{i}}\rho^{\mathrm{s}}+n_p^{\mathrm{i}}\rho^{\mathrm{w}}\right\}r\,dr\,d\theta\,ds, \quad \text{(D.21)}$$

where θ is the azimuthal angle, $Z^{\mathrm{b:e}}$ is the thickness of the accreted layer, and $r\,dr\,d\theta\,ds$ is the differential volume of accreted ice. The quantities n_p^{i} and λ^{i} represent local averages throughout the remainder of this derivation.

Melting conditions: mass loss

Assuming that the concentration of sediment does not change with time in the accreted layer as ice melts, the local rate of change of mass becomes

$$\left\{\left(1-n_p^{\mathrm{i}}\right)\left(1-\lambda^{\mathrm{i}}\right)\rho^{\mathrm{i}}+\left(1-n_p^{\mathrm{i}}\right)\lambda^{\mathrm{i}}\rho^{\mathrm{s}}+n_p^{\mathrm{i}}\rho^{\mathrm{w}}\right\}\left\{\frac{\pi}{2}\frac{\partial}{\partial t}\left[\left(R^{\mathrm{b}}+Z^{\mathrm{b:e}}\right)^2-\left(R^{\mathrm{b}}\right)^2\right]\right\}= -\left\{\left[1+\frac{n_p^{\mathrm{i}}\rho^{\mathrm{w}}}{(1-\lambda^{\mathrm{i}})(1-n_p^{\mathrm{i}})\rho^{\mathrm{i}}}\right]m+\Psi^{\mathrm{i}}\right\}, \quad \text{(D.22a)}$$

$$\left\{\left(1-n_p^{\mathrm{i}}\right)\left(1-\lambda^{\mathrm{i}}\right)\rho^{\mathrm{i}}+\left(1-n_p^{\mathrm{i}}\right)\lambda^{\mathrm{i}}\rho^{\mathrm{s}}+n_p^{\mathrm{i}}\rho^{\mathrm{w}}\right\}\left\{\pi Z^{\mathrm{b:e}}\left.\frac{\partial R^{\mathrm{b}}}{\partial t}\right|_{\mathrm{close}}+\pi\left(R^{\mathrm{b}}+Z^{\mathrm{b:e}}\right)\frac{\partial Z^{\mathrm{b:e}}}{\partial t}\right\}= -\left\{\left[1+\frac{n_p^{\mathrm{i}}\rho^{\mathrm{w}}}{(1-\lambda^{\mathrm{i}})(1-n_p^{\mathrm{i}})\rho^{\mathrm{i}}}\right]m+\Psi^{\mathrm{i}}\right\}, \quad \text{(D.22b)}$$

where $\partial R^{\mathrm{b}}/\partial t|_{\mathrm{close}}$ is the closure of the channel resulting from creep. This term is not the full change in radius from the mass balance of the channel because the melt terms are on the right hand side of these equations. Separating for the rate of accreted layer thickness change gives

$$\frac{\partial Z^{\mathrm{b:e}}}{\partial t} = -\frac{1}{\pi\left\{R^{\mathrm{b}}+Z^{\mathrm{b:e}}\right\}\left\{\left(1-n_p^{\mathrm{i}}\right)\left(1-\lambda^{\mathrm{i}}\right)\rho^{\mathrm{i}}+\left(1-n_p^{\mathrm{i}}\right)\lambda^{\mathrm{i}}\rho^{\mathrm{s}}+n_p^{\mathrm{i}}\rho^{\mathrm{w}}\right\}}\left\{\Psi^{\mathrm{i}} + \left[1+\frac{n_p^{\mathrm{i}}\rho^{\mathrm{w}}}{(1-\lambda^{\mathrm{i}})(1-n_p^{\mathrm{i}})\rho^{\mathrm{i}}}\right]m\right\} - \frac{Z^{\mathrm{b:e}}}{R^{\mathrm{b}}+Z^{\mathrm{b:e}}}\left.\frac{\partial R^{\mathrm{b}}}{\partial t}\right|_{\mathrm{close}}. \tag{D.23}$$

Freezing conditions: mass gain

The local form of the mass balance with a change in the concentration of sediment in the ice becomes

$$\frac{d}{dt}\left(\left\{\left(1-n_p^{\mathrm{i}}\right)\left(1-\lambda^{\mathrm{i}}\right)\rho^{\mathrm{i}}+\left(1-n_p^{\mathrm{i}}\right)\lambda^{\mathrm{i}}\rho^{\mathrm{s}}+n_p^{\mathrm{i}}\rho^{\mathrm{w}}\right\}\left\{\frac{\pi}{2}\left[\left(R^{\mathrm{b}}+Z^{\mathrm{b:e}}\right)^2-\left(R^{\mathrm{b}}\right)^2\right]\right\}\right) = -\left\{\left[1+\frac{n_p^{\mathrm{i}}\rho^{\mathrm{w}}}{(1-\lambda^{\mathrm{i}})(1-n_p^{\mathrm{i}})\rho^{\mathrm{i}}}\right]m+\Psi^{\mathrm{i}}\right\}, \tag{D.24a}$$

$$\left\{\left(1-n_p^{\mathrm{i}}\right)\left(1-\lambda^{\mathrm{i}}\right)\rho^{\mathrm{i}}+\left(1-n_p^{\mathrm{i}}\right)\lambda^{\mathrm{i}}\rho^{\mathrm{s}}+n_p^{\mathrm{i}}\rho^{\mathrm{w}}\right\}\left\{\pi Z^{\mathrm{b:e}}\left.\frac{\partial R^{\mathrm{b}}}{\partial t}\right|_{\mathrm{close}}+\pi\left(R^{\mathrm{b}}+Z^{\mathrm{b:e}}\right)\frac{\partial Z^{\mathrm{b:e}}}{\partial t}\right\} + \frac{\pi}{2}\left\{2R^{\mathrm{b}}Z^{\mathrm{b:e}}+\left(Z^{\mathrm{b:e}}\right)^2\right\}\left\{\left(1-n_p^{\mathrm{i}}\right)\left(\rho^{\mathrm{s}}-\rho^{\mathrm{i}}\right)\frac{\partial\lambda^{\mathrm{i}}}{\partial t}\right\} = -\left\{\left[1+\frac{n_p^{\mathrm{i}}\rho^{\mathrm{w}}}{(1-\lambda^{\mathrm{i}})(1-n_p^{\mathrm{i}})\rho^{\mathrm{i}}}\right]m+\Psi^{\mathrm{i}}\right\}. \tag{D.24b}$$

The local balance is of sediment in the ice is

$$\frac{d}{dt}\left\{\frac{\pi}{2}\rho^{\mathrm{s}}\lambda^{\mathrm{i}}\left[\left(R^{\mathrm{b}}+Z^{\mathrm{b:e}}\right)^2-\left(R^{\mathrm{b}}\right)^2\right]\right\} = -\Psi^{\mathrm{i}}, \tag{D.25a}$$

$$\frac{\pi}{2}\rho^{\mathrm{s}}\left[2R^{\mathrm{b}}Z^{\mathrm{b:e}}+\left(Z^{\mathrm{b:e}}\right)^2\right]\frac{\partial\lambda^{\mathrm{i}}}{\partial t}+\frac{\pi}{2}\rho^{\mathrm{s}}\lambda^{\mathrm{i}}\left[2Z^{\mathrm{b:e}}\left.\frac{\partial R^{\mathrm{b}}}{\partial t}\right|_{\mathrm{close}}+2\left(R^{\mathrm{b}}+Z^{\mathrm{b:e}}\right)\frac{\partial Z^{\mathrm{b:e}}}{\partial t}\right] = -\Psi^{\mathrm{i}}. \tag{D.25b}$$

From the local balance of sediment in the ice, the rate of change of sediment concentration is

$$\frac{\partial\lambda^{\mathrm{i}}}{\partial t} = \frac{1}{2R^{\mathrm{b}}Z^{\mathrm{b:e}}+\left(Z^{\mathrm{b:e}}\right)^2}\left\{-\frac{2}{\pi\rho^{\mathrm{s}}}\Psi^{\mathrm{i}}-2\lambda^{\mathrm{i}}\left[Z^{\mathrm{b:e}}\left.\frac{\partial R^{\mathrm{b}}}{\partial t}\right|_{\mathrm{close}}+\left(R^{\mathrm{b}}+Z^{\mathrm{b:e}}\right)\frac{\partial Z^{\mathrm{b:e}}}{\partial t}\right]\right\}. \tag{D.26}$$

Substituting equation (D.26) into equation (D.24b) and rearranging gives

$$\frac{\partial Z^{\mathrm{b:e}}}{\partial t} = \frac{1}{\pi\left\{R^{\mathrm{b}}+Z^{\mathrm{b:e}}\right\}\left\{\left(1-n_p^{\mathrm{i}}\right)\rho^{\mathrm{i}}+n_p^{\mathrm{i}}\rho^{\mathrm{w}}\right\}}\left\{\left[\left(1-n_p^{\mathrm{i}}\right)\left(1-\frac{\rho^{\mathrm{i}}}{\rho^{\mathrm{s}}}\right)-1\right]\Psi^{\mathrm{i}} - \left[1+\frac{n_p^{\mathrm{i}}\rho^{\mathrm{w}}}{(1-\lambda^{\mathrm{i}})(1-n_p^{\mathrm{i}})\rho^{\mathrm{i}}}\right]m\right\} - \frac{Z^{\mathrm{b:e}}}{R^{\mathrm{b}}+Z^{\mathrm{b:e}}}\left.\frac{\partial R^{\mathrm{b}}}{\partial t}\right|_{\mathrm{close}}. \tag{D.27}$$

This equation is similar to equation (D.20) with the main difference being that creep closure is included in equation (D.27).

Appendix E

Semiempirical sediment transport relations

van Rijn (1984a,b) developed procedures to apply sediment transport relations. The aim of this appendix is to present the transport relations rather then derive them. Because of this aim, the procedures are presented first; and the supporting equations follow. This format is operationally succinct. The derivations use theoretical and empirical considerations. I refer the reader to the original papers for these derivations.

E.1 Bed load

Procedure

1. Compute the particle parameter D_* using equation (E.1).
2. Compute the critical bed-shear velocity according to the Shields criterion (eq. E.7, Fig. E.1, eq. E.5).
3. Compute Chézy coefficient related to grains C' using equation (E.8).
4. Compute the effective bed shear velocity using equation (E.3).
5. Compute the transport stage parameter $\mathcal{T}$ (E.2).
6. Compute the equilibrium bed load transport $\tilde{q}_{e:b}$ using equation (E.9).

Formulation

van Rijn advocated two nondimensional numbers to describe sediment motion. The particle parameter describes the nondimensional grain size and is derived from the particle Froude and Reynolds numbers,

$$D_* = D \left\{ \frac{\left(\frac{\rho^{\mathrm{s}}}{\rho^{\mathrm{w}}} - 1 \right) g}{\nu^2} \right\}^{\frac{1}{3}} , \tag{E.1}$$

where D is a characteristic grain size and ν is the kinematic viscosity of water. If this relationship is applied to the entire alluvial bed, D can be replaced with D_{50} the median of the grain size distribution. This substitution implies that D_{50} is an accurate representation of the sediment distribution. The second nondimensional number is transport stage parameter, which

characterizes an excess shear stress available to move sediment,

$$\mathcal{T} = \frac{(u'_*)^2 - (u_{*,cr})^2}{(u_{*,cr})^2}. \tag{E.2}$$

The transport stage parameter is a normalized difference of shear stresses, where the bed shear velocity accounts for the lessening of shear stress away from the bed. In (E.2),

$$u'_* = u^{\mathrm{b}} \left(\frac{g^{\frac{1}{2}}}{C'} \right), \tag{E.3}$$

is the bed shear velocity related to the grains where C' is the grain Chézy coefficient. The maximum value of the bed shear velocity related to grains is the bed shear velocity,

$$u_* = \sqrt{\frac{\tau_0}{\rho^{\mathrm{w}}}}, \tag{E.4}$$

where τ_0 is the shear along the hydraulic perimenter (eq. 2.24).

In equation (E.1), $u_{*,cr}$ is the critical bed shear velocity from the Shields criterion

$$\theta_{cr} = \frac{u^2_{*,cr}}{\left(\frac{\rho^{\mathrm{s}}}{\rho^{\mathrm{w}}} - 1 \right) gD}, \tag{E.5}$$

where θ_{cr} is a critical mobility parameter. The Shields threshold criterion is commonly used to express the critical shear stress necessary for motion,

$$\tau_{cr} = (\rho^{\mathrm{s}} - \rho^{\mathrm{w}})\, gD\theta_{cr}. \tag{E.6}$$

Shear stresses below this critical value will not cause motion of the sediments. While arguments against this criterion exist (*e.g.,* Yang, 1996, p. 22–23), no relationship is in more common usage for the initial motion of sediments. An analytic form of the critical mobility parameter is

$$\theta_{cr} = \begin{cases} 0.24\, D_*^{-1} & \text{for} \quad D_* \leq 4.5, \\ 0.14\, D_*^{-0.64} & \text{for} \quad 4.5 < D_* \leq 10, \\ 0.04\, D_*^{-0.10} & \text{for} \quad 10 < D_* \leq 18, \\ 0.013\, D_*^{0.29} & \text{for} \quad 18 < D_* \leq 144, \\ 0.055 & \text{for} \quad 144 < D_*, \end{cases} \tag{E.7}$$

where I have modified the original form given by van Rijn (1984a) to make the curve smoother. A value of 0.6 for $D_* > 144$ indicates tightly packed, uniform beds. The gray area in Figure E.1 represents a lower value because of mixed-sized beds. Values higher than 0.06 are possible provided that the bed is structured in a way that reinforces the grains at the bed (for a review, see Church 2006).

The Chézy coefficient related to the grains C' in the bed shear relationship is

$$C' = 18 \log_{10} \left(\frac{12 R_h}{3 D_{90}} \right), \tag{E.8}$$

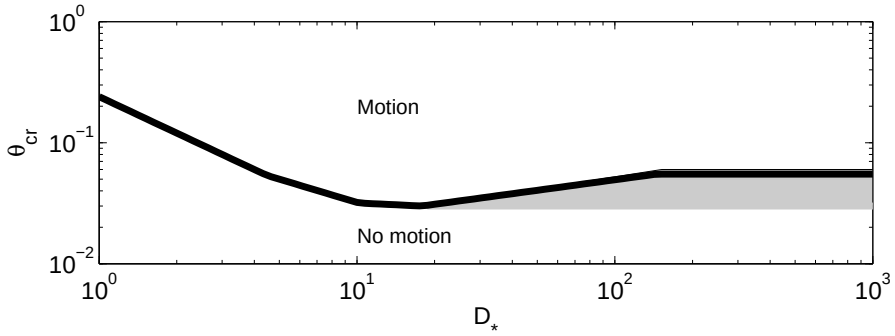

Figure E.1: Shields diagram. An illustration of equation (E.7). The gray area represents the range discussed by Church (2006) for a mixture of different sediment sizes.

where D_{90} is the size of the 90th percentile of the grain size distribution. The equivalent sand roughness is $3D_{90}$ as reviewed by van Rijn (1984a). The grain C' is a form of the Chézy coefficient parameterized to the original Nikuradse experiments of water flowing over a sand bed (*e.g.,* Henderson, 1966, p. 94). The grain Chézy coefficient can be converted to a grain Darcy-Weisbach friction factor (eq. 2.24) via $(f'_d)^{-1/2} = C'/\sqrt{8g}$. However, the form of equation (4.33) is the one that is most compatible with the equations presented thus far, and I opt for that formulation rather than equation (E.8).

The bed load flux (eq. 4.19) is equal to the product of the concentration of bed load material (eq. 4.22), bed load layer thickness (eq. 4.21), and bed load velocity (eq. 4.20). In terms of the transport stage parameter and the grain size characteristics, the bed load flux is

$$\tilde{q}_{e:b} = 0.053 \frac{\mathcal{T}^{2.1}}{D_*^{0.3}} \left[\left(\frac{\rho^{\mathrm{s}}}{\rho^{\mathrm{w}}} - 1 \right) g \right]^{\frac{1}{2}} D_{50}^{\frac{3}{2}}, \tag{E.9}$$

where semiempirical relations are used for the concentration and bed load height relations. This equation is the relation given in eq. (4.24). The bed load flux is in units of cubic meters per second per meter channel width.

E.2 Suspended load

van Rijn (1984b) developed a method of calculating the suspended sediment load for particles in the size range 0.1–0.5 mm. The procedure presented here is taken from van Rijn (1984b).

Procedure

1. Compute the particle parameter D_* using equation (E.1).
2. Compute the critical bed-shear velocity $u_{*,cr}$ using equations (E.5) and (E.7).
3. Compute the transport stage parameter $\mathcal{T}$ (eq. E.2).
4. Compute the reference level δ_s using equation (E.17).
5. Compute the reference concentration $\lambda^{\mathrm{b}}_{s;0}$ using equation (E.16).
6. Compute the particle size of suspended sediment using equation (E.19) or another method.
7. Compute the fall velocity of suspended sediment w_s using equation (E.11).
8. Compute the β^{s} factor (eq. E.13).
9. Compute the overall bed shear velocity u_* using equation (E.4).
10. Compute the φ factor using equation (E.15).
11. Compute the suspension parameters $\mathcal{Z}$ and $\mathcal{Z}'$ using equations (E.12) and (E.14), respectively.
12. Compute the correction factor $\mathcal{F}_s$ using equation (E.23).
13. Compute the volumetric concentration of suspended sediment λ^{b}_s using equation (E.22).
14. Compute the suspended load transport $\tilde{q}_s$ using equation (E.21)

Formulation

The initiation of suspended load is commonly given in terms of the fall velocity of a sediment particle as well as the shear velocity of the water. Based on experimental results, van Rijn (1984b) formulated his own criterion for the initiation of suspended load,

$$u_{*,crs} = \begin{cases} \dfrac{4w^{\mathrm{s}}}{D_*} & \text{for} \quad 1 < D_* \leq 10, \\ 0.4w^{\mathrm{s}} & \text{for} \quad 10 < D_*, \end{cases} \tag{E.10}$$

where $u_{*,crs}$ is the critical shear velocity necessary for entrainment into suspension, and w^{s} is the fall velocity of a grain. For large grain sizes, $u_{*,crs}$ takes the value $0.4w^{\mathrm{s}}$. The sediment fall

velocity is

$$w^{\mathrm{s}} = \begin{cases} \dfrac{\left(\dfrac{\rho^{\mathrm{s}}}{\rho^{\mathrm{w}}} - 1\right) g D^2}{18\nu} & \text{for} \quad D \leq 0.1 \text{ mm}, \\ 10\dfrac{\nu}{D}\left(\left[1 + \dfrac{0.01\left(\dfrac{\rho^{\mathrm{s}}}{\rho^{\mathrm{w}}} - 1\right) g D^3}{\nu^2}\right]^{\frac{1}{2}} - 1\right) & \text{for} \quad 0.1 < D \leq 1.0 \text{ mm}, \\ 1.1\left[\left(\dfrac{\rho^{\mathrm{s}}}{\rho^{\mathrm{w}}} - 1\right) g D\right]^{\frac{1}{2}} & \text{for} \quad 1.0 < D. \end{cases} \tag{E.11}$$

A suspension parameter $\mathcal{Z}$ relates the downward fall of sediments to upward turbulent motions,

$$\mathcal{Z} = \frac{w^{\mathrm{s}}}{\beta^{\mathrm{s}} \kappa^{\mathrm{s}} u_*}, \tag{E.12}$$

where κ^{s} is von Karman's constant and β^{s} describes how the sediments interact with the individual turbulent eddies. Values of β^{s} greater than unity indicate that the sediments are propelled to the outside of the individual eddies. The justification is that sediments at the outside of the eddies mix more readily in the flow (van Rijn, 1984b). The β^{s} parameter is

$$\beta^{\mathrm{s}} = 1 + 2\left(\frac{w^{\mathrm{s}}}{u_*}\right)^2 \quad \text{for} \quad 0.1 < \frac{w_s}{u_*} < 1. \tag{E.13}$$

If the fall velocity is greater than the bed shear velocity in equation (E.13), then the particle cannot be in suspension. Particles in the flow will occupy space, damp turbulence, and reduce the particle fall velocity. As a result, a simple correction to the suspension parameter is introduced,

$$\mathcal{Z}' = \mathcal{Z} + \varphi, \tag{E.14}$$

where φ is the correction for these additional effects. van Rijn developed this parameter to correct the theory relative to measured vertical profiles of sediment concentration. The correction is

$$\varphi = 2.5\left(\frac{w^{\mathrm{s}}}{u_*}\right)^{0.8}\left(\frac{\lambda^{\mathrm{b}}_{s:0}}{\lambda^{\mathrm{b}}_{b:0}}\right)^{0.4} \quad \text{for} \quad 0.01 \leq \frac{w_s}{u_*} \leq 1, \tag{E.15}$$

where $\lambda^{\mathrm{b}}_{s:0}$ is the sediment concentration at reference level δ_s, and $\lambda^{\mathrm{b}}_{b:0}$ is the maximum sediment concentration of the bed. This maximum concentration is equivalent to the solid fraction of the bed, $(1 - n^{\mathrm{s}}_p)$, commonly assumed to be 0.65. The reference value for suspended sediment is

$$\lambda^{\mathrm{b}}_{s:0} = 0.015\frac{D_{50}}{\delta_s}\frac{\mathcal{T}^{\frac{3}{2}}}{D_*^{0.3}}. \tag{E.16}$$

The suspended sediment reference level can take a reasonable value near the bed. This level may be the bedform height Δ^{s}, or the Nikuradse sand bed roughness k^{s}. Because the sand bed roughness appears in equation (E.8) as $3D_{90}$, that value may be applied here.

$$\delta_s = 0.5\Delta^{\mathrm{s}} \quad \text{or} \quad \delta_s = k^{\mathrm{s}} = 3D_{90} \tag{E.17}$$

such that $\min(\delta_s) = 0.01 d^{\mathrm{b}}$. The bedform height is not of significant interest here, but I keep it in fairness to the original formulation. The bedform height can be approximated as

$$\Delta^{\mathrm{s}} = 0.11 \left(d^{\mathrm{b}}\right)^{0.7} (D_{50})^{0.3} \left(1 - \exp\{-0.5\mathcal{T}\}\right)\left(25 - \mathcal{T}\right), \tag{E.18}$$

where d^{b} is the water layer thickness. If the bed is flat, the bed load layer thickness (eq. 4.21) can be used.

The mean size of the suspended load will most likely differ from the mean grain size of the bed. To account for this difference, D_s is a characteristic suspended grain size,

$$D_s = D_{50}\left[1 + 0.011\,(\sigma_s - 1)\,(\mathcal{T} - 25)\right]. \tag{E.19}$$

where σ_s is the geometric standard deviation of the sediment distribution. The standard deviation is

$$\sigma_s = 0.5(D_{84}/D_{50} + D_{16}/D_{50}), \tag{E.20}$$

where D_{84} and D_{16} are the 84th and 16th percentile of the grain size distribution. Calculating σ_s from equation (E.20) is excessive for this study. Arbitrarily choosing a pertinent grain size from the fall velocities or the grain size range 0.1–0.5 mm, the which is the range of validity, might yield more insight.

The suspended load can then be calculated as the product of the mean flow velocity u^{b}, the water depth d^{b}, and the suspended load concentration $\lambda^{\mathrm{b}}_{s:0}$,

$$\tilde{q}_{e:s} = u^{\mathrm{b}} d^{\mathrm{b}} \lambda^{\mathrm{b}}_{e:s}. \tag{E.21}$$

The volumetric sediment concentration is

$$\lambda^{\mathrm{b}}_{e:s} = \mathcal{F}_s \lambda^{\mathrm{b}}_{s:0}, \tag{E.22}$$

where the correction factor $\mathcal{F}_s$ is

$$\mathcal{F}_s = \frac{\left(\dfrac{\delta_s}{d^{\mathrm{b}}}\right)^{\mathcal{Z}'} - \left(\dfrac{\delta_s}{d^{\mathrm{b}}}\right)^{1.2}}{\left(1 - \dfrac{\delta_s}{d^{\mathrm{b}}}\right)^{\mathcal{Z}'} (1.2 - \mathcal{Z}')}. \tag{E.23}$$

Appendix F

Numerical formulation

Balance law numerical formulation

Chapters 2, 4, and 5 are formulated in a similar fashion using the balance laws. Because all of the equations are implemented using MATLAB, the formulation and averaging schemes are an important component of the numerical implementation. These discretizations are made for use with the numerical method of lines (Schiesser, 1991).

Use of MATLAB implies that the solution in time is relatively simple to implement using the ODE15S package. This package is specifically for stiff numerical systems and uses a numerical differentiation formula (NDF) that is similar in form to the more common backward differentiation formulae (BDF) (Shampine & Reichelt 1997; see also Ascher & Petzold 1998, Chap. 5). Both NDF and BDF are multistep methods. In addition, ODE15S uses an adaptive step to advance in time.

F.1 Sheet and channel numerical formulation

Because the sheet and channel are one dimensional in that the quantities of interest vary in s, both have similar discretizations and boundary conditions. I employ a staggered grid and assign each of the variables to either the cell centers or cell edges (Patankar, 1980).

F.1.1 Grid and discretization

Implementation of the governing equations (eqs. 2.15–2.17, 2.27, and 2.29) requires an along-path coordinate system. Generally, the path is regular in x, but not necessarily regular in s. Figure F.1a illustrates a case where Δs is regularly spaced in x. However, a change in z for any of those points without a change in x would make the grid irregular (Fig. F.1b). The irregular grid appears in all the s-derivatives.

For a general variable Ω that lies on the centered grid (Table F.1), first derivatives in s lie on the staggered grid such that

$$\frac{\partial \Omega}{\partial s} = \frac{\partial \Omega}{\partial x}\frac{\partial x}{\partial s} \simeq \left.\frac{\Delta \Omega}{\Delta x}\frac{\Delta x}{\Delta s}\right|_{i+\frac{1}{2}} = \left(\frac{\Omega_{i+1} - \Omega_i}{x_{i+1} - x_i}\right)\left(\frac{x_{i+1} - x_i}{s_{i+1} - s_i}\right). \tag{F.1}$$

For a general variable ω that lies on the staggered grid the first derivative is

$$\frac{\partial \omega}{\partial s} = \frac{\partial \omega}{\partial x}\frac{\partial x}{\partial s} \simeq \left.\frac{\Delta \omega}{\Delta x}\frac{\Delta x}{\Delta s}\right|_{i} = \left(\frac{\omega_{i+\frac{1}{2}} - \omega_{i-\frac{1}{2}}}{x_{i+\frac{1}{2}} - x_{i-\frac{1}{2}}}\right)\left(\frac{x_{i+\frac{1}{2}} - x_{i-\frac{1}{2}}}{s_{i+\frac{1}{2}} - s_{i-\frac{1}{2}}}\right). \tag{F.2}$$

While these equations appear to be intuitive from the perspective of the chain rule, the $\Delta s/\Delta x$ terms need to be calculated from the along-path coordinates. If $s(x)$ only, then this term can

Table F.1: Subglacial water flow quantities on the centered and staggered grids.

Centered		Staggered	
$z^{\mathrm{b}}(x)$	Glacier base elevation	$\frac{\partial z^{\mathrm{b}}}{\partial s}(s,t)$	Gradient of the base
$z^{\mathrm{s}}(x)$	Glacier sediment bed elevation		
$z^{\mathrm{r}}(x)$	Glacier surface elevation		
$Z^{\mathrm{i}}(x)$	Ice thickness		
$p^{\mathrm{i}}(x,t)$	Ice overburden pressure		
$p^{\mathrm{b}}(s,t)$	Subglacial water pressure		
$\phi^{\mathrm{b}}(s,t)$	Hydraulic potential	$\frac{\partial \phi^{\mathrm{b}}}{\partial s}(s,t)$	Potential gradient
$T^{\mathrm{b}}(s,t)$	Water temperature	$\frac{\partial T^{\mathrm{b}}}{\partial s}(s,t)$	Temperature gradient
$n_p^{\mathrm{i}}(s,t)$	Ice porosity		
		$u^{\mathrm{b}}(s,t)$	Water velocity
Channel-specific quantities			
$R^{\mathrm{b}}(s,t)$	Channel radius		
$S^{\mathrm{b}}(s,t)$	Cross sectional area		
$m(s,t)$	Melt rate		
P^{w}	Hydraulic perimeter		
P^{i}	Melting perimeter		
Sheet-specific quantities			
$H^{\mathrm{b}}(s,t)$	Mean sheet thickness		
$\tilde{m}(s,t)$	Melt rate per unit width		
$\frac{\partial(\overline{H^{\mathrm{b}}}u^{\mathrm{b}})}{\partial s}(s,t)$	Flux divergence		
$\left(\frac{\partial H^{\mathrm{b}}}{\partial t}(s,t)\right)_{\mathrm{close}}$	Closure rate		

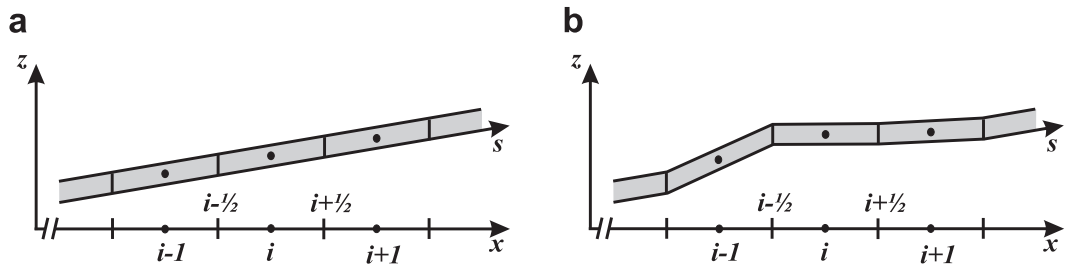

Figure F.1: One dimensional grid for subglacial water flow. Centered values reside at points denoted by integer values such as $i-1$, i, and $i+1$. Staggered values inhabit points at integer values plus or minus one half such as $i-\frac{1}{2}$ and $i+\frac{1}{2}$. (a) Illustration of a regular grid in x and s. (b) A similar illustration where the grid in s is irregular. Note that the grid in x is exactly the same for both cases.

be set prior to finding the numerical solution. However, if $s(x,t)$, as in the case of an eroding bed, then $\Delta s/\Delta x$ must be calculated at every time step.

Often there will be quantities that require values on both the centered and staggered grid. For example, the melt rate is needed on both grids. In such cases, quantities on the centered grid can be averaged according to

$$\overline{\Omega_{i+\frac{1}{2}}} = \frac{V_{i+1}\Omega_{i+1} + V_i\Omega_i}{V_{i+1}+V_i}, \tag{F.3a}$$

$$V_i = H_i^{\mathrm{b}} W \left(s_{i+\frac{1}{2}} - s_{i-\frac{1}{2}}\right) \qquad \text{sheet,} \tag{F.3b}$$

$$V_i = S_i^{\mathrm{b}} \left(s_{i+\frac{1}{2}} - s_{i-\frac{1}{2}}\right) \qquad \text{channel,} \tag{F.3c}$$

where the overline denotes an average and V_i is the volume of the ith cell. Similarly, quantities on the staggered grid are averaged to the centered grid according to

$$\overline{\omega_i} = \frac{V_{i+\frac{1}{2}}\omega_{i+\frac{1}{2}} + V_{i-\frac{1}{2}}\omega_{i-\frac{1}{2}}}{V_{i+\frac{1}{2}} + V_{i-\frac{1}{2}}}, \tag{F.4a}$$

$$V_{i+\frac{1}{2}} = \overline{H^{\mathrm{b}}_{i+\frac{1}{2}}} W \left(s_{i+1} - s_i\right) \qquad \text{sheet,} \tag{F.4b}$$

$$V_{i+\frac{1}{2}} = \overline{S^{\mathrm{b}}_{i+\frac{1}{2}}} \left(s_{i+1} - s_i\right) \qquad \text{channel.} \tag{F.4c}$$

Using equations (F.4) and (F.4), it is now possible to discretize the time derivatives for the time derivatives. The discretized forms of the mass balance equations (eqs. 2.15–2.17) are

$$\frac{\partial H^{\mathrm{b}}}{\partial t}_{i} = \frac{\tilde{m}_i}{\left(1 - n^{\mathrm{i}}_{p:i}\right)\rho^{\mathrm{i}}} + \left(\frac{\partial H^{\mathrm{b}}}{\partial t}\right)_{\mathrm{close}:i} \qquad \text{sheet,} \quad \text{(F.5a)}$$

$$\frac{\partial S^{\mathrm{b}}}{\partial t}_{i} = \frac{m_i}{\rho^{\mathrm{i}}\left(1 - n^{\mathrm{i}}_{p:i}\right)} - 2S^{\mathrm{b}}_i \operatorname{sgn}(p^{\mathrm{i}}_i - p^{\mathrm{b}}_i)\left(\frac{|p^{\mathrm{i}}_i - p^{\mathrm{b}}_i|}{n\mathcal{B}}\right)^n \qquad \text{channel,} \quad \text{(F.5b)}$$

$$\frac{\partial p^{\mathrm{b}}}{\partial t}_{i} = -\frac{1}{\gamma^{\mathrm{b}} H^{\mathrm{b}}_i}\left\{\frac{\partial H^{\mathrm{b}}}{\partial t}_{i} + \frac{\overline{H^{\mathrm{b}}_{i+\frac{1}{2}}}u^{\mathrm{b}}_{i+\frac{1}{2}} - \overline{H^{\mathrm{b}}_{i-\frac{1}{2}}}u^{\mathrm{b}}_{i-\frac{1}{2}}}{s_{i+\frac{1}{2}} - s_{i-\frac{1}{2}}} - \frac{\left(1 - n^{\mathrm{i}}_{p:i}\right)\rho^{\mathrm{i}} + n^{\mathrm{i}}_{p:i}\rho^{\mathrm{w}}}{\left(1 - n^{\mathrm{i}}_{p:i}\right)\rho^{\mathrm{i}}\rho^{\mathrm{w}}}\tilde{m}_i\right\} \quad \text{sheet,} \quad \text{(F.5c)}$$

$$\frac{\partial p^{\mathrm{b}}}{\partial t}_{i} = -\frac{1}{\gamma^{\mathrm{b}} S^{\mathrm{b}}_i}\left\{\frac{\partial S^{\mathrm{b}}}{\partial t}_{i} + \frac{\overline{S^{\mathrm{b}}_{i+\frac{1}{2}}}u^{\mathrm{b}}_{i+\frac{1}{2}} - \overline{S^{\mathrm{b}}_{i-\frac{1}{2}}}u^{\mathrm{b}}_{i-\frac{1}{2}}}{s_{i+\frac{1}{2}} - s_{i-\frac{1}{2}}} - \frac{\left(1 - n^{\mathrm{i}}_{p:i}\right)\rho^{\mathrm{i}} + n^{\mathrm{i}}_{p:i}\rho^{\mathrm{w}}}{\left(1 - n^{\mathrm{i}}_{p:i}\right)\rho^{\mathrm{i}}\rho^{\mathrm{w}}}m_i\right\} \text{channel.} \quad \text{(F.5d)}$$

The melt rate and melt rate per unit width become

$$m_i = \frac{0.023\left(\overline{\mathsf{Re}_i}\right)^{4/5}\mathsf{Pr}^{2/5}K^{\mathrm{w}}_T\Delta T_{\mathrm{mp}:i}P^{\mathrm{i}}_i}{4R_{h:i}L} \qquad \text{channel,} \quad \text{(F.6a)}$$

$$\tilde{m}_i = \frac{0.023\left(\overline{\mathsf{Re}_i}\right)^{4/5}\mathsf{Pr}^{2/5}K^{\mathrm{w}}_T\Delta T_{\mathrm{mp}:i}}{H^{\mathrm{b}}_i L} \qquad \text{sheet,} \quad \text{(F.6b)}$$

which are not interesting except that the Reynolds number needs to be averaged such that,

$$\mathsf{Re}_{i+\frac{1}{2}} = \begin{cases} \dfrac{4\overline{R_{h:i+\frac{1}{2}}}\left|u^{\mathrm{b}}_{i+\frac{1}{2}}\right|\rho^{\mathrm{w}}}{\mu} & \text{channel,} \\ \dfrac{\overline{H^{\mathrm{b}}_{i+\frac{1}{2}}}\left|u^{\mathrm{b}}_{i+\frac{1}{2}}\right|\rho^{\mathrm{w}}}{\mu} & \text{sheet.} \end{cases} \quad \text{(F.7)}$$

In this equation, assignment of the Reynolds number to the staggered grid limits the number of averaging steps necessary to obtain the melt rate on both the staggered and centered grids.

Physically, the melt rate must match on the staggered and centered grids; however, numerically, the melt rate is more important on the centered grid than on the staggered grid. As a result, the melt rate is defined on the centered grid. In the momentum equation, the melt rate terms are small and can be approximated by the melt rate averages. Using the average melt rate ensures that they are smooth on the staggered grid. The melt rate terms do not appear in the steady state momentum equations (eqs. 2.26) because the assumption that the melt rate is small is valid under most flow conditions.

When discretized, the momentum equations (2.27) become

$$\frac{\partial u^{\mathrm{b}}}{\partial t}_{i+\frac{1}{2}} = -\frac{1}{2}\frac{\left(u^{\mathrm{b}}_{i+\frac{1}{2}}\right)^2 - \left(u^{\mathrm{b}}_{i-\frac{1}{2}}\right)^2}{s_{i+1}-s_i} - \frac{\left(1-n^{\mathrm{i}}_{p:i}\right)\rho^{\mathrm{i}} + n^{\mathrm{i}}_{p:i}\rho^{\mathrm{w}}}{\left(1-n^{\mathrm{i}}_{p:i}\right)\rho^{\mathrm{i}}}\frac{\overline{m_{i+\frac{1}{2}}}u^{\mathrm{b}}_{i+\frac{1}{2}}}{\rho^{\mathrm{w}}\overline{S^{\mathrm{b}}_{i+\frac{1}{2}}}}$$
$$-\frac{1}{\rho^{\mathrm{w}}}\frac{\overline{p^{\mathrm{b}}_{i+\frac{1}{2}}} - \overline{p^{\mathrm{b}}_{i+\frac{1}{2}}}}{s_{i+1}-s_i} - g\frac{z^{\mathrm{b}}_{i+1}-z^{\mathrm{b}}_i}{s_{i+1}-s_i} - \frac{\overline{P^{\mathrm{w}}_{i+\frac{1}{2}}}\tau_{0:i+\frac{1}{2}}}{\overline{S^{\mathrm{b}}_{i+\frac{1}{2}}}\rho^{\mathrm{w}}} \qquad \text{channel,} \quad \text{(F.8a)}$$

$$\frac{\partial u^{\mathrm{b}}}{\partial t}_{i+\frac{1}{2}} = -\frac{1}{2}\frac{\left(u^{\mathrm{b}}_{i+\frac{1}{2}}\right)^2 - \left(u^{\mathrm{b}}_{i-\frac{1}{2}}\right)^2}{s_{i+1}-s_i} - \frac{\left(1-n^{\mathrm{i}}_{p:i}\right)\rho^{\mathrm{i}} + n^{\mathrm{i}}_{p:i}\rho^{\mathrm{w}}}{\left(1-n^{\mathrm{i}}_{p:i}\right)\rho^{\mathrm{i}}}\frac{\overline{\tilde{m}_{i+\frac{1}{2}}}u^{\mathrm{b}}_{i+\frac{1}{2}}}{\rho^{\mathrm{w}}\overline{H^{\mathrm{b}}_{i+\frac{1}{2}}}}$$
$$-\frac{1}{\rho^{\mathrm{w}}}\frac{\overline{p^{\mathrm{b}}_{i+\frac{1}{2}}} - \overline{p^{\mathrm{b}}_{i+\frac{1}{2}}}}{s_{i+1}-s_i} - g\frac{z^{\mathrm{b}}_{i+1}-z^{\mathrm{b}}_i}{s_{i+1}-s_i} - \frac{2\tau_{0:i+\frac{1}{2}}}{\overline{H^{\mathrm{b}}_{i+\frac{1}{2}}}\rho^{\mathrm{w}}} \qquad \text{sheet,} \quad \text{(F.8b)}$$

where the first term on the right hand side is upwinded. Similarly, discretizing equations (2.29) yields

$$\frac{\partial T^{\mathrm{b}}}{\partial t}_{i} = -u^{\mathrm{b}}_{i-\frac{1}{2}}\frac{T^{\mathrm{b}}_i - T^{\mathrm{b}}_{i-1}}{s_i - s_{i-1}} - \frac{m_i}{\rho^{\mathrm{w}}c^{\mathrm{w}}_p S^{\mathrm{b}}_i}\left\{L + c^{\mathrm{w}}_p\Delta T_{\mathrm{mp}:i} - \frac{\left(1-n^{\mathrm{i}}_{p:i}\right)\rho^{\mathrm{i}} + n^{\mathrm{i}}_{p:i}\rho^{\mathrm{w}}}{\left(1-n^{\mathrm{i}}_{p:i}\right)\rho^{\mathrm{i}}}\frac{\left(\overline{u^{\mathrm{b}}_i}\right)^2}{2}\right\}$$
$$+\frac{P^{\mathrm{w}}_i}{S^{\mathrm{b}}_i}\frac{\overline{(\tau_0 u^{\mathrm{b}})_i}}{\rho^{\mathrm{w}}c^{\mathrm{w}}_p} \qquad \text{channel,} \quad \text{(F.9a)}$$

$$\frac{\partial T^{\mathrm{b}}}{\partial t}_{i} = -u^{\mathrm{b}}_{i-\frac{1}{2}}\frac{T^{\mathrm{b}}_i - T^{\mathrm{b}}_{i-1}}{s_i - s_{i-1}} - \frac{\tilde{m}_i}{\rho^{\mathrm{w}}c^{\mathrm{w}}_p H^{\mathrm{b}}_i}\left\{L + c^{\mathrm{w}}_p\Delta T_{\mathrm{mp}:i} - \frac{\left(1-n^{\mathrm{i}}_{p:i}\right)\rho^{\mathrm{i}} + n^{\mathrm{i}}_{p:i}\rho^{\mathrm{w}}}{\left(1-n^{\mathrm{i}}_{p:i}\right)\rho^{\mathrm{i}}}\frac{\left(\overline{u^{\mathrm{b}}_i}\right)^2}{2}\right\}$$
$$+\frac{2}{H^{\mathrm{b}}_i}\frac{\overline{(\tau_0 u^{\mathrm{b}})_i}}{\rho^{\mathrm{w}}c^{\mathrm{w}}_p} \qquad \text{sheet.} \quad \text{(F.9b)}$$

Overall, these equations strike the proper balance for the discretization of internal energy. However, one of the discouraging aspects of this energy discretization is that the $\partial T^{\mathrm{b}}/\partial s$ terms lie on the staggered grid and are simply moved to the centered grid. This feature guarantees upwinding but introduces a small amount of error to the second-order accurate scheme in space. Any other scheme would require T_{i-1}, T_i, T_{i+1}, which arbitrarily bridges the solution from the $i-1$ to $i+1$ nodes. Obviously, when water flow is opposite to the upwinding, the scheme presented in equations (F.9) needs to be modified.

F.1.2 Boundary conditions

Upstream

Two conditions are necessary at the upstream boundary. These conditions are commonly employed as a condition on water pressure and water discharge.

Without a surface melt and infiltration condition applied to the model presented here, it is useful to borrow ideas from outburst floods. Ice-dammed lakes release through a conduit where

the temperature and configuration of the lake are either known or assumed at the upstream end of the channel (*e.g.,* Clarke, 2003). Instead of a lake, it is possible to create a similar situation by imposing a crevasse at the upstream end of the subglacial water system such that,

$$\frac{dZ^{\mathrm{c}}}{dt} = \frac{Q_{\mathrm{melt}} - Q^{\mathrm{b}}}{A^{\mathrm{c}}}, \tag{F.10}$$

where $Z^{\mathrm{c}} = z^{\mathrm{c}} - z^{\mathrm{s}}$ is water depth in the crevasse, z^{c} is the water elevation in the crevasse relative to a fixed datum, Q_{melt} represents recharge from a supraglacial water system, Q^{b} is a water flux to the subglacial water system, A^{c} is the representative cross-sectional area normal to z, and dz^{s}/dt is the rate of change of the elevation of the bed below the crevasse (see Fig. F.2). Equation (F.10) neglects any crevasse opening or closing mechanisms via melting/freezing or mechanical opening/closing. Because this equation does not directly account for the boundaries at the surface or base of the crevasse, penalty functions similar to equation (5.27) prevent the crevasse water height from being above the surface of the glacier or below the bed elevation,

$$\frac{dZ^{\mathrm{c}}}{dt} = \begin{cases} \frac{1}{\tau^{\mathrm{c}}}\left(Z^{\mathrm{i}} - Z^{\mathrm{c}}\right) & \text{for} \quad \left[Z^{\mathrm{c}} + \tau^{\mathrm{c}}\left(\frac{Q_{\mathrm{melt}} - Q^{\mathrm{b}}}{A^{\mathrm{c}}}\right)\right] > Z^{\mathrm{i}}, \\ \frac{Z^{\mathrm{c}}}{\tau^{\mathrm{c}}} & \text{for} \quad \left[Z^{\mathrm{c}} + \tau^{\mathrm{c}}\left(\frac{Q_{\mathrm{melt}} - Q^{\mathrm{b}}}{A^{\mathrm{c}}}\right)\right] < 0. \end{cases} \tag{F.11}$$

In each of the cases, τ^{c} is a characteristic time scale for the crevasse. These relations can be implemented such that the penalty function is used when the water depth approaches the limits in (F.11).

Alternatively, the rate of change of the crevasse water elevation can be prescribed directly without the use of a recharge rate. The advantage of this method is that the crevasse water height is known for all time. The disadvantage is that the water elevation change is not based upon the outflow from the crevasse, which would be expected. I avoid this representation.

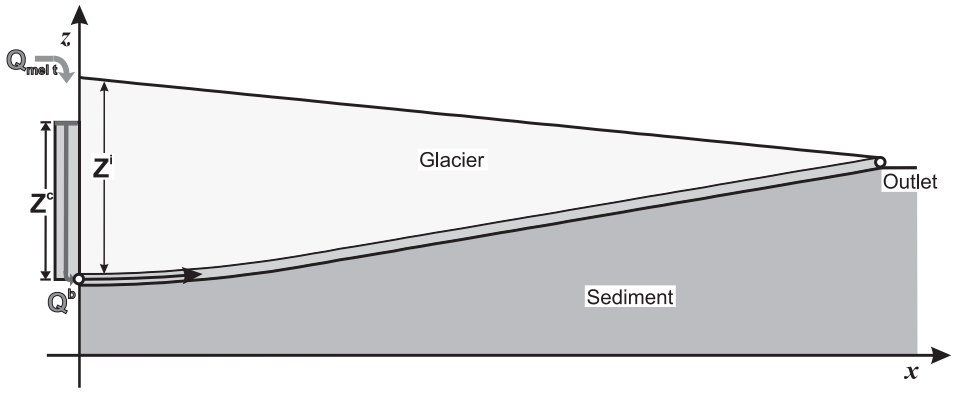

Figure F.2: Ice geometry with upstream crevasse. Water flows into the crevasse at a predetermined rate, Q_{melt} (gray arrow) and flows out of the crevasse into the subglacial water system at a rate Q^{b}.

From the water depth in the crevasse, the upstream conditions of pressure and temperature are

$$\frac{dp^{\mathrm{c}}}{dt} = \rho^{\mathrm{w}} g \frac{dZ^{\mathrm{c}}}{dt}, \tag{F.12a}$$

$$\frac{dT^{\mathrm{c}}}{dt} = \beta \frac{dp^{\mathrm{c}}}{dt}. \tag{F.12b}$$

Equation (F.12a) states that the upstream pressure condition is hydrostatic, and equation (F.12b) states that the upstream temperature evolution is based on the Clausius-Clapeyron equation.

The discharge from the crevasse into the subglacial system is defined as

$$Q^{\mathrm{b}}_{\frac{3}{2}} = S^{\mathrm{b}}_2 u^{\mathrm{b}}_{\frac{3}{2}} \qquad \text{channel,} \tag{F.13a}$$

$$Q^{\mathrm{b}}_{\frac{3}{2}} = H^{\mathrm{b}}_2 W u^{\mathrm{b}}_{\frac{3}{2}} \qquad \text{sheet,} \tag{F.13b}$$

where the implied boundary conditions[16] are that $\partial S^{\mathrm{b}}/\partial s = 0$ and $\partial H^{\mathrm{b}}/\partial s = 0$ for the channel and sheet, respectively. By setting the two mass balance equations (eqs. 2.14 and eqs. 2.16) equal, the boundary conditions on $\partial u^{\mathrm{b}}/\partial s$ become

$$\frac{\partial u^{\mathrm{b}}}{\partial s}_{\frac{3}{2}} = -\frac{1}{S^{\mathrm{b}}_2}\left\{\left(\frac{1}{\rho^{\mathrm{i}}} - \frac{1}{\rho^{\mathrm{w}}}\right) m_2 - 2S^{\mathrm{b}}_2 \operatorname{sgn}\left(p^{\mathrm{i}} - p^{\mathrm{b}}_2\right)\left(\frac{|p^{\mathrm{i}} - p^{\mathrm{b}}_2|}{n\mathcal{B}}\right)^n\right\} \quad \text{channel,} \tag{F.14a}$$

$$\frac{\partial u^{\mathrm{b}}}{\partial s}_{\frac{3}{2}} = -\frac{1}{H^{\mathrm{b}}_2}\left\{\left(\frac{1}{\rho^{\mathrm{i}}} - \frac{1}{\rho^{\mathrm{w}}}\right)\tilde{m}_2 + \left(\frac{\partial H^{\mathrm{b}}}{\partial t}\right)_{\text{close:2}}\right\} \qquad \text{sheet.} \tag{F.14b}$$

These relationships substitute directly into equations (F.8) for the divergence terms.

Downstream

Only a pressure boundary condition is necessary downstream. This condition can be either a Dirichlet or Neumann condition. For the discretization employed here, this condition is applied as a Dirichlet condition meaning that the outflow pressure must be known. Commonly, water exits the glacier at atmospheric pressure, which is a natural choice for the pressure. In some situations, water exits the subglacial water system into a lake. In addition, at some of the hydraulic vents at the margin of Matanuska Glacier, water flow is artesian. Both the lake case and the artesian case can be prescribed as Dirichlet boundary conditions.

The other boundary condition option is to prescribe the derivative as a Neumann boundary condition. If Neumann boundary conditions are applied, it is possible that open channel flow might occur. However, the equations presented in Chapter 2 are not compatible with open channel flow. Thus, not only does a Dirichlet boundary condition approximate the bound, but this condition also prevents the equations from behaving nonphysically. Open channel flow is observed at many glaciers near the terminus, but its subglacial extent is not clear.

Both the ice mass balance (eqs. F.5a and F.5a) and the thermal energy balance (eqs. F.9) require a melt rate at the exit. A Reynolds number appears in this melt rate and requires an appropriate velocity at the final centered cell,

$$\overline{u^{\mathrm{b}}_N} = \frac{Q^{\mathrm{b}}_{N-\frac{1}{2}}}{S^{\mathrm{b}}_N} \qquad \text{channel,} \tag{F.15a}$$

$$\overline{u^{\mathrm{b}}_N} = \frac{\tilde{Q}^{\mathrm{b}}_{N-\frac{1}{2}}}{H^{\mathrm{b}}_N} \qquad \text{sheet,} \tag{F.15b}$$

where N denotes the final grid-centered cell, and $\tilde{Q}^{\mathrm{b}}$ is the average discharge per unit width. The discharge between cells is conserved, and as a result, dividing the discharge at the final

[16] In these equations, numbered subscripts indicate the relative position of the ith location on the grid. For example $Q^{\mathrm{b}}_{\frac{3}{2}}$ is exactly $Q^{\mathrm{b}}_{i=\frac{3}{2}}$. Near the outflow boundary, i may take a value based on N.

staggered point by the final cross-section is a reasonable approximation to the velocity there. With the melt rate term defined and because the thermal energy balance is already upwinded with respect to its divergence term, this equation can be applied at the outflow boundary without complication. Similarly, the ice mass balance can be applied directly to the final centered grid cell.

F.1.3 Initialization

Because a numerical model integrates over time, the initial conditions are paramount. Initial conditions that are ill-posed will not be corrected by numerical integration.

Of the fields that need to be specified, the cross-sectional area S^{b}, and the water layer thickness H^{b}, are the most difficult to ascertain. Essentially, reasonable guesses for these terms are necessary. Both Clarke (2003) and Ng (1998) chose S^{b} to match known examples. Clarke (2003) also tested initial values of S^{b} and concluded that the overall sensitivity was limited. It stands to reason that H^{b} must also be chosen arbitrarily. For the velocity, pressure, and temperature equations, natural initial conditions stem from applying the steady state velocities (eqs. 2.26), setting the water pressure equal to ice overburden pressure, and then applying the Clausius-Clapeyron relation (2.8), respectively.

F.2 Sediment transport numerical formulation

Governing equations for sediment in the subglacial water system are given by equations (4.11), (4.12), (4.14), and (4.15). There are also the balances of sediment in the water (eqs. 4.10) and the rate of change of the bed elevation (4.7). Other equations that are necessary are the supply from the ice (4.34) as well as the semiempirical sediment transport relations (eqs. 4.19–4.30). Many of these equations have a numerical formulation that parallels the formulation for water flow without sediment transport. As a result, I only touch on the portions of the numerical formulation that are either exclusive to sediment transport or require additional clarification.

F.2.1 Grid and discretization

The grid is the same as that of the subglacial water flow (Fig. F.1). Additional quantities that fall on this grid are listed in Table F.2.

Table F.2: Sediment transport quantities on the centered and staggered grids.

Centered		Staggered	
$\frac{\partial q^{\mathrm{s}}}{\partial s}(s,t)$, $\frac{\partial \tilde{q}^{\mathrm{s}}}{\partial s}(s,t)$	Sediment flux divergence	q^{s}, $\tilde{q}^{\mathrm{s}}$	Sediment flux
		q_e^{s}, $\tilde{q}_e^{\mathrm{s}}$	Equilibrium sediment flux
$\Psi^{\mathrm{i}}(s,t)$, $\tilde{\Psi}^{\mathrm{i}}(s,t)$	Sediment supply from ice		
$\lambda^{\mathrm{b}}(s,t)$	Sediment concentration in flow		
$\lambda^{\mathrm{i}}(s,t)$	Sediment concentration in ice		

In the four sets of governing equations (eqs. 4.11, 4.12, 4.14, and 4.15), there are necessary modifications of the discretization presented for flow equations presented above because of the inclusion of the sediment concentration λ^{b} and the source terms $\tilde{\Psi}^{\mathrm{s}}$, $\tilde{\Psi}^{\mathrm{i}}$, and Ψ^{s}. In the mass

balance equations, λ and Ψ terms are straightforward with the exception of flux divergence of sediment concentration $u^{\mathrm{b}}(\partial\lambda^{\mathrm{b}}/\partial s)$ in equations (4.11b) and (4.12b). In these equations, this term averages via equations (F.4) to

$$\overline{\left(u^{\mathrm{b}}\frac{\partial\lambda^{\mathrm{b}}}{\partial s}\right)}_i = \frac{V_{i+\frac{1}{2}}u^{\mathrm{b}}_{i+\frac{1}{2}}\left(\frac{\lambda^{\mathrm{b}}_{i+1}-\lambda^{\mathrm{b}}_i}{s_{i+1}-s_i}\right)+V_{i-\frac{1}{2}}u^{\mathrm{b}}_{i-\frac{1}{2}}\left(\frac{\lambda^{\mathrm{b}}_i-\lambda^{\mathrm{b}}_{i-1}}{s_i-s_{i-1}}\right)}{V_{i+\frac{1}{2}}+V_{i-\frac{1}{2}}}. \tag{F.16}$$

In the momentum equations, Ψ^{i}, $\tilde{\Psi}^{\mathrm{i}}$, and $\tilde{\Psi}^{\mathrm{s}}$ need to be averaged to the staggered grid via equations (F.3) to make $\overline{\Psi^{\mathrm{i}}}_{i+\frac{1}{2}}$, $\overline{\tilde{\Psi}^{\mathrm{i}}}_{i+\frac{1}{2}}$, and $\overline{\tilde{\Psi}^{\mathrm{s}}}_{i+\frac{1}{2}}$. There are no additional discretizations necessary for the balance of internal energy that are not discussed above.

The rate of change of the sediment concentration requires two modifications. The definition of sediment flux appears in equation (4.3a) as $\tilde{q}^{\mathrm{s}} = u^{\mathrm{s}}\lambda^{\mathrm{b}}H^{\mathrm{b}}$, its numerical discretization on the staggered grid is

$$\tilde{q}^{\mathrm{s}}_{i+\frac{1}{2}} = u^{\mathrm{s}}_{i+\frac{1}{2}}\overline{(\lambda^{\mathrm{b}}H^{\mathrm{b}})}_{i+\frac{1}{2}}, \tag{F.17}$$

where averaging is done according to equation (F.3). Divergence of this flux then falls on the centered grid.

The total sediment flux is the sum of the bed load and suspended load such that

$$\tilde{q}^{\mathrm{s}} = \tilde{q}^{\mathrm{s}}_b + \tilde{q}^{\mathrm{s}}_s, \tag{F.18a}$$

$$\tilde{q}^{\mathrm{s}} = u_b\delta_b\lambda^{\mathrm{b}}_b + u^{\mathrm{b}}H^{\mathrm{b}}\lambda^{\mathrm{b}}_s \qquad \text{sheet}, \tag{F.18b}$$

$$\tilde{q}^{\mathrm{s}} = u_b\delta_b\lambda^{\mathrm{b}}_b + u^{\mathrm{b}}\left(\frac{\pi R^{\mathrm{b}}}{4}\right)\lambda^{\mathrm{b}}_s \qquad \text{semicircular channel}. \tag{F.18c}$$

To obtain the water depth in equation (F.18c), the semicircular cross sectional area is approximated by a rectangle of equal area whose width is the the width of the channel $2R^{\mathrm{b}}$. The water depth is then the height of this rectangle $\pi R^{\mathrm{b}}/4$ or $\left(\pi S^{\mathrm{b}}/2\right)^{\frac{1}{2}}$ in terms of S^{b}. A second modification appears in equation (4.4) where the difference of the equilibrium and actual sediment fluxes yields a sediment supply. In this case,

$$\tilde{\Psi}^{\mathrm{s}}_i = \frac{\rho^{\mathrm{s}}}{L^{\mathrm{s}}}\left(\overline{\tilde{q}^{\mathrm{s}}_{e:i}} - \overline{\tilde{q}^{\mathrm{s}}_i}\right), \tag{F.19}$$

where the fluxes are averaged from the staggered grid to the centered grid. Equation (4.10) does not require additional modification.

The semiempirical bed load flux and suspended load flux equations (4.19)–(4.30) have centered and staggered quantities in them. In general, these can be moved via equations (F.3) and (F.4) when necessary. There are also quantities such as δ_b and D_{50} that lie on the centered grid. Treatment of these secondary quantities is not critical. Provided that they are all treated in a careful systematic fashion relative to the other fields and fluxes, their discretization does not merit further consideration.

Change in bed elevation and along-path coordinate

Erosion or deposition results in a change in z^{s}. The change in z^{s} results in a change in the path length,

$$\Delta s_{i+\frac{1}{2}} = \sqrt{\left(z^{\mathrm{s}}_{i+1}-z^{\mathrm{s}}_i\right)^2+\left(x_{i+1}-x_i\right)^2}, \tag{F.20}$$

where the length of the Δs array is one less than the length of the x or z^{s} arrays. The along-path coordinate is then

$$s_{i+1} = s_1 + \sum_{1}^{N-1} \Delta s_{i+\frac{1}{2}}, \tag{F.21}$$

where $s_1 = 0$ and N is the number of grid cells. With z^{s} defined on the centered grid, its values on the the staggered grid are found using linear interpolation. The equivalent relations to equations (F.20) and (F.21) are

$$\Delta s_i = \sqrt{\left(z^{\mathrm{s}}_{i+\frac{1}{2}} - z^{\mathrm{s}}_{i-\frac{1}{2}}\right)^2 + \left(x_{i+\frac{1}{2}} - x_{i-\frac{1}{2}}\right)^2}, \tag{F.22a}$$

$$s_{i+\frac{1}{2}} = s_{\frac{1}{2}} + \sum_{1}^{N-1} \Delta s_i. \tag{F.22b}$$

F.2.2 Boundary conditions

Upstream

Several conditions are necessary at the upstream boundary. The crevasse boundary conditions remain the same as in the case of clear water flows (eqs. F.10 and F.11). In addition, the upstream pressure and temperature conditions are also exactly those for clear water flows (eqs. F.12).

The discharge from the crevasse into the subglacial system is defined using equations (F.13) where $\partial S^{\mathrm{b}}/\partial s = 0$ and $\partial H^{\mathrm{b}}/\partial s = 0$ for the channel and sheet, respectively. Using this condition, the boundary conditions on $\partial u^{\mathrm{b}}/\partial s$ result from setting the two mass balance equations for the channel (eqs. 4.11a and 4.11b) and sheet (4.12a and 4.12b) equal,

$$\begin{aligned}
\frac{\partial u^{\mathrm{b}}}{\partial s}_{\frac{3}{2}} =& \frac{1}{S_2^{\mathrm{b}}} \frac{\rho^{\mathrm{w}}}{\overline{\rho^{\mathrm{f}}_{\frac{3}{2}}}} \Bigg\{ \left[\frac{1}{\rho^{\mathrm{s}}} - \frac{1}{\left(1-\lambda_2^{\mathrm{i}}\right)\left(1-n_p^{\mathrm{i}}\right)\rho^{\mathrm{i}} + n_p^{\mathrm{i}}\rho^{\mathrm{w}} + \lambda_2^{\mathrm{i}}\left(1-n_p^{\mathrm{i}}\right)\rho^{\mathrm{s}}} \right] \Psi_2^{\mathrm{i}} \\
&+ \left[\frac{1}{\rho^{\mathrm{w}}} - \frac{1}{\left(1-\lambda_2^{\mathrm{i}}\right)\left(1-n_p^{\mathrm{i}}\right)\rho^{\mathrm{i}} + n_p^{\mathrm{i}}\rho^{\mathrm{w}} + \lambda_2^{\mathrm{i}}\left(1-n_p^{\mathrm{i}}\right)\rho^{\mathrm{s}}} \right] \left[1 + \frac{n_p^{\mathrm{i}}\rho^{\mathrm{w}}}{\left(1-\lambda_2^{\mathrm{i}}\right)\left(1-n_p^{\mathrm{i}}\right)\rho^{\mathrm{i}}} \right] m_{\frac{3}{2}} \\
&+ 2S_2^{\mathrm{b}} \operatorname{sgn}(p^{\mathrm{i}} - p_2^{\mathrm{b}}) \left(\frac{|p^{\mathrm{i}} - p_2^{\mathrm{b}}|}{n\mathcal{B}} \right)^n + \left(\frac{\rho^{\mathrm{s}}}{\rho^{\mathrm{w}}} - 1 \right) \left(\frac{\partial q^{\mathrm{s}}}{\partial s} - S_2^{\mathrm{b}} u^{\mathrm{b}}_{\frac{3}{2}} \frac{\partial \lambda^{\mathrm{b}}}{\partial s} \right) \Bigg\},
\end{aligned} \tag{F.23a}$$

$$\begin{aligned}
\frac{\partial u^{\mathrm{b}}}{\partial s}_{\frac{3}{2}} =& \frac{1}{H_2^{\mathrm{b}}} \frac{\rho^{\mathrm{w}}}{\overline{\rho^{\mathrm{f}}_{\frac{3}{2}}}} \Bigg\{ \left[\frac{1}{\rho^{\mathrm{s}}} - \frac{1}{\left(1-\lambda_2^{\mathrm{i}}\right)\left(1-n_p^{\mathrm{i}}\right)\rho^{\mathrm{i}} + n_p^{\mathrm{i}}\rho^{\mathrm{w}} + \lambda_2^{\mathrm{i}}\left(1-n_p^{\mathrm{i}}\right)\rho^{\mathrm{s}}} \right] \tilde{\Psi}_2^{\mathrm{i}} \\
&+ \left[\frac{1}{\rho^{\mathrm{w}}} - \frac{1}{\left(1-\lambda_2^{\mathrm{i}}\right)\left(1-n_p^{\mathrm{i}}\right)\rho^{\mathrm{i}} + n_p^{\mathrm{i}}\rho^{\mathrm{w}} + \lambda_2^{\mathrm{i}}\left(1-n_p^{\mathrm{i}}\right)\rho^{\mathrm{s}}} \right] \left[1 + \frac{n_p^{\mathrm{i}}\rho^{\mathrm{w}}}{\left(1-\lambda_2^{\mathrm{i}}\right)\left(1-n_p^{\mathrm{i}}\right)\rho^{\mathrm{i}}} \right] \tilde{m}_{\frac{3}{2}} \\
&+ \left(\frac{\partial H^{\mathrm{b}}}{\partial t} \right)_{\text{close:2}} + \left(\frac{\rho^{\mathrm{s}}}{\rho^{\mathrm{w}}} - 1 \right) \left(\frac{\partial \tilde{q}^{\mathrm{s}}}{\partial s} - H_2^{\mathrm{b}} u^{\mathrm{b}}_{\frac{3}{2}} \frac{\partial \lambda^{\mathrm{b}}}{\partial s} \right) \Bigg\},
\end{aligned} \tag{F.23b}$$

where equations (F.23a) and (F.23b) are for the channel and sheet, respectively. The sediment divergence terms $\partial \lambda^{\mathrm{b}}/\partial s$, $\partial q^{\mathrm{s}}/\partial s$, and $\partial \tilde{q}^{\mathrm{s}}/\partial s$ can be estimated by assuming that the water flows

in with an equilibrium concentration of sediment. Water velocities are estimated by assuming that the discharge does not vary significantly over the first cell, such that

$$u_1^{\mathrm{b}} = \frac{Q_{\frac{3}{2}}}{S_2^{\mathrm{b}}} \qquad \text{channel,} \tag{F.24a}$$

$$u_1^{\mathrm{b}} = \frac{Q_{\frac{3}{2}}}{H_2^{\mathrm{b}} W} \qquad \text{sheet.} \tag{F.24b}$$

Because sediment concentration is at equilibrium, the first cell cannot evolve its bed elevation via equations (4.7) and (4.4) because $\tilde{\Psi}^{\mathrm{s}} = 0$. However, the spatial derivative of the bed figures into equation (4.14). As a result, on the first cell $\partial z^{\mathrm{s}}/\partial s_{\frac{1}{2}} = 0$, which is equivalent to saying that the erosion or aggradation rate in the first cell is equal to that of the second cell.

F.2.3 Initialization

The initialization of the subglacial velocity via equation (2.26) allows calculation of both bed and suspended load via the semiempirical sediment transport relationships. The other important initialization is the concentration of sediment in the ice λ^{i}, and it is not clear what this should be set as. In consequence, I take it as a free parameter.

F.3 Englacial aquifer numerical formulation

Equations (5.1), (5.15), and (5.18) form the system of governing equations. These governing equations are subject to the supplementary relations in equations (5.19), (5.23), and (5.25). The conditions at the surface of the aquifer and base of the aquifer given in equations, (5.28–5.32, 5.26, and 5.27). The values of pressure and temperature at the top of the glacier are assumed to be atmospheric and 0°C, respectively. Pressure and temperature values at the base of the aquifer are given by equation (eqs. 2.16b and 2.29b). Note that at this point it must be clear that the aquifer is only over the sheet. This prevents a correction for the radial divergence of water over a channel.

F.3.1 Vertical coordinate transformation

Because the thickness of the englacial aquifer can evolve through time, and because the aquifer is assumed to be contiguous, a vertical coordinate transformation is useful. This coordinate transformation, and its resulting change in derivatives, is presented in Appendix G. Quantities that vary in the vertical dimension transform via equation (G.1a). The irregularly spaced vertical derivatives in z become regular vertical derivatives in ξ^{w} for numerical operations. Terms containing ξ^{w} map directly back to z via

$$\xi^{\mathrm{w}} = \frac{z - z^{\mathrm{b}}}{Z^{\mathrm{e}}}, \tag{F.25}$$

where ξ^{w} takes values in the range (0, 1) dependent on the assignment of z. The vertical derivative of (F.25) is

$$\frac{\partial \xi^{\mathrm{w}}}{\partial z} = \frac{1}{Z^{\mathrm{e}}}. \tag{F.26}$$

Equations (F.25) and (G.1a) can then be used to create the other derivatives according to

$$\frac{d\xi^{\mathrm{w}}}{dX} = -\frac{1}{Z^{\mathrm{e}}}\left(\frac{dz^{\mathrm{b}}}{dX} + \xi^{\mathrm{w}}\frac{dZ^{\mathrm{e}}}{dX}\right), \tag{F.27}$$

where X represents either x or t depending on the situation. When the independent variable is time t or longitudinal position x, the derivatives gain an extra term based on this equation. Because z^{b} and Z^{e} do not vary vertically, the derivatives in equation (F.27) are relatively simple to calculate. Simple calculations such as these are some of the advantages of a vertical coordinate transformation.

Each of the four governing equations for flow within the aquifer assumes a form in ξ^{w}. Darcy's law (eq. 5.1a) changes slightly with the change of variable,

$$q_z^{\mathrm{w}} = -\frac{1}{Z^{\mathrm{e}}}\frac{K_H^{\mathrm{w}}}{\rho^{\mathrm{w}} g}\frac{\partial \phi^{\mathrm{w}}}{\partial \xi}, \tag{F.28a}$$

$$q_x^{\mathrm{w}} = -\frac{K_H^{\mathrm{w}}}{\rho^{\mathrm{w}} g}\left\{\frac{\partial \phi^{\mathrm{w}}}{\partial x} - \frac{1}{Z^{\mathrm{e}}}\frac{\partial \phi^{\mathrm{w}}}{\partial \xi}\left(\frac{dz^{\mathrm{b}}}{dx} + \xi^{\mathrm{w}}\frac{dZ^{\mathrm{e}}}{dx}\right)\right\}. \tag{F.28b}$$

Equations (5.15) and (5.18) become

$$\frac{\partial n_p^{\mathrm{i}}}{\partial t} = \frac{m_v - d_v}{\rho^{\mathrm{i}}} - \frac{\partial n_p^{\mathrm{i}}}{\partial \xi}\frac{1}{Z^{\mathrm{e}}}\left(\frac{dz^{\mathrm{b}}}{dt} + \xi^{\mathrm{w}}\frac{dZ^{\mathrm{e}}}{dt}\right), \tag{F.29a}$$

$$\frac{\partial p^{\mathrm{w}}}{\partial t} = -\frac{1}{n_p^{\mathrm{i}}\alpha^{\mathrm{w}} + (1-n_p^{\mathrm{i}})\alpha^{\mathrm{i}}}\left\{\nabla\cdot\mathbf{q}^{\mathrm{w}} + \left(1 - \frac{\rho^{\mathrm{i}}}{\rho^{\mathrm{w}}}\right)\frac{\partial n_p^{\mathrm{i}}}{\partial t}\right\} - \frac{\partial p^{\mathrm{w}}}{\partial \xi}\frac{1}{Z^{\mathrm{e}}}\left(\frac{dz^{\mathrm{b}}}{dt} + \xi^{\mathrm{w}}\frac{dZ^{\mathrm{e}}}{dt}\right), \tag{F.29b}$$

$$\begin{aligned}\frac{\partial T^{\mathrm{w}}}{\partial t} = &-\left\{\frac{q_x^{\mathrm{w}}}{n_p^{\mathrm{i}}}\left[\frac{\partial T^{\mathrm{w}}}{\partial x} - \frac{1}{Z^{\mathrm{e}}}\frac{\partial T^{\mathrm{w}}}{\partial \xi}\left(\frac{dz^{\mathrm{b}}}{dx} + \xi^{\mathrm{w}}\frac{dZ^{\mathrm{e}}}{dx}\right)\right] + \frac{1}{Z^{\mathrm{e}}}\frac{q_z^{\mathrm{w}}}{n_p^{\mathrm{i}}}\frac{\partial T^{\mathrm{w}}}{\partial \xi}\right\} \\ &- \frac{m_v - d_v}{\rho^{\mathrm{w}} c_p^{\mathrm{w}} n_p^{\mathrm{i}}}\left(L + c_p^{\mathrm{w}}\Delta T_{\mathrm{mp}}\right) + \frac{g}{c_p^{\mathrm{w}} K_H^{\mathrm{w}}}\left(\frac{q^{\mathrm{w}}}{n_p^{\mathrm{i}}}\right)^2 - \frac{\partial T^{\mathrm{w}}}{\partial \xi}\frac{1}{Z^{\mathrm{e}}}\left(\frac{dz^{\mathrm{b}}}{dt} + \xi^{\mathrm{w}}\frac{dZ^{\mathrm{e}}}{dt}\right).\end{aligned} \tag{F.29c}$$

The divergence of specific discharge $\nabla\cdot\mathbf{q}^{\mathrm{w}}$ that appears in equations (5.15b) and its transformed equivalent (eq. F.29b) expands to

$$\nabla\cdot\mathbf{q}^{\mathrm{w}} = \frac{\partial q_x^{\mathrm{w}}}{\partial x} - \frac{1}{Z^{\mathrm{e}}}\frac{\partial q_z^{\mathrm{w}}}{\partial \xi}\left(\frac{dz^{\mathrm{b}}}{dx} + \xi^{\mathrm{w}}\frac{dZ^{\mathrm{e}}}{dx}\right) + \frac{1}{Z^{\mathrm{e}}}\frac{\partial q_z^{\mathrm{w}}}{\partial \xi}. \tag{F.30}$$

The other equations necessary for numerical implementation of the aquifer (eqs. 5.23, 5.25, 5.28, 5.30, 5.31, 5.26, 5.27) are either applied along the boundaries or do not have a dependence on z. As a result, these equations are not transformed via equation (F.25) or its derivatives.

F.3.2 Discretization

In general, the englacial aquifer grid is positioned with respect to the subglacial sheet. The staggered grid is similarly determined. With two grids, distinction must be made between the values that reside on the centered grid and those that reside on the staggered grid. Figure F.3 illustrates this grid. In addition, this figure illustrates the difference between the z- and ξ^{w}-grids. The advantage of the ξ^{w}-grid is that it is regular and uniform.

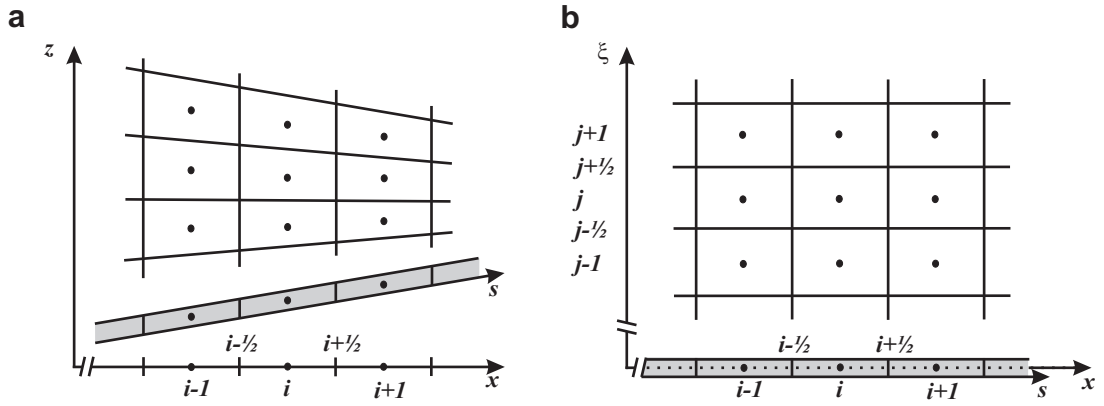

Figure F.3: Two dimensional grid for englacial water flow. Centered values reside at points denoted with integer values such as $i-1$, i, and $i+1$ for x and $j-1$, j, and $j+1$ for ξ^{w}. Staggered values inhabit points at integer values plus or minus one half such as $i-\frac{1}{2}$ and $i+\frac{1}{2}$ for x and $j-\frac{1}{2}$ and $j+\frac{1}{2}$ for ξ^{w}. (a) Illustration of a regular grid in x and z. (b) A similar illustration where the grid in ξ^{w} is uniform.

For a general variable Ω, that lies on the centered grid in x–z coordinates, the vertical, horizontal, and time derivatives can be approximated in x–ξ coordinates as,

$$\frac{\partial \Omega}{\partial z} = \frac{\partial \Omega}{\partial \xi}\frac{\partial \xi}{\partial z} \simeq \frac{\Delta \Omega}{\Delta \xi}\frac{\partial \xi}{\partial z}\bigg|_{i,j+\frac{1}{2}} = \frac{1}{Z^{\mathrm{e}}_i}\,\frac{\Omega_{i,j+1}-\Omega_{i,j}}{\xi^{\mathrm{w}}_{j+1}-\xi^{\mathrm{w}}_{j}}, \tag{F.31a}$$

$$\frac{\partial \Omega}{\partial x} = \frac{\partial \Omega}{\partial x} + \frac{\partial \Omega}{\partial \xi}\,\frac{\partial \xi^{\mathrm{w}}}{\partial x} \simeq \frac{\Delta \Omega}{\Delta x}\bigg|_{i+\frac{1}{2},j} - \frac{\Delta \Omega}{\Delta \xi^{\mathrm{w}}}\,\frac{1}{Z^{\mathrm{e}}}\left(\frac{\Delta z^{\mathrm{b}}}{\Delta x} + \xi^{\mathrm{w}}\frac{\Delta Z^{\mathrm{e}}}{\Delta x}\right)\bigg|_{i,j+\frac{1}{2}}, \tag{F.31b}$$

$$\simeq \frac{\Omega_{i+1,j}-\Omega_{i,j}}{x_{i+1}-x_i} - \frac{1}{Z^{\mathrm{e}}_i}\,\overline{\frac{\Delta \Omega}{\Delta \xi^{\mathrm{w}}}}_{i+\frac{1}{2},j}\left(\frac{z^{\mathrm{b}}_{i+1}-z^{\mathrm{b}}_{i}}{x_{i+1}-x_i} + \xi^{\mathrm{w}}_j\,\frac{Z^{\mathrm{e}}_{i+1}-Z^{\mathrm{e}}_{i}}{x_{i+1}-x_i}\right), \tag{F.31c}$$

$$\frac{\partial \Omega}{\partial t} = \frac{\partial \Omega}{\partial t} + \frac{\partial \Omega}{\partial \xi}\,\frac{\partial \xi^{\mathrm{w}}}{\partial t} \simeq \frac{\partial \Omega_{i,j}}{\partial t} - \frac{1}{Z^{\mathrm{e}}_i}\,\overline{\frac{\Delta \Omega}{\Delta \xi^{\mathrm{w}}}}_{i,j}\left(\frac{\partial z^{\mathrm{b}}_i}{\partial t} + \xi^{\mathrm{w}}_j\frac{\partial Z^{\mathrm{e}}_i}{\partial t}\right). \tag{F.31d}$$

In equations (F.31b) and (F.31d), equation (F.27) has been substituted for the relevant derivative in x or t.

In equation (F.31b), the $\partial\Omega/\partial\xi$ term lies on the vertical points of the staggered grid on $(i, j+\frac{1}{2})$. As a result, this term needs to be averaged to the $(i+\frac{1}{2}, j)$ gridpoints in equation (F.31c) using a four point average of differences,

$$\overline{\frac{\Delta \Omega}{\Delta \xi^{\mathrm{w}}}}_{i+\frac{1}{2},j} = \frac{1}{4}\left(\frac{\Delta \Omega}{\Delta \xi^{\mathrm{w}}}_{i+1,j+\frac{1}{2}} + \frac{\Delta \Omega}{\Delta \xi^{\mathrm{w}}}_{i,j+\frac{1}{2}} + \frac{\Delta \Omega}{\Delta \xi^{\mathrm{w}}}_{i+1,j-\frac{1}{2}} + \frac{\Delta \Omega}{\Delta \xi^{\mathrm{w}}}_{i,j-\frac{1}{2}}\right) \tag{F.32}$$

where the relevant vertical derivatives in ξ are given in equation (F.31a). The four differences require six field points in this equation. Derivatives in t in equation (F.31d) require a simpler stencil for the vertical averages,

$$\overline{\frac{\Delta \Omega}{\Delta \xi^{\mathrm{w}}}}_{i,j} = \frac{1}{2}\left(\frac{\Omega_{i,j+1}-\Omega_{i,j}}{\xi^{\mathrm{w}}_{j+1}-\xi^{\mathrm{w}}_{j}} + \frac{\Omega_{i,j}-\Omega_{i,j-1}}{\xi^{\mathrm{w}}_{j}-\xi^{\mathrm{w}}_{j-1}}\right). \tag{F.33}$$

Table F.3: Englacial water flow quantities on the centered and staggered grids.

Centered		Staggered	
$n_p^{\mathrm{i}}(x,\xi,t)$	Ice porosity	$\dfrac{\partial n_p^{\mathrm{i}}}{\partial \xi}(x,\xi,t)$	Vertical porosity gradient
$p^{\mathrm{w}}(x,\xi,t)$	Water pressure	$\dfrac{\partial p^{\mathrm{w}}}{\partial x}(x,\xi,t)$, $\dfrac{\partial p^{\mathrm{w}}}{\partial \xi}(x,\xi,t)$	Pressure gradient
$\nabla \cdot \mathbf{q}^{\mathrm{w}}$	Flux divergence	$q_x^{\mathrm{w}}(x,\xi,t)$, $q_\xi^{\mathrm{w}}(x,\xi,t)$	Specific discharge
q^{w}	Magnitude of $\mathbf{q}^{\mathrm{w}}$		
$T^{\mathrm{w}}(x,\xi,t)$	Water temperature	$\dfrac{\partial T^{\mathrm{w}}}{\partial x}(x,\xi,t)$, $\dfrac{\partial T^{\mathrm{w}}}{\partial \xi}(x,\xi,t)$	Temperature gradient
$\phi^{\mathrm{w}}(x,\xi,t)$	Hydraulic potential	$\dfrac{\partial \phi^{\mathrm{w}}}{\partial x}(x,\xi,t)$, $\dfrac{\partial \phi^{\mathrm{w}}}{\partial \xi}(x,\xi,t)$	Potential gradient
		$\dfrac{\partial z^{\mathrm{b}}}{\partial x}(x,\xi,t)$	Gradient of glacier base
		$\dfrac{\partial Z^{\mathrm{e}}}{\partial x}(x,\xi,t)$	Aquifer thickness gradient
F_ℓ, b	Fracture parameters		
K_H^{w}	Hydraulic conductivity		
d_v, m_v	Source terms		

If $\Delta\xi^{\mathrm{w}}$ is constant, then equation (F.33) reduces to

$$\overline{\frac{\Delta\Omega}{\Delta\xi^{\mathrm{w}}}}_{i,j} = \frac{\Omega_{i,j+1} - \Omega_{i,j-1}}{2\Delta\xi^{\mathrm{w}}}. \tag{F.34}$$

Both equations (F.32) and (F.34) utilize the fact that ξ^{w} is a uniform grid because additional weightings are not necessary for the averages. At the boundary, either forward or backward differences are necessary.

Discretizations for the water fluxes given by equations (F.28) follow as,

$$q^{\mathrm{w}}_{z:i,j+\frac{1}{2}} = -\frac{1}{Z_i^{\mathrm{e}}} \overline{\frac{K^{\mathrm{w}}_{H:i,j+\frac{1}{2}}}{\rho^{\mathrm{w}} g}} \left(\frac{\phi^{\mathrm{w}}_{i,j+1} - \phi^{\mathrm{w}}_{i,j}}{\xi^{\mathrm{w}}_{i,j+1} - \xi^{\mathrm{w}}_{i,j}} \right), \tag{F.35a}$$

$$q^{\mathrm{w}}_{x:i+\frac{1}{2},j} = -\overline{\frac{K^{\mathrm{w}}_{H:i+\frac{1}{2},j}}{\rho^{\mathrm{w}} g}} \left\{ \left(\frac{\phi^{\mathrm{w}}_{i+1,j} - \phi^{\mathrm{w}}_{i,j}}{x_{i+1} - x_i} \right) - \frac{1}{\overline{Z^{\mathrm{e}}_{i+\frac{1}{2}}}} \overline{\frac{\partial \phi^{\mathrm{w}}}{\partial \xi}}_{i+\frac{1}{2},j} \left(\frac{z^{\mathrm{b}}_{i+1} - z^{\mathrm{b}}_i}{x_{i+1} - x_i} \right. \right.$$
$$\left. \left. + \xi^{\mathrm{w}}_{i+\frac{1}{2},j} \frac{Z^{\mathrm{e}}_{i+1} - Z^{\mathrm{e}}_i}{x_{i+1} - x_i} \right) \right\}. \tag{F.35b}$$

The $\overline{\partial\phi^{\mathrm{w}}/\partial\xi_{i+\frac{1}{2},j}}$ term can be constructed using equation (F.32). In addition, the hydraulic conductivity in equations (F.35) is defined on the centered grid because equations (5.19) and (5.20) are dependent on n_p^{i}, F_ℓ, and b that reside on the centered grid (Table F.3). Typically, harmonic averages are used for flux perpendicular to layering and arithmetic averages are used for flux parallel to layering. For the anisotropic, nonlayered case, geometric averaging is appropriate. Without prior knowledge of the internal structure of the glacier, I assign the averages

as geometric,

$$\overline{K^{\mathrm{w}}_{H:i,j+\frac{1}{2}}} = \sqrt{K^{\mathrm{w}}_{H:i,j} K^{\mathrm{w}}_{H:i,j+1}} \sqrt{\frac{V_{i,j} V_{i,j+1}}{V^2_{i,j+\frac{1}{2}}}}, \tag{F.36a}$$

$$\overline{K^{\mathrm{w}}_{H:i+\frac{1}{2},j}} = \sqrt{K^{\mathrm{w}}_{H:i,j} K^{\mathrm{w}}_{H:i+1,j}} \sqrt{\frac{V_{i,j} V_{i+1,j}}{V^2_{i+\frac{1}{2},j}}}, \tag{F.36b}$$

where V is the individual volume of the cell. These volumes are defined by,

$$V_{i,j} = W \left(x_{i+\frac{1}{2}} - x_{i-\frac{1}{2}} \right) \left(\xi^{\mathrm{w}}_{j+\frac{1}{2}} - \xi^{\mathrm{w}}_{j-\frac{1}{2}} \right), \tag{F.37a}$$

$$V_{i+\frac{1}{2},j+\frac{1}{2}} = W \left(x_{i+1} - x_i \right) \left(\xi^{\mathrm{w}}_{j+1} - \xi^{\mathrm{w}}_{j} \right), \tag{F.37b}$$

where W indicates that the volumes have unit width. Combinations of subscripts are quickly realized using equations (F.37) as a template.

The mass balances and the thermal balance (eqs. F.29) are all discretized using a second-order finite volume technique. The evolution of porosity becomes,

$$\frac{\partial n^{\mathrm{i}}_p}{\partial t}_{i,j} = \frac{m_{v:i,j} - d_{v:i,j}}{\rho^{\mathrm{i}}} - \overline{\frac{\partial n^{\mathrm{i}}_p}{\partial \xi}}_{i,j} \frac{1}{Z^{\mathrm{e}}_i} \left(\frac{dz^{\mathrm{b}}}{dt}_{i} + \xi^{\mathrm{w}}_j \frac{dZ^{\mathrm{e}}}{dt}_{i} \right), \tag{F.38}$$

where the closure rate (eq. 5.23) has an obvious discretization,

$$d_{v:i,j} = \rho^{\mathrm{i}} n^{\mathrm{i}}_{p:i,j} \operatorname{sgn}\left(p^{\mathrm{i}}_{i,j} - p^{\mathrm{w}}_{i,j} \right) \left(\frac{|p^{\mathrm{i}}_{i,j} - p^{\mathrm{w}}_{i,j}|}{n\mathcal{B}} \right)^n. \tag{F.39}$$

In this equation, there are no averages or gradients that require a special formulation. Additionally, the melt rate from equation (5.25) becomes,

$$m_{v:i,j} = 1.27 \left(\frac{\rho^{\mathrm{w}} c^{\mathrm{w}}_p K^{\mathrm{w}}_T \overline{q^{\mathrm{w}}_{i,j}}}{n^{\mathrm{i}}_{p:i,j} b_{i,j}} \right)^{\frac{1}{2}} \frac{F_{\ell:i,j} \Delta T_{\mathrm{mp}:i,j}}{L}, \tag{F.40}$$

where $\overline{q^{\mathrm{w}}_{i,j}}$ requires elucidation. Because $\mathbf{q}^{\mathrm{w}}$ lies on the staggered grid, $\overline{q^{\mathrm{w}}_i}$ is an averaged magnitude such that

$$\overline{q^{\mathrm{w}}_i} = \frac{1}{2} \left\{ \left(q^{\mathrm{w}}_{x:i+\frac{1}{2},j} + q^{\mathrm{w}}_{x:i-\frac{1}{2},j} \right)^2 + \left(q^{\mathrm{w}}_{z:i,j+\frac{1}{2}} + q^{\mathrm{w}}_{z:i,j-\frac{1}{2}} \right)^2 \right\}^{\frac{1}{2}}. \tag{F.41}$$

The final term that is necessary in equation (F.38) is $\overline{\partial n^{\mathrm{i}}_p / \partial \xi_{i,j}}$, which is simply an average of the differences via equation (F.33).

The second mass balance equation and the thermal balance are discretized in a similar fashion to equation (F.38),

$$\begin{aligned}\left.\frac{\partial p^{\mathrm{w}}}{\partial t}\right|_{i,j} =& -\frac{1}{n^{\mathrm{i}}_{p:i,j}\alpha^{\mathrm{w}} + (1-n^{\mathrm{i}}_{p:i,j})\alpha^{\mathrm{i}}}\left\{(\nabla\cdot\mathbf{q}^{\mathrm{w}})_{i,j} + \left(1-\frac{\rho^{\mathrm{i}}}{\rho^{\mathrm{w}}}\right)\left.\frac{\partial n^{\mathrm{i}}_p}{\partial t}\right|_{i,j}\right\} \\ & - \overline{\left.\frac{\partial p^{\mathrm{w}}}{\partial \xi}\right|_{i,j}}\frac{1}{Z^{\mathrm{e}}_i}\left(\left.\frac{dz^{\mathrm{b}}}{dt}\right|_i + \xi^{\mathrm{w}}_i\left.\frac{dZ^{\mathrm{e}}}{dt}\right|_i\right), \qquad \text{(F.42a)}\\ \left.\frac{\partial T^{\mathrm{w}}}{\partial t}\right|_{i,j} =& -\left\{\frac{\overline{q^{\mathrm{w}}_{x:i,j}}}{n^{\mathrm{i}}_{p:i,j}}\left[\overline{\left.\frac{\partial T^{\mathrm{w}}}{\partial x}\right|_{i,j}} - \frac{1}{Z^{\mathrm{e}}_i}\overline{\left.\frac{\partial T^{\mathrm{w}}}{\partial \xi}\right|_{i,j}}\left(\overline{\left.\frac{dz^{\mathrm{b}}}{dx}\right|_i} + \xi^{\mathrm{w}}_j\overline{\left.\frac{dZ^{\mathrm{e}}}{dx}\right|_i}\right)\right] + \frac{\overline{q^{\mathrm{w}}_{z:i,j}}}{n^{\mathrm{i}}_{p:i,j}Z^{\mathrm{e}}_i}\overline{\left.\frac{\partial T^{\mathrm{w}}}{\partial \xi}\right|_{i,j}}\right\} \\ & - \frac{m_{v:i,j}-d_{v:i,j}}{\rho^{\mathrm{w}}c^{\mathrm{w}}_p n^{\mathrm{i}}_{p:i,j}}\left(L + c^{\mathrm{w}}_p\Delta T_{\mathrm{mp}:i,j}\right) + \frac{g}{c^{\mathrm{w}}_p K^{\mathrm{w}}_{H:i,j}}\left(\frac{\overline{q^{\mathrm{w}}_{i,j}}}{n^{\mathrm{i}}_{p:i,j}}\right)^2 \\ & - \frac{1}{Z^{\mathrm{e}}_i}\overline{\left.\frac{\partial T^{\mathrm{w}}}{\partial \xi}\right|_{i,j}}\left(\left.\frac{dz^{\mathrm{b}}}{dt}\right|_i + \xi^{\mathrm{w}}_j\left.\frac{dZ^{\mathrm{e}}}{dt}\right|_i\right). \qquad \text{(F.42b)}\end{aligned}$$

In equation (F.42a), averaging of $\overline{\partial p^{\mathrm{w}}/\partial\xi_{i,j}}$ to the centered grid is accomplished via equation (F.33). In equation (F.42b), $\overline{\partial T^{\mathrm{w}}/\partial\xi_{i,j}}$ is similarly averaged using equation (F.33), and $\overline{q^{\mathrm{w}}_{i,j}}$ is obtained via equation (F.41). The difficulty in discretizing equation (5.18) is the first term, $-(\mathbf{q}^{\mathrm{w}}\cdot\nabla T^{\mathrm{w}})/n^{\mathrm{i}}_p$, which enlarges because of the coordinate transformation in equation (F.29c). The result of this difficulty is that there are six averages in equation (F.42b) with one of these being repeated. Luckily, these are simple averages where $\overline{q^{\mathrm{w}}_{x:i,j}}$, $\overline{\partial T^{\mathrm{w}}/\partial x_{i,j}}$, $\overline{dz^{\mathrm{b}}/dx_i}$, and $\overline{dZ^{\mathrm{e}}/dx_i}$ are averaged from the horizontal staggered grid to the centered grid. Similarly, $\overline{\partial T^{\mathrm{w}}/\partial\xi_{i,j}}$ and $\overline{q^{\mathrm{w}}_{z:i,j}}$ are simple vertical averages from the vertical staggered grid to the centered grid.

Implementation of equations (F.38) and (F.42) and their supporting equations uses computational matrix operators as well as MATLAB's sparse matrix functions. The discretization is formally second-order accurate, but averages may slightly reduce this level of accuracy.

F.3.3 Boundary conditions

The upstream and downstream Dirichlet conditions on temperature and pressure outside the aquifer are necessary. Downstream, the pressure is atmospheric, and the temperature is taken to be zero degrees. Upstream, the hydrostatic pressure in the crevasse is the boundary condition. Glaciers undoubtedly exchange water between a more rapidly filling and draining system of crevasses and a slower englacial hydrology, and other models incorporate this feature (*e.g.,* Flowers, 2000).

F.3.4 Initialization

From the initial water height, the initial temperature profile can be found by assuming that the water is at the equilibrium zero. This assumption requires that the pressure in the water be known. The obvious choice for the pressure is simply setting the englacial water pressure equal to local hydrostatic pressure,

$$p^{\mathrm{e}}(x,z,0) = \rho^{\mathrm{w}}g\left(z^{\mathrm{e}}-z\right). \qquad \text{(F.43)}$$

For a regular but nonuniform grid in z, an average pressure over the nonuniform portion of the grid is necessary. The technique used to obtain this average pressure is shown in equation

(G.5). Temperature is then found from pressures using the Clausius-Clapeyron relationship. Initial porosities and fracture densities must be set arbitrarily.

F.4 Sheet closure

The discussion of subglacial sediments in Chapter 4 notes that large grains are poorly represented by most sampling techniques. However, in Chapter 3, it is clear that larger grain sizes are important for sheet closure. A reasonable way through this conundrum is to extend the grain size distribution using the fractal distribution (eq. 3.23 or 4.18) along the Φ scale.

Grain sizes are commonly classified using the Φ scale where

$$\Phi = -\log_2 D, \tag{F.44}$$

and D is a characteristic grain diameter in millimeters. The Φ scale is usually constructed from $\Phi = -8$ ($D = 0.256$ m, boulder gravel) to $\Phi = 8$ ($D \simeq 0.91 \times 10^{-6}$ m, clay) and centered at $\Phi = 0$ ($D = 0.001$ m, coarse sand) for a total of 17 grain sizes. Extending the scale to $\Phi = -9$ ($D = 0.512$ m, boulder) gives a reasonable distribution for the closure relation (Fig. F.4). While not a perfect match, any reported data for larger grain sizes would fall along or could be easily converted to the Φ scale.

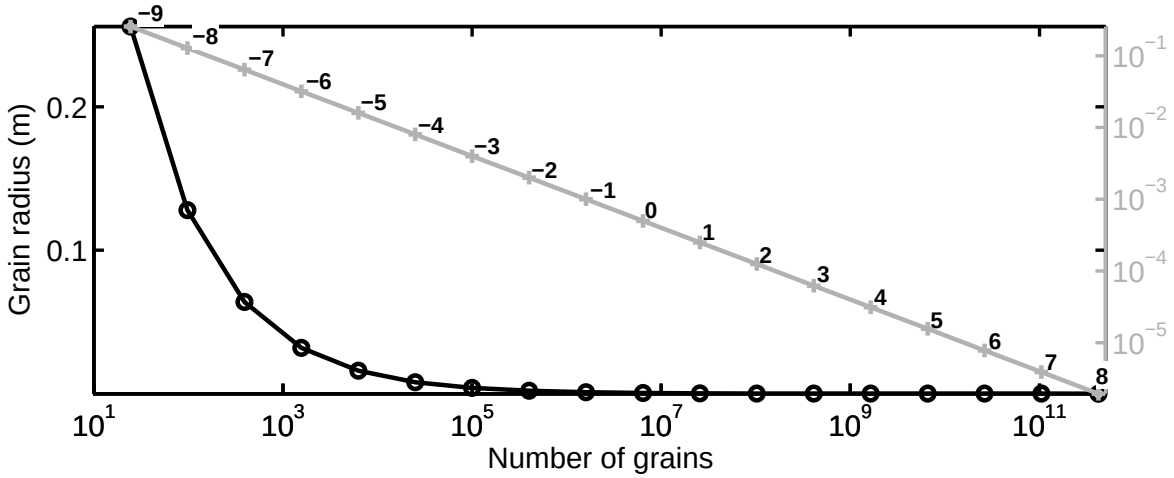

Figure F.4: Grain size distribution used in the model. Vertical axis on the left size is linear and corresponds to the black line. Right vertical axis is logarithmic and corresponds to the gray line. Numbers along the gray line are the corresponding Φ values. Both lines contain the same information. The number of grains corresponds to 100 m^2 but will change depending on the grid cell size. The relations among the points and curves will remain the same, however.

When the value of water pressure is lower than the value of ice overburden stress, sheet closure occurs according to equations (3.17). Solution of these equations requires using Newton's method for $N+1$ variables, where N is the number of grain sizes on the bed exposed to the ice. Performing these iterations for all spatial grid cells becomes computationally expensive within a few time steps.

Equations (3.17) describe a steady-state process, and the erosion rules presented in Chapter 4 do not change the distribution of sediments governing sheet closure. These two details can

be exploited to make a lookup table whereby the steady state values are computed for a range of reasonable overburden stresses and water pressures prior to integrating the water flow model through time. The closure rates should be insensitive to low erosion rates because sheet closure depends more strongly on larger grains. Erosion will affect the grains smaller than $\Phi = -1$. Furthermore, the effective length scales (eqs. 3.18–3.22) are insensitive to a change in the grid size provided that the grain size distributions are linked directly to A^{i} and that partial grains are used in the grain size distributions. Physically, partial grains are those sediment grains that intersect more than one grid cell or intersect the unit width of flow in the y-direction.

Closure velocities for the synthetic longitudinal section are presented in Figure F.5 (see also Fig. A.1) where the half grain case is used (eqs. 3.20). The numerical solution in Figure F.5a is calculated every 0.002 m from 0.001 m to 0.255 m. Driving stress is calculated at 25 equally spaced points between zero and ten meters of ice equivalent driving stress (equivalent to spacing 0.42 m or 3750 Pa). From 10 meters of ice equivalent driving stress to the stress, there are 75 equally spaced points (equivalent to 0.56 m of ice equivalent driving stress or 5000 Pa). The driving stress grid is intentionally tighter at lower driving stresses because water pressures in subglacial sheets should be near the ice overburden stress. The maximum ice thickness for the synthetic section is 46.86 meters (Table A.1). Because ice may accrete throughout a model run, the maximum driving stress in Figures F.5 is 51.3 meters or 110% of the maximum ice thickness in the synthetic section.

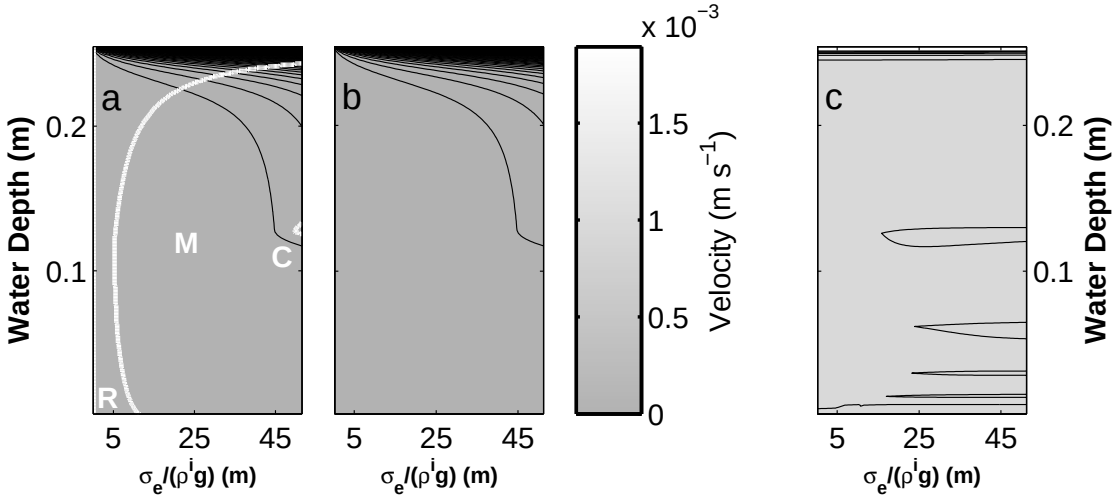

Figure F.5: Comparison of calculated and interpolated closure schemes. Contours for Figures (a) and (b) are spaced at 1.0×10^{-6} m s^{-1}. (a) Calculated closure velocities. Regelation, mixed, and creep regimes are delineated by white contours and denoted by white R, M, and C, respectively. (b) Closure velocities interpolated from Figure (a). Closure regimes are the same as in (a). (c) Normalized residual between the calculated and interpolated values. Contour intervals are 0.025.

Between Figures F.5a and F.5b, there is little noticeable difference. Figure F.5b shows the values interpolated halfway between the numerical solution points discussed above. Figure F.5c shows the normalized residual. Horizontal lines are contours at 0.00 normalized error. The importance of this figure is not in the values, but in the locations of the maximum errors. The contours capture the seven largest grain sizes. The maximum errors for each of these grain sizes at the radius height is recapitulated in Table F.4. The error results from the change in closure

velocity as the number of grains touching the overlying ice changes. For r_1 the maximum error occurs at a low driving stress. Obviously, if the water depth meets or exceeds the maximum grain size, there will be a numerical instability as the ice floats off its bed. Thus, error from the largest grain size is not of principal concern because that grain size is problematic for physical reasons ab initio. For all other grain sizes, maximum error occurs at the maximum driving stress. For water depths at or below r_3 the absolute value of the maximum error is less than 0.03 such that a lookup table appears to be a reasonable approximation to the closure relationship. Furthermore, the errors introduced by interpolation via a lookup table are much smaller than the probable errors introduced by assuming a grain size distribution.

Note that when the value of water pressure is greater than the value of the ice overburden stress, the closure relation reverts to creep closure (eq. 3.8). Because creep is not dependent on a Newton-Raphson numerical iteration, creep velocities are computed whenever necessary in the appropriate time step.

Table F.4: Maximum interpolation errors for each of the largest grain sizes.

Grain	Radius (m)	Error	$\sigma_e/(\rho^{\mathrm{i}}g)$ (m)
r_1	0.256	1.220	0.21
r_2	0.128	0.002	0.21
r_3	0.064	0.001	51.3
r_4	0.032	0.0004	51.3
r_5	0.016	0.0003	51.3
r_6	0.008	0.0001	51.3
r_7	0.004	-0.0002	51.3

Negative error values indicate that the interpolated solution is greater than the numerical solution.

F.4.1 Grain volume

Because the largest grains take a portion of the volume of the sheet the maximum thickness of the sheet $H^{\mathrm{b}}_{\mathrm{max}}$, is not the same as the average thickness H^{b}. However, the closure relationship acts on the maximum thickness rather than the average thickness. Because the distribution of sediments that define the closure relationship is known a priori, the relationship between the maximum and average thickness is also known a priori. For the half grain case with a distribution given by Figure F.4, the average thickness is

$$H^{\mathrm{b}} = \frac{1}{A^{\mathrm{i}}}\left\{ n_a^{\mathrm{w}} A^{\mathrm{i}} H^{\mathrm{b}}_{\mathrm{max}} + \left(A^{\mathrm{i}} - n_a^{\mathrm{w}} A^{\mathrm{i}}\right)\left(H^{\mathrm{b}}_{\mathrm{max}} - \sum_{i=1}^{18} N^{\mathrm{s}}_{a:i}\left[\frac{2}{3}\pi r_i^3 - V_{e:i}\right]\right)\right\} \tag{F.45}$$

where n_a^{w} is the fractional area of the bed that is not covered by sediment, 18 is the number of grain sizes, and $V_{e:i}$ is the effective volume in the ice. The fractional area of the bed not covered with sediment is equivalent to the fractional area of the bed covered by water in Chapter 3. When the effective volume is zero, the volume of a grain in the flow is exactly half the volume of the sphere. The volume of the water sheet is then solely dependent on n_a^{w}, which forces the thickness of the water sheet to always be finite. This relationship is plotted in Figure F.6.

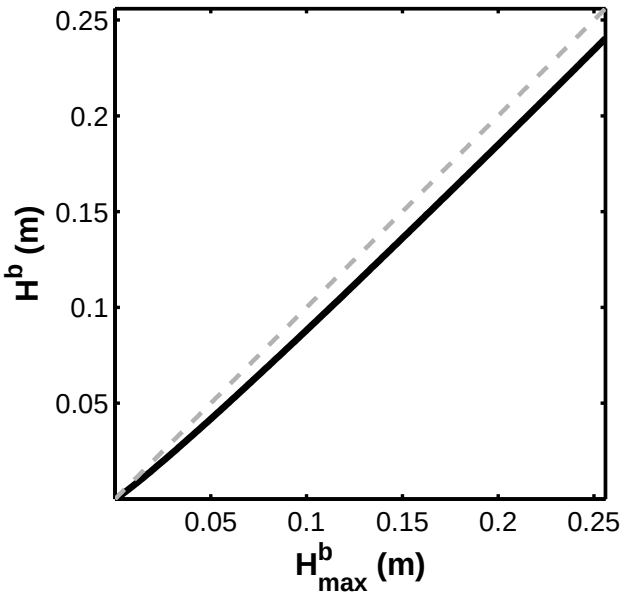

Figure F.6: Average sheet thickness versus maximum sheet thickness. The black line gives the relationship in equation (F.45) where $V_{e:i}$ is given by equation (3.20a). The dashed gray line gives $H^{\mathrm{b}} = H^{\mathrm{b}}_{\mathrm{max}}$. The average sheet thickness is less than the maximum sheet thickness.

The initialization of the sheet thickness and the closure relationship are done simultaneously so that there are no inconsistencies in the volume of either. For example, the amount of obstacle that is within the water layer must not cause the volume of water to be less or more than the average value of H^{b} indicates.

Appendix G

Additional discretization characteristics

G.1 Vertical coordinate transformation

For coordinates that change during the course of a simulation, mapping a grid that changes with time to a set, regular grid is particularly useful. The idea is that a grid may be irregular, but the these irregularly spaced points map to a regular grid. The regular grid remains constant through time while the irregular coordinates evolve with time. Haltiner & Williams (1980, p. 14–15) formulated grid mappings in general terms for partial and ordinary derivatives.

For a function $f(X, z)$, where X represents time and/or additional space coordinates and z is its vertical dependence, it is useful to have a set of mathematical rules for transforming the derivatives from z to ξ or vice versa. I recapitulate Haltiner & Williams's (1980) as well as parts of Marshall's (1996) derivation for completeness of the change of derivatives, where

$$\frac{\partial f(X,z)}{\partial X} = \frac{\partial \tilde{f}(X,\xi)}{\partial X} + \frac{\partial \tilde{f}(X,\xi)}{\partial \xi}\,\frac{\partial \xi}{\partial X}, \tag{G.1a}$$

$$\frac{\partial f(X,z)}{\partial z} = \frac{\partial \tilde{f}(X,\xi)}{\partial \xi}\,\frac{\partial \xi}{\partial z}, \tag{G.1b}$$

$$\begin{aligned}\frac{\partial^2 f(X,z)}{\partial z^2} &= \frac{\partial}{\partial z}\left\{\frac{\partial \tilde{f}(X,\xi)}{\partial \xi}\,\frac{\partial \xi}{\partial z}\right\},\\ &= \frac{\partial^2 \tilde{f}(X,\xi)}{\partial \xi^2}\left(\frac{\partial \xi}{\partial z}\right)^2 + \frac{\partial \tilde{f}(X,\xi)}{\partial \xi}\frac{\partial \xi}{\partial z}\,\frac{\partial}{\partial \xi}\left(\frac{\partial \xi}{\partial z}\right),\\ &= \frac{\partial^2 \tilde{f}(X,\xi)}{\partial \xi^2}\left(\frac{\partial \xi}{\partial z}\right)^2 + \frac{\partial \tilde{f}(X,\xi)}{\partial \xi}\,\frac{\partial^2 \xi}{\partial z^2}.\end{aligned} \tag{G.1c}$$

In these equations, f and $\tilde{f}$ have the same value but are be labeled as different variables because of the change in vertical coordinate.

G.2 Finite volume averages on non-rectilinear meshes

For any two-dimensional mesh, the four corners around point (i, j) are defined as $(i-\frac{1}{2}, j-\frac{1}{2})$, $(i+\frac{1}{2}, j-\frac{1}{2})$, $(i-\frac{1}{2}, j+\frac{1}{2})$, and $(i+\frac{1}{2}, j+\frac{1}{2})$ (Fig. G.1a). Each of these points has a corresponding x and z that define mesh location. For a mesh with only a vertical transformation, $x_{i-\frac{1}{2},j-\frac{1}{2}}$ and $x_{i-\frac{1}{2},j+\frac{1}{2}}$ have the same numerical value; and $x_{i+\frac{1}{2},j-\frac{1}{2}}$ and $x_{i+\frac{1}{2},j+\frac{1}{2}}$ have the same numerical value (Fig. G.1). The numerical values of $z_{i-\frac{1}{2},j-\frac{1}{2}}$, $z_{i-\frac{1}{2},j+\frac{1}{2}}$, $z_{i+\frac{1}{2},j-\frac{1}{2}}$, and $z_{i+\frac{1}{2},j+\frac{1}{2}}$ can all be different.

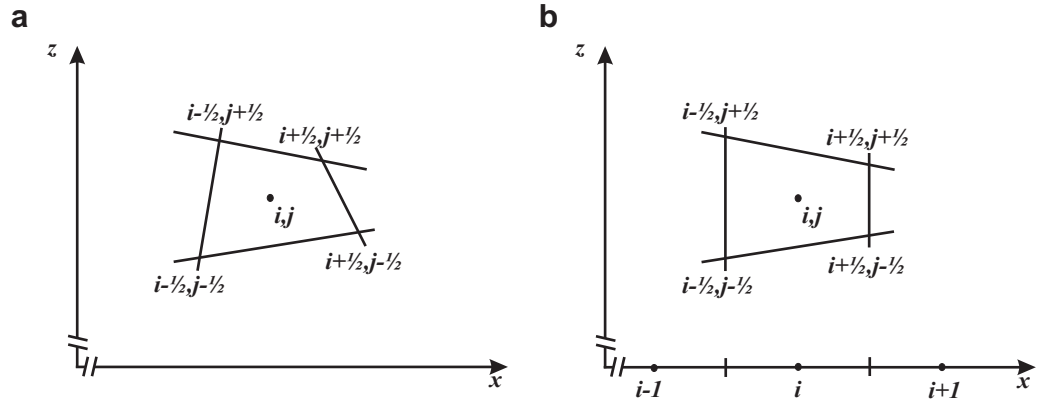

Figure G.1: Four-cornered two-dimensional grid. (a) Illustration of an irregular grid in x and z. (b) A similar illustration where the grid in x is uniform.

The finite volume method relies on the smooth scalar quantity $f(x,z)$ being represented by a volume-average of that quantity placed at the centroid of the cell. Mathematically, this integration looks like a two-dimensional average,

$$\overline{f(x_{ij},z_{ij})} = \frac{1}{A_{ij}} \int_{x_{i-\frac{1}{2}}}^{x_{i+\frac{1}{2}}} \int_{z_{\text{lower}}}^{z_{\text{upper}}} f(x,z)\, dz\, dx, \tag{G.2}$$

where the area A_{ij} is simply the area of the trapezoid,

$$A_{ij} = \frac{1}{2}\left(x_{i+\frac{1}{2}} - x_{i-\frac{1}{2}}\right)\left\{\left(z_{i+\frac{1}{2},j+\frac{1}{2}} - z_{i+\frac{1}{2},j-\frac{1}{2}}\right) + \left(z_{i-\frac{1}{2},j+\frac{1}{2}} - z_{i-\frac{1}{2},j-\frac{1}{2}}\right)\right\}. \tag{G.3}$$

In equation (G.2) the limits of integration in z are simply the lines associated with the lower and upper limits of the trapezoid,

$$z_{\text{upper}} = \frac{z_{i+\frac{1}{2},j+\frac{1}{2}} - z_{i-\frac{1}{2},j+\frac{1}{2}}}{x_{i+\frac{1}{2}} - x_{i-\frac{1}{2}}}\left(x - x_{i-\frac{1}{2}}\right) + z_{i-\frac{1}{2},j+\frac{1}{2}}, \tag{G.4a}$$

$$z_{\text{lower}} = \frac{z_{i+\frac{1}{2},j-\frac{1}{2}} - z_{i-\frac{1}{2},j-\frac{1}{2}}}{x_{i+\frac{1}{2}} - x_{i-\frac{1}{2}}}\left(x - x_{i-\frac{1}{2}}\right) + z_{i-\frac{1}{2},j-\frac{1}{2}}, \tag{G.4b}$$

where both equations are in standard linear notation.

An example of the usage of the integration in equation (G.2) is the averaging of a variable that is linear in depth. One example of this type of variable is the gravitational potential $\rho^{\text{w}} g z$. In this case $f(x,z)$ is simply the vertical coordinate z, and integration yields

$$\begin{aligned}\overline{z_{ij}} &= \frac{1}{A_{ij}} \int_{x_{i-\frac{1}{2}}}^{x_{i+\frac{1}{2}}} \int_{z_{\text{lower}}}^{z_{\text{upper}}} z\, dz\, dx, \\ &= \frac{1}{3}\left(\frac{z^2_{i+\frac{1}{2},j+\frac{1}{2}} + z_{i+\frac{1}{2},j+\frac{1}{2}} z_{i-\frac{1}{2},j+\frac{1}{2}} + z^2_{i-\frac{1}{2},j+\frac{1}{2}} - z^2_{i+\frac{1}{2},j-\frac{1}{2}} - z_{i+\frac{1}{2},j-\frac{1}{2}} z_{i-\frac{1}{2},j-\frac{1}{2}} - z^2_{i-\frac{1}{2},j-\frac{1}{2}}}{z_{i+\frac{1}{2},j+\frac{1}{2}} + z_{i-\frac{1}{2},j+\frac{1}{2}} - z_{i+\frac{1}{2},j-\frac{1}{2}} - z_{i-\frac{1}{2},j-\frac{1}{2}}}\right).\end{aligned} \tag{G.5}$$

Equation (G.5) can be expanded to include six vertices of an irregular solid volume. In its present form, equation (G.5) is also the weighting per unit glacier width.

G.3 Interpolation of bed and surface topography

For surface and bed topography data from glaciers without regular sampling, it is important to interpolate the irregular sampling to a regular grid. For the purposes of presentation, the irregular grid has M points and will be denoted with M when the grid is indicated. Similarly, the regular grid N, has N points.

The M points of the irregular grid have an ordinate, z^{s}_i, and an abscissa, x_i. From these values, an along path coordinate is, in a simple Pythagorean sense,

$$\Delta s_{\mathrm{M}:i} = \left\{ \left(z^{\mathrm{s}}_{\mathrm{M}:i+1} - z^{\mathrm{s}}_{\mathrm{M}:i} \right)^2 + \left(x_{\mathrm{M}:i+1} - x_{\mathrm{M}:i} \right)^2 \right\}^{\frac{1}{2}}, \tag{G.6}$$

where the beginning of the grid is set at $s_{\mathrm{M}:1} = 0$. The resulting values of $s_{\mathrm{M}:i}$ are

$$s_{\mathrm{M}:i+1} = s_{\mathrm{M}:1} + \sum_{i=1}^{M-1} \Delta s_{\mathrm{M}:i}. \tag{G.7}$$

The differenced regular grid between cell centers is

$$\Delta s_{\mathrm{N}} = \frac{s_{\mathrm{M}:M} - s_1}{M-1}. \tag{G.8}$$

As opposed to the irregular grid, all points on the regular grid have a common spacing,

$$s_{\mathrm{N}:i} = s_{\mathrm{M}:1} + (i-1)\Delta s_{\mathrm{N}}, \tag{G.9}$$

but both grids start at $s_{M:1} = s_{N:1} = 0$.

The staggered grid is computed via

$$s_{\mathrm{N}:i+\frac{1}{2}} = s_{\mathrm{N}:i} + \frac{\Delta s_{\mathrm{N}}}{2} \quad \text{for} \;\; i = 1 : N-1. \tag{G.10}$$

If any of the interpolated values for s_{N} fall on the s_{M} values, then $x_{\mathrm{N}:i}$ and $z_{\mathrm{N}:i}$ are assigned the values of $x_{\mathrm{M}:i}$ and $z_{\mathrm{M}:i}$, respectively. If a new grid point, $s_{\mathrm{N}:j}$ falls between two old grid points, $s_{\mathrm{M}:j}$ and $s_{\mathrm{M}:j+1}$, then a linear interpolation scheme is used to find the new values for $x_{\mathrm{N}:j}$ and $z^{\mathrm{s}}_{\mathrm{N}:j}$,

$$x_{\mathrm{N}:j} = (s_{\mathrm{N}:j} - s_{\mathrm{M}:i}) \, \frac{x_{\mathrm{M}:i+1} - x_{\mathrm{M}:i}}{s_{\mathrm{M}:i+1} - s_{\mathrm{M}:i}} + x_{\mathrm{M}:i}, \tag{G.11a}$$

$$z^{\mathrm{s}}_{\mathrm{N}:j} = (s_{\mathrm{N}:j} - s_{\mathrm{M}:i}) \, \frac{z^{\mathrm{s}}_{\mathrm{M}:i+1} - z^{\mathrm{s}}_{\mathrm{M}:i}}{s_{\mathrm{M}:i+1} - s_{\mathrm{M}:i}} + z^{\mathrm{s}}_{\mathrm{M}:i}. \tag{G.11b}$$

Similarly, the surface topography of the glacier is interpolated with a linear scheme such that $z^{\mathrm{r}}_{\mathrm{M}}$ is interpolated to $z^{\mathrm{r}}_{\mathrm{N}}$. The thickness of the glacier is thus $Z^{\mathrm{i}}_i = z^{\mathrm{r}}_{\mathrm{N}:i} - z^{\mathrm{b}}_{\mathrm{N}:i}$. Terms on the staggered grid $x_{\mathrm{N}:j+\frac{1}{2}}$ and $z_{\mathrm{N}:j+\frac{1}{2}}$, are created in much the same way as $s_{\mathrm{N}:j+\frac{1}{2}}$ in equation (G.10). From these relations, $\partial z / \partial s_{\mathrm{N}:+\frac{1}{2}}$ can be created.